Bhuvanesh Gupta
Anup K. Ghosh
Atsushi Suzuki
Sunita Rattan *Editors*

Advances in Polymer Sciences and Technology

Select Papers from APA 2017

Springer

Materials Horizons: From Nature to Nanomaterials

Series editor

Vijay Kumar Thakur, School of Aerospace, Transport and Manufacturing, Cranfield University, Bedford, UK

Materials are an indispensable part of human civilization since the inception of life on earth. With the passage of time, innumerable new materials have been explored as well as developed and the search for new innovative materials continues briskly. Keeping in mind the immense perspectives of various classes of materials, this series aims at providing a comprehensive collection of works across the breadth of materials research at cutting-edge interface of materials science with physics, chemistry, biology and engineering.

This series covers a galaxy of materials ranging from natural materials to nanomaterials. Some of the topics include but not limited to: biological materials, biomimetic materials, ceramics, composites, coatings, functional materials, glasses, inorganic materials, inorganic-organic hybrids, metals, membranes, magnetic materials, manufacturing of materials, nanomaterials, organic materials and pigments to name a few. The series provides most timely and comprehensive information on advanced synthesis, processing, characterization, manufacturing and applications in a broad range of interdisciplinary fields in science, engineering and technology.

This series accepts both authored and edited works, including textbooks, monographs, reference works, and professional books. The books in this series will provide a deep insight into the state-of-art of *Materials Horizons* and serves students, academic, government and industrial scientists involved in all aspects of materials research.

More information about this series at http://www.springer.com/series/16122

Bhuvanesh Gupta · Anup K. Ghosh
Atsushi Suzuki · Sunita Rattan
Editors

Advances in Polymer Sciences and Technology

Select Papers from APA 2017

Editors
Bhuvanesh Gupta
Department of Textile Technology
Indian Institute of Technology Delhi
New Delhi, Delhi, India

Anup K. Ghosh
Department of Materials Science
    and Engineering, Centre for Polymer
    Science and Engineering (CPSE)
Indian Institute of Technology Delhi
New Delhi, Delhi, India

Atsushi Suzuki
Yokohama National University
Yokohama, Japan

Sunita Rattan
Amity Institute of Applied Sciences
Amity University
Noida, Uttar Pradesh, India

Preface

Polymers offer enormous opportunities towards newer applications in technologically important areas. There is a great necessity to have an integral approach towards this complementary relationship of polymers and their performance. These polymeric materials have shown multidirectional growth in several areas of technological innovations, which ranges from biomedical polymers to the fascinating field of smart materials. A precise understanding of the molecular architecture and its role in governing physical characteristics is extremely useful to understand their applications.

The International Conference on Advances in Polymer Science and Technology was organized with the aim to provide a common forum for eminent scientists, technologists, entrepreneurs and research scholars to present their work and discuss the latest advances in this exciting area of research and add on new dimensions in different application areas.

It is with great pleasure that we bring out this volume, which includes papers selected from the presentations made at the International Conference on Advances in Polymer Science and Technology held during 23–25 November 2017 at New Delhi, India. This event was attended by about 450 participants from all continents.

The conference was organized under the auspices of Asian Polymer Association (APA), a professional society dedicated to the science of polymers, in collaboration with Indian Institute of Technology (IIT) Delhi, Central Institute of Plastics Engineering & Technology (CIPET), Society for Biomaterials & Artificial Organs (Delhi, India) and Indo-Italian Forum on Biomaterials & Tissue. The conference was dedicated to the world of polymers with an extensive interaction among academicians, researchers, technologists and policy planners.

This special edition introduces new classes of polymeric materials with unique applications. The articles cover health, medicine and biotechnology, a rapidly developing domain based largely on known materials but moving to designed and engineered polymers, and information and communications, an emerging field for polymers significantly based on their electronic properties. These two areas are attracting a great deal of attention, particularly among researchers who are not

traditional specialists in polymer science. The growing importance of these fields makes the interdisciplinary aspect of polymer research abundantly clear.

We are sure that all the latest results and findings reported here will be useful to the researchers and scientists working in these areas. It will also be found immensely useful by the advanced-level students of physics, chemistry, materials science, electronics specializing in polymers, as well as students of electronics, chemical and metallurgical engineering having courses in polymer technology/ materials science and technology.

We applaud the efforts of the conference participants and encourage their current and future personal and collaborative efforts in this important field of scientific endeavour.

The proceedings and the rich scientific knowledge exchanged between the participants are the result of the sincere efforts of a large team of people who volunteered their time to contribute to this international conference. We are indebted to them for their assistance and support and extend our heartfelt thanks, on behalf of the APA 2017, for their significant contributions.

<div align="right">
With warm regards,
Prof. Bhuvanesh Gupta
Prof. Anup K. Ghosh
Prof. Atsushi Suzuki
Prof. Sunita Rattan
</div>

New Delhi, India
New Delhi, India
Yokohama, Japan
Noida, India

Contents

About the Editors

Bhuvanesh Gupta is Professor in the Department of Textile Technology at the Indian Institute of Technology (IIT) Delhi. He completed his M.Phil. and Ph.D. at the Vikram University, Ujjain, India, and IIT Delhi, respectively. He worked as a scientist at various institutions in Switzerland, France and Sweden before returning to IIT Delhi as a faculty member. His research interests include modification of polymers, membranes, medical textiles, biomaterials and tissue engineering. He has authored eight books and more than 170 research papers, holds 25 patents and serves on the editorial boards of seven international journals.

Prof. Anup K. Ghosh is Professor and Head of the Centre for Polymer Science and Engineering at the Indian Institute of Technology Delhi. He has over 29 years of research and teaching experience and holds seven patents. He is known for his accomplishments in the field of polymer processing and rheology and has significantly contributed in the areas of reactive processing of polymer blends and alloys, polymer packaging and microcellular processing of polymeric materials. He obtained an M.Tech. in chemical engineering from IIT Kanpur, India, and a Ph.D. in chemical engineering from the State University of New York at Buffalo, USA. He worked as Postdoctoral Research Fellow at the University of Pittsburgh, USA, before joining IIT Delhi in 1991. He is Fellow of the National Academy of Sciences, India, and a recipient of numerous prestigious awards, including Meritorious Service Award by the Indian Plastics Institute, Mumbai, India, and the IIT Delhi Teaching Excellence Award. He also held the prestigious Reliance Chair Professorship at IIT Delhi from 2006 to 2011. He is Associate Editor of the Journal of Packaging Technology and Research and is a member of the Editorial Board of the Journal of Plastics Film & Sheeting and International Journal of Plastics Technology.

Atsushi Suzuki is Professor in the Division of Artificial Environment and Information at the Yokohama National University, Japan. He completed his Ph.D. in engineering at the University of Tokyo. His research interests include gel science and technology, smart hydrogels and ecomaterials.

Sunita Rattan is Professor and Additional Director at the Amity Institute of Applied Sciences, Amity University, Uttar Pradesh, India. She completed her M.Sc. and Ph.D. in organic chemistry at Himachal Pradesh University, Shimla, India. She has more than 20 years of research and teaching experience, and her research interests include nanocomposites, smart hydrogels, chemiresistive sensors and polymer/fly ash composites. She holds 11 patents and has authored five books and more than 45 scientific papers in respected journals and conferences.

Designing and Nanofunctionalization of Infection-Resistant Polyester Suture

Sadiya Anjum and Bhuvanesh Gupta

Abstract Antimicrobial behavior in suture materials is a desirable feature that can potentially improve the healing process by inhibiting microbial growth. In this article, we demonstrate a method for the development of antimicrobial polyethylene terephthalate based sutures by plasma functionalization, followed by the immobilization of triclosan (as bioactive agent). The surface functionalization was observed by investigating carboxyl content with varying plasma exposure time. Mechanical strength, surface topography, and morphology were analyzed on these sutures. The homogeneous distribution of triclosan in suture was observed by energy dispersive X-ray analysis. Antimicrobial studies suggest that resulting PET sutures have excellent bacteriostatic and bactericidal properties against *S. aureus* and *E. coli*. Our study suggests that developed sutures can inhibit bacterial adherence and colonization on the surgical site and appears to be a promising material for surgical applications.

Keywords Polyethylene terephthalate · Antimicrobial sutures · Biofilm
Surface functionalization · Triclosan

1 Introduction

Smart wound care requires materials which provide scar free optimum healing without any risk of surgical site infection (SSI). Wound closure requires postoperative suturing of a tissue which leaves behind the strong possibility of infection migration through the suture site [1]. Moreover, if the wound is infectious, bacteria may colonize on the suture surface and may lead to serious complications. The investigation of the infection is certainly related to the nature and origin of the suture. This would influence the bacterial adhesion and its transmittance into the wound. The magnitude of the infection is related to the nature and the origin of the suture which would

S. Anjum · B. Gupta (✉)
Bioengineering Laboratory, Department of Textile Technology, Indian Institute
of Technology, New Delhi 110016, India
e-mail: bgupta@textile.iitd.ernet.in

influence the bacterial adhesion, its colonization, and penetration into the tissue. The infection may sometimes grow to such an extent that it may cause septicemia as well [2]. Almost 23% of SSI are due to the colonization leading to significantly high healthcare expenses.

Efforts are being made to develop sutures which are inherently antimicrobial in nature and do not allow bacterial adhesion or invasion by virtue of the bacteriostatic or bactericidal nature against different microbes [3]. The ideal situation would be to have a suture which is antimicrobial in nature and does not allow any infection to grow in its vicinity leading to a healthy tissue growth. Ethicon has developed poly(lactic-co-glycolic acid) suture which is marketed as *Vicryl+* and is effective against a large number of microbes. This invention led to a large number of people entering into the suture technology where infection resistance against different bacteria may be achieved [4]. Both the biostable and biodegradable sutures are being investigated for creating the structure that would offer required features in a surgical kit for wound healing systems [5].

Immobilization of the biomolecules on suture surface is an essential aspect to create or generate antimicrobial nature. The important requirement is the surface should be bioreceptive in nature so that biomolecules may be anchored on the surface [6]. One of the obvious approaches may be to coat the suture surface by a bioactive component. However, this needs the suture surface to be bioreceptive so that it may bind with the biomolecule in such a way that it acts against microbes in an effective manner. After surface functionalization and bioimmobilization of bioactive agent on the suture material, the suture must retain its biocompatibility during in vivo application [7]. The nature of the bioactive agent is a prominent factor determining the effectiveness of the suture against microbes. A large number of bioactive moieties exist which show antimicrobial nature. Triclosan, *2,4,4′*-trichloro-*2*-hydroxydiphenylether is the effective antimicrobial and also possesses antifungal and antiviral properties. This has shown a very effective nature in Vicryl+. However, due to ubiquitous situation, researches are trying to get an effective alternative to triclosan [8, 9].

2 Experimental

2.1 Materials

Polyethylene terephthalate (PET) chips used in this study were supplied by Reliance Industries Ltd., India. Triclosan was purchased from Sigma Aldrich. Toluidine Blue O (TBO) (Qualigens, India), glutaraldehyde, sodium hydroxide, and acetic acid from Merck, India were used. Luria broth and agar-agar were obtained from Hi Media Laboratories, India. Bacterial strains of *S. aureus* and *E. coli* were provided by IIT Delhi. All chemicals were of analytical grade and used without further purification. Carbon dioxide gas cylinders of high purity were procured from a local supplier.

2.2 Development of PET Monofilament

Initially, PET chips were vacuum dried for 24 h at 70 °C, then dried chips were fed through the hopper and melt spun at 270 °C to obtain undrawn filaments. These extruded filaments passed through a water bath at 4 °C and were collected by a take-up winder at 30 m/min. Further, undrawn filaments were drawn on a two-stage drawing machine (Cybertex) to different draw ratios at 120 °C, respectively [7]. Drawn PET filament at a draw ratio of 2.5 had a thickness of 235 μm was used for further experiments.

2.3 Plasma Functionalization of PET Monofilament

PET monofilaments were plasma treated with carbon dioxide plasma in a capacitively coupled RF reactor operating at 13.6 MHz. The monofilament was mounted over a sample holder and rotated at 40 rpm by a motor for homogeneous exposure of plasma. The cylindrical vessel was first evacuated to 10^{-5} Torr and then carbon dioxide gas was purged introduced under the control of mass flow controller. Variables for plasma treatment were exposure time (0–180 s), gas pressure of 100 mTorr, and discharge power 40 W [7].

2.4 Determination of Carboxyl Content

The carboxyl content from the filament surface was determined by colorimetric method with TBO (toluidine blue O) staining, as reported in the literature [10]. Basic solution of TBO dye was prepared and the plasma exposed filament was placed in this solution for 6 h at room temperature. The filament was subsequently removed and washed with sodium hydroxide solution to remove noncomplexed dye adhering on the filament surface. The dye was desorbed from the filament in 50% acetic acid solution and the optical density of the solution was measured by using a UV–Visible spectrophotometer (Perkin Elmer Lambda E Z 201) at 623 nm. The carboxyl content was obtained from the calibration plot of the optical density versus dye concentration with the assumption of 1:1 ratio between the dye and the carboxyl groups.

2.5 Triclosan Immobilization on the Functionalized PET Filament

The plasma exposed PET monofilament was then immediately dipped into triclosan solution. The generated carboxyl groups were interacted with active sites of bioactive

agents and hence get attached to the filament surface. Plasma exposed samples were dipped into 1% solution of triclosan in water and ethanol phase. Treated samples were gently washed with water to remove unreacted material and dried at room temperature (henceforth called as suture).

2.6   Energy Dispersive X-ray Analysis (EDX)

The elemental analysis of pristine, triclosan immobilized PET suture was monitored by EDX analysis. The samples were placed on an aluminum stub and coated with carbon using Auto-Fine Coater JFC-1600 (Joel, USA Inc., USA). The images and the elemental quantification of the samples were obtained with RONTEC's EDX Model QuanTax 200 (SDD technology, USA).

2.7   Mechanical Studies of PET Suture

Mechanical properties of the virgin, plasma exposed, and triclosan immobilized PET sutures were performed on tensile tester, Instron model 4301. Mechanical properties of the samples were observed with a crosshead speed of 50 mm/min and gauge length of 50 mm in ambient conditions of 27 ± 2 °C and $65\% \pm 2\%$ relative humidity. Tensile strength and elongation are obtained from the stress–strain curves which are an average for 10 specimens [10].

2.8   Surface Topography of PET Suture

Surface topographical information of samples was obtained in air at room temperature by Solver Pro SPM (NT–MDT, Russia) atomic force microscopy (AFM) in semi-contact mode with NSG 10 series tips. Scanning size of each image was kept 2.5 μ × 2.5 μ and scanning rate of 1 Hz was used. Five to ten different locations were analyzed on each sample.

2.9   Antimicrobial Study

Antibacterial study of suture was carried out by colony reduction method against *E. coli* and *S. aureus* [11, 12]. Fresh cultured bacterial colonies were suspended in Luria Broth with turbidity of 0.5 McFarland standards. The suture samples (~20 mg) were placed in 6 mL bacterial suspension in Luria Broth having 10^6 CFU mL^{-1}. All suspensions of bacteria in broth were vortexed and incubated at 37 °C for 24 h.

The inoculum (200 µL) was uniformly spread on nutrient agar plate using a sterile L-shape spreader. Plates were incubated at 37 °C and the colonies were counted after 24 h.

Bacterial adherence on suture surface was observed by field emission scanning electron microscope (FEI Quanta 200F, Netherlands) with gold coating. Each suture sample was inoculated in freshly prepared suspension consisting of 1 mL of bacterial colonies and 3 mL of Luria broth. Suture samples were cultured for 24 h overnight incubation at 37 °C, 95% air/5% CO_2. Suture samples were rinsed with sterile water to remove non-adherent bacteria from the surface. Subsequently, suture samples were transferred to a sterile glass tube using sterile forcep, containing 3 mL of 2.5% glutaraldehyde solution for 24 h for the fixation of the substratum for FE-SEM analysis. Excess glutaraldehyde was removed by gentle rinses with sterile water and then serially dehydrated in ethanol than mounted on metal stubs, and sputter coated with gold [13].

3 Results and Discussion

3.1 Plasma Functionalization

The designing of an antimicrobial suture is extremely careful approach where the right choice of the material and the antimicrobial processing need to be integrated so that material retains it biocompatibility and inherent physical features during its application. The processing however involves the functionalization and the immobilization of a bioactive agent to the suture surface. The functionalization route itself may be executed depending on the nature of the suture material. PET suture may be functionalized by plasma processing. It is interesting to see that desired functional groups are created by proper selection of the carrier gas in the plasma system. While ammonia creates amino groups, CO_2 leads to the formation of the carboxyl functionality. However, oxygen creates hydroxyl as well as peroxide functionality on the suture surface (Fig. 1).

The peroxide may be subsequently used to initiate a graft polymerization process so that a high level of functional groups is achieved. The beauty of plasma activation is that it creates specific functional groups on the surface without any impact on the bulk properties and has been demonstrated to be an effective approach towards developing antimicrobial surgical implants [14]. This approach has been used to develop PET sutures with effective control over microbial infection. The functionalization in fact requires a very short exposure of few seconds leading to the activation confined to the nanoscale on the surface.

The variation of carboxyl content with plasma exposure time is shown in Fig. 2. It is evident that from 2 to 180 s plasma exposure time, the carboxyl content value increases with the increase in plasma exposure time. The increase in carboxyl content is achieved due to an increase in the number of active sites, resulting from increases
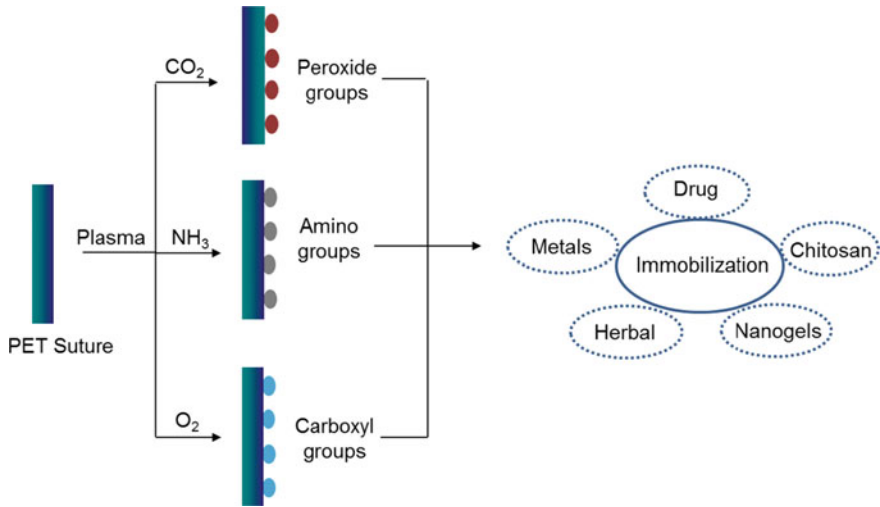
Fig. 1 Plasma functionalization route for antimicrobial sutures
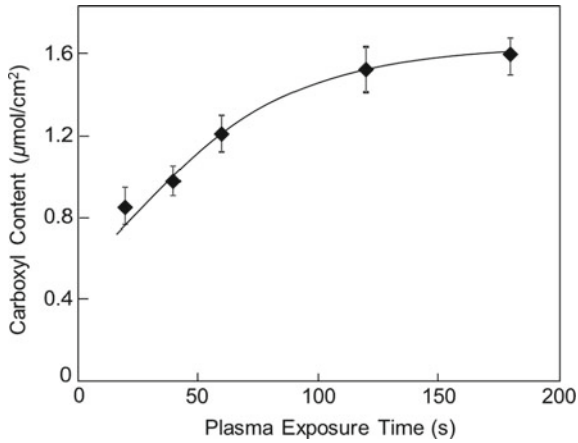
Fig. 2 Variation of the carboxyl content with the plasma exposure time. Conditions: gas, CO_2; gas pressure, 100 mTorr; discharge power, 40 W

in plasma exposure time. The presence of readily active carboxyl groups on the PET suture surface is allowed to the subsequent immobilization of biofunctional molecules such as triclosan on the PET suture surface (Fig. 3).

Fig. 3 Representation of the triclosan—immobilized PET suture (PET-TCH)
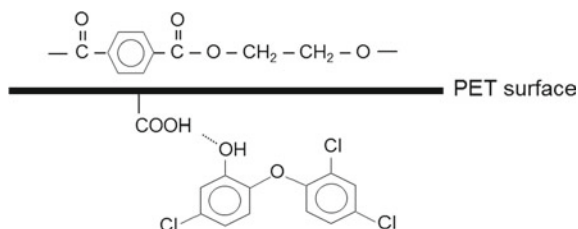
Fig. 4 Variation of the tensile strength with the plasma exposure time. Conditions: plasma exposure time, 120 s; gas, CO_2; gas pressure, 100 mTorr; discharge power, 40 W
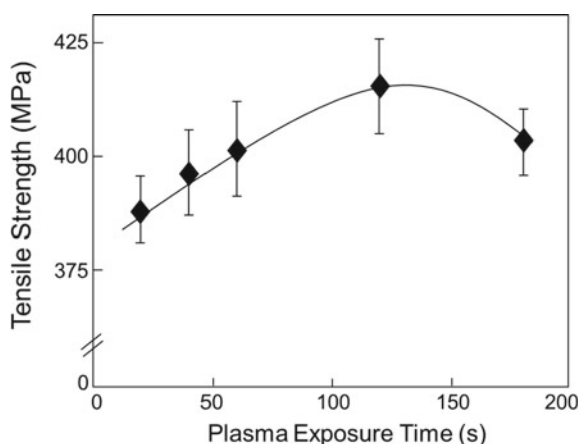
3.2 Characterizations

The tensile strength of PET suture after plasma functionalization is presented in Fig. 4. Initially, PET suture has tensile strength of 393 MPa while after plasma treatment this value increases as plasma time is increased.

At 120 s of plasma treatment, the tensile strength value reaches to 416 MPa after 120 s of plasma and this value does not show any relevant change. The tensile strength value of triclosan immobilized PET suture is almost similar to plasma functionalized suture because immobilization of triclosan has not altered the bulk property of the material.

The elemental analysis of pristine and triclosan immobilized samples was carried out by EDX analysis and presented in Fig. 5. The EDX spectrum of pristine PET suture (Fig. 5a) shows a distinctive energy peak at around 0.2 keV, characteristic peaks of carbon and oxygen with total content of O and C with 43.9, and 54.8% respectively. In PET-triclosan suture along with characteristic peaks, one new strong peak appears at ~2.5 keV, which confirmed the presence of chlorine (Fig. 5b). Furthermore, the EDX pattern of the material was found to be Cl, O, and C with 3.2, 48.7, and 47.2%, respectively.

Surface topography of the pristine, plasma functionalized, and triclosan immobilized PET suture were studied by AFM and depicted in Fig. 6. AFM image of
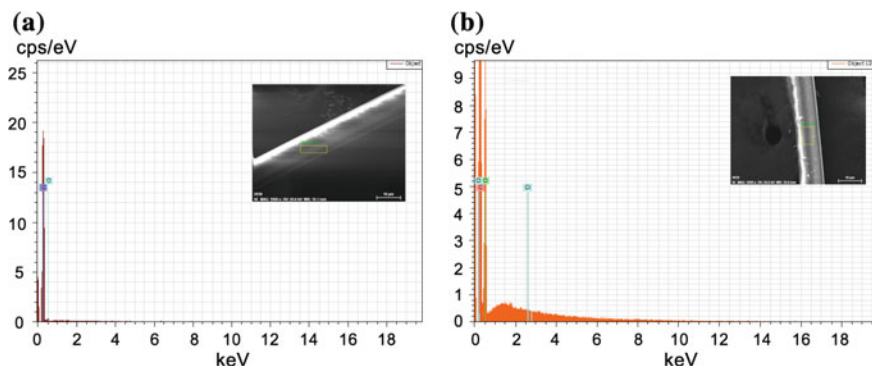
Fig. 5 EDX studies of pristine PET and triclosan immobilized PET suture. Conditions: plasma exposure time, 120 s; gas, CO_2; gas pressure, 100 mTorr; discharge power, 40 W

pristine PET suture shows relatively flat and homogeneous surface, having Sq of 6.27 ± 4.7 nm with the presence of fibrils in the direction of filament long axis (Fig. 6a).

The aspect of the statistical distribution of z-values within the image confirmed that the suture surface was uniform. After plasma functionalization, the PET suture surface shows hill valley structure with significant nonhomogeneity where surface started filling up with small conical protrusions. Further, these conical protrusions converted into nano hills and valley structure (Fig. 6b). After triclosan immobilization, the surface topography did not show any appreciable change as compared to the plasma exposed sample because triclosan is single molecule which can be placed in between the small conical protrusions. Surface roughness of triclosan immobilized sample was Sq of 12 ± 5.7 nm which is very much identical to the plasma exposed sample (Fig. 6c).

3.3 Bacterial Adherence on PET Suture

Bacterial adherence on suture samples was investigated by FE-SEM analysis and images are shown in Fig. 7. In bacterial adherence study, the results are evaluated after 24 h of incubation of suture samples and observe the biofilm formation. Regarding the adherence of *S. aureus* and *E. coli* onto the samples, drastic change is observed in the number of viable colonies adhered onto the surface of triclosan immobilized sample as compared to the pristine PET sample implying the efficiency of the modifications in reducing the adherence of bacteria onto the surface. Bacterial adhesion on suture samples might assist the infection on site and impaired wound healing so to overcome this issue, here we used triclosan as an antimicrobial agent. Triclosan is found to be effective against a broad range of microbes with documented safety along with both bactericidal as well as bacteriostatic property, depending on its concentration.

Fig. 6 AFM images of **a** pristine PET, **b** plasma functionalized PET and **c** triclosan PET sutures
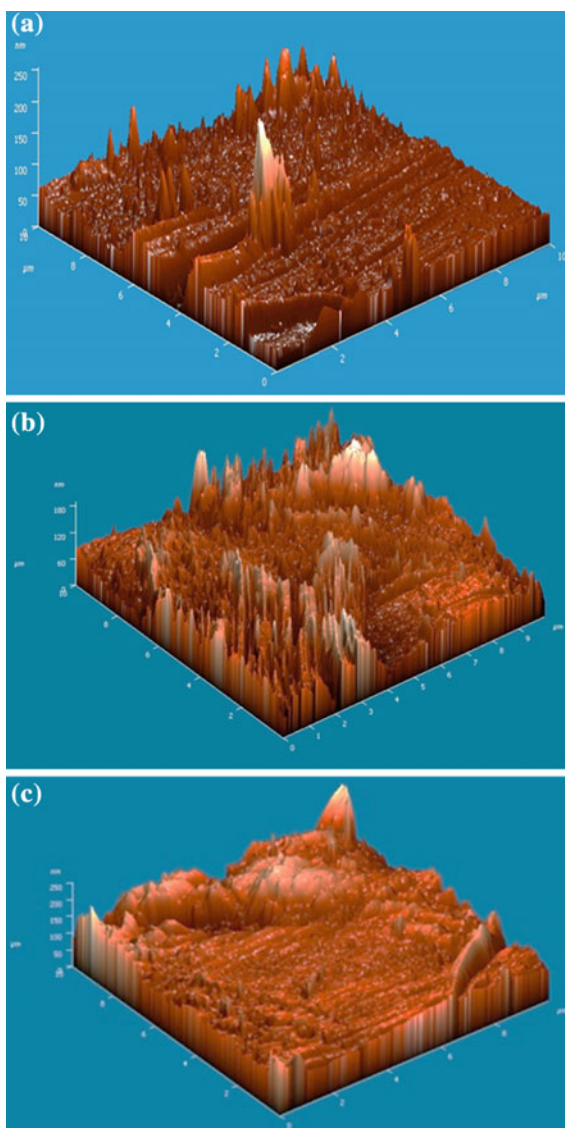
Therefore, triclosan immobilized suture samples did not allow any bacterial growth on the surface and help in infection control.

The antibacterial activity of suture was evaluated against *S. aureus* and *E. coli* by colony formation methods and result shown in Fig. 8. It is seen that the triclosan immobilized PET suture has high antibacterial activity as evidenced by maximum reduction in the bacterial growth. The antimicrobial action of triclosan involves inhibiting fatty acid synthesis that is necessary for building and reproducing cell

PET   PET-TCH
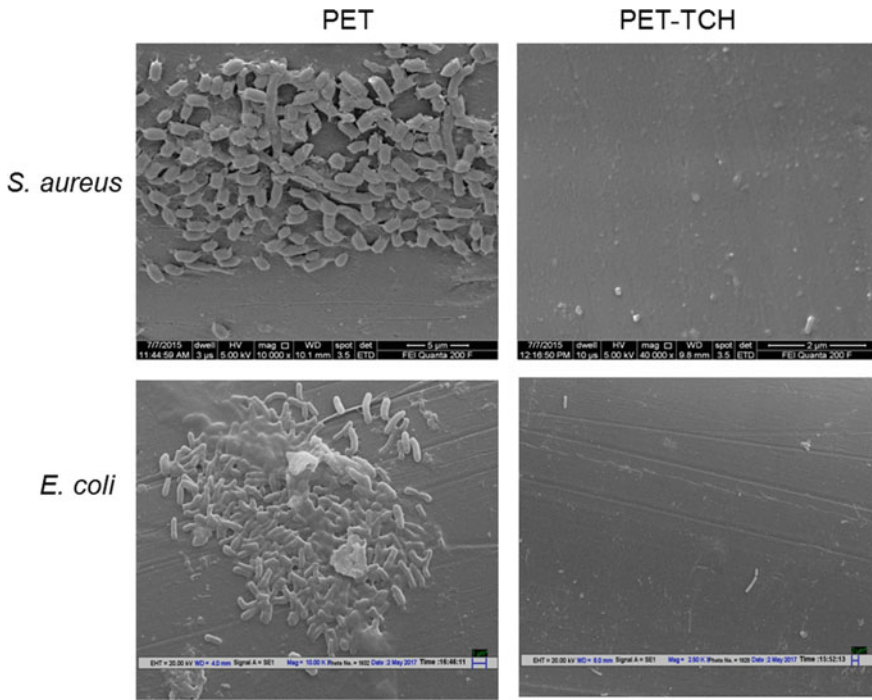
Fig. 7 Bacterial adherence on pristine and triclosan immobilized PET suture (PET-TCH) samples against *S. aureus* and *E. coli*

membranes [15]. Triclosan binds to bacterial enoyl-acyl carrier protein reductase (ENR) enzyme which increases the enzyme's affinity for nicotinamide adenine dinucleotide (NAD^+).

This results in the formation of a stable, ternary complex of ENR-NAD^+-triclosan, which is unable to participate in fatty acid synthesis. This way, triclosan permeabilizes the bacterial envelope which allows for leakage of components leading to cell death.

4   Conclusion

Infection during wound closure is a serious problem and needs a very precise approach to this problem. The proactive approach may be to design a suture that would exhibit antimicrobial nature and would be effective against all the microbes. Sutures, therefore, need to be biofunctionalized in such a way that they acquire antimicrobial nature but without any compromise over the physical properties and the biocompatibility. Plasma processing to create specific functionality and the immobilization of the bioactive component is an attractive approach to develop infection-resistant
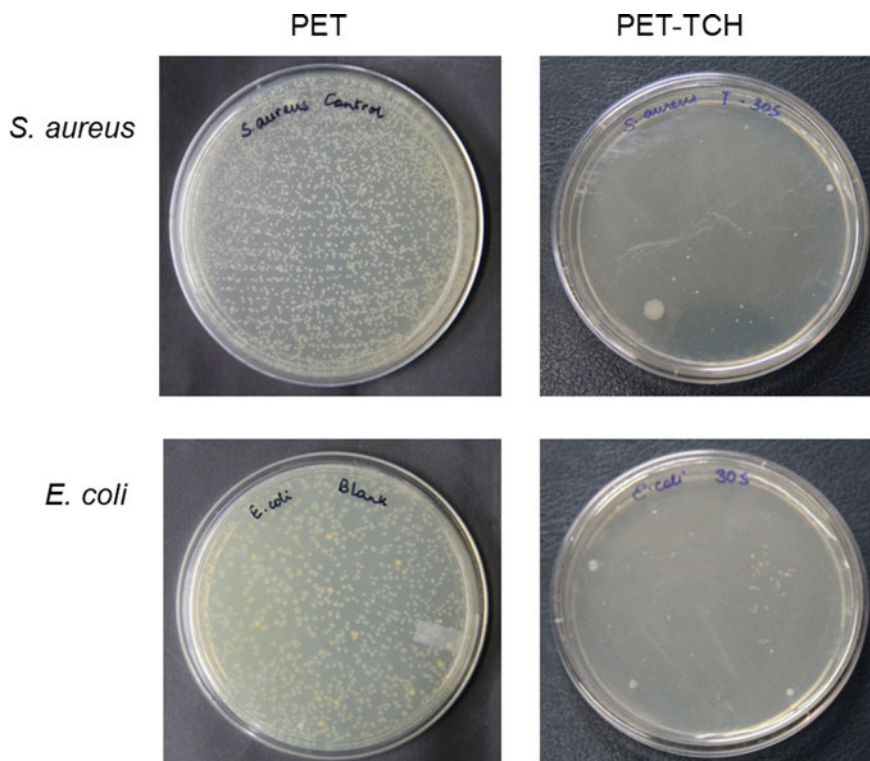
Fig. 8 Colony reduction percentage of sutures against *S. aureus* and *E. coli* of control and triclosan immobilized PET sutures (PET-TCH)

sutures. Triclosan used as bioactive moiety and exhibited excellent antibacterial activity at much lower concentration. Results of the antimicrobial studies explicitly prove that the material is effective against microbes and has bacteriostatic and bactericidal nature.

References

1. Masini, B.D., Stinner, D.J., Waterman, S.M., Wenke, J.C.: Bacterial adherence to suture materials. J. Surg. Educ. **68**, 101–104 (2011). https://doi.org/10.1016/j.jsurg.2010.09.015
2. Tummapalli, M., Anjum, S., Kumari, S., Gupta, A., Gupta, B.: Antimicrobial surgical sutures: recent developments and strategies. Polym. Rev. **56**, 607–630 (2016). https://doi.org/10.1080/15583724.2015.1119163
3. Li, Y., Kumar, K.N., Dabkowski, J.M., Corrigan, M., Scott, R.W., Nüsslein, K., Tew, G.N.: New bactericidal surgical suture coating. Langmuir **28**, 12134–12139 (2012). https://doi.org/10.1021/la302732w

4. Marco, F., Vallez, R., Gonzalez, P., Ortega, L., de la Lama, J.; Lopez-Duran, L.: Study of the efficacy of coated vicryl plus antibacterial suture in an animal model of orthopedic surgery. Surg. Infect. (Larchmt) **8**, 359–366 (2007). https://doi.org/10.1089/sur.2006.013

5. Bretcanu, O., Verne, E., Borello, L., Boccaccini, A.R.: Bioactivity of degradable polymer sutures coated with bioactive glass. J. Mater. Sci. Mater. Med. **15**, 893–899 (2004). https://doi.org/10.1023/b:jmsm.0000036277.99450.a2

6. Anjum, S., Gupta, A., Sharma, D., Dadal, P., Gupta, B.: Skin biocompatibility and infection-resistance in plasma functionalized nanogel coated polypropylene nonwoven fabric. Mater. Sci. Eng. C **69**, 1043–1050 (2016). https://doi.org/10.1016/j.msec.2016.08.009

7. Anjum, S., Gupta, A., Sharma, D., Kumari, S., Sahariah, P., Bora, J., Bhan, S., Gupta, B.: Antimicrobial nature and healing behavior of plasma functionalized polyester suture. J. Bioact. Comp. Polym. **32**, 263–279 (2017). https://doi.org/10.1177/0883911516668665

8. Galal, I., El-Hindawy, K.: Impact of using triclosan-antibacterial sutures on incidence of surgical site infection. Am. J. Surg. **202**, 133–138 (2011). https://doi.org/10.1016/j.amjsurg.2010.06.011

9. Edmiston, C.E., Daoud, F.C., Leaper, D.: Is there an evidence-based argument for embracing an antimicrobial (triclosan)-coated suture technology to reduce the risk for surgical-site infections? A meta-analysis. Surgery **154**, 89–100 (2013). https://doi.org/10.1016/j.surg.2013.03.008

10. Saxena, S., Ray, A.R., Gupta, B.: Graft polymerization of acrylic acid onto polypropylene monofilament by RF plasma. J. Appl. Polym. Sci. **116**, 2884–2892 (2010). https://doi.org/10.1002/app.31823

11. Anjum, S., Gupta, A., Sharma, D., Gautam, D., Kapil, A., Sharma, A., Bhan, S., Gupta, B.: Development of novel wound care systems based on nanosilver nanohydrogels of polymethacrylic acid with aloe vera and curcumin, Mater. Sci. Eng. C **64**, 157–166 (2016). https://doi.org/10.1016/j.msec.2016.03.069

12. Anjum, S., Arora, A., Alam, M.S., Gupta, B.: Development of antimicrobial and scar preventive chitosan hydrogel wound dressings. Int. J. Pharm. **508**, 92–101 (2016). https://doi.org/10.1016/j.ijpharm.2016.05.013

13. Ahmad, A., Igor, N., Marián, L., Vladimir, S., Alenka, V., Ita, J., Petr, S., Ivan, C.: An in vitro bacterial adhesion assessment of surface-modified medical-grade PVC. Colloids Surf. B Biointerfaces **77**, 246–256 (2010). https://doi.org/10.1016/j.colsurfb.2010.02.006

14. Lee, H.S., Park, S.H., Lee, J.H., Jeong, B.Y., Ahn, S.K., Choi, Y.M., Choi, D.J., Chang, J.H.: Antimicrobial and biodegradable PLGA medical sutures with natural grapefruit seed extracts. Mater. Lett. **95**, 40–43 (2013). https://doi.org/10.1016/j.matlet.2012.12.090

15. Sadeghnejad, A., Aroujalian, A., Raisi, A., Fazel, S.: Antibacterial nano silver coating on the surface of polyethylene films using corona discharge. Surf. Coat Technol. **245**, 1–8 (2014). https://doi.org/10.1016/j.surfcoat.2014.02.023

Mandelic Acid Incorporated Antimicrobial Soy Protein Film Fabricated by Solution Casting

Rakesh Kumar and **Priya Rani**

Abstract Soy protein exists in the market as soy flour (SF), soy protein concentrate (SPC), and soy protein isolate (SPI) and they differ in their protein contents. SPI contains about 90–92% of protein content followed by SPC having 70–72% protein. SPI films can be prepared by solution casting or compression molding method. In this work, different amounts of mandelic acid (1–5% wrt SPI) were added to glycerol plasticized SPI. The pH of the film-forming SPI suspension was maintained between 10 and 10.5. Mandelic acid incorporated SPI films were obtained after subjecting the solution casted SPI suspension on a glass plate for 24 h at 60 °C. The resulting SPI films with mandelic acid were subjected to antimicrobial, water uptake, transmittance, and tensile strength studies. The results indicated that with the increase in the concentration (till 4%) of mandelic acid, tensile strength and elongation at break increased from 6.5 to 7.5 MPa and 79 to 126%, respectively. The water uptake of the SPI films with mandelic acid decreased indicating less hydrophilicity of the resulting SPI film. Mandelic acid incorporated SPI film also showed antimicrobial nature that can be used for packaging.

Keywords Soy protein isolate · Mandelic acid · Protein film

1 Introduction

Soy protein isolate (SPI) having a protein content of 90–92% is obtained from the renewable resources. It is available in the form of powder and can be easily processed into light yellow film either by solution casting method or compression molding method (Fig. 1). Thus, SPI has very good film-forming ability and the product is considered as environmentally safe industrial products and can be used as environment-friendly packaging materials [1]. Several acid additives such as citric

R. Kumar (✉) · P. Rani
Biotechnology Program, Centre for Biological Sciences,
Central University of South Bihar, Patna 800014, Bihar, India
e-mail: krrakesh72@gmail.com
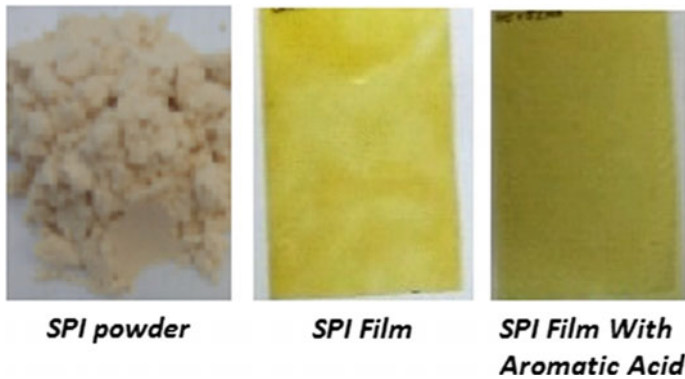
Fig. 1 Photograph of SPI in form of powder and film

acid, malic acid, lactic acid, tartaric acid [2], mandelic acid [3], and adipic acid [4] have been incorporated in SPI solution to fabricate modified SPI films. The presence of these acid additives changes the color of the film from yellow to brown and dark brown (Fig. 1). Ferulic acid has been used as a crosslinking agent in the preparation of SPI modified films with antimicrobial properties [5, 6].

The mechanical properties of the fabricated SPI films can be altered by the addition of different acids in the SPI films [7]. Mandelic acid is an alpha hydroxy acid with one aromatic ring and has been explored as an additive for soy protein films prepared by compression molding technique [3]. In this study, mandelic acid incorporated SPI films have been fabricated by solution casting methods. The as-prepared films were characterized by mechanical, transmittance, water uptake, and antibacterial studies.

2   Materials and Methods

2.1   Materials

SPI was purchased from Zhenghou Ruikang Enterprise Co., Ltd (Zhengzhou, China). It contained around 90.27% of protein on dry basis. Mandelic acid (mp: 119–121 °C, molwt: 152.15) was purchased from Sigma-Aldrich and used as received. Glycerol was purchased from Fisher Scientific. *E. coli/*BL21strain was procured from Gbiosciences. Luria Bertani (LB) powder was purchased from HiMedia.

2.2 Preparation of Soy Protein Isolate Film

About 4 g of SPI was added slowly in 50 ml of distilled water maintained at 65 °C. The pH of the resulting SPI suspension was adjusted from 9.5 to 10.0 by adding required amount of 1 N NaOH followed by addition of glycerol (30% w/w with respect to SPI). The SPI suspension was stirred continuously at 60 °C for about 1 h. The resulting SPI suspension was kept for 3–4 h in a vacuum desiccators so as to remove the air bubbles and then it was poured on the glass plates and kept at 50–60 °C for 24 h. After the designated time, the dried film was kept at an RH of 75% (maintained by using saturated salt solution of NaCl) and subsequently it was peeled off from the glass plate.

2.3 Preparation of Mandelic Acid Incorporated SPI Films

Mandelic acid (0–5% with respect to SPI) was added to the as-prepared SPI suspension. For adding mandelic acid in SPI, mandelic acid was first dissolved in 5 ml distilled water in microwave oven and then added to the SPI suspension. Final pH of the mandelic acid incorporated SPI suspension was maintained around 10.5 by the addition of 1 N NaOH. The resulting mandelic acid incorporated SPI suspension was stirred continuously at 60 °C for about 30 min. Again, the resulting suspension was kept for 3–4 h in a vacuum desiccator to remove the air bubbles. The suspension was then poured on the glass plates and kept at 50–60 °C for 24 h. After the designated time, the dried film was kept at an RH of 75% and subsequently it was peeled off from the glass plate. The resulting mandelic acid incorporated SPI films were designated as S-0M, S-1M, S-2M, S-3M, S-4M, and S-5M where the numeral values with M denote the percentage (w/w) of mandelic acid in SPI.

2.4 Antimicrobial Studies

E. coli cells having 0.01 optical density at 600 nm were put into molten LB agar. It was then allowed to become solid at room temperature to get plate with uniform *E. coli* cells. SPI films in presence of mandelic acid were placed on the LB plates with uniform *E. coli* cells. The LB agar plate was then incubated at 37 °C for overnight. The growth of bacteria in LB agar plates containing SPI films in the presence and absence of mandelic acid were analyzed.

2.5   Characterizations

The tensile tests were carried out according to ASTM D882 on a Universal Tensile Testing machine from Zwick, Germany at IIT Patna, Bihar, India. The tensile specimens with a dimension of 80 mm × 10 mm with thickness of around 0.25 ± 0.02 mm were cut from samples prepared by solution casting.

The optical transmittances of the SPI films with and without mandelic acid were measured with an ultraviolet–visible spectrophotometer (UV-160A, Shimadzu). For the transmittance studies, the SPI films were cut into small strips of 4 cm length and 1 cm breadth. The strips were kept in glass cuvette and their transmittance was taken at varying wavelength ranging from 400 to 800 nm.

The water uptake properties of SPI films in the presence and absence of mandelic acid were determined according to ASTM D570-81. The films were cut in small square pieces (1 cm × 1 cm) and preconditioned at 60 °C in hot air oven for 24 h. After that, it was cooled in desiccators at 0% RH and weighed (W_0). The film pieces were then dipped in distilled water for 24 h. After that, it was taken out and dried with tissue paper. By this process, excess water from the surface of the wet film was removed and then the film was weighed (W_1).

$$\text{Water uptake}(\%) = \frac{W_1 - W_0}{W_0}$$

3   Results and Discussion

Table 1 shows the mechanical properties of SPI films in the presence and absence of mandelic acid. Soy protein film without mandelic acid (S-0M) exhibited tensile strength of 6.5 MPa and elongation at break as 80.33%. S-4M showed the increase in tensile strength and elongation at break from 6.5 to 8.03 MPa and 80.33 to 125.06%, respectively. In the literatures, it has been reported that caffeic acid, nisin, and adipic acid incorporated SPI film exhibited tensile strength of 6.5, 5.11, and 6.2 MPa, respectively [2, 4, 8]. Thus, the tensile strength tended to decrease with the addition of aromatic rings but till particular concentration of mandelic acid [1]. At 5% of mandelic acid, the tensile strength of SPI film decreased slightly but elongation at break decreased significantly (36.4%) due to rigidity exhibited by aromatic rings of the mandelic acid.

Table 2 shows that there is decrease in water uptake of SPI film at high percentage of mandelic acid. Soy protein film without mandelic acid (S-0M) showed high water uptake (730.3%). After the addition of mandelic acid, water uptake decreased from 430 to 138%. The aromatic groups present in mandelic acid were responsible for low water uptake as observed in SPI film with mandelic acid.

Table 3 shows the transmittance of neat and mandelic acid incorporated SPI films. The percentage of transmittance increased with the wavelength showing the highest transmittance at 700 nm for each film. For S-3M film, the highest transmittance was

Table 1 Mechanical properties of SPI films in the presence and absence of mandelic acid

Sample	Tensile strength (MPa)	Elongation (%)
S-0M	6.50	80.33
S-1M	6.46	82.65
S-2M	7.15	93.46
S-3M	7.46	108.43
S-4M	8.03	125.06
S-5M	7.53	36.4

Table 2 Water uptake of SPI films in the presence and absence of mandelic acid

Sample	Water uptake (%)
S-0M	730.3
S-1M	430
S-2M	486
S-3M	402
S-4M	124
S-5M	138

Table 3 Transmittance data of SPI films in the presence and absence of mandelic acid

Wavelength (nm)	S-0M	S-1M	S-2M	S-3M	S-4M	S-5M
400	8.606	35.044	8.1	13.7	4.8	2.68
500	46.2	55.3	35.4	53.6	37.57	28.57
600	52.5	50.9	39.7	68.6	47.32	37.8
700	58.13	53.7	42.3	69.06	48.4	38.9

observed. However, for sample S-5M, the percentage transmittance decreased when compared to S-1M. The decrease in the transmittance of mandelic acid incorporated SPI films may be attributed to the particle nature of mandelic acid. This signifies that mandelic acid incorporated SPI film has better ability to prevent light emission.

Figure 2 shows the antimicrobial properties of SPI films in the presence of mandelic acid. In the absence of mandelic acid, SPI film showed no antibacterial property. On the other hand, the mandelic acid incorporated SPI film showed antibacterial property because there was no microbial growth on the films after 24 h. The presence of phenolic groups in mandelic acid is responsible for the antimicrobial activities [9]. The aromatic groups of mandelic acid potentially alter the normal functioning of *E. coli* cell membranes. This in turn retards the growth and multiplication of bacteria. Hence antimicrobial SPI film can be prepared by addition of mandelic acid.
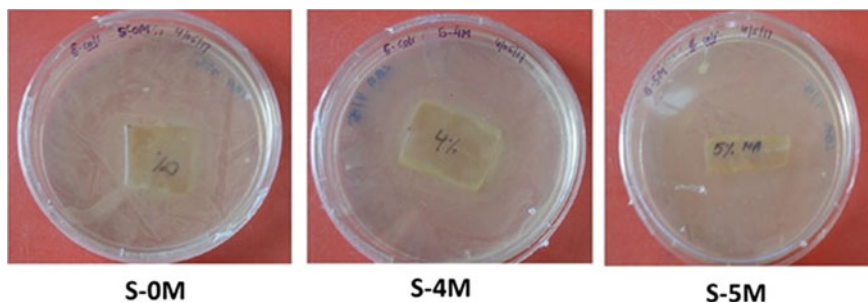
Fig. 2 Antimicrobial properties of mandelic acid incorporated SPI film

4 Conclusions

Homogeneous SPI films at different contents of mandelic acid (0–5%) were successfully fabricated. SPI films showed increased hydrophobicity and tensile properties till 4% contents of the mandelic acid. Mandelic acid incorporated SPI films showed low water uptake due to the presence of aromatic groups in the mandelic acid. No growth of *E. coli* on the surface of mandelic acid incorporated SPI films suggested the antibacterial nature of the SPI films. This work gives an idea of networking of soy oil industry with plastic industry where the protein waste can be used as bioplastics.

References

1. Song, F., Tang, D.-L., Wang, X.-L., Wang, Y.-Z.: Biodegradable soy protein isolate-based materials: a review. Biomacromol **12**, 3369–3380 (2011)
2. Eswaranandam, S., Hettiarachchy, N.S., Johnson, M.G.: Effects of citric, lactic, malic, and tartaric acids on antimicrobial activity of nisin-incorporated soy protein film against Listeria monocytogenes, *Escherichia coli* O157:H7, and Salmonella gaminara. J. Food Sci. **69**(3), 79–84 (2004)
3. Kumar, R., Anandjiwala, R.D., Kumar, A.: Thermal and mechanical properties of mandelic acid-incorporated soy protein films. J. Therm. Anal. Calorim. **123**, 1273–1279 (2016)
4. Sellivama, R.K.C.P., Husseinsyaha, S., Lenga, T.P., Zakariaa, M.M., Ismail, H.: Effect of adipic acid content on properties of soy protein isolate/kapok husk biocomposite films. Procedia Chem. **19**, 891–896 (2016)
5. Cao, N., Fu, Y., He, J.: Preparation and physical properties of soy protein isolate and gelatin composite films. Food Hydrocoll. **21**, 1153–1162 (2007)
6. Ou, S., Wang, Y., Tang, S., Huang, C., Jackson, M.G.: Role of ferulic acid in preparing edible films from soy protein isolate. J. Food Eng. **70**, 205–210 (2005)
7. Dawson, P.L., Hirt, D.E., Rieck, J.R., Acton, J.C., Sotthibandhu, A.: Nisin release from films is affected by both protein type and film-forming method. Food Res. Int. **36**, 959–968 (2003)

8. Kang, H., Wang, Z., Zhang, W., Li, J., Zhang, S.: Physico-chemical properties improvement of soy protein isolate films through caffeic acid incorporation and tri-functional aziridine hybridization. Food Hydrocoll. **61**, 923–932 (2016)
9. Lin, Y.T., Labbe, R.G., Shetty, K.: Inhibition of *Listeria monocytogenes* in fish and meat systems by use of oregano and cranberry phytochemical synergies. Appl. Environ. Microbiol. **70**, 5672–5678 (2004)

Structural and Morphological Analysis of Newly Synthesized CuO@Alginate Nanocomposite with Enriched Electrical Properties

Vasi Uddin Siddiqui, Imran Khan, Afzal Ansari, Weqar Ahmad Siddiqui and Md. Khursheed Akram

Abstract CuO@Alginate (CuO@Alg) nanocomposite has been synthesized by simple, inexpensive and highly efficient Sol-Gel method. The morphology and structural properties of synthesized nanocomposite (CuO@Alg) and pure CuO nanoparticles have been analyzed as a function of temperature. The morphological and structural properties were investigated by using TEM, SEM, EDX, and X-ray diffraction. The crystalline nature of CuO nanocomposite showed by X-ray diffraction (XRD) pattern and average crystalline size was observed approximately 18.09 nm. The effect of size quantization on morphology was also observed. Dielectric behavior of CuO and CuO@Alg has been also studied as a function of increasing frequency by LCR meter. With the increase in frequency, the dielectric constant was found to decrease and alternative current (A.C.) conductivity value was found to increase. This study was also representing a useful step towards the establishment of a structure–property relationship for CuO nanocomposite.

Keywords Copper oxide · Electrical conductivity · Nanocomposite

V. U. Siddiqui (✉) · I. Khan · A. Ansari · W. A. Siddiqui
Applied Sciences and Humanities, Faculty of Engineering
and Technology, Jamia Millia Islamia, New Delhi 110025, India
e-mail: vasi168968@st.jmi.ac.in

Md. Khursheed Akram
Applied Sciences and Humanities Section, University Polytechnic, Faculty
of Engineering and Technology, Jamia Millia Islamia, New Delhi 110025, India

I. Khan
Applied Sciences and Humanities Section, University Polytechnic, Faculty
of Engineering and Technology, Aligarh Muslim University, Aligarh 202002, India

1 Introduction

Excellent chemical and physical properties of materials have been achieved by altering the surface to volume ratio with the advancement of nanotechnology. Inclusions of materials specifically metal oxide nanomaterials (NMs) into polymer matric subjected to composite with enhanced mechanical, thermal, electrical, and gas sensor properties have been widely reported [1–4]. Moreover, semiconductor nanomaterials, viz., transition metal oxide have drawn attention in past years because of better electronic conductivity, higher specific capacitance and enhanced cycling stability [5, 6]. Among all the transition metal oxide, copper oxide nanoparticles gained special interest due to its narrow band gap ($E_g = 1.2$ eV) superconducting properties for the use of photoconductivity and photothermal activities. It is a p-type capacitive material used as an active and passive component in renewable energy source technology, e.g., Solar cell technology [7]. Usually, dielectrics have Pb and Li, copper oxide (CuO) is free from these metals resulting in more eco-friendly. Numerous studies reported the dielectric properties which are temperature and frequency dependence of single and nanocrystalline CuO. Kang et al. [1] reported the size-controlled fabrication of CuO with natural polymer sodium alginate and studied the fast and high lithium storage capability of CuO, the oil-soluble PVDF also effect on the structural stability of water-based CuO-Alginate (Alg) nanocomposite. da Silva et al. [8] investigate the drastic change in dielectric permittivity and dielectric loss with the conductive filler content for CuNW/PVDF and MWCNT/PVDF. A. Bello et al fabricate the surfactant assist synthesis of CuO nano-leaf like structure. Impedance spectroscopy analyzes the transfer resistant resulting small particle size distribution with small domain for energy storage applications. Deepthi et al. [9] used sol-gel method to prepare CuO ceramic powder. With the increase in frequency, dielectric studies showed the depression in the imaginary and real part of the dielectric constant, and the mechanism is explained using CBH model.

In this work, we report a simple, inexpensive, and highly efficient sol-gel method to fabricate CuO and CuO@Alg nanocomposite. The obtained nanocrystals have been characterized by XRD, SEM, TEM, and EDX spectroscopy. The resulting CuO sample and CuO@Alg nanocomposite within an alginate matrix investigated how its dielectric properties dependent at varying frequency. The probable mechanism of conduction is discussed in detail.

2 Experimental Details

2.1 Synthesis of Copper Oxide and Copper Oxide Nanocomposite with Alginate

Chemicals—Copper nitrate trihydrate, sodium hydroxide, and sodium alginate pure were purchased from Sigma Aldrich. Double-distilled water was used for all solu-

tion preparations. All the chemicals were of analytical grade and used without any additional purification.

The synthesis procedure is divided in two parts, viz., Part A consists the synthesis of pure copper oxide (CuO) formation and Part B confers the details of copper oxide-Alginate (CuO@Alg) nanocomposites.

Part A—In the present experiment, copper nitrate trihydrate $[Cu(NO_3)_2 \cdot 3H_2O]$ and sodium hydroxide [NaOH] were used as precursors. Two separate solutions, NaOH (8 M) and copper nitrate trihydrate (1.0 M) in distilled water, were prepared. 1.0 M solution of copper nitrate trihydrate stirred with 8 M solution of sodium hydroxide drop by drop on magnetic stirrer at 70 °C with 600 rpm till gel formation. Then do stirring at 100 °C with 600 rpm for 3 h. Then centrifuge it at 7000 rpm for 1 h and washed 3–4 times with distilled water. After collecting sample dried at 70–80 °C for 24 h.

The alkaline reaction takes place in the formation as,

$$Cu(NO_3)_2.3H_2O + 2NaOH \rightarrow Cu(OH)_2 + 2NaNO_3$$
$$Cu(OH)_2 + NaOH \rightarrow NaCuO_2^- + H_2O$$
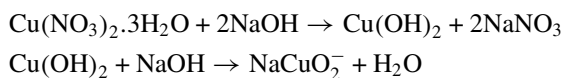
Solubility product increased as the solution was heated and finally, the solution gets precipitated. On the substrate, the uniform film of CuO was formed by the following reaction.

$$NaCuO^- + H^+ \rightarrow CuO + NaOH$$
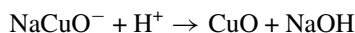
Part B—To prepare CuO@Alg nanocomposites, add 1.0 g sodium alginate in 1.0 M solution of copper nitrate trihydrate which was stirred in 50 mL of distilled water for a minimum time of one hour with 8.0 M NaOH added dropwise. After 4 h, the composite was filtered and with distilled water and washed several times and to get nanocomposite sample, it is dried in an oven for 24 h. Figure 1 shows the probable mechanism of alginate matrices with copper oxide.
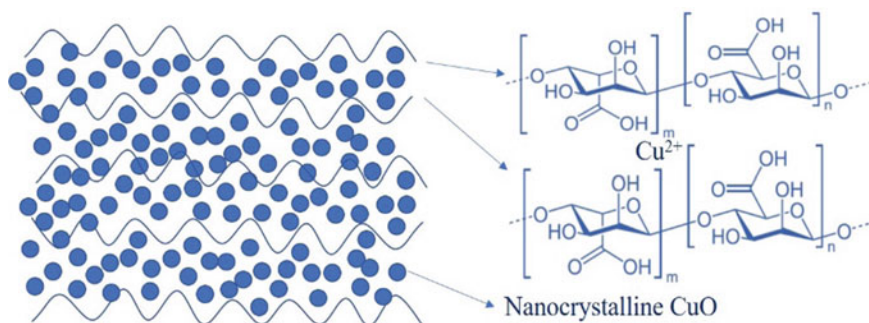
Fig. 1 Structural representation of CuO@Alg nanocomposite

2.2 Characterization Techniques

The structural analysis by X-ray diffractometry of the obtained product was done by means of a Rigaku Advance X-ray diffractometer with monochromatic Cu Kα radiation (λ = 1.54 A°) in the angular range 20°–70° of 2θ. The morphology of as-prepared samples was examined using a JEOL (JEOL, Tokyo, Japan) 200 kV transmission electron microscope (TEM). The elemental study of the sample was determined by instruments INCAx-sight energy dispersive X-ray (EDAX) spectrometer equipped SEM (JSM 6510LV JEOL, Tokyo, Japan). For dielectric measurement, the as-synthesized product was shaped into cylindrical pellets of 1 mm thickness and 12 mm diameter in a hydraulic press by applying a pressure of 4.5 tons for 2 min. The prepared pellet was used as a dielectric medium by using silver pellets on both sides of the pellet as electrode within the frequency range of 100 Hz–1 MHz mm.

3 Results and Discussion

3.1 Structural and Morphological Analysis

The X-ray diffraction (XRD) pattern of CuO and CuO@Alg nanocomposite is shown in Fig. 2. The peaks in terms of standard XRD JCPDS (card no. 05-0661) of monoclinic CuO confirmed the shape of synthesized nanoparticle and nanocomposite [10]. The peak area represents the high crystallinity and according to FWHM (full width at half maximum) value through Debye Scherrer equation given by

$$D = \frac{0.9\lambda}{\beta \cos\theta}$$

where β, D, λ, and θ is FWHM of strong intensive peak, crystallite size, wavelength of the X-ray, and Bragg angle, respectively [11], synthesized CuO and CuO@Alg found 18.09 nm average crystallite size. Which also confirmed by the morphological feature represent by scanning electron microscope (SEM) and transmission electron microscope (TEM) analysis in Figs. 3 and 4, respectively. In Fig. 3, the EDAX spectra also shows the purity of synthesized nanomaterial.

3.2 Dielectrical Analysis

The dielectric constant (ε_r) is evaluated using the relation

$$\varepsilon_r = \frac{Cd}{\varepsilon_0 A}$$
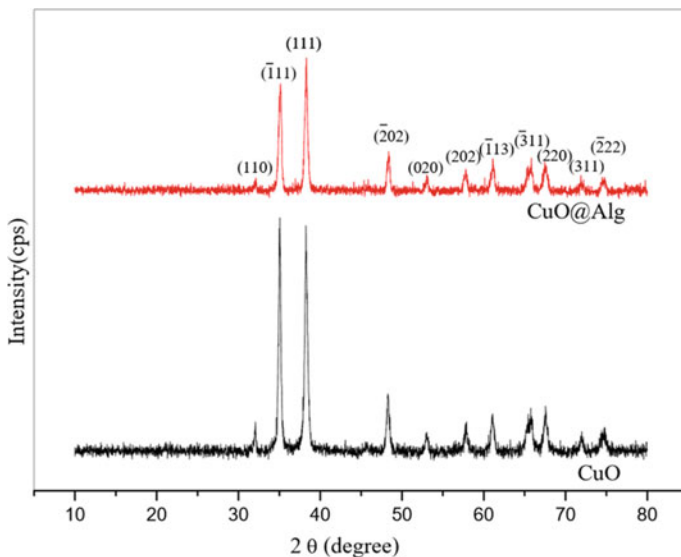
Fig. 2 X-ray diffraction (XRD) pattern of CuO and CuO@Alg nanocomposite
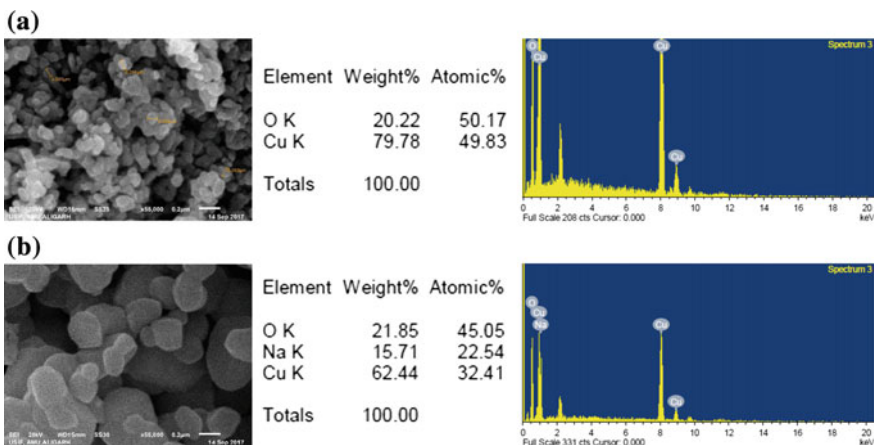
Fig. 3 SEM and EDX images of **a** CuO **b** CuO@Alg nanocomposite

where A is the area of the sample, d is a thickness of the sample, C is the capacitance of the sample and ε_0 is permittivity of free space (8.854×10^{-12} F/m). In Fig. 5, the descending order of dielectric constant with increase in frequency is the result of the unavailability of dipoles at higher frequency, due to the low relaxation time and lagging of the dipole in the field. Consequently, the decrease in polarization drop dielectric constant to a lower value. Figure 6 shows electrical property of AC
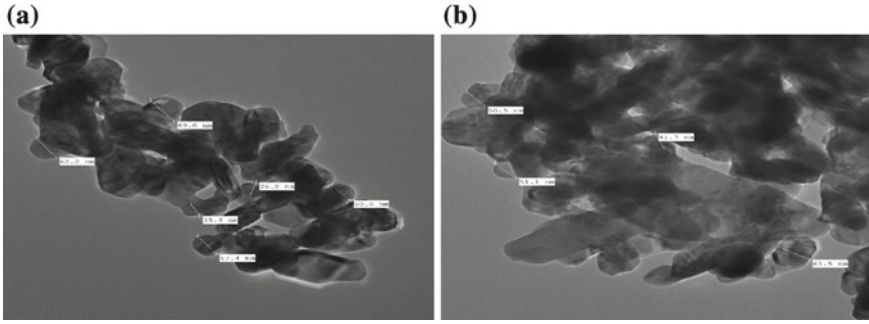
Fig. 4 TEM images of **a** CuO **b** CuO@Alg nanocomposite
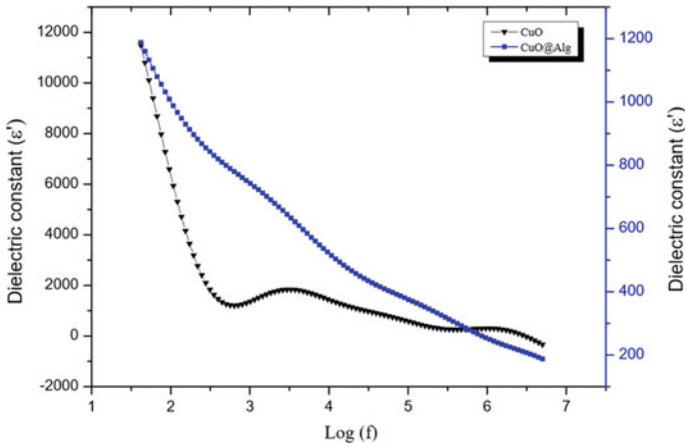
Fig. 5 Dielectric constant plot with the frequency of CuO and CuO@Alg nanocomposite

conductivity (σ_{ac}) as function of frequency are obtained through the relation given by

$$\sigma_{ac} = \varepsilon' \varepsilon_0 \omega \tan \delta$$

where ω, ε_0, and ε' are the angular frequency, permittivity of free space, and dielectric constant respectively.

4 Conclusions

In summary, we synthesized nanoparticle of CuO and CuO@Alg nanocomposite using the sol-gel method. The average crystallite of the particles is calculated using
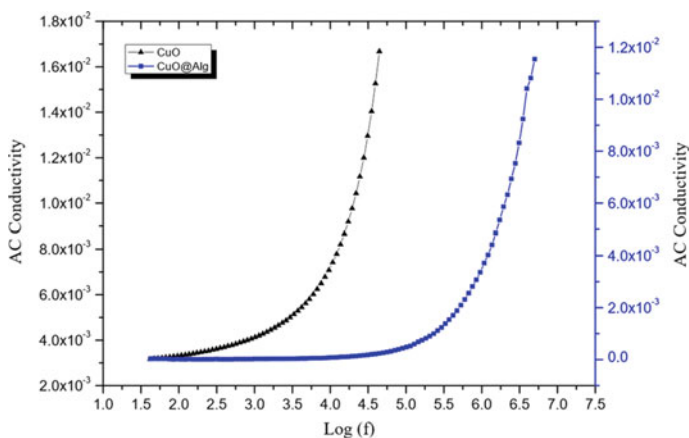
Fig. 6 AC conductivity plot with the frequency of CuO and CuO@Alg nanocomposite

XRD studies and the particle size is found to be 18.93 nm. The monoclinic structure was confirmed through the SEM and TEM analysis. The AC conductivity and dielectric constant of the CuO and CuO@Alg nanocomposite are monitored in the frequency range of 50 Hz–5 MHz. Studies on dielectric reveal the diminution of both the dielectric constant with increase in frequency. The AC conductivity shows marginal upward trends with increasing frequency. So, all the parameters show the better electrical approach of CuO@Alg nanocomposite than pure CuO.

References

1. Kang, W., Zhao, C., Shen, Q.: Lithium storage capability of nanocrystalline CuO improved by its water-based interactions with sodium alginate. Int. J. Electrochem. Sci. **7**(9), 8194–8204 (2012)
2. Sagadevan, S., Murugasen, P.: Electrical properties of copper oxide nanoparticles. J. Nano Res. **30**, 1–8 (2015)
3. Dubal, D.P., Dhawale, D.S., Salunkhe, R.R., Jamdade, V.S., Lokhande, C.D.: Fabrication of copper oxide multilayer nanosheets for supercapacitor application. J. Alloys Compd. **492**(1–2), 26–30 (2010)
4. Tai, H., Jiang, Y., Xie, G., Yu, J., Chen, X.: Fabrication and gas sensitivity of polyaniline-titanium dioxide nanocomposite thin film. Sens. Actuators B Chem. **125**(2), 644–650 (2007)
5. Lang, X., Hirata, A., Fujita, T., Chen, M.: Nanoporous metal/oxide hybrid electrodes for electrochemical supercapacitors. Nat. Nanotechnol. **6**(4), 232–236 (2011)

6. Guan, C., et al.: Hybrid structure of cobalt monoxide nanowire @ nickel hydroxidenitrate nanoflake aligned on nickel foam for high-rate supercapacitor. Energy Environ. Sci. **4**(11), 4496 (2011)
7. Senthil Kumar, A., Perumal, K., Thirunavukkarasu, P.: Structural and optical properties of chemically sprayed CuO thin films. Optoelectron. Adv. Mater. Rapid Commun. **4**(6), 831–833 (2010)
8. da Silva, A.B., Arjmand, M., Sundararaj, U., Bretas, R.E.S.: Novel composites of copper nanowire/PVDF with superior dielectric properties. Polymer (United Kingdom) **55**(1), 226–234 (2014)
9. Deepthi, K.R., Pandiyarajan, T., Karthikeyan, B.: Vibrational, giant dielectric and AC conductivity properties of agglomerated CuO nanostructures. J. Mater. Sci.: Mater. Electron. **24**(3), 1045–1051 (2013)
10. Khan, I., Khan, S., Ahmed, H., Nongjai, R.: Structural and dielectric properties of Mn doped copper oxide (CuO) nanostructure. AIP Conf. Proc. **1536**, 241–242 (2013)
11. Bouazizi, N., Bargougui, R., Oueslati, A., Benslama, R.: Effect of synthesis time on structural, optical and electrical properties of CuO nanoparticles synthesized by reflux condensation method. Adv. Mater. Lett. **6**(2), 158–164 (2015)

Synthesis of Lysine Mimicking Membrane Active Antimicrobial Polymers

Ankita Arora ⓘ, Wan Zheng, Hongjun Liang and Abhijit Mishra ⓘ

Abstract Antibiotic resistance in bacteria is a major health concern. Antimicrobial Peptides (AMPs) are efficient in killing most microbes and yet the development of resistance to AMPs is rare. Although AMPs show promising antimicrobial activities, commercializing them as antibiotics is difficult as in vitro extraction and purification of AMPs is complicated and expensive. AMP mimicking antimicrobial polymers can overcome such problems while maintaining the necessary features of AMPs. Here, we have developed meth-acrylamide based polymers to mimic AMPs which possess high antimicrobial activities with low cytotoxicity. Bactericidal and scanning electron microscopy studies show that the synthesized polymers are effective against Gram-positive and Gram-negative bacteria. We find that these polymers are lethal to bacteria and at the same time, they are also non-cytotoxic to mammalian cells, thereby increasing the potential of these polymers to be used as antibiotics.

Keywords Antimicrobial polymers · Lysine mimicking polymer
Antimicrobial peptides · Methacrylamide

1 Introduction

Acquisition of antibiotic-resistance genes by all the major disease-causing bacteria and their quick transmission is a major health concern worldwide [1]. Apart from using antibiotics in the past, it depicts a troublesome picture of antibiotic resistance emergence, development, propagation, and persistence, with various risky features [2–4]. If not treated this troublesome problem could result in 10 million deaths in next

A. Arora · A. Mishra (✉)
Department of Materials Science and Engineering, Indian Institute
of Technology, Gandhinagar 382355, Gujarat, India
e-mail: amishra@iitgn.ac.in

W. Zheng · H. Liang
Department of Cell Physiology and Molecular Biophysics,
Texas Tech University Health Science Center, Lubbock, TX 79430, USA

30 years [5]. In this alarming situation we urgently need new antimicrobial agents that allow us to handle this problem. Antimicrobial peptides (AMPs), a broad and diverse range of peptides that kill a wide variety of microbes such as bacteria, protozoa, fungi, and virus are considered as suitable substitutes due to their broad spectrum of antibacterial activity, reduced bacterial resistance propensity and low immune response [6]. These are widely distributed throughout multicellular organisms as part of their defense mechanism and selectively fight back with microbes without host damage [7]. Antibiotic resistance against these naturally occurring AMPs is very limited [8], however, their transfer from bench to bedside is hindered because of their complex secondary and tertiary structures, tedious extraction and isolation, expensive production on large scale, pharmacokinetic properties and chemical instability have limited their use as antibiotics [9]. The challenge lies in developing AMP mimics which suppress such restrictions while maintaining the necessary features of an active antimicrobial agent i.e. high activity and low cytotoxicity.

In nature, AMPs are often cationic which enables them to interact with the negatively charged bacterial membranes due to electrostatic force, while remaining inactive to the zwitterionic mammalian cells [10, 11]. Another peculiar characteristic of AMPs is their net hydrophobicity which describes their membrane disrupting properties [12]. Cationicity and hydrophobicity are the two important components of AMPs. It has been reported (Fig. 1) that the arginine/lysine content and hydrophobicity of such AMPs are correlated, with lower arginine content necessitating increased lysine content and increased hydrophobicity.

In this study, we synthesize lysine mimicking homopolymer and lysine mimicking copolymer with hydrophobic group and study their antimicrobial activity against both Gram-positive and Gram-negative bacteria. The advantage of using such antibiotic polymers over conventional AMPs is their scalability, cost-effectiveness and chemical stability in in vivo environment [14].

Fig. 1 Correlation between arginine/lysine content and hydrophobicity for AMPs [13]
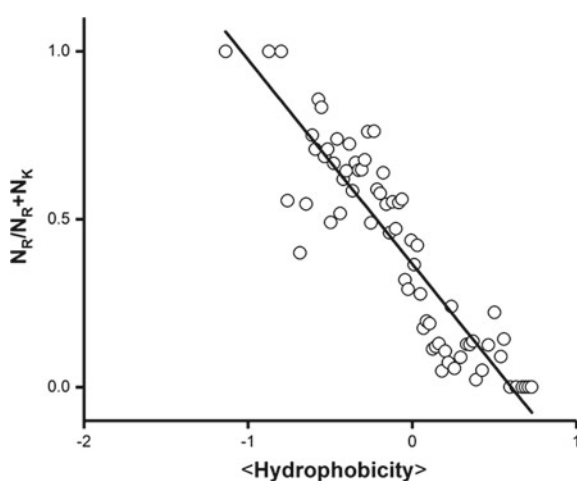
2　Materials and Methods

2.1　Materials

N-(3-aminopropyl)methacrylamide hydrochloride (APMA, 98%), α,α,′-azoisobutyronitrile (AIBN), 4-cyano-4-[(dodecylsulfanylthiocarbonyl) sulfanyl] pentanoic acid (CDSP), methacrylic acid (MAA), N,N'- dicyclohexylcarbodiimide (DCC), N-hydroxysuccinimide (NHS), trimethylamine (TEA, ≥99%), 1-ethylpiperidine hypophosphite (EPHP, 95%), dimethyl sulfoxide (DMSO, ≥99.5%), potassium phosphate monobasic (KH_2PO_4, ≥99%), agar and glutaraldehyde solution (50%) are purchased from Sigma-Aldrich (St. Louis, MO). All other chemicals, unless otherwise discussed, are reagent grade and used as received from Sigma-Aldrich. The Gram-negative and Gram-positive bacterial strains *Escherichia coli* (ATCC 25922) and *Staphylococcus aureus* (ATCC 25923) respectively, are purchased from American Type Culture Collection (ATCC) (Manassas, VA) and subcultured according to the instructions from ATCC. Fresh human red blood cell (HRBC) is purchased from Innovative Research Inc. (Novi, MI), stored at 4 °C and used within 2 weeks. Mueller Hinton (MH) broth is purchased from Becton, Dickinson and Company (BD) (Franklin Lakes, NJ) and used as received.

2.2　Methods

2.2.1　Polymer Synthesis

Polymerization of aminopropyl methacrylamide P(APMA). The schematic diagram as shown in Fig. 2, we synthesized P(APMA) by RAFT polymerization where RAFT agent CDSP (0.075 mmol), initiator AIBN (0.015 mmol) and monomer APMA (3.75 mmol) are dissolved in DMSO in a round-bottomed schlenk flask under nitrogen. After degassed by three freeze–pump–thaw cycles, the flask is vacuum-packed and dipped in a constant temperature bath. For all polymerizations, Raft agent/Initiator = 5. The polymerization is conducted at 70 °C for 24 h [15]. The solution is precipitated in acetone and dried overnight in vacuum oven. After the product is collected, a reduction step is performed using EPHP to remove the trithiocarbonate moieties to obtain final product.

　　Synthesis of butyl methacrylamide (BMA). For the synthesis of BMA, methacrylic acid (0.15 mol) is mixed with NHS (0.16 mol), DCC (0.15 mol) and Dioxane (with some THF), stirred overnight at 0 °C, the solution is filtered resulting in the formation of an intermediate product. After recrystallization in hexanes, undissolved impurities are removed and the filtrate is dissolved in anhydrous THF. The solution is mixed with butylamine and triethylamine, stirred at 0 °C the impurities are removed and the solvent is removed with rotavapor. Light yellow solution appears which is run through the column (Si gel), the solvent used is ethyl acetate
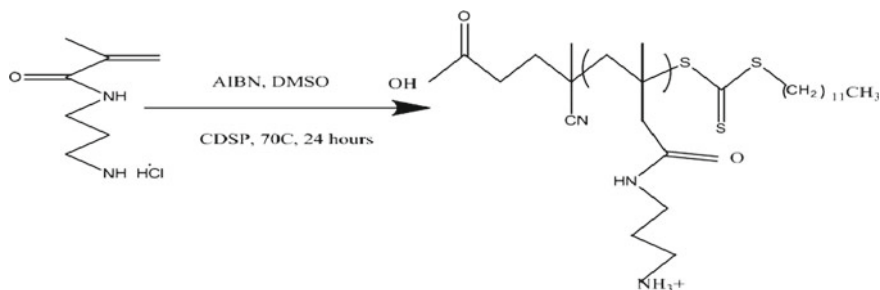
Fig. 2 Schematic synthesis of P(APMA)
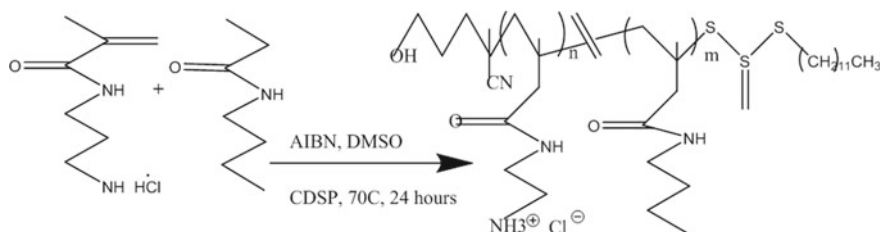
Fig. 3 Schematic synthesis of P(APMA-BMA)

and hexane with 5/4 ratio on the basis of their polarity. The solvent is finally pumped out and butyl meth-acrylamide is obtained.

Polymerization of copolymer P(APMA-BMA). The schematic diagram as shown in Fig. 3, we synthesized P(APMA-BMA) by RAFT polymerization where RAFT agent CDSP (0.067 mmol), initiator AIBN (0.0134 mmol), monomers APMA (2.4 mmol) and BMA (0.27 mmol) are dissolved in DMSO and methanol in a round-bottomed schlenk flask under nitrogen. After degassed by three freeze–pump–thaw cycles, the flask is vacuum-packed and dipped in a constant temperature bath. The reaction mixture is stirred at 70 °C for 24 h. The solution is precipitated in petroleum ether and acetone and dried overnight in vacuum oven. After the product is collected, a reduction step is performed using EPHP to remove the trithiocarbonate moieties to obtain product. For characterizing the successful synthesis of products, we use ^{1}H NMR and UV–Vis Spectrophotometer.

2.2.2 NMR

^{1}H NMR is performed with a JEOL ECS 400 MHz NMR Spectrometer in D_2O to determine monomer purity. The NMR is used to identify the structures of P(APMA) and P(APMA-BMA) homopolymers and copolymer, respectively. For every experiment, 64 scans are taken. For each of the homopolymers, a characteristic peak is

assigned and the copolymer constituents are analyzed via peak integration of the APMA and BMA monomer residues, respectively.

2.2.3 Bacterial Killing Assay

The bactericidal activity is determined based on the protocol suggested by Clinical and Laboratory Standards Institute (CLSI) and literature [16, 17]. *E. coli* (ATCC 25922) and *S. aureus* (ATCC 25923) are selected as prototypical Gram-negative and Gram-positive bacteria, respectively. Bacteria are grown in MH broth at 37 °C for 18 h, and then diluted into fresh MH broth for re-growth. Growth in bacterial cells is observed by optical density at 600 nm (OD_{600}) using a UV–Vis spectrometer (Hewlett Packard 8435, Palo Alto, CA). After the mid-log phase ($OD_{600} = 0.5$–0.6) is reached, the bacteria are washed twice with sterile PBS buffer (10 mM KH_2PO_4, 150 mM NaCl, pH 7.0) and centrifuged for 5 min at 10,000 rpm. The harvested bacteria are re-suspended and diluted by PBS. To determine the minimum bactericidal concentration (MBC), polymers are diluted in microplate and different range of concentrations is tested. To each well of polymer, diluted bacterial suspension with final concentration ∼5×10^5 CFU/ml is added. The plates are incubated at 37 °C for 3 h. Serial 10-fold dilution is subsequently made with PBS buffer. For each dilution, 20 µl of the solution is taken and plated onto MH agar plates, which are then incubated at 37 °C overnight to yield visible colonies. The minimum bactericidal concentration 99 (MBC_{99}) is defined as the minimum antimicrobial concentration that resulted in $\leq 1\%$ bacterial survival rate. All experiments are performed two times, each in triplicates on different days.

2.2.4 Scanning Electron Microscopy (SEM) Characterization

The bacterial suspension is first grown to mid-log phase ($OD_{600} = 0.5$–0.6) and the cells are collected by centrifugation at 5000*g* for 10 min and washed with sterile PBS buffer for 2 times. The bacterial cells are then resuspended in PBS buffer and incubated with polymer solutions for 3 h. Bacteria incubated without polymer solutions are used as a control. After the incubation, bacteria suspensions are washed by PBS buffer for 2 times and then fixed by the PBS buffer consisting of glutaraldehyde (2.5%) solution for 24 h [18]. Finally, the bacterial cells are further washed with sterile millipore water for three times, then dehydrated using a cycle of ethanol wash and dried in a lyophilizer. The dried bacterial cell sample is placed on a carbon tape, which is mounted onto an aluminum stud and coated with a thin layer of gold prior to analysis using a JEOL JSM7000F Field Emission SEM (Peabody, MA) with an accelerating voltage of 20 kV and a medium probe current.

2.2.5 Hemagglutination

Hemagglutination is formation of blood aggregates or clots due to toxicity. Fresh HRBC suspension (600 µl) is washed twice with PBS buffer (12 ml) and harvested by centrifugation at 3000 rpm (1000g), then re-dispersed in PBS buffer (15 ml) to reach a HRBC concentration of ~1.0%. Aliquots of this HRBC suspension (800 µl) are then mixed with polymer solutions of different concentration (200 µl) in 24 well microplate. PBS buffer (200 µl) mixed with HRBC suspension (800 µl) is used as negative controls. The microplate is kept in shaking incubator at 37 °C at 250 rpm for 60 min and settled for another 60 min before photo recording [19]. The relative hemagglutination is determined as ++++, +++, ++, +, 0, according to the size of blood clot in each well.

3   Results and Discussion

The NMR data of lysine mimicking homopolymer is shown in Fig. 4a, in order to check the purity of the polymer, the peaks are identified corresponding to each proton. For analyzing the degree of polymerization, the monomer peaks e and d are integrated and compared with that of the peak a at bulky hydrocarbon end group by using the following formula:

$$\frac{3n + 23}{4n} = \frac{I_a}{I_{e,d}}$$

where n is the degree of polymerization and Ia is the integrated chemical shift value of peak a. The DP for lysine mimicking homopolymer P(APMA) is 32 units after solving the above equation.
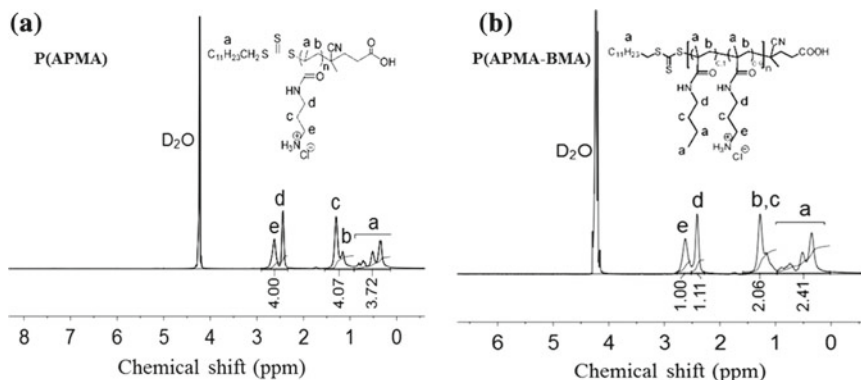
Fig. 4   NMR for **a** P(APMA) and **b** P(APMA-BMA) with D$_2$O
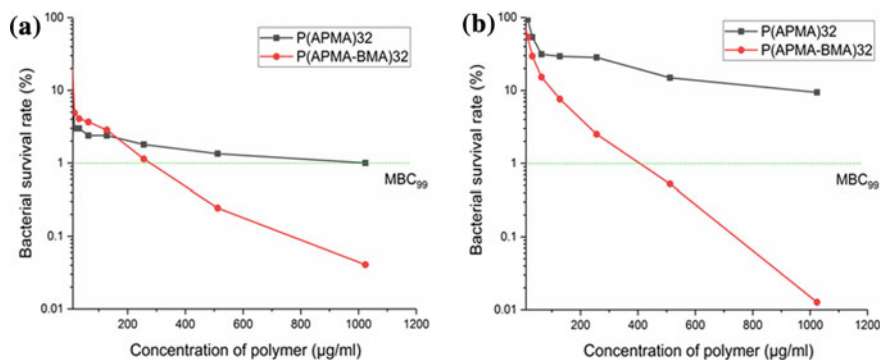
Fig. 5 MBC$_{99}$ of P(APMA) and P(APMA-BMA) with **a** *E. coli* and **b** *S. aureus*

The NMR data of lysine mimic with hydrophobic moiety is shown in Fig. 4b, in case of copolymers the composition of each polymer is characterized by NMR where the characteristic peak in either of the polymer is integrated and given a fixed value, it is then compared with the integrated peaks common to both the polymers, according to the following formula:

$$\frac{I_d}{I_e} = \frac{2_x + 2_y}{2_x} = \frac{1.11}{1} \rightarrow x/y = 9.1$$

where I_d is the integrated chemical shift value of peak *d, I$_d$* is the integrated chemical shift value of peak *d* and *x, y* is the proportion of APMA and BMA, respectively. Therefore the ratio of lysine mimicking polymer to the hydrophobic moiety observed to be 9:1.

The synthesized polymers are studied against Gram-negative *E. coli* and Gram-positive *S. aureus*. The MBC$_{99,}$ i.e., bactericidal concentration at which 99% of bacteria are killed, Fig. 5 shows that P(APMA-BMA) is more effective as compared to the P(APMA). The copolymer has a slightly lower MBC$_{99}$ against *E.coli* (275 µg/ml) as compared to *S. aureus* (420 µg/ml). These results show that hydrophobicity in addition to cationicity is required for an effective antibacterial polymer.

Mode of action of killing by polymers is evaluated using SEM. Surface morphology of bacteria incubated with both the polymers shows multiple blisters like disruptions on the surface of *E. coli* (Fig. 6b, c) as compared to the control *E. coli* shown in Fig. 6a. This indicates that both the polymers have likely punctured the bacterial membrane leading to discharge of intracellular content into the periplasmic space. The SEM results, therefore, indicate a pore-forming mode of action for these polymers.

Increase in hydrophobicity in antimicrobial polymers may stimulate the antibacterial activity but may also show cytotoxicity towards mammalian cells. To test the cytotoxicity of the designed polymers in mammalian cells, hemagglutination assay is carried out where the human red blood cells are treated with P(APMA) and P(APMA-
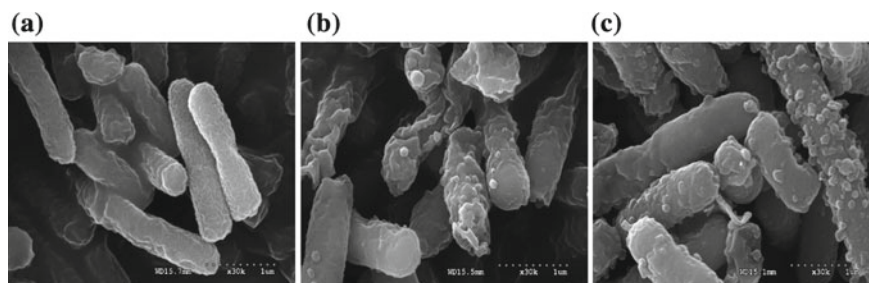
Fig. 6 SEM images for **a** *E. coli* **b** *E. coli* with P(APMA) and **c** *E. coli* with P(APMA-BMA), the scale bar is 1 μm

Table 1 Hemagglutination with P(APMA) and P(APMA-BMA)

Sample	P(APMA)32	P(APMA-BMA)32	Negative control	Positive control
Hemagglutination at 512 μg/ml	0	0	0	++++
Hemagglutination at MBC	0	0	0	+++

BMA) at different concentrations. The results in Table 1 indicate that no aggregates are formed with both polymers even at 512 μg/ml, therefore these are nontoxic to human blood cells.

4 Conclusion

Methacrylamide-based polymers are synthesized to mimic features of AMPs. Here, lysine mimicking homopolymer and 90% lysine mimicking co-polymer with 10% hydrophobic moiety are synthesized and characterized with some biochemical tests against *E. coli* and *S. aureus*. These polymers are found to be effective against both the bacteria at low concentrations with no toxicity to human blood. However, P(APMA-BMA) is observed to be more active as compared to the P(APMA) as cationicity and hydrophobicity are the two critical pre-requisite for an effective antimicrobial polymer. The mode of action of these antimicrobial polymers is pore forming as shown in SEM image, therefore antibiotic resistance is likely to be difficult to achieve. The advantages associated with these polymers are that they are cost-effective, can be commercialized at large scale and are efficient in killing bacteria.

Conflict of Interest The authors declare that they have no conflict of interest.

References

1. Livermore, D.M.: Fourteen years in resistance. Int. J. Antimicrob. Agents **39**, 283–294 (2012)
2. Zhang, Y., Overview, A.H.: Characteristics, T. B. mechanisms of antibiotic resistance in the microbial world. Baltimore 1–10 (1943)
3. Bush, K., et al.: Tackling antibiotic resistance. Nat. Publ. Gr. **9**, 894–896 (2011)
4. Andersson, D.I., Hughes, D.: Antibiotic resistance and its cost: is it possible to reverse resistance? Nat. Publ. Gr. **8**, 260–271 (2010)
5. WHO: Global antimicrobial resistance surveillance system. manual for early implementation. Who 1–44 (2015)
6. Zasloff, M.: Antimicrobial peptides of multicellular organisms. Nat. Rev. Artic. **415**, 389–395 (2002)
7. Zasloff, M.: Antibiotic peptides as mediators of innate immunity. Curr. Opin. Immunol. **4**, 3–7 (1992)
8. Seo, M.-D., Won, H.-S., Kim, J.-H., Mishig-Ochir, T., Lee, B.-J.: Antimicrobial peptides for therapeutic applications: a review. Molecules **17**, 12276–12286 (2012)
9. Hancock, R.E.W.: Review Cationic peptides : effectors in innate immunity and novel antimicrobials. LANCET Infect. Dis. **1** (2001)
10. Zhu, K., Gao, B., Zhu, S.: Characterization of a chimeric antimicrobial peptide uncovers evolutionary significance of exon-shuffling. Biochem. Biophys. Res. Commun. **428**, 360–364 (2012)
11. Yeaman, M.R., Yount, N.Y.: Mechanisms of antimicrobial peptide action and resistance. Pharmacol. Rev. **55**, 27–55 (2003)
12. Aoki, W., Ueda, M.: Characterization of antimicrobial peptides toward the development of novel antibiotics. Pharmaceuticals **6**, 1055–1081 (2013)
13. Mishra, A., et al.: Translocation of HIV TAT peptide and analogues induced by multiplexed membrane and cytoskeletal interactions. Proc. Natl. Acad. Sci. U. S. A. **108**, 16883–16888 (2011)
14. Palermo, E.F., Kuroda, K.: Structural determinants of antimicrobial activity in polymers which mimic host defense peptides. Appl. Microbiol. Biotechnol. **87**, 1605–1615 (2010)
15. Exley, S.E., et al.: Antimicrobial peptide mimicking primary amine and guanidine containing methacrylamide copolymers prepared by raft polymerization. Biomacromol **16**, 3845–3852 (2015)
16. Andrews, J.M., Andrews, J.M.: Determination of minimum inhibitory concentrations. J. Antimicrob. Chemother. **48**, 5–16 (2001)
17. Wiegand, I., Hilpert, K., Hancock, R.E.W.: Agar and broth dilution methods to determine the minimal inhibitory concentration (MIC) of antimicrobial substances. Nat. Protoc. **3**, 163–175 (2008)
18. Liu, L., et al.: Self-assembled cationic peptide nanoparticles as an efficient antimicrobial agent. Nat. Nanotechnol. **4**, 457–463 (2009)
19. Cerda-Cristerna, B.I., et al.: Hemocompatibility assessment of poly(2-dimethylamino ethylmethacrylate) (PDMAEMA)-based polymers. J. Control. Release **153**, 269–277 (2011)

Antibacterial Activity of Antimicrobial Peptide (AMP) Grafted Polystyrene Surface

Sasmita Majhi ⓘ **, Ankita Arora** ⓘ **and Abhijit Mishra** ⓘ

Abstract Bacterial colonization and infections associated with biomaterial surfaces pose common threat to patient safety and health care. Antibacterial coating on such surfaces provides significant approach toward addressing this clinical issue. Antimicrobial peptides (AMPs) are suitable alternative to conventional antibiotics because of their broad-spectrum antimicrobial activity, low propensity toward pathogen resistance, and low immune response. In this study, a designed peptide, CKLLLRL-RKLLRR (CKLR), is immobilized on maleimide-activated polystyrene plates via maleimide–thiol reaction of the sulfhydryl (–SH) group available at its N-terminal. Qualitative screening method including colony-forming units (CFU) assay is performed in 96-well plate to evaluate antibacterial efficacy of immobilized CKLR. Bacterial viability assays show nearly 100% reduction in the growth of both *Escherichia coli* and *Staphylococcus aureus*. Findings of this study indicate that CKLR is potent to develop infection-resistant biomaterial surfaces. Such efficient immobilization strategies can be tailored to eliminate bacterial infections arising from surfaces, thereby rendering antimicrobial biomaterials.

Keywords Antimicrobial peptides · Immobilization · Polystyrene Antibacterial activity

1 Introduction

Surface contamination contributes to community-acquired as well as nosocomial infection that transmits through fomites (substance capable of carrying infectious organisms). Persistent contamination occurs usually due to the formation of biofilm on any contact surface. As documented, infectious diseases are responsible for tens of millions of deaths and it is also estimated that 80% of the human infections are

S. Majhi · A. Arora · A. Mishra (✉)
Department of Materials Science and Engineering, Indian Institute
of Technology Gandhinagar, Gandhinagar, Gujarat, India
e-mail: amishra@iitgn.ac.in

associated with biofilm formation [1]. Furthermore, increase in antibiotic-resistant microbes has enhanced the requirement for developing self-decontaminating surfaces. So far, various strategies have been proposed to eliminate the infections prevailing from any contact surfaces through the use of different antimicrobial agents such as metals, disinfectants, antibiotics, antimicrobial polymers, and antimicrobial peptides [2, 3]. But these compounds are at times cytotoxic and are associated with the development of antibacterial resistance [4].

Antimicrobial peptides (AMPs) (also called host defence peptides) have the potential to tackle the problem of infection as well as contamination because of its distinguishing features compared to others. AMPs are short polypeptides of 10–50 amino acid (AA) residues having cationicity and hydrophobicity [5, 6]. AMPs generally show broad-spectrum antimicrobial activity with limited immunogenicity and less susceptible to proteolysis. Importantly, AMPs used to target the membrane of pathogens, which reduces its ability to become resistant, as fundamental function of membrane is to maintain metabolism, viability, and microbial homeostasis [7, 8]. These advantages make AMPs an ideal antimicrobial candidate for coating applications. However, a crucial prerequisite for the development of AMP-based coating is maintenance of peptide activity and stability after immobilization.

This study intends to develop antibacterial surface by immobilizing short antimicrobial peptide (13 residues). This is because short peptides can be synthesized easily in large quantity at low cost which can further reduce the burden of R&D units in industry. The antimicrobial peptide used here is derived from human β-Defensin 3 (hBD-3) C-terminal residues 54–65 with all the non-cationic residues replaced by leucine residues to increase its hydrophobicity and thereby its antibacterial activity [9]. In order to covalently immobilize this peptide onto polystyrene (PS) surface, cysteine (C) residue is added to the N-terminal forming CKLR (CKLLLRLRK-LLRR), as peptide of interest. Further, microtiter plates are used as coating platform, to simplify coating procedure and reduce the amount of resources employed for the development of such coatings. A method of exclusive site-directed N-terminal coupling of CKLR was performed on maleimide-activated surfaces via maleimide–thiol conjugation reaction to examine effectiveness of tethered CKLR.

2 Material and Methods

2.1 Materials

Pierce maleimide-activated 96-well microtiter plates and Tris-(2 car-boxyethyl)phosphine (TCEP) were obtained from Thermo Fisher Scientific (Waltham, MA, U.S.A.), Corning® 96 well plates (non-treated, polystyrene flat bottom), sodium phosphate, Tween® 20, and Ethylenediaminetetraacetic acid (EDTA) were obtained from Sigma and used without further purification. Sodium chloride,

potassium chloride, disodium hydrogen phosphate, and potassium dihydrogen phosphate were purchased from HiMedia.

2.2 Bacterial Strain and Media

Bacterial strains were procured from Microbial Type Culture Collection and Gene Bank (MTCC), Chandigarh, India. *Escherichia coli* (ATCC 25922) and *Staphylococcus aureus* (ATCC 25923) were considered for bacterial Gram-negative and Gram-positive strain challenges, respectively. Mueller–Hinton (MH) media (broth/agar) of HiMedia was prepared as per manufacturer's specification for growth of bacterial strains.

2.3 Peptide

High purity (>95%) peptide CKLR (CKLLLRLRKLLRR) was purchased from Cusabio Life Science (MD, U.S.A.) and used in experiments in solution form.

2.4 Antibacterial Activity of CKLR in Solution

The antibacterial activity of CKLR in solution was evaluated using broth microdilution test against both *E. coli* and *S. aureus*. Minimum inhibitory concentration (MIC_{90}) was determined as the lowest peptide concentration that inhibited bacterial growth by 90% at 18 h of incubation. For this, loopful of bacteria was grown overnight at 37 °C in Mueller-Hinton Broth (MHB), and then bacterial cells were inoculated into fresh MHB at 10^2 dilution and grown at 37 °C until mid-log phase ($OD_{600} = 0.5 - 0.7$) was reached. After the attainment of mid-log phase, cells were diluted in MHB and adjusted to obtain a cell concentration of 5×10^5 colony-forming units per milliliter (CFU/ml). Peptide stock was prepared in milliQ water and final peptide concentration ranging from 512 to 1 µg/ml was added to each well of microtiter plate (Corning® 96 well plate). A 90 µl aliquot of diluted cell culture (5×10^5 CFU/ml) was further added to each well containing 10 µl of peptide solution (having 1 mM TCEP). TCEP was used as disulfide reducing agent in peptide solution. The positive control comprised of diluted cell culture, and negative control was only media without cell culture. The percentage of viable cell culture was determined by absorbance [optical density (OD)] measured at 600 nm using a microplate reader (EnVision Multilabel, Perkin Elmer, Waltham, MA, U.S.A.) after being incubated for 18 h at 37 °C. The percentage of survival rate of bacteria was calculated from Eq. (1)
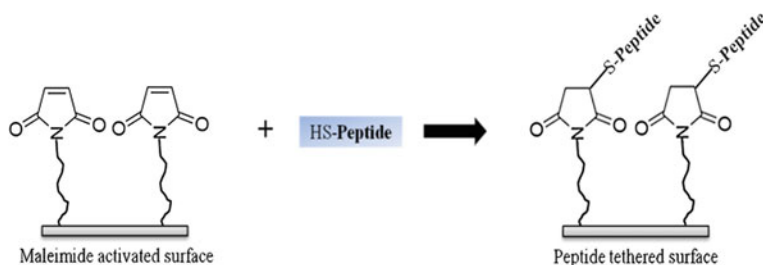
Fig. 1 Specific reaction for conjugation of CKLR peptide onto maleimide-activated microwells

$$\text{Survival rate of bacteria}\,(\%) = \frac{\text{Sample OD} - \text{Negative control OD}}{\text{Positive control OD} - \text{Negative control OD}} \times 100$$

$$(1)$$

2.5 CKLR Immobilization on Modified Microwells

CKLR was covalently conjugated to maleimide-modified wells of maleimide-activated 96-well microtiter plate (PS-MAL) through specific reaction between N-terminal cysteine of CKLR and maleimide as depicted in Fig. 1.

Each microwell was washed three times using 200 µl of wash buffer (0.1 M sodium phosphate, 0.15 M sodium chloride, 0.05% Tween®-20; pH 7.2). 2–0.0625 mg/ml of varying peptide concentration was prepared in binding buffer (0.1 M sodium phosphate, 0.15 M sodium chloride, 10 mM EDTA; pH 7.2). Next, 100 µl of peptide solution was added to appropriate maleimide-modified microwells and incubated for 2.5 h at room temperature with mild shaking. After completion of conjugation reaction, microwells were washed with autoclaved milliQ water three times to remove any physisorbed peptide [10].

2.6 Antibacterial Activity Determination of CKLR Immobilized PS Surface (PS-MAL-CKLR)

To determine antibacterial activity of AMP tethered PS-MAL surface, mid-log phase bacterial cell culture was washed and resuspended in 1X PBS; pH 7.2. Then, cell concentration was further diluted and adjusted to 5×10^5 CFU/ml in 1X PBS. An aliquot of 50 µl cell culture (5×10^5 CFU/ml) was incubated on CKLR immobilized PS-MAL surface for 4 h at 37 °C. After incubation, cells were diluted in 1X PBS for plating and CFU determination. Each sample was carried out in duplicates and 20 µl of each diluted cell suspension was plated on Mueller-Hinton agar (MHA) plates and incubated for 12 h at 37 °C for CFU counting. The percentage of bacteria

killed was calculated from Eq. (2), considering maleimide-activated well surface as control [11].

$$Bacteria\,killed\,(\%) = \frac{CFU\,of\,control - CFU\,of\,sample}{CFU\,of\,control} \times 100 \qquad (2)$$

2.7 Surface Segregation of Peptide

Quantification of surface peptide was determined using bromophenol blue (BPB). 0.5% aqueous bromophenol blue solution was reacted with each coating for 1–3 min, wherein BPB was allowed to bind to the amines on surface. Followed to it microwells were washed with milliQ water to remove excess of bromophenol blue from surfaces. Attached bromophenol blue was then recovered using 0.05 M HCl in ethanol [12]. Absorbance of the solution was observed at 425 nm using spectrophotometer, the spectral absorbance was then correlated with concentration of segregated peptide according to Beer's law as described below [13]:

$$S[NH_2] = \frac{OD_{605} \times V}{\varepsilon_{605} \times A \times d} \qquad (3)$$

where V is the volume of eluent solution (in cm^3). ε_{425} is the molar extinction coefficient of BPB at 425 nm 5690 M^{-1} cm^{-1}. A is the area of coating (in cm^2) and d is the optical path length of cuvette (in cm).

3 Results

3.1 Antibacterial Activity of Soluble CKLR

Our designed peptide CKLR is found to be active against both *E. coli* and *S. aureus* having MIC$_{90}$ value of 125 µg/ml (74.36 µM) for both strains, as shown in Fig. 2.

3.2 Antibacterial Activity of Immobilized CKLR

The surface antibacterial activity of PS-MAL-CKLR exhibited 100% killing activity toward both *E. coli* and *S. aureus* (approximately, 10^5 CFU/ml) as tabulated in Table 1. 100% of bacteria were killed even at a low concentration of 62.5 µg/ml.

Fig. 2 Minimum inhibitory concentration (MIC) of CKLR in solution determined using broth microdilution method against *E. coli* and *S. aureus*
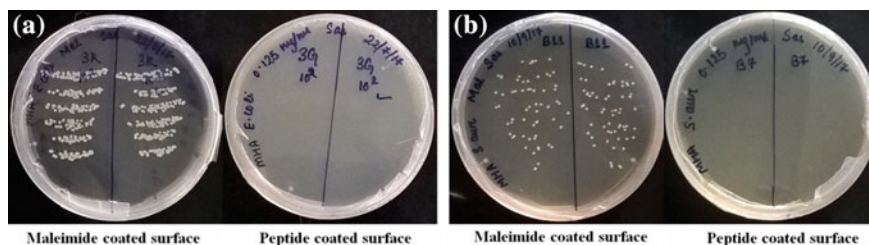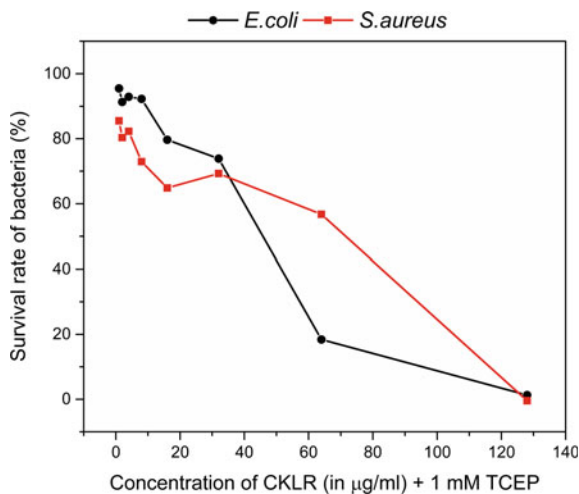
Fig. 3 Photographs of CFU count of **a** *E. coli* and **b** *S. aureus* on PS-MAL-CKLR and PS-MAL surfaces for 10^2 *dilution*

Table 1 Colony-forming unit (CFU) assay of *E. coli* and *S. aureus* incubated with CKLR modified surfaces (also depicted in Fig.3)

Surfaces	Bacteria killed (%) calculated for CKLR immobilized on maleimide-activated surface	
	E. coli	*S. aureus*
500 µg/ml of CKLR	100	100
250 µg/ml of CKLR	100	100
125 µg/ml of CKLR	100	100
62.5 µg/ml of CKLR	100	100
Maleimide	0	0

3.3   Surface Segregation of Peptide

To determine the amount of surface segregated peptide, bromophenol blue (BPB) solution was used as an indicator. OD of recovered samples was taken at 425 nm

using UV–Vis spectrophotometer and same was incorporated in Beer–Lambert's law described above, to calculate amine content on each coating and is directly converted into amount of peptides on surface. Thus, 35% of total available peptide was found to be attached on surface.

4 Conclusion

Designed peptide, CKLR, was employed for AMP immobilization study on maleimide-activated polystyrene surface. The maleimide–thiol chemistry provides a facile and strong covalent immobilization method to tether CKLR onto maleimide-activated polystyrene microtiter plates. The peptide-tethered surfaces displayed almost 100% killing efficiency against bacteria. This study lays a foundation for potential application of short antimicrobial peptide as antibacterial agent coated on plastic substrates. Although this work involved polystyrene microwell plates, this strategy could be extended to other polymeric substrates with different degrees of complexities and applications.

Conflict of Interest The authors declare that they have no conflict of interest.

References

1. Campoccia, D., Montanaro, L., Arciola, C.R.: A review of the biomaterials technologies for infection-resistant surfaces. Biomaterials **34**, 8533–8554 (2013)
2. Zhao, L., Chu, P.K., Zhang, Y., Wu, Z.: Antibacterial coatings on titanium implants. J. Biomed. Mater. Res. B Appl. Biomater. **91**, 470–480 (2009)
3. Alves, D., Olívia Pereira, M.: Mini-review: antimicrobial peptides and enzymes as promising candidates to functionalize biomaterial surfaces. Biofouling **30**, 483–499 (2014)
4. Campoccia, D., Montanaro, L., Speziale, P., Renata, C.: Biomaterials antibiotic-loaded biomaterials and the risks for the spread of antibiotic resistance following their prophylactic and therapeutic clinical use q. Biomaterials **31**, 6363–6377 (2010)
5. Wang, G.: Database-guided discovery of potent peptides to combat HIV-1 or superbugs. Pharmaceuticals **6**, 728–758 (2013)
6. Wang, G., Li, X., Wang, Z.: APD3: the antimicrobial peptide database as a tool for research and education. Nucleic Acids Res. **44**, 1087–1093 (2016)
7. Hale, J.D.F., Hancock, R.E.W.: Alternative mechanisms of action of cationic antimicrobial peptides on bacteria. Expert Rev. Anti. Infect. Ther. **5**, 951–959 (2007)
8. Guaní-Guerra, E., Santos-Mendoza, T., Lugo-Reyes, S.O., Terán, L.M.: Antimicrobial peptides: general overview and clinical implications in human health and disease. Clin. Immunol. **135**, 1–11 (2010)
9. Hoover, D.M., Wu, Z., Tucker, K., Lu, W., Lubkowski, J.: Antimicrobial characterization of human beta-defensin 3 derivatives. Antimicrob. Agents Chemother. **47**, 2804–2809 (2003)

10. Smyth, D.G., Blumenfeld, O.O., Konigsberg, W.: Reactions of N-ethylmaleimide with peptides and amino acids. Biochem. J. **91**, 589–595 (1964)
11. Li, X., et al.: Acta biomaterialia antimicrobial functionalization of silicone surfaces with engineered short peptides having broad spectrum antimicrobial and salt-resistant properties. Acta Biomater. **10**, 258–266 (2014)
12. Fulmer, P., Lundin, J.G., Wynne, J.H.: Development of antimicrobial peptides (AMPs) for use in self-decontaminating coatings. ACS Appl. Mater. Interfaces **2**, 1266–1270 (2010)
13. Akkoyun, A., Bilitewski, U.: Optimisation of glass surfaces for optical immunosensors. Biosens. Bioelectron. **17**, 655–664 (2002)

Novel Polymeric Adsorbent for the Remediation of Cu(II) Ions from Water

Nida Fakhar, Weqar Ahmad Siddiqui and Masood Alam

Abstract Toxicities caused by hazardous elements encountered in water is problem to be dealt with. The present work focusses on the synthesis of polymeric composite material (Adsorbent) and explores its adsorption properties towards certain heavy metal. Sol-gel was used as a method of synthesis. The polymeric material prepared is polyaniline Tin (IV) Phosphate and the emphasis was on its adsorption behavior of towards heavy metal ion. The advantages of this composite are not only its easy and rapid separation but also its selectivity towards target pollutants through its polymeric matrixes. The experimental data show that polyaniline/Sn(IV) phosphate composite has reasonable good adsorption capacities for Cu(II). Studies of adsorption are taken out via Batch method. The optimum condition for excellent removal efficiency of the material was fulfilled by altering certain framework like concentration, pH, temperature, adsorbent dose, and time. The morphology of the surface of prepared composite prior to and after Cu(II) adsorption was determined by scanning electron microscopy. EDX analysis shows the presence of C, O, S, P, and Sn but after adsorption a new peak of Cu(II) appeared indicating the Cu(II) uptake onto composite polyaniline/Sn(IV) Phosphate. It was acknowledged that uptake of Cu(II) was pH vulnerable. The result of the adsorption almost suited to the Langmuir, D-R isotherm and Freundlich framework. The kinetics data for Cu(II) adsorption were ultimately suited to pseudo-second-order framework. The mechanism was spontaneous and endothermic as ensured by the thermodynamic parameter about adsorption experiment. Thermodynamic parameter ensured about the adsorption experiment that process was endothermic and spontaneous. The composite can be utilized so that the pre-concentration including recovery of Cu(II) ions from water as well as wastewater.

Keywords Adsorbent · Polymeric material · Heavy metal

N. Fakhar (✉) · W. A. Siddiqui · M. Alam
Department of Applied Science and Humanities, Faculty of Engineering
and Technology, Jamia Millia Islamia, New Delhi 110025, India
e-mail: nidafakhar20@gmail.com

1 Introduction

Brisk upgradation in lifestyle and ultra-modernization has taken us to the stage of global crisis leading to the generation of toxic substance from industries. This causes contamination of water sources, owing to their disposal threatening life of organism around. This includes various heavy metals and dyes that induce lethal effect which may not only carcinogenic effect but mutagenic too. Both aquatic and terrestrial life are greatly affected due to these poisonous heavy metal ions released from industries and automobile exhausts [1, 2]. Exposure to metals of relatively high density such as Cu(II), Cd(II), Hg(II), Pb(II), Ni(II), and Co(II) even at trace level has been linked with risk for human beings such as developmental cause severe damages to kidney, brain, liver, and reproductive system on prolonged accumulation in the body [3, 4]. To get rid of these poisonous effluents from the environment is one of the alarming task faced by environmentalists. The efforts are being taken to ensure successful removal of these pollutants from industrial water which later discharged into water bodies. Many processes were employed to get rid of these harmful pollutants from water but most of the processes have several limitations including partial metal removal, use of high-cost equipment, and high energy expenditure. Several conventional methods include adsorption, filtration, oxidation/reduction membrane separation, chemical precipitation, ion exchange, electrochemical coagulation, solvent extraction, etc. [5–7]. Above all mentioned techniques, the adsorption technique is almost economical and very prevelent i.e a desirable technique because it is cheap and perform maximum removal even if metals are present in traces [8]. Many adsorbents were employed in water treatment which are based on polymer are explored by many authors. Since last few years, authors strive to make these adsorbent polymers better which first resulted on the basis of ion exchange resins. On the other hand, the adoption of new techniques introduced the evolution of finely porous polymers with high specific surface area. Polymeric adsorbents adopted for the heavy metals to be adsorbed because of their easy regeneration and strong mechanical properties in comparison with other adsorbents like activated carbon [9], cellulose, [10] and silica gel. To improve the adsorption quality, nowadays, reliable hybrid polymers, that is organic–inorganic in nature, have been utilized for the separation of harmful pollutants from wastewater [11]. Recently, the ion exchange composite material which is organic–inorganic in nature depending on conducting polymers like polypyrole, polyaniline, poly-anis dine, etc. has revolutionized the separation science due to their unique proton dupability, electrical conductivity, granulometric nature, high thermal and mechanical stability, cost-effective synthesis, and selectivity for heavy metal ions [12, 13].

2 Experimental

2.1 Materials and Method

Polyaniline/Sn(IV) phosphate composite was made from combining partly volume of 5% Aniline and 0.1 Ammonium per sulfate and continuously stirred by the magnetic stirrer. Gel of polyaniline was obtained which was green in color by subjecting the solution at less than 10 °C for 30 min. Combination of 0.1 M stannic chloride solution in an aqueous solution of orthophosphoric acid at room temperature, a precipitate of Sn(IV) phosphate was processed. The white precipitate was observed where via combining aqueous ammonia, the pH of the mixtures was set to 1, proceeded by stirring continuously. The organic phase, i.e., gel polyaniline was combined with inorganic white precipitate of Sn(IV) phosphate and then combined completely followed by instant stirring. The colorful gel was stored for 1 day at 25 °C for the digestion. With the help of suction, the gel was refined. DMW was used to get rid of excess acid through washing and the prepared item was dehydrated at 50 °C in oven. The dehydrated form was then crushed to fine powdered form.

Reaction mechanism
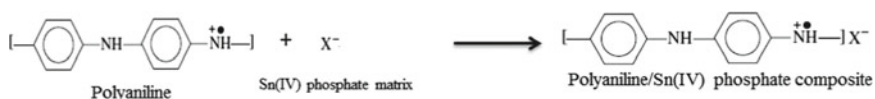
2.2 Preparation of Solution of Adsorbate

Solution in stock was prepared of Cu(II) ions (1000 mg/L) from combining the required amount of copper nitrate (A.R. grade) in demineralized dissolving their chlorides or nitrates in DMW, while the Cr(VI) solution was prepared using $K_2Cr_2O_7$ water (DMW). Likewise, other metal ions (1000 mg/L) were accomplished.

2.3 Studies of Adsorption Experiment

Batch Method was used to study adsorption studies. In the conical flask, 0.1 g of adsorbent was taken and combined with solution of 10 ml metal ions of required concentration. For mixture shaking, shaker incubator was utilized for 1 day. The desired mixture was filtered. Atomic absorption spectroscopy of GBC 902 instrument was required to measure in the filtrate the metal ion concentration so called final concentration. To estimate the amount of adsorption of metal ion, final concentration was subtracted from the initial concentration.

The percent adsorption of adsorbed and equilibrium adsorption (q_e) can be defined as

$$\%\text{Adsorption} = (C_o - C_e)/C_o \times 100$$

$$\text{Adsorption capacity}(q_e)(\text{mg/g}) = [(C_o - C_e)] \times V/M$$

In which, C_o, and C_e are the metal ions initial concentration (mg/L); Equilibrium adsorbate concentration (mg/L) of adsorbate; M is the composite mass; V is the volume of the solution.

3 Result and Discussion

3.1 Adsorption Behavior of the Composite Polyaniline/Sn(IV) Phosphate Composite Towards Heavy Metals Ions

The adsorption behavior of polyaniline/Sn(IV) composite towards different heavy metals ions was studied using single metal ions solutions each having a concentration initial of 50 mg/L. As shown in Fig. 1 the maximum detection of Cu(II)ions adsorption was discovered to be (98.4%), followed by Pb(II) (97.0%), Ni(II) (89.3%), Cd(II) (58.01%), Cr(IV) (52.12%).

Scanning electron microscopy (SEM) analysis:

The scanning electron microscopy (SEM) was required to determine the characteristics of surface polyaniline/Sn(IV) phosphate composite prior to and after Cu (II) adsorption which is presented in Fig. 2 The surface of the adsorbent becomes noticeably porous and irregular before adsorption (Fig. 2a). After adsorption, adherence of Cu(II) ions was noticed within the pores (Fig. 2b).

Fig. 1 Adsorption percentage of different metal ions noticed in aqueous solution. Experimental state: Cu(II) = 50 mg/L; volume = 10 ml; adsorbent = 0.1 g Temp = 30 °C
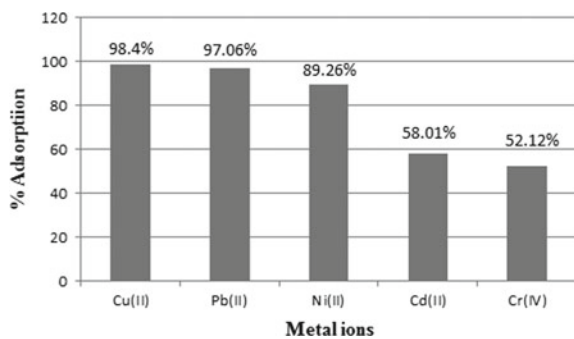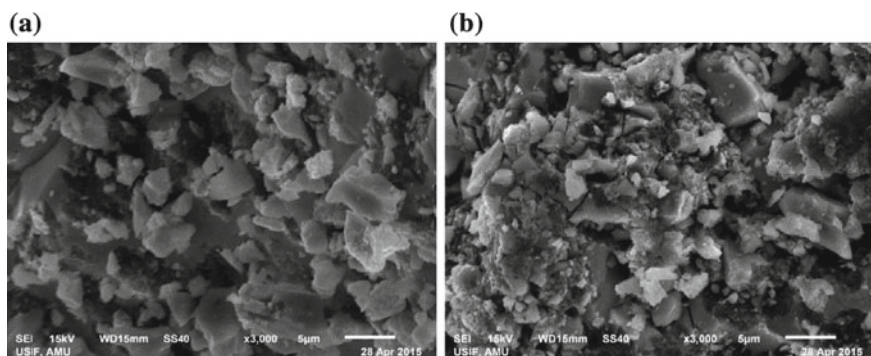
Fig. 2 **a** Prior to adsorption and **b** after
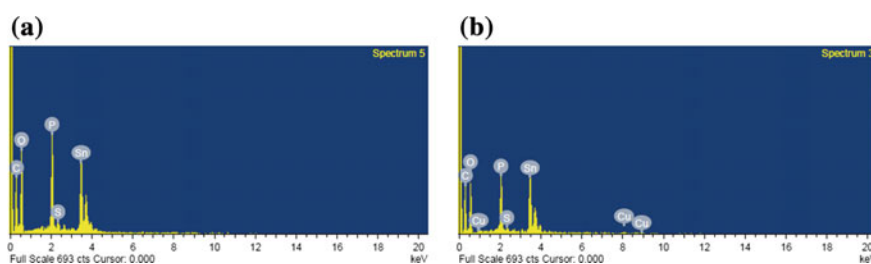
Fig. 3 Spectrum of Energy Dispersive X-ray for adsorbent **a** Prior to and **b** after Cu(II) adsorption

Table 1 EDX analysis of polyaniline/Sn(IV) phosphate

Elements	Prior to adsorption		After adsorption	
	Weight %	Atomic %	Weight %	Atomic %
C	25.69	40.01	28.29	44.53
O	43.87	51.30	39.40	47.04
P	8.08	4.88	6.60	4.03
S	0.65	0.38	0.47	0.28
Sn	21.71	3.42	23.69	3.77
Cu	–	–	1.15	0.34

Energy dispersive X-ray(EDX)Analysis:

The Fig. 3 represent composite polyaniline/Sn(IV) phosphate EDX spectrum of uptake of Cu(II) ions prior to and after adsorption.

The EDX analysis (Table 1) shows the presence of C, O, P, S and Sn, but after adsorption, a new peak of Cu(II) appeared indicating the uptake of Cu(II) on to the polyaniline/Sn(IV) composite phosphate.
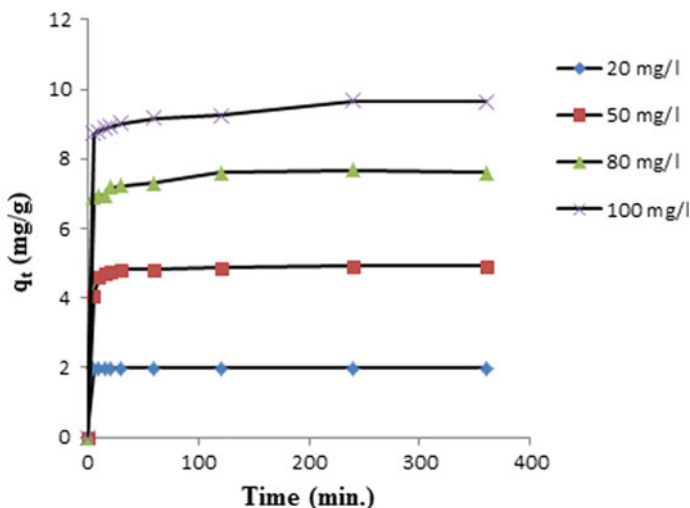
Fig. 4 Effect of contact time on the uptake at dissimilar initial concentrations of Cu(II) from aqueous solution

3.2 Effect of Contact Time and Initial Concentration

Uptake of Cu(II) over the surface of composite at various initial Cu(II) concentration (20–100 mg/L) was performed at varied time intervals. At equilibrium, the major composite contribution in the uptake of Cu(II) came out to be 1.99, 4.86, 7.61 and 9.25 mg/g at 20, 50, 80, and 100 mg/L initial concentration respectively. In the initial stages, it was that adsorption was increased and slowed down in subsequently up till equilibrium was reached. Reaction balanced time for adsorption of Cu(II) at concentration 20 mg/L came out to be 20 min, for 50 mg/L it was 30 min, and at concentration of Cu(II) above 50 mg/L was 120 min, highlighting the time at which the reaction was balanced which was based on the Cu(II) initial concentration (Fig. 4).

3.3 Effect of pH

When the initial value of pH (pH$_i$) of the aqueous solution raised, adsorption of Cu(II) raised. The influence of pH was measured to the extent of 1–10. The higher adsorption occurred at pH 6 (Fig. 5). In acidic solution (low pH values), the uptake of Cu(II) ions is inhibited because of the elevated concentration H$^+$ ions concentration competing with Cu(II) ions for the available uptake positions over the surface. The final pH (pH$_f$) recorded in the figure was the pH of the solution at equilibrium. This is also crucial feature since many adsorption reactions have been considered
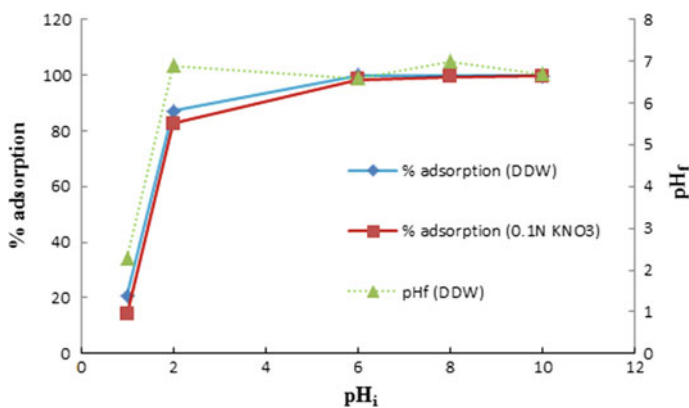
Fig. 5 Influence of pH over the Cu(II) uptake from aqueous solution

under equilibrium conditions. Thus, when the initial pH of the system was 1, the final pH was virtually the same ($pH_f = 1.2$), showing that the solution was acidic and contained fairly high concentrations of H^+ ions; thus, H^+ ions compete for the adsorption sites followed by minimum 18% uptake. When the initial pH was set at 2, the final pH value raised rapidly ($pH_f = 6.9$) simultaneously, the uptake of Cu(II) became 87.2%. The adsorption of such a large quantity of Cu(II) together with H^+ ions led to the decrease in H^+ ions concentration in the solution, resulting in increment in final equilibrium pH. With the rising pH, adsorption of Cu(II) continued to raise and became constant beyond pH 6. The influence offered by the electrolyte (KNO_3) due to the uptake of Cu(II) was noticed and which discovered that the electrolyte had almost no effect over the Cu(II) uptake as depicted in Fig. 5.

3.4 Effect of Doses

The influence of desired doses was resolved by altering the dose of adsorbent from 0.05 to 0.5 g. The results obtained presented in Fig. 6. It can be revealed through the plot where the percent adsorption raised while adsorption capacity lowered with increasing prepared composite dose. The percent adsorption of Cu(II) increased, perhaps because as the adsorbent dose increased, the available sides for adsorption to occur also increased. Furthermore, more the composite dose, lessen the adsorption capacity because few uptake positions rendered unsaturated throughout the experiment.
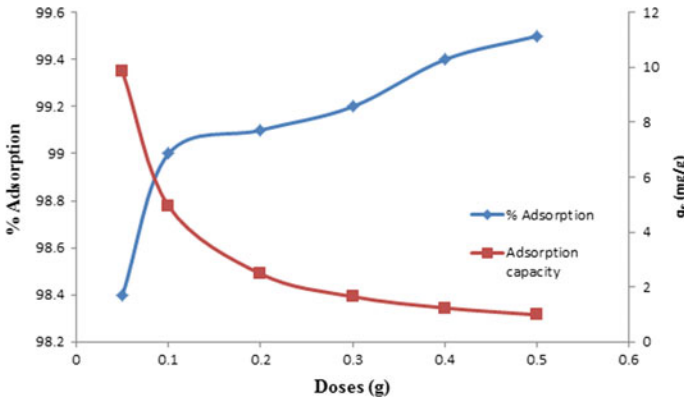
Fig. 6 Effect of doses. Conditions: Cu(II) 50 mg/L; volume = 10 ml; adsorbent = 0.1 g Temp = 30 °C

3.5 Kinetics of Adsorption

Kinetic parameters that are pseudo-first-order, pseudo-second-order and intraparticle diffusion kinetic parameter were interpreted the kinetics of adsorption and effectiveness of these three kinetic parameters were investigated and depicted in Fig. 7a–c which were based on linearized equation.

Pseudo-first-order relation:

$$\log(q_e - q_t) = \log q_e - \frac{k1t}{2.303R}$$

where q_e and q_t represent the quantity of adsorbed Cu(II) at equilibrium; at time t (min), K_1 is the pseudo-first-order rate constant and t is the adsorption time (min)

Pseudo-second-order relation:

$$\frac{1}{q_t} = \frac{1}{k_2 q_e^2} + \frac{t}{q_e}$$

where q_e represents the quantity of adsorbed (mg/g) Cu(II) at the equilibrium and q_t adsorbed at time t (min), K_2 called as rate constant pseudo-second order and t is the adsorption time (min). For the pseudo-second-order plot t/q_t versus t presented straight line and by the slope and intercept of the graph $q_{e\ and}\ k_2$ can be detected, respectively.
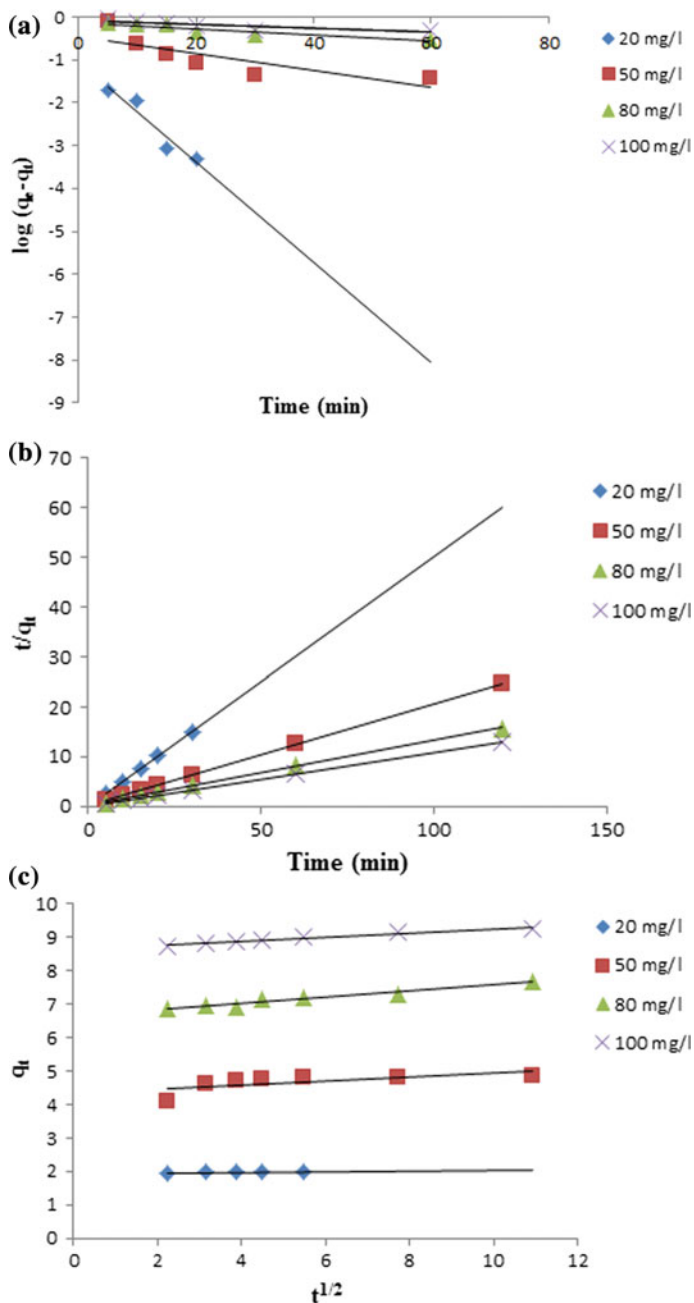
Fig. 7 a plot for the pseudo–first-order kinetic framework; **b** plot for pseudo-second-order kinetic framework; **c** plot for intraparticle diffusion framework

Intraparticle diffusion equation:

$$q_e = K_i \cdot t^{0.5} + C$$

where k_i is the rate constant intraparticle diffusion; C corresponds to intercept, linked to the thickness of boundary layer. Regarding the intraparticle diffusion framework, the values of constant were achieved through the intercept of the straight line graph of q_t against $t^{0.5}$.

An observation of the experimental adsorption capacities with corresponding calculated values as received from Fig. 7a–c and Table 2, showed the q_e (cal.) for the pseudo-first-order kinetic parameter altered considering from q_e (exp.) and the R^2 values were not close to 1, which means the adsorption phenomenon avoid the pseudo-first-order kinetic parameter. While the q_e (cal.) and q_e (exp.) were almost same and the R^2 values were very close to 1 for pseudo-second-order kinetic framework, which implied better suitability to this model.

From Fig. 7c, From the origin, the deviation of the plot for all Cu(II) concentration indicating dispersion through the pore was not particularly rate controlling factor however, in adsorption mechanism, the process like diffusion through film was also engaged [14, 15].

Table 2 Kinetic framework for the Cu(II) uptake

Pseudo-first-order parameters

Concentration (mg/L)	q_e (experimental)	q_e (calculated)	K_1	R^2
20	1.98	0.09	−0.268	0.9241
50	4.86	0.36	−0.046	0.6637
80	7.61	0.75	−0.016	0.8261
100	9.25	0.85	−0.011	0.7407

Pseudo-second-order parameters

Concentration (mg/L)	q_e (experimental)	q_e (estimated)	h	K_2	R^2
20	1.98	1.99	26.015	6.578	1
50	4.86	4.88	7.932	0.336	1
80	7.61	7.65	5.503	0.095	0.9996
100	9.25	9.97	4.534	0.053	0.9984

Intraparticle diffusion parameters

Concentration (mg/L)	k_{id}	C	R^2
20	0.0063	1.9477	0.8745
50	0.0582	4.3521	0.9241
80	0.0896	6.6734	0.9417
100	0.0618	8.6271	0.9514
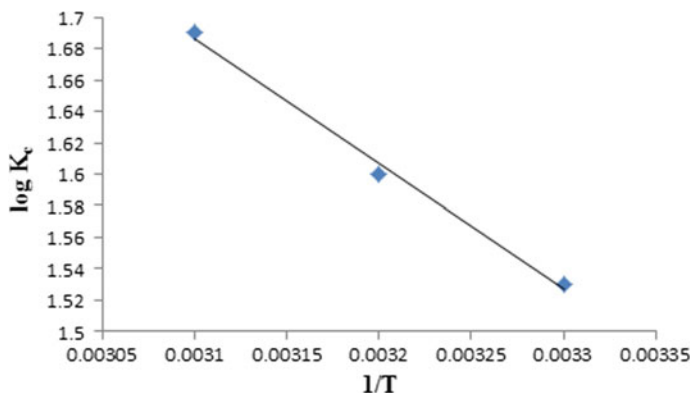
Fig. 8 Van't Hoff graph

3.6 Thermodynamic Studies

The equilibrium constants (K_c) at 30, 40, and 50 °C were estimated from the given relationship:

$$K_c = C_{AC}/C_e$$

where C_{AC} and C_e are the concentrations (mg/L) at equilibrium of Cu(II) involving both composite and solution, respectively.

The change in standard free energy, $\Delta G°$, can be estimated via the following relation:

$$\Delta G° = -RT \ln K_c$$

where R is the gas constant; T is the temperature in degrees Kelvin, while the change in standard E ($\Delta H°$) and change in standard entropy ($\Delta S°$) values were estimated via the following relationship:

$$\log K_C = \frac{\Delta S°}{2.303R} - \frac{\Delta H°}{2.303RT}$$

The slope and intercept of the liner plot of log K_c versus $1/T$ (Fig. 8) were used to estimate the values of $\Delta S°$ and $\Delta H°$. The endothermic nature of the experiment was revealed by the positive value of $\Delta H°$, while the spontaneous nature of experiment was revealed by the negative value of $\Delta G°$, and spontaneity intensified with rising temperature. Increment in randomness occurred at the solid/liquid interface throughout the adsorption experiment as suggested by positive value of $\Delta S°$ as table 3 suggested.

Table 3 Thermodynamic framework for the Cu(II) uptake

Temperature (°C)	K_c	$\Delta G°$ (kJ/mol)	$\Delta H°$ (kJ/mol)	$\Delta S°$ [kJ/(mol K)]
30	34.46	−8.92	15.31	0.079
40	40.66	−9.63		
50	49.00	−10.45		
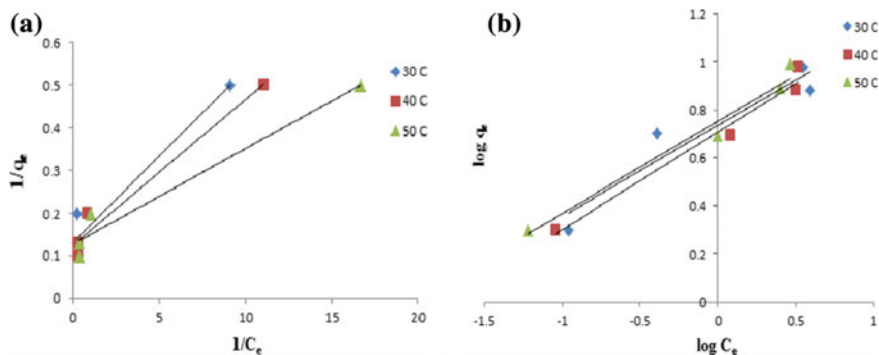
Fig. 9 **a** Langmuir isotherm and **b** Freundlich isotherm

3.7 Adsorption Isotherm

Langmuir, Freundlich, Dubinin–Radushkevich (D-R), and Temkin were isotherm framework which were relevant for better applicability of result from studies.

Langmuir Isotherm:

Plotting $1/q_e$ against $1/C_e$ for the data obtained experimentally at 30, 40, and 50 °C led to a straight line (Fig. 9a). The values of K_L and q_m obtained at all the various temperatures are represented in Table 4. This indicates that the Langmuir isotherm suited to the experimental result at 40 °C but deviated from the same at low temperature.

Freundlich Isotherm:

A graph of log q_e versus log C_e resulted in straight line, the slope, and intercept of which corresponds to $1/n$ and log K_F. Figure 9b depicts the Freundlich isotherm obtained for the experimental data at the various temperatures studied. The values of the corresponding Freundlich constants are represented in Table 4. When the correlation coefficient (R^2) had its high-value result obtained could be suited well by the Freundlich model at 40–50 °C but at low temperature increasing deviations occurred. However, the elevation in the value of K_F with temperature exhibited that the uptake process was favored by higher temperatures.

The D-R isotherm:

The D-R isotherm, which takes into account the adsorbent surface heterogenous nature, was used to predict whether the adsorption occurred via a Physsorption or chemisorption process.

The values of q_m and β^2 attained through the intercept and slope from the graph of ln q_e versus ε^2 while the mean free energy of adsorption, E, can be estimated via given equation:

$$E = -\frac{1}{2\beta^{1/2}}$$

The D-R framework shown in Fig. 10 and the mean free energy values are enlisted in Table 5. The values of E attained comes out to be between 13.7 and 15 kJ/mol, which were within the energy limit expected for a chemisorption reaction.

Tempkin isotherm:

Tempkin parameter is represented as:

$$q_e = B \ln A + B \ln C_e$$

where $B = RT/bT$, called as the Tempkin constant associated to heat of adsorption while R is the universal gas constant, A is the equilibrium binding constant analogous

Table 4 Langmuir and Freundlich isotherm framework for the Cu(II) uptake

Temperature (°C)	q_m	K_L	R^2
Langmuir isotherm parameters			
30	7.55	3.28	0.9474
40	7.92	3.30	0.9654
50	7.71	5.88	0.9624
Freundlich isotherm parameters			
Temperature (°C)	n	K_F	R^2
30	2.64	5.44	0.9052
40	2.47	5.10	0.9707
50	2.60	5.65	0.9709

Table 5 D-R Isotherm framework for the adsorption of Cu(II)

Temperature, °C	$\beta \times 10^{-9}$	$q_m \times 10^{-4}$ (mol/g)	E (kJ/mol)	R^2
30	2.668	7.0508	13.7	0.9283
40	2.559	6.9918	14.0	0.9603
50	2.208	6.4472	15.0	0.9599
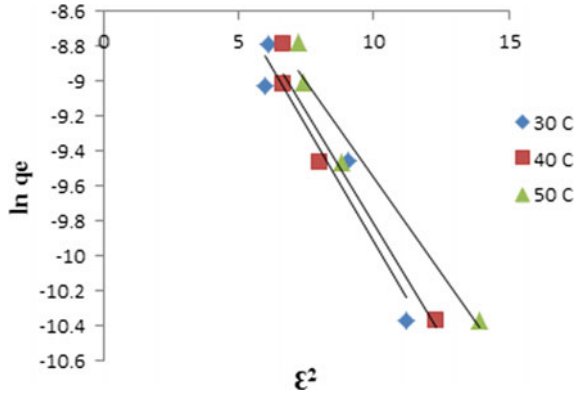
Fig. 10 The D-R isotherm
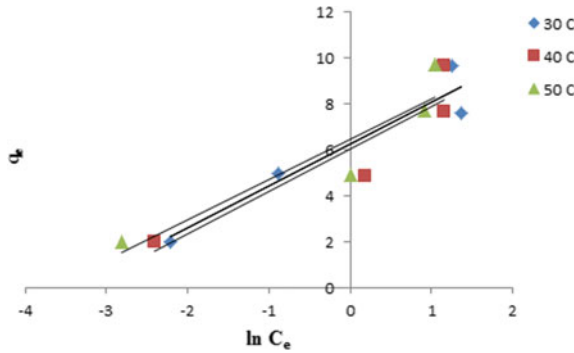
Fig. 11 Tempkin isotherm

Table 6 Temkin isotherm framework for the Cu(II) uptake

Temperature, °C	B	A	R^2
30	1.8348	30.57	0.9192
40	1.8407	26.31	0.8556
50	1.7413	40.44	0.8609

to the ultimate binding energy, and T is the absolute temperature of solution. As shown in figure 11, a liner graph was obtained with B as slope and B (ln A) as the intercept when q_e versus ln C_e was plotted. Table 6 illustrated that experimental data did not fit Tempkin isotherm.

Breakthrough Experiment:

The practicability and production of the process can be investigated by Breakthrough capacity curves. These curves were significant in process adsorption Fig. 12 shows that the solution of 100 mL of Cu(II) could be allowed to run from the column
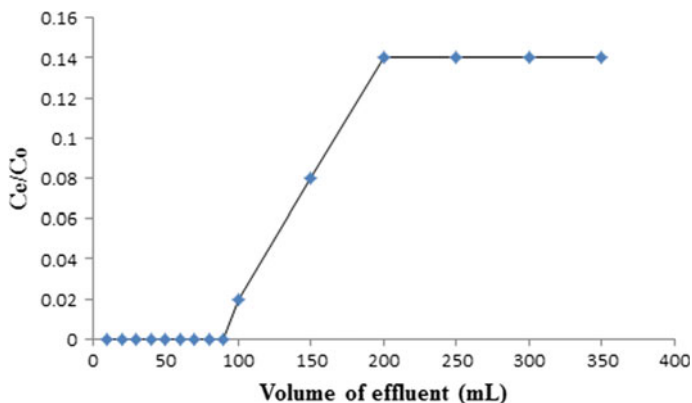
Fig. 12 Breakthrough capacity

not detecting any Cu(II) ions in the effluent when 0.2 g adsorbent was employed. The exhaustive and breakthrough capacities were discovered to be 50 and 100 mg/g, respectively.

Condition: Cu(II) = 50 mg/L; adsorbent = 0.2 g; flow rate = 1 ml/min.

Desorption Studies:

Column method was employed to take into account the desorption studies. The used column accomplished by the breakthrough process was employed in this study. Thus, in breakthrough process, a total of 9.7 mg of Cu(II) ions was held back when 400 ml of Cu(II) solution of concentration 50 mg/L run in the column. For desorbing Cu(II) ions, 0.1 M HCl solution was run in the column. As shown in Fig. 13, a total of 9.3 mg of Cu(II) ions (95.8%) was regained on elution within 80 ml of the effluent.

4   Conclusion

Peak Cu(II) uptake was pH vulnerable and was found to be at pH-6. The data of kinetics for Cu(II) uptake were finely suited to pseudo-second-order kinetic framework as visible from the regression coefficients ($R^2 = 0.99$). The adsorption result was best suited to the Langmuir, D-R, Freundlich isotherm framework. The process of chemisorption involved which is designated by the mean free energy of adsorption. For the spontaneity and endothermic nature of uptake mechanism, thermodynamic parameters $\Delta H°$ and $\Delta G°$ were studied. The experimental data shows that polyaniline/Sn(IV) phosphate composite has reasonable good adsorption capacities for Cu(II). The composite can be utilized so that there are recovery and pre-concentration of Cu(II) ions from water as well as wastewater.
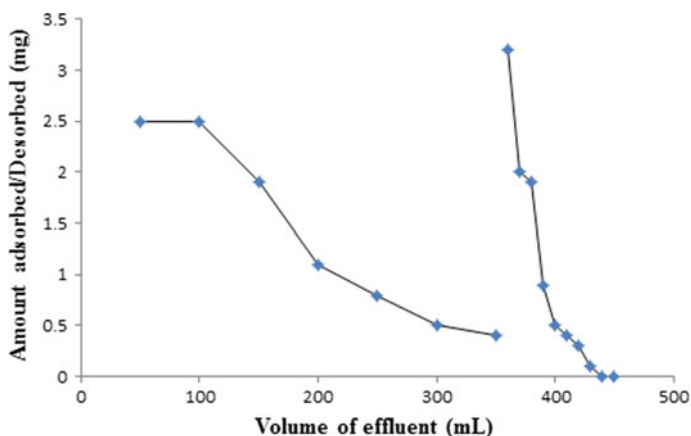
Fig. 13 Desorption of Cu(II) from polyaniline/Sn(IV)phosphate composite employing column methods. Experimental conditions: adsorbent dosage = 0.5 g; flow rate = 1 mL/min; eluent = 0.1 M HCl

References

1. Gündoğan, R., Acemioğlu, B., Alma, M.H.: Copper (II) adsorption from aqueous solution by herbaceous peat. J. Colloid Interface Sci. **269**(2), 303–309 (2004)
2. Järup, L.: Hazards of heavy metal contamination. Br. Med. Bull. **68**(1), 167–182 (2003)
3. Ansari, M.I., Malik, A.: Biosorption of nickel and cadmium by metal resistant bacterial isolates from agricultural soil irrigated with industrial wastewater. Biores. Technol. **98**(16), 3149–3153 (2007)
4. Costerton, J.W., Stewart, P.S., Greenberg, E.P.: Bacterial biofilms: a common cause of persistent infections. Science **284**(5418), 1318–1322 (1999)
5. Lameiras, S., Quintelas, C., Tavares, T: Biosorption of Cr(VI) using a bacterial biofilm supported on granular activated carbon and on zeolite. Bioresour. Technol. **99**(4), 801–806 (2008)
6. Gupta, V.K., Jain, R., Mittal, A., Saleh, T.A., Nayak, A., Agarwal, S., Sikarwar, S.: Photocatalytic degradation of toxic dye amaranth on TiO_2/UV in aqueous suspensions. Mater. Sci. Eng., C **32**(1), 12–17 (2012)
7. Owlad, M., Aroua, M.K., Daud, W.A.W., Baroutian, S.: Removal of hexavalent chromium-contaminated water and wastewater: a review. Water Air Soil Pollut. **200**(1–4), 59–77 (2009)
8. Popuri, S.R., Vijaya, Y., Boddu, V.M., Abburi, K.: Adsorptive removal of copper and nickel ions from water using chitosan coated PVC beads. Biores. Technol. **100**(1), 194–199 (2009)
9. Jha, V.K., Matsuda, M., Miyake, M.: Sorption properties of the activated carbon-zeolite composite prepared from coal fly ash for Ni^{2+}, Cu^{2+}, Cd^{2+} and Pb^{2+}. J. Hazard. Mater. **160**(1), 148–153 (2008)
10. Nabi, S.A., Naushad, M.: Synthesis, characterization and analytical applications of a new composite cation exchanger cellulose acetate-Zr(IV) molybdophosphate. Colloids Surf., A **316**(1), 217–225 (2008)
11. Nabi, S.A., Akhtar, A., Khan, M.D.A., Khan, M.A.: Synthesis, characterization and electrical conductivity of Polyaniline-Sn(IV) tungstophosphate hybrid cation exchanger: analytical application for removal of heavy metal ions from wastewater. Desalination **340**, 73–83 (2014)
12. Abbasizadeh, S., Keshtkar, A.R., Mousavian, M.A.: Preparation of a novel electrospun polyvinyl alcohol/titanium oxide nanofiber adsorbent modified with mercapto groups for uranium (VI) and thorium (IV) removal from aqueous solution. Chem. Eng. J. **220**, 161–171 (2013)

13. Kampalanonwat, P., Supaphol, P.: Preparation and adsorption behavior of aminated electrospun polyacrylonitrile nanofiber mats for heavy metal ion removal. ACS Appl. Mater. Interfaces. **2**(12), 3619–3627 (2010)
14. Rao, R.A.K., Khan, M.A., Rehman, F.: Batch and column studies for the removal of lead (II) ions from aqueous solution onto lignite. Adsorpt. Sci. Technol. **29**(1), 83–98 (2011)
15. Rao, R.A.K., Ikram, S.: Sorption studies of Cu(II) on gooseberry fruit (emblica officinalis) and its removal from electroplating wastewater. Desalination **277**(1), 390–398 (2011)

Artificial Neural Network Modeling to Predict Bacterial Attachment on Composite Biopolymeric Scaffold

Shailendra Singh Shera, Shraddha Sahu and Rathindra Mohan Banik

Abstract Biomaterial-associated infection is a significant cause of concern in health care and clinical field. It is widely acknowledged that material with intended use in a medical application must not support colonization and attachment of bacteria on its surfaces. This has encouraged the search for the newer polymeric biomaterial with anti-adhesive and anti-adherence properties to resist bacterial attachment. Firsthand information about the combined effect of various material properties that affects bacterial attachment to biomaterial surface during the development of anti-adhesive material is always useful. In this work, computer-aided techniques, i.e., the neural network was applied to build a model using biomaterial properties such as surface roughness, swelling ratio, and pore size as input and number of surface adhered bacterial cells as output response. Various blending combinations of silk fibroin and xanthan were used to generate biocomposites with varying surface roughnesses. The surface roughness of the composite scaffold was determined through Atomic Force Microscopy (AFM), and surface parameter was evaluated using inbuilt software provided with AFM, and the number of bacteria attached to biocomposite surface was estimated through ImageJ. The coefficient of determination (R^2) and Mean Absolute Percentage Error (MAPE) of the neural model were determined as 0.990 and 0.26%, respectively. Thus, confirming that the developed model has excellent prediction accuracy. This model, when used for prediction with the entirely unseen dataset, gave R^2 as 0.982, pointing towards the robustness of model in predicting the similar type of system within the limit of the trained data set.

Keywords Biomaterial · Biocomposite scaffold · Artificial neural network Predictive modeling · Anti-adhesive · Anti-adherence

S. S. Shera · S. Sahu · R. M. Banik (✉)
School of Biochemical Engineering, Indian Institute of Technology,
Banaras Hindu University, Varanasi, India
e-mail: rmbanik@gmail.com

S. S. Shera
e-mail: shailendra.shera@gmail.com

S. Sahu
e-mail: ssahu.rs.bce11@itbhu.ac.in

1   Introduction

Biomaterial related infection due to bacterial adhesion and biofilm formation is one of the leading barriers to the extended use of biomaterials in biomedical applications [1]. Adhesion of pathogenic bacteria at biomaterial surfaces causes contamination problems in the healthcare setting such as medical devices, diagnostic devices, surgical instruments, dentistry, food processing, water treatment, and other areas that directly affect human health and life. These contaminations often prove fatal and seriously endanger precious human life. A recent study published as early as 2011 on health care related infection revealed that almost 25.6% infection was due to contamination caused by adhered bacteria on medical devices [2]. The biomaterials' ability to inhibit sticking of bacteria to its surface is an essential factor for clinical success.

Two strategies are commonly employed to prevent biomaterial-related infections: (1) killing the surface attached bacteria by intervention through antibiotic or silver nanoparticle (2) use of anti-adhesive biomaterial through surface modification. The latter is emerging as a promising strategy to control bacterial adhesion due to the limited success of the first approach. Bacterial attachment to biomaterial surface is mostly dependent on material properties such as surface topography (surface roughness), hydrophilicity, pore size, surface energy, and chemical composition [3]. Surface roughness plays a more critical role in bacterial–material interaction leading to sticking of bacteria to the material surface.

Several models have been used to predict bacterial adhesion on biomaterial surface as a strategy to develop anti-adhesive surface efficiently, but none is able to predict efficiently because all models consider an effect of a single factor for determination and prediction of bacterial adhesion, e.g., some models only consider electrostatic repulsion, some surface chemistry, some material composition, some hydrophilicity, and hydrophobicity of material. Moreover, they are complicated and cumbersome to understand. So, there is a need to develop a combinatorial model to predict bacterial adhesion based on various material properties.

The complexity and lack of proper understanding of living systems and their interactions with biomaterials present significant challenge conceptually as well as practically, which needs to be overcome for application of cutting edge technology and discovery tools in design and synthesis of new biomaterials. This complexity has been minimized to a certain extent with the advent of new tools and methodology in mathematics and statistics. Experimental design coupled with statistical and computational modeling methods can play important role in understanding data, and provide quantitative predictions of bacterial attachment. Therefore, mathematical and computational methods with the capacity to predict cellular response to implanted biomaterials would be instrumental in the design of new medical devices [4].

Artificial neural network (ANN) is a mathematical representation of neurological functioning of the human brain. This is a data-driven technique, which primarily dwells on input–output data [5]. Neural network further uses these data to learn the particular relationship between input and output parameters. ANN is a well-known

and useful computational approach widely applied in all fields of science and technology for predictive modeling [6–10]. ANN is a powerful technique which can deal with the high level of variability and uncertainty typically associated with microbial responses [11]. This is a model-independent technique capable of predicting highly variable and nonlinear system with high accuracy. Therefore, the ANN was used to build a model for predicting the number of bacterial cells on the biomaterial surface.

In the present study, the ANN model developed from material properties such as surface roughness, swelling ratio, and pore size to predict the number of bacterial cells attached to the surface of the composite scaffold. The surface roughness was calculated to be in nanorange whereas the pore size was in micro-range. The incorporation of nanoscale to microscale material properties as input parameter enables robust development of ANN network for prediction of response.

2 Materials and Methods

Materials

Silk cocoons of B. mori for extraction of silk fibroin, Xanthan gum (SRL, Mumbai), Lithium Bromide (SRL, Mumbai), Phosphate Buffer Saline, snakeskin dialysis membrane (MWCO = 12 k–14 kDa), Closure clips.

2.1 Methods

Fabrication of Composite Scaffold

A composite scaffold was fabricated by blending 7% aqueous solution of silk fibroin with 0.3% xanthan solution in various ratios. The blended solutions were molded and frozen at −50 °C followed by freeze-drying for 48 h to prepare porous composite scaffolds.

2.2 Determination of Input Parameters

Swelling Ratios

Swelling study was performed as per the previously reported literature [5]. Briefly, 10 mm disks were carved from the fabricated scaffolds and weighed (W_d). Afterwards, these disks were placed in vials containing aqueous phosphate buffer saline (PBS) pH 7.4 and incubated at room temperature for 24 h. After 24 h, scaffold disks were taken out from PBS solution, wiped gently with tissue paper and weighed (W_s) again. The swelling ratio was calculated according to Eq. 1:

$$\text{Swelling ratio} = \frac{W_s - W_d}{W_d} \tag{1}$$

W_s Weight of swelled disk
W_d Weight of dried disk

Surface Roughness

The surface roughness of biocomposite was measured on a scanning probe microscope Nova P9 (NT-MDT, Russia), in the air at room temperature (22 °C), in tapping mode. The tip width was 10–30 nm and scanned areas of the samples were 15 μm × 15 μm. The image acquisition and calculation of surface texture parameter were performed on NT-MDT Nova software. The samples were prepared by wetting distilled water for 10 min and fixing it on a cover slip by pressing gently. The samples were air-dried overnight before AFM analysis. The 3D surface parameter root mean square roughness (Sq) was calculated from AFM image using inbuilt Nova software employing ASME B46.1 parameter.

Pore Size

The pore size of prepared biocomposite scaffold was calculated from SEM images using ImageJ software (NIH, Maryland).

2.3 Bacterial Adherence Activity

An overnight grown bacterial suspension of *E. coli* was centrifuged, and pellets suspended in 0.5% LB medium and diluted to 0.5 Mcfarland standard. Replicate disks of SFX82, SFX64 and SFX55 were carved out, placed in 6-well flat bottom tissue culture plate and wholly immersed with aliquots of the bacterial suspension (4 ml) with a cell density of 1×10^8 CFU ml^{-1}. The culture plates were incubated at 37 °C for 48 h, and samples were fixed with 2.5% glutaraldehyde in distilled water at 4 °C. Afterward, the dressings were thoroughly washed and dehydrated with absolute ethanol. The surface adhered bacteria were counted from SEM image using Image J.

2.4 Design Matrix

Bacterial adhesion depends upon surface topographical parameter (Sq). Besides surface parameter, hydrophilicity/hydrophobicity (Here swelling ratio used as the measure of hydrophilicity) and pore size is known to influence bacterial adhesion to the biomaterial surface. The range and levels of the three independent factors studied are given in Table 1. A face-centered central composite design (CCD) was applied to the three independent factors, and the experimental design was obtained using *ccdesign*

Table 1 The independent variables used in modeling along with their levels. Zero represents central value, (1) represents the low level, (+1) represents the high level. The units for root mean square roughness is in nanometer (nm) and pore size in micrometer (μm)

Input variable	−1	0	+1
Root mean square roughness (Sq)	50	217	385
Swelling ratio (SR)	10.90	15.05	19.20
Pore size (PS)	46	52	58

Table 2 CCD matrixes of three factors along with experimental and ANN predicted numbers of bacterial cells adhered to the composite scaffold

S. no	Sq	Swelling ratio	Pore size	Experimental	ANN predicted
1	217	15.05	58	6414	6415
2	217	15.05	52	6414	6386
3	217	15.05	52	6414	6386
4	385	10.9	58	9194	9186
5	50	19.2	46	3815	4680
6	217	15.05	52	6414	6386
7	385	19.2	46	9194	9178
8	50	10.9	46	3815	3738
9	50	19.2	58	3815	3810
10	385	10.9	46	9194	9360
11	50	15.05	52	3815	3781
12	217	15.05	52	6414	6386
13	50	10.9	58	3815	3807
14	217	10.9	52	6414	6242
15	217	15.05	52	6414	6386
16	217	19.2	52	6414	6384
17	385	19.2	58	9194	8479
18	217	15.05	52	6414	6386
19	217	15.05	52	6414	6386
20	217	15.05	46	6414	6319
21	217	15.05	46	6414	6319
22	217	15.05	46	6414	6319
23	217	15.05	46	6414	6319
24	217	15.05	46	6414	6319

command of MATLAB (Mathswork). The range and levels of the three independent variables along with the central values used for modeling were listed in Table 2.

Fig. 1 ANN architecture consisting of Input layer (X1, X2, X3), Neurons in hidden layer (N1, N2, N3, …, N10) and Output layer (Y)
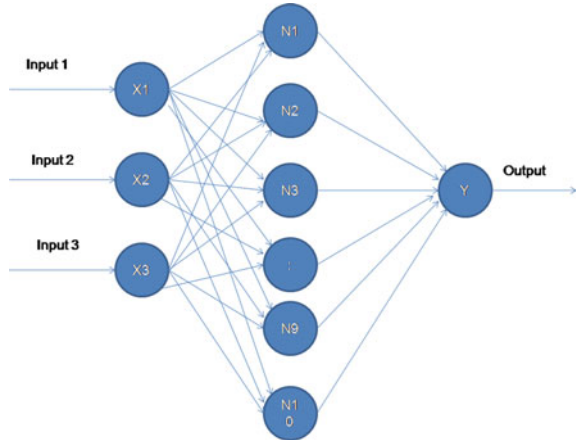
2.5 Artificial Neural Network Modeling

A multilayer feed forward back propagation neural network was applied for modeling and prediction of bacterial attachment to the polymeric surface. The neural model was constructed in MATLAB 2012a (Mathswork, Natick USA) using neural fitting toolbox (invoked by command *nftool*) with three input variables (Sq, SR, and PS) and one output variables (number of bacteria). The network architecture is as: an input layer, one hidden layer, one output layer with one output. The input and output dataset were divided into three sets: Training (16), Validation (4) and Testing (4). Levenberg–Marquardt learning algorithm was applied to train the network. The desired level of network accuracy was achieved by training the network multiple times and adjusting the number of neurons in the hidden layer. The network performance was monitored through performance plot and regression analysis at each training, testing and validation phase. The typical ANN architecture consisting of input layer, hidden layer, and output layer is shown in Fig. 1.

2.6 Evaluation of Model Predictability of Neural Network

The performance and prediction efficiency measured by the regression coefficient (R^2) and Mean Absolute Percentage Error (MAPE) was calculated according to Eq. 1

$$\text{MAPE} = \frac{100}{n} \sum_{i=1}^{n} |\text{Yi, observed} - \text{Yi, predicted}/\text{Yi, observed}| \qquad (2)$$
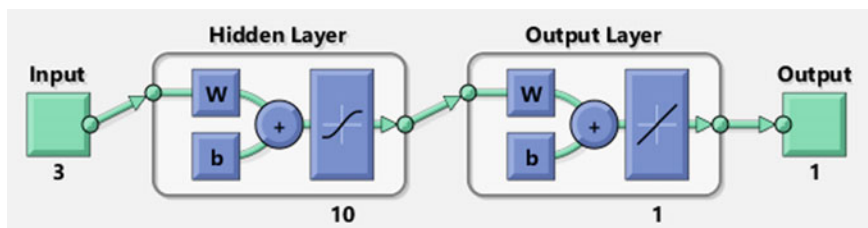
Fig. 2 Final optimized ANN topology with 3 input variable, 10 neurons with Tansigmoid activation function in hidden layer and 1 output variable with purelin activation function

3 Result and Discussions

ANN model was developed with surface roughness, swelling ratio as measure of hydrophilicity and pore size of composite scaffold as model input, and the output of the ANN is a quantitative prediction of the amount of the number of bacteria attached to the surface of polymeric composite scaffold. The surface roughnesses were calculated from AFM images and pore size from SEM images. Similarly, the output response (no. of bacterial cells) was calculated from SEM images (image data not shown). The ANN is capable of capturing nonlinear behavior of input parameter which affects the output of the system. In our study, the three input parameter used has shown large variation in high and low level which indicates towards the nonlinearity of the system. Therefore, ANN modeling was the method of choice. The trial and error method was employed to determine the precise number of neuron to train the ANN network. A 3-10-1 network topology was found to be optimum and is shown in Fig. 2.

The ANN predicted values of response (number of bacterial cells attached to scaffold) for different ranges of scaffold properties (input variable) were listed in Table 2. The network performance and prediction efficiency of ANN model were measured through regression coefficient (R^2) and MAPE, which were 0.990 and 0.26%, respectively. The regression analysis for all the three training, validation and testing stage was shown in Fig. 3. The coefficient of determination (R^2) value close to unity confirms the excellent performance of ANN network. This indicated that the model was able to explain 99% of variability in data. The prediction accuracy was evaluated with MAPE. The MAPE $\leq$ 10% indicated high prediction accuracy, 10% $\leq$ MAPE $\leq$ 20% suggests good prediction, 20% $\leq$ MAPE $\leq$ 50% suggests reasonable prediction, and MAPE $\geq$ 50% suggests inaccurate prediction [5]. A small value of MAPE indicated an excellent prediction efficiency of model. Together R^2 and MAPE confirmed an efficient neural model for prediction of responses.

It was reported that ANN model has tendency of overfitting when trained multiple times, which is undesirable because it affects prediction efficiency and gives inaccurate prediction despite giving high regression coefficient during training phase. The similar characteristics of validation and test curve in Fig. 3 suggest that no-overfitting has occurred.
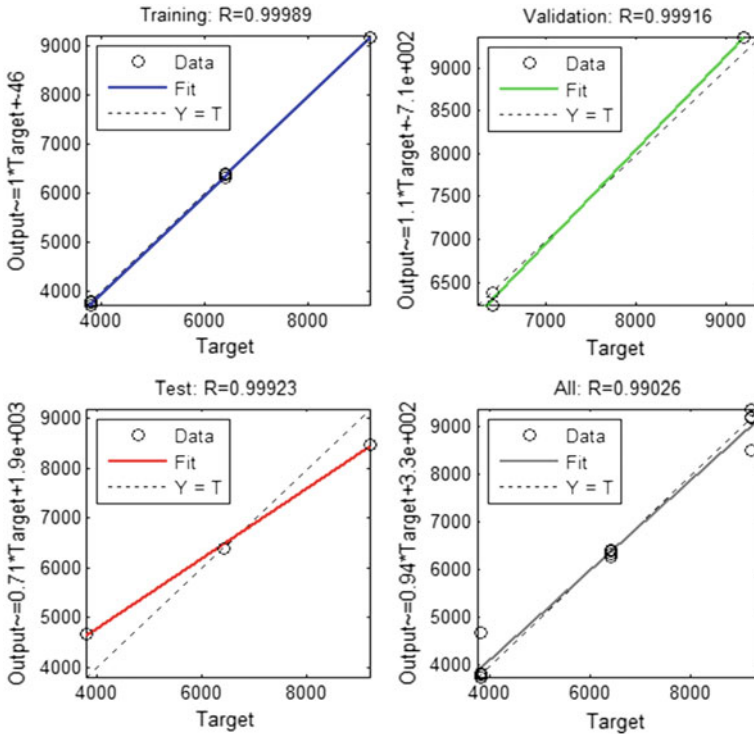
Fig. 3 Regression analysis of ANN model during training, testing and validation phase

The ANN model presented in this work was so robust that when this model was applied on similar system with an entirely unseen dataset, it predicted bacterial attachment with excellent accuracy as evident by regression coefficient of 0.982 (Fig. 4). This indicates that even on unseen dataset only 2% variability remained unexplained by the model. From Fig. 4, it can also be seen that the fitted response is below the target line. This is because the target data used to train the network is higher than the predicted data set. This shows higher generalization capacity of the ANN model presented in this work, which was due to the universal ability of ANN model to counter nonlinearity of the system.

4   Conclusion

The developed ANN model was successful in predicting the number of bacterial cells adhered on to the surface of biocomposite scaffold that has been designed for biomedical applications. This modeling approach used relevant input parameter of materials which affected bacterial adhesion to surface of polymeric (bio)material

eased selection procedure of prospective material for detailed studies. ANN method was based on rational approach rather than on intuition of researcher. The accurate prediction of bacterial adherence on biomaterial surface minimizes effort, costs, and assists in design and fabrication of anti-adhesive biomaterials. This work will act as a template for predictive modeling and estimation of bacterial cells on any material surface using materials properties as an input parameter.

References

1. Xu, L.C., Siedlecki, C.A.: Surface texturing and control of bacterial adhesion. https://doi.org/10.1016/B978-0-12-803581-8.09295-X
2. Feng, G., Cheng, Y., Wang, S.Y., Borca-Tasciuc, D.A., Worobo, R.W., Moraru, C.I., et al.: Bacterial attachment and biofilm formation on surfaces are reduced by small-diameter nanoscale pores: how small is small enough? Biofilms Microbiomes **1**, 15022 (2015)
3. Habimana, O., Semião, A.J.C., Casey, E.: The role of cell-surface interactions in bacterial initial adhesion and consequent biofilm formation on nano filtration/reverse osmosis membranes. J. Memb. Sci. **454**, 82–96 (2014)
4. Fatemi, M.H., Kerdarshad, A., Rostami, E.G.: In-silico prediction of cellular responses to polymeric biomaterials from their molecular descriptors. Casp. J. Chem. **3**, 23–34 (2014)

5. Shera, S.S., Sahu, S., Banik, R.M.: Preparation of drug eluting natural composite scaffold using response surface methodology and artificial neural network approach. Tissue Eng. Regen. Med. (2018). https://doi.org/10.1007/s13770-017-0100-z

6. Yadav, A.K., Malik, H., Chandel, S.S.: Selection of most relevant input parameters using WEKA for artificial neural network based solar radiation prediction models. Renew. Sustain. Energy Rev. **31**, 509–519 (2014)

7. Wang, J., Wan, W.: Application of desirability function based on neural network for optimizing biohydrogen production process. Int. J. Hydrogen Energy **34**, 1253–1259 (2009)

8. Pendashteh, A.R., Fakhru'l-Razi, A., Chaibakhsh, N., Abdullah, L.C., Madaeni, S.S., Abidin, Z.Z.: Modeling of membrane bioreactor treating hypersaline oily wastewater by artificial neural network. J. Hazard Mater. **192**, 568–575 (2011)

9. Winkler, D.A., Burden, F.R.: Robust QSAR models from novel descriptors and bayesian regularised neural networks. Mol. Simul. **24**, 243–258 (2000)

10. Singh, P., Shera, S.S., Banik, J., Banik, R.M.: Optimization of cultural conditions using response surface methodology versus artificial neural network and modeling of L-glutaminase production by Bacillus cereus MTCC 1305. Bioresour. Technol. **137**, 261–269 (2013)

11. Keeratipibul, S., Phewpan, A., Lursinsap, C.: Prediction of coliforms and Escherichia coli on tomato fruits and lettuce leaves after sanitizing by using artificial neural networks. Food Sci. Technol. **44**, 130–138 (2011)

Triboelectric-Based Kinetic Energy Harvesting Using Polydimethylsiloxane (PDMS)

Amit Sharma and **Poonam Agarwal**

Abstract In this paper, we have presented a metal-to-dielectric attached-electrode parallel-plate contact-mode-type triboelectric energy harvester, which converts vibrational kinetic energy to electrical power. In this, a tribo-pair made of copper as metal and PDMS as dielectric has been demonstrated. A cantilever-based design is proposed in which copper tape is attached to a thick cardboard piece which is acting as tribo-layer as well as top electrode. The bottom electrode is single-side copper clad of FR4 printed circuit board (PCB) on which PDMS is spin coated. The fabricated harvester device has been tested by providing the mechanical vibration with manual tapping on cantilever structured electrode. Measurement has been carried out using digital oscilloscope which showed that peak output voltage, current, and instantaneous power density are 29.6 V, 29.6 μA, and 100.13 μW/cm^2, respectively.

1 Introduction

Technological advancement has scaled down the physical size of devices as well as system drastically, which made possible to operate electronics systems at ultralow power [1, 2]. This low-power requirement has created the possibility of running the electronic gadgets for longer time span with batteries, where batteries are also getting better with their performance. Batch fabrication also reduces the overall cost and price for end-user electronics. All these advancements empower the use of electronics for various applications such as navigation, chemical, biological, military, communication, structural health monitoring, environment monitoring, surveillance, etc. This applicability of electronics with communication has brought the idea of

A. Sharma (✉) · P. Agarwal
Microsystems Lab, School of Computer and Systems Sciences, JNU,
New Delhi 110067, Delhi, India
e-mail: amitsharma.ceeri@gmail.com

"Internet of Things" (IoT) which is being used to make the world smarter day-by-day.

To develop a smart world, primary requirement is wireless communication and monitoring sensors, which is possible with today's electronics. But as the number of electronics modules on board increases, the overall power consumption increases too. In a large distributed wireless sensor network system, power distribution with monitoring is always a challenge. In such a large network, it is not easy to replace the power source time to time and sometimes where energy sources are embedded in structures; it is a tedious job to replace batteries. And battery waste is another source of pollution, as it is not easy to dispose it.

To overcome these challenges, there is a need to develop self-powered systems. As the power requirement is ultralow, which can be generated from the available energy in system environment in the form of heat, light, sound, vibration, or movement using energy harvesters, this will remove the need of energy source and external power.

Here, we are working on kinetic energy harvesting in which mechanical energy, available in the form of vibrations or mechanical movements, is converted into electrical energy. Conventionally, there are three mechanisms used in kinetic energy harvesters, piezoelectric [3–5], electromagnetic [6, 7], and capacitive [8]. Recently, a new approach for kinetic energy harvesting based on conjunction of triboelectrification (contact electrification) and electrostatic induction mechanism came into picture in 2012 by Fan et al. [9]. Triboelectric energy harvesters (TEH) showed unique merits including large output power, high efficiency, low-weight and cost-effective materials, and simple fabrication [10]. In this paper, an in-house fabricated triboelectric energy harvester (TEH) of metal-to-dielectric attached-electrode parallel-plate contact-mode type is proposed, where design, fabrication, and experimental results are discussed in the following sections.

1.1 Principle

In triboelectric energy harvesting devices, two films of different materials with different tribo-polarities, at least one should be dielectric, act as tribo-pair [11]. Tribo-pair of dielectric and conductor where only one is dielectric is shown in Fig. 1a, whereas the trio-pair of two dielectric layers is shown in Fig. 1b.

When a tribo-pair comes in contact by the external mechanical energy, triboelectrification due to slight friction between two layers generate charges on both layers. The nature of charge (+ve or −ve) depends on the tribo-polarity of the materials in a tribo-pair. Here, we are taking a tribo-pair of metal–dielectric (see Fig. 1a) in which metal will be positively charged, while dielectric layer will be negatively charged. When they are in contact, there is no potential difference as the charges are at atomic distance. When these charged layers of tribo-pair start to move away from each other, a potential difference will be developed which is open-circuit voltage (V_{oc}). The working principle of dielectric–dielectric tribo-pair (see Fig. 1b) will be the same. When electrodes attached to these tribo-layers are connected through an
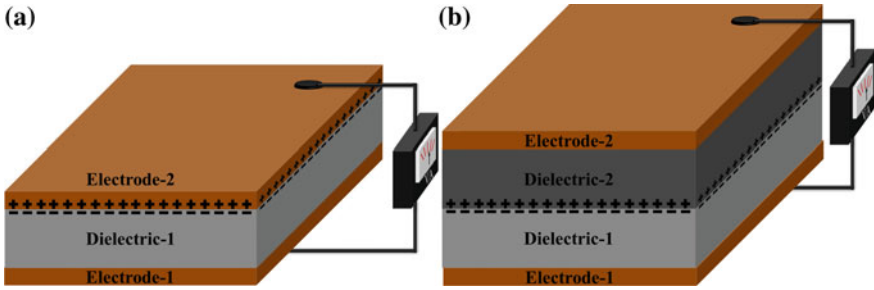
Fig. 1 Basic attached-electrode parallel-plate contact-mode-type triboelectric energy harvesters **a** Metal-to-Dielectric and **b** Dielectric-to-Dielectric
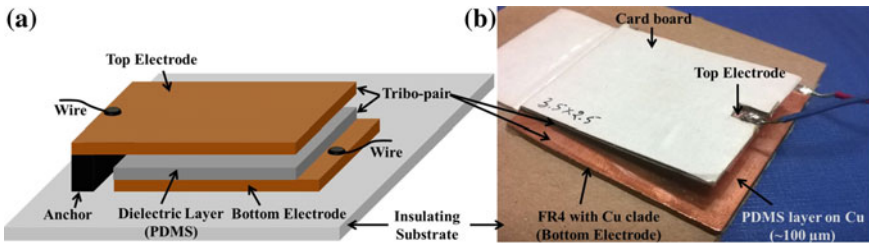
Fig. 2 Triboelectric energy harvester (TEH) **a** schematic and **b** fabricated

external circuit, there will be current flow as the tribo-pair moves. In metal–dielectric (see Fig. 1a), metal layer acts as tribo-layer as well as top electrode.

2 Metal-to-Dielectric Triboelectric Energy Harvester

In this, a cantilever-based design is proposed in which tribo-pair is made of copper metal and PDMS dielectric films. Single-side copper clad PCB is used to make bottom electrode on which PDMS of around 100 µm thickness is spin coated. Copper tape is attached to a cardboard piece which is acting as tribo-layer as well as top electrode, and schematic view is shown in Fig. 2a. In-house fabricated triboelectric energy harvester, in which connections are taken by soldering two wires to the top and bottom electrodes, is shown in Fig. 2b. The fabricated TEH design parameters are listed in Table 1. The fabricated TEH is experimentally tested for performance and demonstrated in system as discussed in the following section.

Table 1 Design parameters of fabricated triboelectric energy harvester

Parameters	Dimensions
Top electrode length	35 mm
Top electrode width	25 mm
Bottom electrode length	40 mm
Bottom electrode width	40 mm
PDMS thickness	~100 μm
Overlap/contact area	875 mm^2
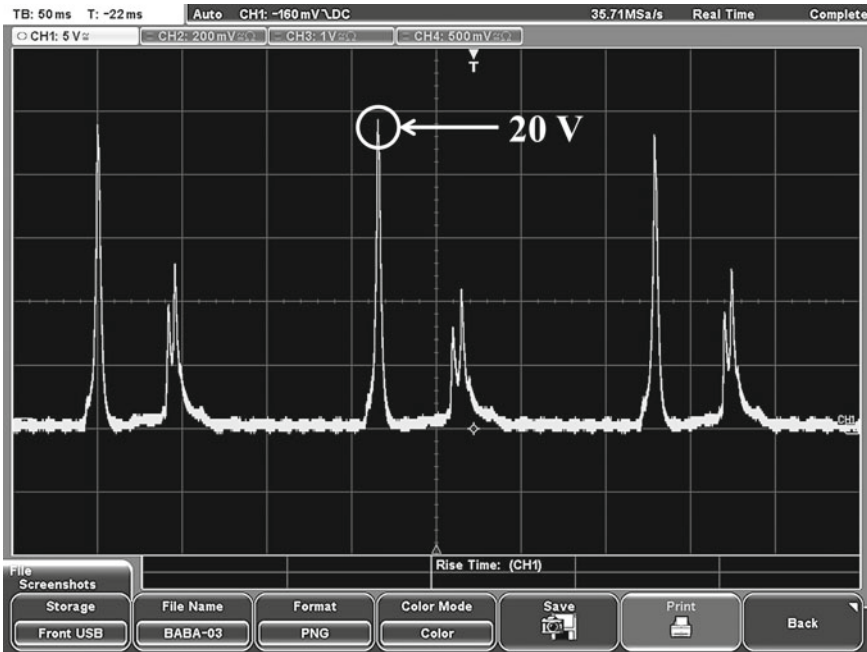
Fig. 3 Rectified output voltage waveform

3 Experimental Results

Fabricated TEH harvester device is experimentally tested using R&S digital oscilloscope. TEH is connected to digital oscilloscope, and mechanical vibrations are provided to cantilever with manual tapping. Measured peak output voltage, current, and instantaneous power density are 20 V, 20 μA, and 45.71 μW/cm^2, respectively (see Fig. 3). Repeated measurements showed that peak output voltage, current, and instantaneous power density are 29.6 V, 29.6 μA, and 100.13 μW/cm^2, respectively (see Fig. 4) which shows TEH output dependency on various parameters such as tapping force, frequency, etc.
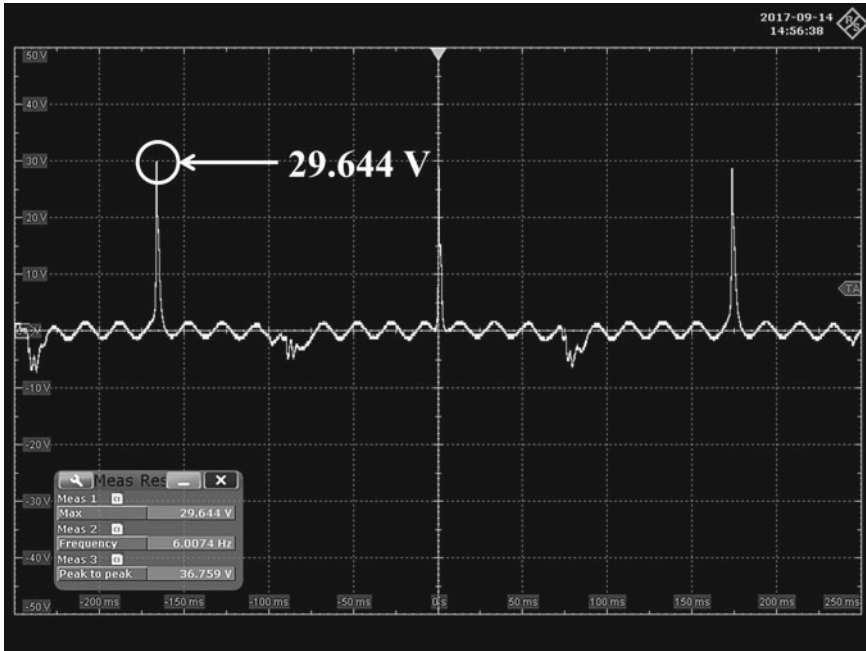
Fig. 4 Output voltage waveform

To demonstrate TEH in system, fabricated TEH is connected to eight red LEDs (each of size 10 mm) connected in series on a breadboard, as presented in Fig. 5. In this, TEH output is rectified with bridge rectifier IC (DF10M). Manual tapping on cantilever led to glow LEDs as shown in inset of Fig. 5.

4   Conclusions

In this paper, we have presented an experimentally tested in-house fabricated TEH device and for verification, we have demonstrated TEH in an LED system. The reported TEH has unique advantages as it is simple to fabricate without any expensive micromachining techniques or materials, and very low cost.
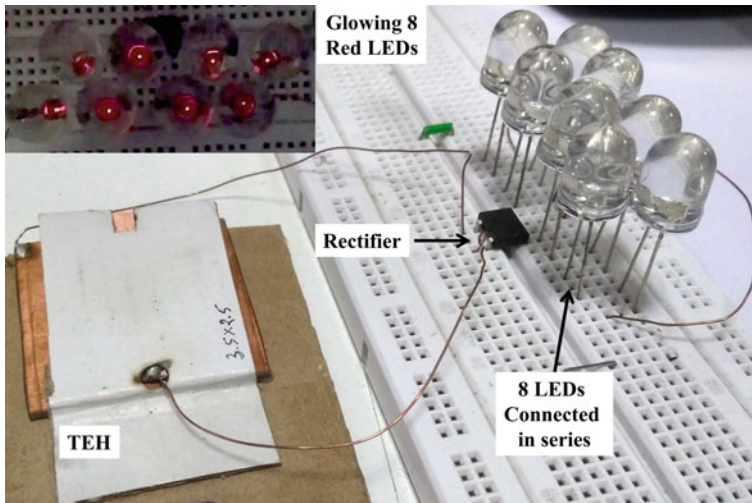
Fig. 5 Circuitry for flashing LEDs using in-house fabricated triboelectric energy harvester. Inset: Glowing eight red LEDs

References

1. Dieffenderfer, J., Goodell, H., Mills, S., McKnight, M., Yao, S., Lin, F., Beppler, E., Bent, B., Lee, B., Misra, V., Zhu, Y., Oralkan, O., Strohmaier, J., Muth, J., Peden, D., Bozkurt, A.: Low power wearable systems for continuous monitoring of environment and health for chronic respiratory disease. IEEE J. Biomed. Health Inform. **20**(5), 1251–1264 (2016). https://doi.org/10.1109/JBHI.2016.2573286
2. Han, J., Zhang, Y., Huang, S., Chen, M., Zeng, X.: An area-efficient error-resilient ultra-low-power subthreshold ECG processor. IEEE Trans. Circ. Syst. II Express Briefs **63**(10), 984–988 (2016). https://doi.org/10.1109/TCSII.2016.2538158
3. Janphuang, P., Lockhart, R.A., Isarakorn, D., Henein, S., Briand, D., de Rooij, N.F.: Harvesting energy from a rotating gear using an AFM-like MEMS piezoelectric frequency up-converting energy harvester. J. Microelectromech. Syst. **24**(3), 742–754 (2015). https://doi.org/10.1109/jmems.2014.2349794
4. Kim, H.S., Kim, J.-H., Kim, J.: A review of piezoelectric energy harvesting based on vibration. Int. J. Precis. Eng. Manuf. **12**(6), 1129–1141 (2011). https://doi.org/10.1007/s12541-011-0151-3
5. Anton, S.R., Sodano, H.A.: A review of power harvesting using piezoelectric materials (2003–2006). Smart Mater. Struct. **16**(3), R1–R21 (2007). https://doi.org/10.1088/0964-1726/16/3/R01
6. Cepnik, C., Lausecker, R., Wallrabe, U.: Review on electrodynamic energy harvesters—a classification approach. Micromachines **4**(2), 168–196 (2013). https://doi.org/10.3390/mi4020168
7. Podder, P., Amann, A., Roy, S.: Combined effect of bistability and mechanical impact on the performance of a nonlinear electromagnetic vibration energy harvester. IEEE/ASME Trans. Mechatron. **21**(2), 727–739 (2016). https://doi.org/10.1109/TMECH.2015.2451016
8. Khan, F.U., Qadir, M.U.: State-of-the-art in vibration-based electrostatic energy harvesting. J. Micromech. Microeng. **26**(10), 28 pp (2016). https://doi.org/10.1088/0960-1317/26/10/103001

9. Fan, F.R., Tian, Z.Q., Wang, Z.L.: Flexible triboelectric generator! Nano Energy **1**(2), 328–334 (2012). https://doi.org/10.1016/j.nanoen.2012.01.004
10. Niu, S., Wang, Z.L.: Theoritical systems of triboelectric nanogenerators. Nano Energy **14**, 161–192 (2015). https://doi.org/10.1016/j.nanoen.2014.11.034
11. Wang, Z.L., Lin, L., Chun, J., Niu, S., Zi, Y.: Triboelectric Nanogenerators. Springer International Publishing, Switzerland (2016). https://doi.org/10.1007/978-3-319-40039-6

Thermal Conductivity Enhancement of Epoxy Composite Based on Hybrid BN and Graphite Particulate Conductive Fillers and Effect of Hybrid Sample Thickness (t) and Filler Fraction on Thermal Resistance (R) and Thermal Conductivity (k)

Rajesh Kumar, Sagar Kumar Nayak, Bishnu P. Panda, Smita Mohanty and Sanjay K. Nayak

Abstract Disc-shaped composite samples of raw graphite powder, boron nitride (BN) with a range of hybrid mass fractions, and epoxy resin were prepared for thermal conductivity improvement of epoxy composite material. The formation of a conducting network through hybrid graphite powder and BN in an insulating epoxy matrix was confirmed from SEM micrograph. The thermal conductivity (W/mK) of the systems increased with increasing hybrid graphite and BN mass fraction achieving a percolation threshold limit. The measured thermal conductivity (k) of hybrid graphite/BN–epoxy composites using the ASTM E1530 standard (at 60 °C) increased with increasing hybrid graphite powder and BN mass fraction. The maximum thermal conductivity for raw hybrid graphite powder and BN–epoxy composites was ~2.01 W/mK, at 60% filler loading, indicating commercial use for high conductivity thermal interface materials (TIMs) and temperature sensor interconnection applications.

Keywords Thermal conductivity (TC) · Hybrid composites · Graphite powder Boron nitride

R. Kumar (✉) · S. K. Nayak · B. P. Panda · S. Mohanty · S. K. Nayak
Laboratory for Advanced Research in Polymeric Materials, B-25, CNI Complex, Patia, Bhubaneswar 751024, Odisha, India
e-mail: rajpolymer83@gmail.com

S. K. Nayak
Central Institute of Plastics Engineering and Technology, Chennai 600032, Tamil Nadu, India

1 Introduction

We know that polymeric materials are becoming more important in designing the new engineering item and products to fulfil the daily required activities of human beings and increasing the standard of human life, because of their low cost, lightweight, high strength, adverse environmental chemical resistant, and tailorability to desired properties which can compete with conventional materials, e.g., stainless steel, aluminium alloy, etc. All polymers have their own inherent properties which may be advantageous or disadvantageous to different needs; further, they can be improved by blending, filler incorporation, stabilizers, etc. We know composites formed via incorporation of different micro/nanomaterials into polymeric materials can enhance and/or change the property of polymeric materials which can suit the desired requirement in efficient way. Generally, polymers are bad conductors of heat and electricity due to the absence of free conductive paths, so they are also used as insulators [1–4]. But for electronic application, polymer has to be conductive like metals and semiconductors. To increase the conductivity different polymers, we have to incorporate with different high conductive micro and nanomaterials which can provide suitable conductive paths inside polymeric chains to conduct heat and electricity without sacrificing the mechanical properties of polymeric materials, so that it can be used in electronic packaging items. Epoxy is one of the polymers which have some inherent conductivity (0.19 W/mK) and it's conductivity further increased by incorporation of commercially available silver, aluminium, boron nitride, graphite-based micro and nanofillers by our researchers [5, 6]. Many commercial thermal adhesives and pastes are available in market. But the conductivity is not so much high. So by modification and treatment of conductive fillers, we can further increase the thermal conductivity of material. Expanded graphite and graphene nanoplatelets (GNP) have very high conductivity (3,000 W/mK, 107 S/m). These are prepared from natural graphite which is abundant on earth [7–13]. Boron nitride is prepared synthetically from boron and shows high thermal conductivity (300 W/mK) only, which can help in breaking the extra electrical pathways of composite system. So boron nitride along with graphite and GNP which can be used with epoxy resin to develop high heat conductive adhesive, thermal paste, and composites in electronic packaging systems where high heat conduction is required. Removal of boron nitride from hybrid filler ratio can give epoxy composite which will have both high electrical and heat conductive properties to replace commercial thermal adhesive and paste [14–16]. In general, most of the computer processors operate at elevated temperature, and the higher thermal conductivity (2.01 W/mK) of hybrid graphite and BN–epoxy at elevated temperatures can ensure efficient heat transfer. Thus increasing the self-life of electronic system by efficiently dissipating heat as it is formed and avoid short circuits due to induction currents [17–19].

2 Experimental Setup

2.1 Materials

(a) **Matrix Material**

The epoxy resin used in this work is Araldite GY 250 which was purchased from M/S Huntsman International (INDIA) Pvt. Ltd. It is basically diglycidyl ether of bisphenol-A (DGEBA). It is a medium viscosity epoxy resin and is suitable for the formulation in different solvent-free coatings and adhesives. It shows better chemical resistance and mechanical properties. It's properties can be further improved by addition of additives and fillers. The corresponding curing agent Aradur® HY 951 IN supplied by M/S Huntsman international (INDIA) Pvt. Ltd. which is added up to 10–12 wt% of epoxy resin for better crosslinking. They are low viscosity aliphatic amines which are basically triethylene tetra amines (TETA).

(b) **Filler Material**

  (i) *Boron Nitride Powder* with dimension ~1 μm and hexagonal shape are obtained from Sigma-Aldrich Co., Germany. The micro-ceramic particles have excellent thermal and chemical stability. Boron nitride is a white solid material whose thermal conductivity and density values are approximately 30–300 W/mK ~at 300 K and 2.29 g/mL at 25 °C respectively.

  (ii) *Graphite Powder* (<20 μm) synthetic is collected from Sigma-Aldrich Co., Switzerland. Graphite is an allotrope of carbon and is a semi-metallic, showing high electrical and thermal conductivity. Synthetic graphite can be prepared by heating carbonaceous precursor in an inert atmosphere. This carbon compound has many characteristics, which makes it suitable as a thermal conductivity enhancer. It has thermal conductivity in the range of 25–500 W/mK.

2.2 Adhesive Composite Preparation

The adhesive composite was prepared by conventional hand-lay-up or mechanical mixing technique, so as to get different composite samples with different hybrid filler formulations. Raw epoxy resin and its curing agent (HY951) were mixed in a ratio of 10:1 with micron-sized boron nitride and graphite particles. Composites of six different filler compositions 10, 20, 30, 40, 50, and 60 wt% of boron nitride and graphite are made with internal hybrid compositions of equal weightage. Samples are casted into a wax-coated polypropylene mould cups and then allowed for curing at room temperature for about 24 h. Then, samples are released from mould cups after application of some external force.
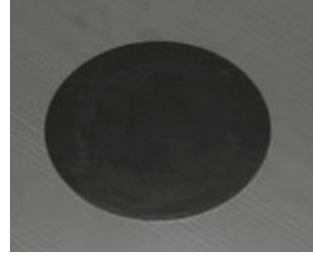
Fig. 2 Equipment used for thermal conductivity analysis Anter Unitherm Model 2022, Anter
Corpo, USA available in LARPM Bhubaneswar, India.

2.3 Specimen Size

As per standard ASTM E1530 Annex A1, for solid plastic and film materials sample
testing discs with 50.8-mm-diameter thickness, range is 0.5–25 mm as required
(Fig. 1).

2.4 Characterization

In this research, the thermal conductivity (k, W/mK) at 60 °C temperature is measured
on circular sample in accordance with ASTM E 1530-06 standard by guarded heat
flow meter technique (Unitherm™ 2022, Anter Corpo, USA) as shown in Fig. 2.
Morphological study of fracture surface of optimum resulted sample is carried out
using scanning electron microscope (Carl Zeiss SMT, Germany, EVO MA 15, Carl
Zeiss SMT). The composite fracture is done by applying the force.

Table 1 List of particulate filled composites fabricated by hand-lay-up techniques

S. No.	Sample name	BN+Gr ratio (wt%)	Thermal conductivity (W/mK)
1	5BN+5Gr-Ep	10	0.239
2	10BN+10Gr-Ep	20	0.513
3	15BN+15Gr-Ep	30	0.556
4	20BN+20Gr-Ep	40	0.662
5	25BN+25Gr-Ep	50	1.2
6	30BN+30Gr-Ep	60	2.025
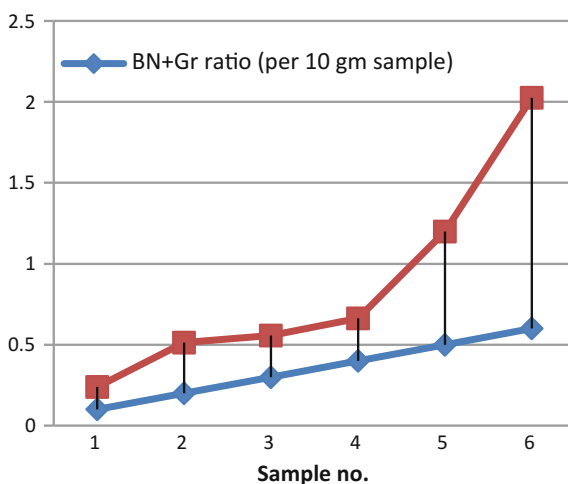
Fig. 3 Line graph showing an increase in thermal conductivity with increasing filler ratio

3 Results and Discussion

3.1 Thermal Conductivity (k)

In this experiment, two particulate microscale fillers of boron nitride (BN) and graphite (Gr) were used to establish the thermal conductivity improvement of epoxy adhesive composites. The thermal conductivity data of all types of epoxy composites is given in Table 1. The thermal conductivity of hybrid epoxy composites filled with particulates of Gr and BN is shown in Figs. 3 and 4. The virgin epoxy exhibits a thermal conductivity of 0.197 W/mK.

For reinforced Gr/BN epoxy composite up to 10% filler fraction, the rise in thermal conductivity is unfruitful. The epoxy composites containing 10 wt% of fillers, **5BN+5Gr-Ep**, exhibit a thermal conductivity of 0.239 W/mK which is not a significant enhancement over neat epoxy. This may be due to the low filler loading,
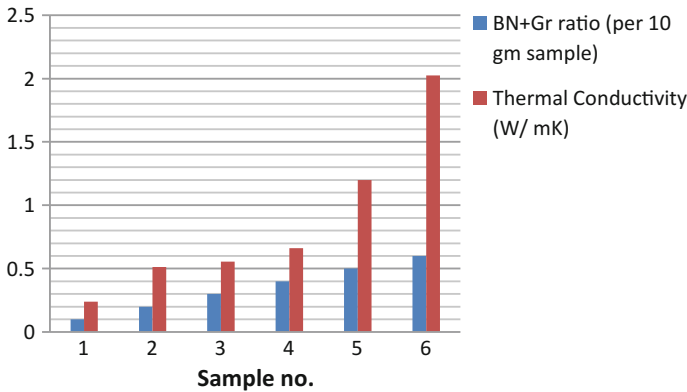
Fig. 4 Column graph showing an increase in thermal conductivity with increasing filler ratio

and hence effective conductive channels are not formed inside epoxy matrix. At lower concentration of filler loading (i.e., lower percolation threshold), conductivity is nearly equal to virgin polymer. This is because below the percolation threshold, the thermal conductivity of the composite material is mainly influenced by the TC of the matrix; to reach the percolation threshold, one must increase the filler concentration in the matrix to a jump in the conductivity values as demonstrated for electrical conductivity [1–4].

Further inclusion of hybrid particulates up to 20, 30, and 40% filler fraction of hybrid graphite and boron nitride inside epoxy matrix causes thermal conductivity hybrid composites to increase linearly. It enhances 0.513 W/mK, 0.516 W/mK, and 0.662 W/mK for **10BN+10Gr-Ep**, **15BN+15Gr-Ep**, and **20BN+20Gr-Ep**, respectively. This shows that BN and graphite have good compatibility with each other, providing mean free path for phonon transfer network through composite matrix above the percolation threshold. This is because layer structure of graphite forms the more heat pathways in the epoxy matrix easily, as we all know that the layer structure fillers are favoured to be connected with each other by relative fewer contact points to form the heat pathway [3, 5]. Further, loading of hybrid particulates up to 50% filler fraction of graphite and boron nitride causes the thermal conductivity hybrid composites to increase abruptly. It increases to 1.2 W/mK for **25BN+25Gr-Ep**. This shows the synergistic behaviour of both at high filler concentration in thermal conductivity enhancement of epoxy composite. This is because the use of hybrid fillers increases the maximum filler loading and may lead to more conductive paths and synergistic behaviour for electrical conductivity (EC) and TC. Therefore, systems containing multiple fillers possess greater TC than individual filler-based systems at a given filler concentration [6].

Further, the addition of hybrid particulates up to 60% filler fraction of graphite and boron nitride causes thermal conductivity of hybrid epoxy composites to increase linearly. It increases to 2.025 W/mK for **30BN+30Gr-Ep**. This is because high filler concentration and high aspect ratio of hybrid fillers combine inside epoxy matrix.

Hybrid fillers with different ratios provide better symmetry in phonon transfer mechanism by lowering the filler/filler and filler/matrix resistance. This is in accordance with the Baruch et al., Kemaloglu et al., and Mahanta et al. [3, 6, 7]. It says that the aspect ratio of the filler plays important role in achieving high thermal conductivity in composite systems; many researchers reported that multiple-filler loading enhances the desired property better than single-filler loading. For example, replacing part of the 70 nm BN by 7 m BN at the same volume fraction yields about 100% increase in TC. Using hybrid fillers, a composite material has the advantages of both fillers and addition of relatively minute amounts of the right nanorange filler (graphene) further enhances the thermal conductivity by providing better thermal transport channel contacts between the primary (microscale) fillers and/or the microscale filler and the matrix [4, 10–13, 19].

3.2 Morphology Study

Before the SEM image of fracture surface of any polymeric composite, it should go through sputtering by any electrically conductive (generally gold nanoparticle) particle due to the principle of SEM. But in case of epoxy hybrid composite, no sputtering is required due to the presence of graphite powder, having electrical conductivity of 107 S/m. By adding BN and Gr (60 wt%) excessively, the dispersion of the hybrid filler through matrix gets curdle. Because of this, the stress concentration points, defects, and gas bubble cause the abasement of mechanical properties of composites as shown in Fig. 5. To achieve more thermal conductive values, the defects have to be reduced and need to be more conscious at the time of composites fabrication. The main objective to form heat conduction network satisfying percolation threshold influences the value of thermal conductivity of hybrid composites. The synergistic effect is due to the iso-structure of both BN and Gr microparticles. The glazing spot in the SEM images shows the agglomeration of particles (Fig. 5).

3.3 Thermal Resistance (R)

In this experiment, two particulate microscale fillers boron nitride (BN) and Graphite (Gr) were used to determine the thermal conductivity enhancement behaviour of reinforced epoxy adhesive composites. Experimental determination of thermal conductivity was done in accordance with ASTM E1530-06 standard. Unitherm™ Model 2022 was used to analyse thermal conductivity of a variety of composite materials. The experimental thermal conductivity (k) and thermal resistance (R) determined by analytical methods of all types of hybrid composites are given in Table 2. The thermal conductivity (k) and thermal resistance (R) of composites filled with particulates of Gr and BN are shown in Figs. 6, 7 and 8.
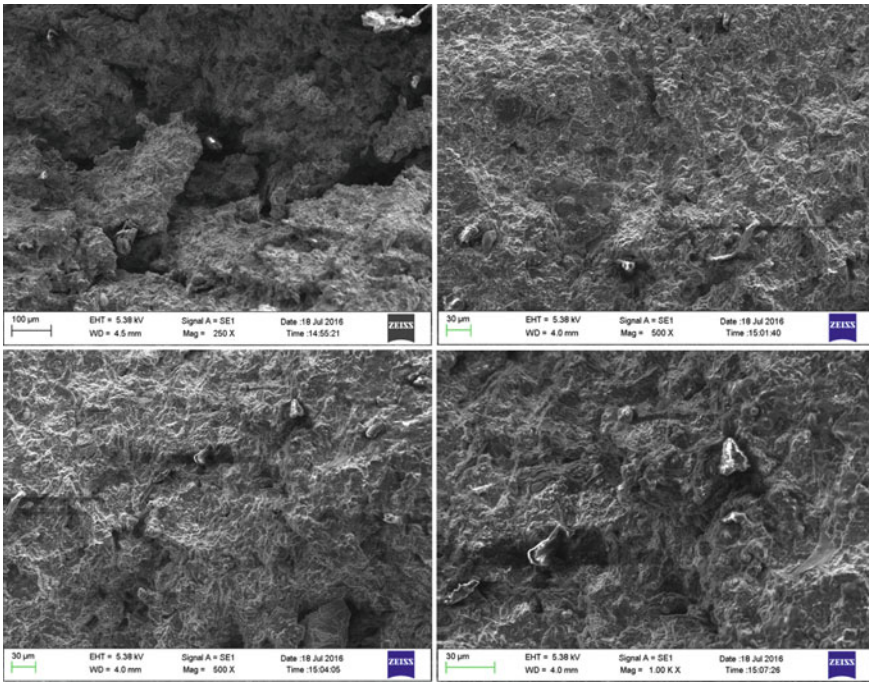
Fig. 5 Cross-sectional view of BN+Gr (60 wt%) adhesives at 250×, 500×, and 1000× magnification

Fig. 6 Line graph showing a decrease in thermal resistance (R) of samples having different thicknesses with increasing filler ratio into epoxy resin
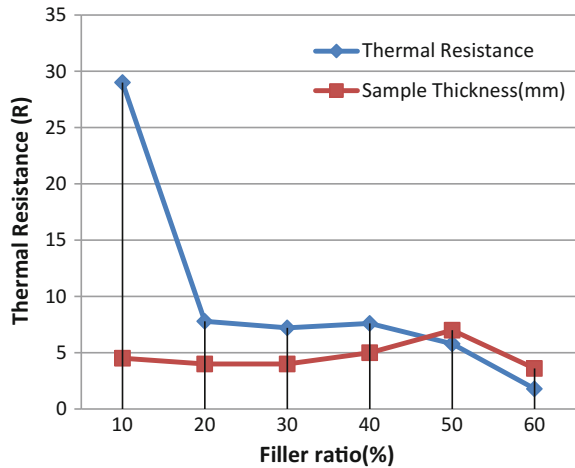
Table 2 Different composite samples prepared by hand-lay-up technique for thermal conductivity/thermal resistance test results

S. No.	Sample name	BN+Gr ratio (%)	Thermal conductivity (W/mK)	Sample thickness (mm)	Thermal resistance (K m²/W)	Equivalent thermal resistance ($R \times 10^{-3}$)
1	5BN+5Gr-Ep	10	0.239	4.5	$0.0188 = 2.9 \times 10^{-2}$	29
2	10BN+10Gr-Ep	20	0.513	4.0	$0.0078 = 7.8 \times 10^{-3}$	7.8
3	15BN+15Gr-Ep	30	0.556	4.0	$0.0072 = 7.2 \times 10^{-3}$	7.2
4	20BN+20Gr-Ep	40	0.662	5.0	$0.0076 = 7.6 \times 10^{-3}$	7.6
5	25BN+25Gr-Ep	50	1.2	7.0	$0.0058 = 5.8 \times 10^{-3}$	5.8
6	30BN+30Gr-Ep	60	2.025	3.6	$0.0018 = 1.8 \times 10^{-3}$	1.8

Fig. 7 Line graph showing an increase in thermal conductivity with increasing filler ratio
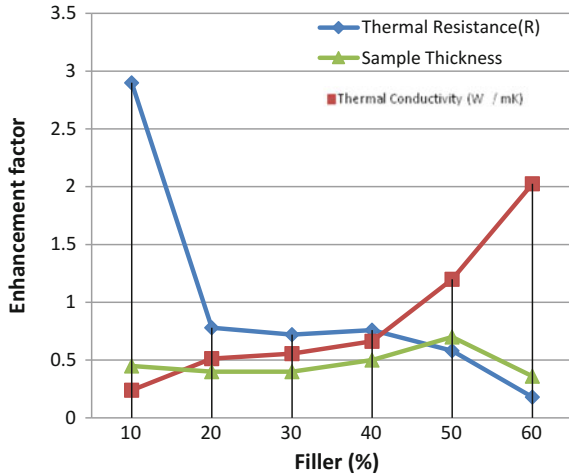
We know

$$R = \frac{\Delta T}{q} = \frac{t}{k}$$

According to the above equation, k is directly proportional to conductive sample thickness (t) and inversely proportional to thermal resistance (R) of conductive composite material. So if we load more conductive fillers having different densities into the resin, more conductive paths are formed for phonon transfer in the matrix

Fig. 8 Column graph showing an increase in thermal conductivity with increasing filler ratio
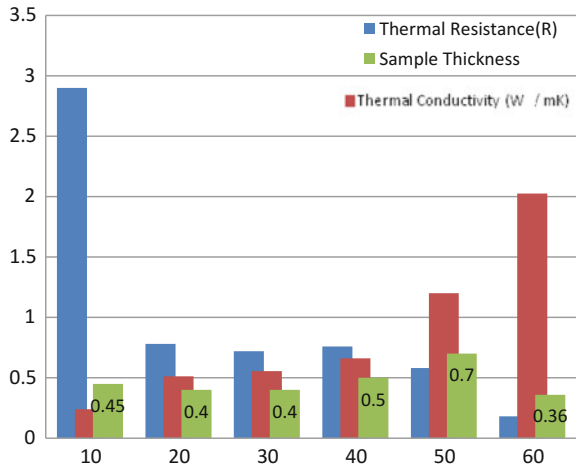
by decreasing matrix–matrix interface resistance of composites at optimum thickness (required to achieve suitable heat transfer network) of sample. But at the same time, thermal resistance (R) factor will decrease so as to increase the conductivity. It may be due to decrease in matrix/matrix interface resistance and suitable channels networks for phonon transfer and decrease in phonon scattering at interfaces [8, 9].

Initially, thermal resistance (R) was very high for Gr/BN epoxy composite up to 10% filler fraction for epoxy composite sample. For 5BN+5Gr-Ep (1st), sample containing 10% fillers and having thickness 4.5 mm exhibit a thermal resistance (R) 2.9×10^{-2} (K m^2/W) which is unfruitful development over neat epoxy. This may be due to low filler loading, and effective conductive paths are not created inside epoxy matrix and high matrix/matrix interface resistances predominate. At lower fraction of filler loading (i.e., lower percolation threshold), conductivity is nearly equal to virgin polymer. This is in accordance with the Baruch et al. and Lee et al. [3, 4]. It says that below the percolation threshold, the TC of the composite material is mainly influenced by the TC of the matrix; to reach the percolation threshold, one needs to increase the filler concentration in the matrix to a jump in the conductivity values as demonstrated for EC and with this relatively low thermal conductivity ratio, the foremost strait for heat conduction was projected to engross the matrix, rather than the percolating network.

Further, the addition of hybrid particulates up to 20, 30, and 40% filler fraction of graphite and boron nitride, thermal resistance R of graphite and boron nitride epoxy composites decreases nonlinearly. The thermal resistance R decreases to 7.8×10^{-3} (K m^2/W), 7.2×10^{-3} (K m^2/W), and 7.6×10^{-3} (K m^2/W) having thickness 4.0 mm, 4.0 mm, and 5.0 mm for **10BN+10Gr-Ep (2nd)**, **15BN+15Gr-Ep (3rd)**, and **20BN+20Gr-Ep (4th)**, respectively. The thermal resistance R of **10BN+10Gr-Ep (2nd)** sample having thickness 4 mm decreases abruptly. This shows that BN and graphite have good compatibility with each other, providing mean free path (decreased filler/filler interface resistance because of high surface area of layered

structure units) for phonon transfer to decrease thermal resistance R of composite matrix above the percolation threshold. This is in accordance with the Baruch et al., Novak et al. and Ren et al. [3, 5, 11]. It says that layer structure of graphite forms the more heat pathways in the epoxy matrix easily, as we all know that the layer structure fillers are favoured to be connected with each other by relative fewer contact points to form the heat pathway, which indicates that the thermal contact resistance of the layer structure of graphite epoxy matrix is lower and thus the thermal conductivity is higher. BN is considered the best due to the following unique properties: BN has a structural resemblance to carbon materials, e.g., cubic BN is analogous to diamond and hexagonal BN is analogous to graphite when the B and N atoms replace the C atoms. The similarity of the hexagonal BN to graphite results in good TC. Despite the structural analogy between graphite and hexagonal BN, the latter has a wide bandgap energy (ranging from 3.6 to 7.1 eV) due to its partial ionic bond properties. The wide bandgap turns the hexagonal BN into one leading filler for maintaining high TC values in composite materials while keeping EC values as low as possible. The thermal resistance (R) of **15BN+15Gr-Ep (3rd)** sample having thickness 4 mm decreases slowly due to increased conductivity at high filler ratio in matrix and small thickness than previous sample. This is in accordance with Park et al. [8]. It graphically shows that R_{TIM} of coating will decrease less if we do not increase the sample thickness while increasing filler ratio in matrix.

The thermal resistance (R) of **20BN+20Gr-Ep (4th)** sample having thickness 5 mm is slightly higher than the third sample but lower than the second sample. This is because of increasing viscosity and t/k predominance factor. Increasing viscosity (due to high filler ratio) during preparation causes voids and surface roughness errors in sample which increases the R; while on the other side, high conductive channels (high k value) are formed due to increasing filler ratio and thickness (t) of the sample. The average of both factors decides predominance in increasing the thermal resistance (R). So, t/k value (i.e. R) is lower for **20BN+20Gr-Ep (4th)** due to increased conductivity (k) in comparison to increased thickness of this sample than previous samples. This is in accordance with Luo et al., Emerson et al. and Sahil et al. [9, 12, 13]. It says that voids are entrapped during the casting process because of the increased viscosity and introduction of nanoparticles formed additional thermal interfaces resistance between the micron-sized silver plates in similarly filled epoxies, thus falling the efficiency of thermal transportation and causing to decrease the bulk thermal conductivity, and graphene thermal coupling to other materials can depend strongly on the surface roughness, the presence or absence of suspended regions in graphene layers, and method of graphene preparation.

Further, the addition of hybrid particulates up to 50% filler fraction of graphite, and boron nitride causes the thermal conductivity of hybrid composites to increase abruptly. The thermal conductivity increases to 1.2 W/mK for **25BN+25Gr-Ep**. The thermal resistance (R) of **25BN+25Gr-Ep (5th)** sample having thickness 7 mm is 5.8×10^{-3} (K m^2/W). The thermal resistance (R) is lower than all other previous samples because of increasing conductive filler ratio and increasing thickness of sample for increasing thermal conductivity [8, 9]. This shows the synergistic behaviour of both at high filler concentration in thermal conductivity enhancement of epoxy com-

posite. This is in accordance with the Browni et al. and Kovacs et al. [14, 15]. It says that the average dimension of the boron–nitride is lesser (under 10 μm) than that of the talc (5–50 μm), and thus they can act as efficient hybrid fillers. The image of the fracture surface of compounds shows even filler distribution and larger aggregates cannot be discovered. The compounds are compacted (filler content is 30 vol%), and thus particles could structure a conductive network in the compound through the wall thickness of the products and improve the thermal conductivity more efficiently and the thermal conductivity normal to the surface followed percolation activities. The higher weight fraction of MWNTs near the surface, the higher purity, and the larger aspect ratio of MWNTs are responsible for significant step up in thermal conductivity of the composites. The obstruction to conduction was the width of the epoxy film separating the MWNTs.

Further, the addition of hybrid particulates up to 60% filler fraction of graphite and boron nitride of equal weightage causes the thermal conductivity of hybrid composites to increase linearly. The thermal conductivity increases to 2.025 W/mK for **30BN+30Gr-Ep**. The thermal resistance (R) of **30BN+30Gr-Ep (6th)** having thickness 3.6 mm is 1.8×10^{-3} (K m^2/W). The thermal resistance (R) is lower than all other previous samples because of high conductivity (k) than thickness (t) of the sample. Here, t/k predominates over other viscosity and sample preparation errors. This is because high filler concentration and high aspect ratio of fillers combination are required to meet high thermal conductivity results inside composites. Hybrid fillers with different ratio provide better symmetry in phonon transfer mechanism by lowering the filler/filler and filler/matrix resistance. The aspect ratio of the filler plays important role in achieving three-dimensional percolation network formation in amalgamated systems and multiple-filler loading enhances the desired property better than single-filler loading [1, 3, 6, 7, 11, 16–18].

4 Conclusion

In this study, the thermal conductivity increased linearly with increase of filler fraction of hybrid particulates. Thermal conductivity shows a synergistic improvement at 60% filler loading fraction having equal weightage of both BN and Gr. Simultaneously, it had less thermal resistance also. Thickness (t) of hybrid GR/BN–epoxy sample plays a little role in increasing the thermal resistance (R) while increasing the hybrid filler fraction inside epoxy matrix. So dimension and aspect ratio of hybrid fillers plays important role in thermal conductivity enhancement of polymer composites.

References

1. Lingamneni, S., Marconnet, A.M.: 3D Packaging Materials Based on Graphite Nanoplatelet and Aluminum Nitride Nanocomposites, Department of Mechanical Enginering, Stanford University, USA, November 2013

2. Srinivas, K., Bhagyashekar, M.S.: Thermal Conductivity Enhancement of Epoxy by Hybrid Particulate Fillers of Graphite and Silicon Carbide, Department of Mechanical Engineering, Don Bosco Institute of Technology, Bangalore, India, 13 Feb 2015

3. Baruch, A.-E., Bielenki, L., Regev, O.: Thermal Conductivity Improvement of Electrically Nonconducting Composite Materials, Department of Chemical Engineering, Ben-Gurion University of the Negev, Beer-Sheva 84105, Israel. Rev. Chem. Eng. **28** (2012)

4. Lee, B., Liu, J.Z., Sun, B., Shen, C.Y., Dai, G.C.: Thermally Conductive and Electrically Insulating EVA Composite Encapsulants for Solar Photovoltaic (PV) Cell, National Key Laboratory of Chemical Engineering, East China University of Science and Technology, 26 Feb 2008

5. Novák, I., Krupa, I.: Electro-Conductive Resins Filled with Graphite for Casting Applications, Department of Composite Thermoplastics, Polymer Institute of the Slovak Academy of Sciences, Dubravska cesta 9, 84236 Bratislava, Slovakia, 21 Nov 2003

6. Kemaloglu, S., Ozkoc, G., Aytac, A.: Properties of Thermally Conductive Micro and Nano Size Boron Nitride Reinforced Silicon Rubber Composites, Department of Chemical Engineering, Kocaeli University, 41040 Kocaeli, Turkey, 16 July 2009

7. Mahanta, N.K., Loos, M.R., Zlocozower, I.M., Abramson, A.R.: Graphite–Graphene Hybrid Filler System for High Thermal Conductivity of Epoxy Composites, Department of Mechanical and Aerospace Engineering, Case Western Reserve University, Cleveland, Ohio 44106, USA, 30 July 2014

8. Park, W., Guo, Y., Li, X., Hu, J., Liu, L., Ruan, X., Chen, Y.P.: High-Performance Thermal Interface Material Based on Few-Layer Graphene Composite. pubs.acs.org/JPCC

9. Luo, H., Weia, Q., Yu, Z.M., Wang, Y., Long, H., Xie, Y.: Effect of Film Thickness on the Temperature Dependence of Thermal Conductivity for Diamond/BeO Composites. Cer. Int. **41**, 12052–12057 (2015)

10. Han, Z., Fina, A.: Thermal conductivity of carbon nanotubes and their polymer nanocomposites: a review. Science **36**, 914–944 (2011)

11. Ren, P.-G., Si, X.-H., Sun, Z.-F., Ren, F., Pei, L., Hou, S.-Y.: Synergistic Effect of BN and MWCNT Hybrid Fillers on Thermal Conductivity and Thermal Stability of Ultra-High-Molecular-Weight Polyethylene Composites with a Segregated Structure, 16 July 2015

12. Emerson, J.A., Rightley, M.J., Galloway, J.A., Rae, D.F., Huber, D.L., Cotts, E.J.: Minimizing the Bond Line Thermal Resistance in Thermal Interface Materials Without Affecting Reliability, Sandia National Laboratories, Binghamton University

13. Shahil, K.M.F., Balandin, A.A.: Thermal Properties of Graphene and Multilayer Graphene: Applications in Thermal Interface Materials. Solid State Commun. **152**, 1331–1340 (2012)

14. Brown, M., Jagannadham, K.: Thermal conductivity of MWNT–epoxy composites by transient thermo reflectance. J. Electron. Mat

15. Kovács, J.G., Suplicz, A.: Improved thermal properties with hybridization of the fillers for thermoplastic materials, Department of Polymer Engineering, Faculty of Mechanical Engineering, Budapest University of Technology and Economics, Muegyetem rkp 3, H-1111 Budapest, Hungary. In: The 19th International Conference on Composite Materials

16. Yu, A., Ramesh, P., Sun, X., Bekyarova, E., Itkis, M.E., Haddon, R.C.: Enhanced thermal conductivity in hybrid graphite nanoplatelet-carbon nanotube filler for epoxy composites. Adv. Mater. **20**, 4740–4744 (2008)

17. King, J.A., Johnson, B.A., Via, M.D., Ciarkowski, C.J.: Effects of carbon fillers in thermally conductive polypropylene based resins. Polym. Compos. **31**, 497–506 (2010)

18. King, J.A., Gaxiola, D.L., Johnson, B.A., Keith, J.M.: Thermal conductivity of carbon-filled polypropylene-based resins. J. Compos. Mater. **44**, 839–855 (2010)

19. Zhou, S., Chen, Y., Zou, H., Liang, M.: 5 Thermally Conductive Composites Obtained by Flake Graphite Filling Immiscible Polyamide 6/Polycarbonate blends, The State Key Laboratory of Polymer Materials Engineering, Polymer Research Institute of Sichuan University, Chengdu 610065, China, Jan 2013

Stabilization Studies of Epoxidized Soybean Oil Plasticized PVC Films in the Presence of Beta-Diketone Additives

M. B. Kulkarni ⓘ, **S. Radhakrishnan** ⓘ, **Nikesh Samarth** ⓘ
and P. A. Mahanwar ⓘ

Abstract Rigid and plasticized PVC is used extensively in a variety of industries like construction, packaging sheet and film, electrical, automotive parts, furniture equipment, clothing, footwear, etc. In recent years, natural biobased materials are being explored for plasticizers for PVC. The present work focuses on the development of different epoxidized soybean oil (ESBO) plasticized PVC formulations in the presence of calcium/zinc stearates and beta-diketone stabilizer such as dibenzoylmethane (DBM). The DBM which has dual property of a UV stabilizer and heat stabilizer was varied from 0 to 10 phr. The PVC films were prepared and analyzed in terms of dehydrochlorination studies. The above PVC films were exposed for 100 h in the accelerated QUV weathering, and the characterization of the exposed products was carried out in terms of mechanical and thermal properties and dehydrochlorination. This ternary system hinders the degradation process and decreases the initial rate of dehydrochlorination. The success of the novel beta-diketones stabilizers can meet higher performance and longer service life of epoxidized soybean oil plasticized PVC films in the presence of zinc/calcium stearates. This will ultimately lead to a positive influence on the environment.

Keywords Polyvinyl chloride (PVC) · Epoxidized soybean oil (ESBO)
Dibenzoylmethane (DBM)

M. B. Kulkarni (✉) · S. Radhakrishnan
Maharashtra Institute of Technology, S124 Paud Road Kothrud, Pune 411038, India
e-mail: malhari.kulkarni@mitpune.edu.in

S. Radhakrishnan
e-mail: radhakrishnan.s@mitpune.edu.in

N. Samarth · P. A. Mahanwar
Polymer and Surface Science, Institute of Chemical Technology, Mumbai 200019, India

1 Introduction

Plasticized PVC is used in a large number of applications such as automotive, electrical, furniture/office equipment, packaging, clothing, footwear, etc. [1], and outdoor applications, with window frames, being a prime example of PVC materials [2]. PVC has comparatively low thermal stability and rapid photo-ageing behavior leading to chain scission and cross-linking. The formation of oxidized structures results in the loss of mechanical properties and discoloration due to polyene formation in PVC products. During polymerization, unsaturated chain ends and many oxidized structures, such as ketones and hydroperoxides, are formed which are responsible for PVC degradations, and the presence of weak chain links and branches makes more complicated. The presence of thermal stabilizers also helps in protecting the film from UV radiation. Uses of lead salts and organic tin stabilizers are restricted due to their toxicity, even they have high efficiency to stabilize PVC. On the other hand, rare earth stabilizer and Ca/Zn stabilizers are restrained because of their low efficiency. Recently, stabilization of PVC has been carried out using several inorganic compounds and organic secondary stabilizers such as epoxides, polyols, phosphites, beta-diketones, dihydropyridine, etc. Epoxy structures are well known as typical non-metallic stabilizers for PVC. They are generally used as secondary stabilizers used to enhance the effectiveness of metal soaps. The effect of rare earth stabilizers combined with Ca/Zn stabilizers on the PVC stabilization was also investigated [2–5]. With continued advancements in the formulations field, there is now a real need to use complex novel nontoxic green stabilizers in order to reduce the degradation of PVC [6–10]. Hence, the present work focused on development of different epoxidized soybean oil (ESBO) plasticized PVC formulations in the presence of zinc and calcium stearates and beta-diketone stabilizer such as dibenzoylmethane (DBM) which has dual property of a UV stabilizer and heat stabilizer. The success of the novel beta-diketone stabilizers can meet higher performance and longer service life of epoxidized soybean oil plasticized PVC films in the presence of zinc and calcium stearates. This will eventually lead to a positive impact on the environment.

2 Experimental

2.1 Materials

PVC of suspension grade with K value 65–67 was obtained from Reliance Industry Ltd., Mumbai, India. Soybean oil (refined) was obtained from IPOL, India. Commercial glacial acetic acid, p-toluene sulfonic (p-TSA) acid, stearic acid, and a solution of hydrogen peroxide (50% w/w) were procured from S. D Fine Chemicals Ltd., Mumbai, India, which were used. Commercial heat stabilizer complex Ca/Zn based was obtained from local supplier. Dibenzoylmethane (DBM) was purchased from Sigma Aldrich Chemicals, India. Fly ash was supplied by Envirotech Engineers,

Table 1 Reaction conditions for epoxidation of soybean oil

Mole ratio (acid:oil:peroxide)	Agitation (rpm)	Catalyst (*p*-TSA)	Temperature (°C)	Time (h)
0.3:1:1.5	500	1	60	8
0.5:1:1.5	500	1	60	8
0.7:1:1.5	500	1	60	8
0.5:1:1	500	1	60	8
0.5:1:1.5	500	1	60	8
0.5:1:2	500	1	60	8
0.5:1:1.5	500	1	50	8
0.5:1:1.5	500	1	60	8
0.5:1:1.5	500	1	70	8
0.5:1:1.5	500	1	80	8

Pune, India, used as filler. All chemicals were used as received. Epoxidized soybean oil was especially prepared for the present studies.

2.2 Synthesis of Epoxidized Soybean Oil (ESBO)

Peracetic acid generated in situ by reacting hydrogen peroxide (50% w/w) with excess glacial acetic acid in the presence of *p*-toluene sulfonic acid as a catalyst was used for the epoxidation of soybean oil at 60 °C. Prior to the epoxidation reaction, SBO was analyzed to determine its initial oxirane content and iodine value. The extent of epoxidation was determined using a standard oxirane content analytical method [6]. The effect of mole ratios of reactant, temperature, and time on oxirane oxygen content was studied, and different reaction conditions of epoxidation are summarized in Table 1, and the reaction mechanism of epoxidized soybean oil is presented in Scheme 1.

2.3 Preparation of PVC Sheets

First, optimum loading of epoxidized soybean oil (ESBO) in PVC matrix was determined as a substitute of di-octyl phthalate by increasing loading from 20, 40, 60, 80, and 100 phr of total plasticizer. The plasticizer was compounded with PVC resin on a two-roll mill at 170 °C. The sheets were compression molded at the operating temperature of 180 °C for 10–15 min.

On the basis of the variation in tensile strength and elongation at break variations 20 phr loading of ESBO was maintained for further development of unfilled and fly ash (20 phr) filled PVC formulations stabilized in the presence of 1.5 gm of Ca/Zn
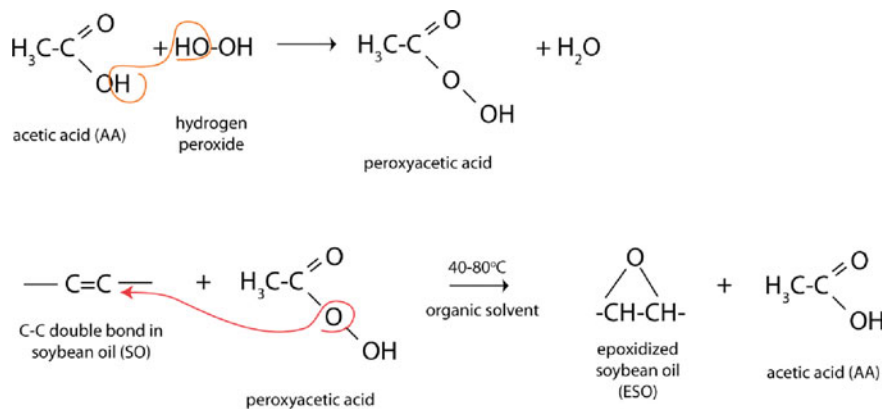
Scheme 1 Reaction mechanism of epoxidized soybean oil

Table 2 Preparation of PVC/ESBO/Ca/Zn stearates/DBM (without fly ash loading)

PVC	ESBO	Heat stabilizer	DBM	Stearic acid
100	20	1.5	0	1
100	20	1.5	1.5	1
100	20	1.5	3.0	1
100	20	1.5	5	1
100	20	1.5	10	1

Table 3 Preparation of PVC/ESBO/Ca/Zn stearates/DBM (with fly ash loading)

PVC	ESBO	Heat stabilizer	DBM	Stearic acid	Fly ash
100	20	1.5	0	1	20
100	20	1.5	1.5	1	20
100	20	1.5	3.0	1	20
100	20	1.5	5	1	20
100	20	1.5	10	1	20

stearate combinations in the presence of beta-diketone, i.e., DBM stabilizer (0–10 phr) and 1 gm of stearic acid as lubricant. All unfilled and fly ash filled PVC along with complex novel nontoxic green stabilizers were compounded on a two-roll mill at 170 °C. The various PVC formulations stabilized with ESBO, Ca/Zn stearate, DBM in the absence and presence of fly ash are given in Table 2 (without fly ash loading) and Table 3 (with fly ash loading).

2.4 Sample Characterization and Testing

FTIR Analysis

Fourier transform infrared spectra (FTIR) of synthesized ESBO samples along with soybean oil raw material were recorded using a Perkin-Elmer spectrum one spectrometer. The changes in FTIR spectra after exposure to the accelerated weathering for 100 h were also recorded by using accelerated QUV weatherometer.

Evaporation of Plasticizer

The loss of additives, particularly of plasticizers, from plasticized polymers is interesting from the point of view of processability of polymer materials and optimization of the process as well as for the evaluation of lifetime of plasticized polymer products in use. In order to calculate the rate of evaporation of plasticizer from the PVC sheet, the PVC sheet is heated at 180 °C for 120 min. The weight loss of additives was calculated from weight after heating divided by initial weight sample.

Mechanical Testing

The tensile specimens were cut out from the molded sheets according to the ASTM methods. The tensile strength, elongation at break, and elastic modulus of the PVC formulated sheets were determined at room temperature using a universal testing machine (Lloyd LR 50K) according to ASTMD638, and procedure at crosshead speed of 50 mm/min was maintained for testing. The changes in mechanical properties to the accelerated weathering for 100 h were also recorded using accelerated QUV weatherometer.

Thermal Analysis

Differential thermal analysis of prepared PVC samples in terms of differential thermogravimetric (DTG) and thermogravimetric (TG) curves was recorded with a Perkin-Elmer DSC-7 apparatus using open aluminum crucibles. The weight of the sample used was in the range of 10–12 mg. The samples were heated in a nitrogen atmosphere in the range of 20–800 °C and a heating rate of 10 °C/min.

3   Results and Discussion

It is well identified that the ability to prevent discoloration and dehydrochlorination of PVC is an important characteristic in the evaluation of stabilizing effect. The addition of ESO in the presence of Ca/Zn stearates helps to prevent the development of discoloration and dehydrochlorination, and this effect is strongly dependent upon the extent of epoxidation of soybean oil. The higher the value of oxirane oxygen, the enhanced is the effect on stabilization of PVC [6]. So first the effect of mole ratios of reactant, temperature, and time of reaction on oxirane oxygen content is
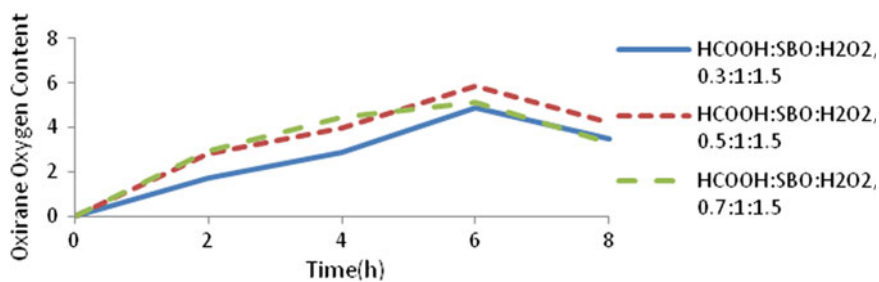
Fig. 1 Effect of mole ratios of reactants versus time of reaction on oxirane oxygen content of ESBO
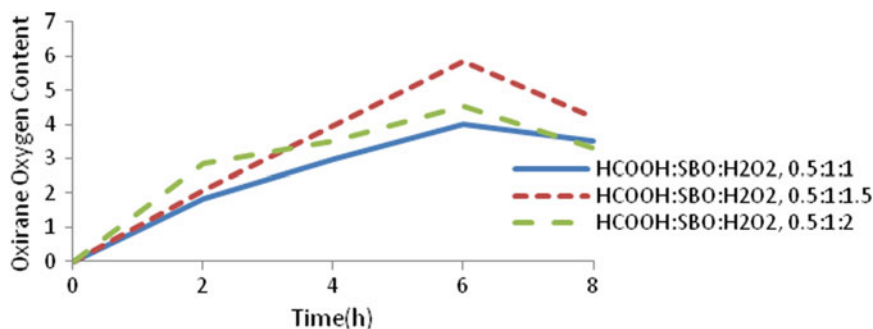
Fig. 2 Effect of variation in H_2O_2 versus time of reaction on oxirane oxygen content of ESBO

Table 4 Chemical characteristics of soybean oil (SBO) before and after epoxidation

	Specific gravity @27 °C	Viscosity @25 °C (cP)	Iodine value (gmI$_2$/100gm)	Saponification value (mg KOH/gm)	Acid value (mg KOH/gm)	Oxirane oxygen content (%)
SBO	0.916	80	121	180	0.86	–
ESBO	0.98	217	20	192	3.9	5.87

summarized in Figs. 1, 2 and 3, respectively. From the data, the high optimum level of oxirane oxygen content was achieved at a temperature of 60 °C for 8 h, using 1:0.5:1.5 mol ratios of ethylenic unsaturation to acetic acid and hydrogen peroxide in the presence of *P*-toluene sulfonic acid as a catalyst. Chemical analysis and FTIR spectra of soybean oil and epoxidized soybean oil are shown in Table 4 and Fig. 4a–b, respectively. The presence of new peaks in the FTIR spectrum of ESBO at 904.6 cm^{-1}, attributed to the epoxy group, confirmed the success of the epoxidation reaction of SBO. The other new peak at the around 3500 cm^{-1} was responsible for the hydroxyl functional group, derived from the epoxy functional group via partial epoxy ring opening reaction. The opening of epoxy ring reaction could occur either by acid catalysis in the presence of water associated with aqueous solution of H_2O_2 used.

Fig. 3 Effect of temperature on oxirane oxygen content of ESBO at fixed mole ratio of reactants
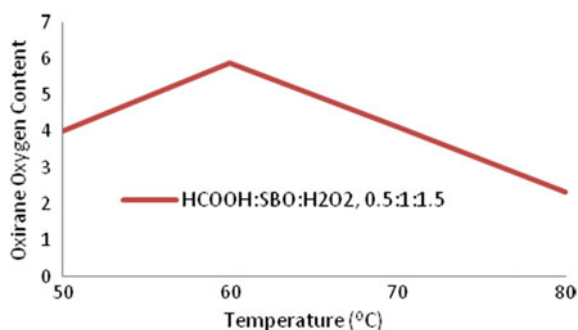
From Fig. 5, it is observed that with the addition of ESBO, the plasticization effect of PVC compositions increased as the values of tensile strength decreased beyond 20 phr and elongation at break increased beyond 60 phr level. On the basis of the mechanical properties such as tensile strength and percent elongation at break variations, 20 phr loading of ESBO was maintained for further development of fly ash filled PVC formulations and it is also observed that with the addition of fly ash beyond 20 phr level tensile strength and percent elongation at break values decreased at higher rates as shown in Fig. 6. Hence, on the basis of tensile strength and percent elongation at break variations and evaporation of plasticizer, 20 phr loading of ESBO was maintained for further development of unfilled and fly ash (20 phr) filled PVC formulations stabilized in the presence of 1.5 gm of Ca/Zn stearate combinations in the presence of beta-diketone, i.e., DBM stabilizer (0–10 phr) and 1 gm of stearic acid as lubricant.

Table 5 represents the variation in tensile modulus, tensile strength, and percent elongation at break of ESBO (20 phr) plasticized unfilled and fly ash (20 phr) filled PVC formulations before and after 100 h exposed to the accelerated QUV weathering condition in the presence of zinc and calcium stearates and in the presence of DBM which was varied from 1.5 to 10 phr loading. From Table 5, it is observed that no major change in tensile modulus and tensile strength and percent elongation at break was increased marginally after 100 h exposure to the accelerated QUV weathering condition. This variation supports the excellent plasticization effect and stabilization effect using novel ternary system.

In Fig. 7a–b, it was observed that 20 phr loading of ESBO for unfilled and fly ash (20 phr) filled PVC stabilized formulations showed optimum weight loss.

The thermal degradation of unfilled and fly ash (20 phr) filled PVC/ESBO (20 phr) stabilized with zinc and calcium stearates with and without DBM (5 phr) was investigated using differential thermal analysis. The thermogravimetric curves obtained are shown in Fig. 8 with four zones having different chemical processes involved in degradation. The thermal degradation of PVC was a two-step process. The first steps (up to 280–350 °C) mainly involve the dehydrochlorination of PVC resulting in the formation of conjugated double bonds that undergo cracking during the second step (up to 480–500 °C). In the second step, the degradation of polymer continued with
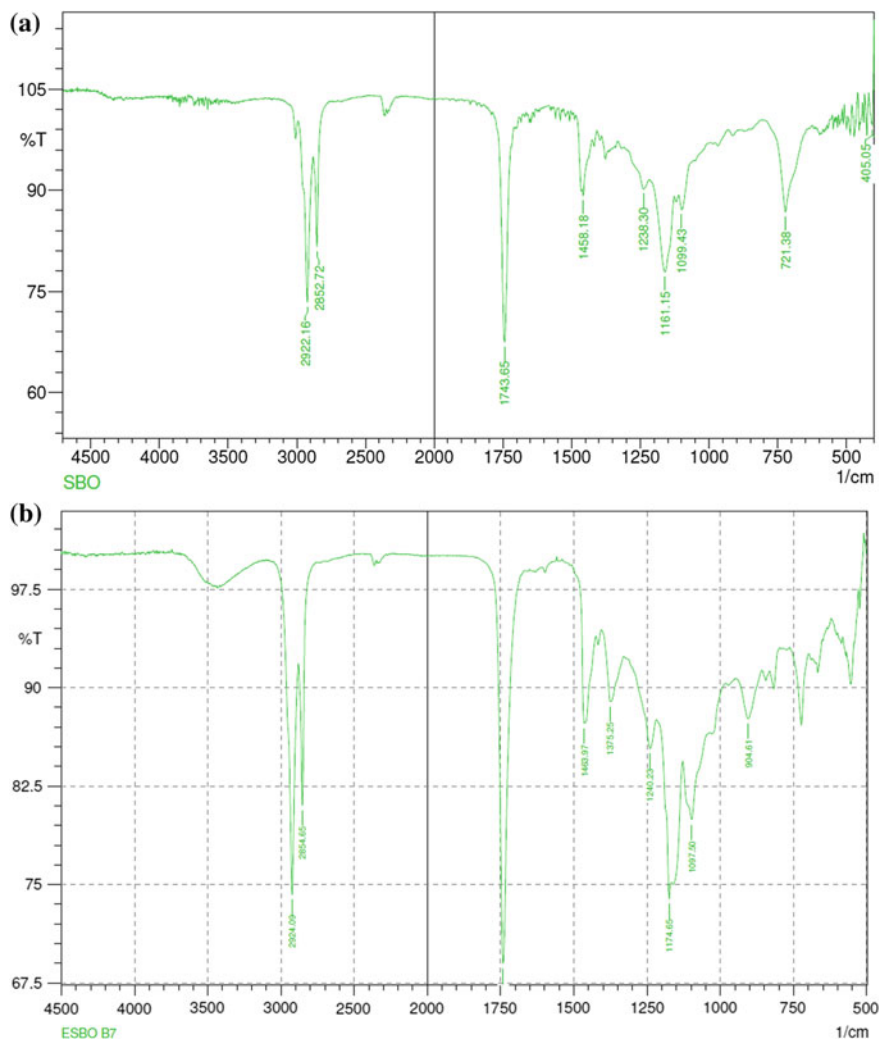
Fig. 4 **a** FTIR spectra of soybean oil (SBO). **b** FTIR spectra of epoxidized soybean oil (ESBO)

cracking and pyrolysis to low hydrocarbons with linear or cyclic structure. From Zone 4, it was observed that the effect of fly ash helped to improve thermal stability of PVC composition and suppresses the carbonization effect of PVC composition.

Table 6 shows the data obtained from the thermogravimetric curves and observed that with the addition of ESBO stabilized with zinc and calcium stearates in the absence and presence of DBM (5 phr) in PVC helped to decrease of weight loss. The temperature of maximum weight loss also improved for ternary system, while the corresponding residue% at 800 °C increased in the presence of FA.

Table 5 Mechanical properties of unfilled and fly ash filled PVC/ESBO/Ca/Zn stearates/DBM (Before and after 100 h accelerated QUV weathering condition)

Compositions	Tensile modulus (MPa)		Elongation at break (%)		Tensile strength (MPa)	
	Before	After	Before	After	Before	After
UFAPVC-ESBO-DBM1.5	129.27	150.67	44.74	52.27	19.26	19.69
UFAPVC-ESBO-DBM3	139.69	158.54	53.27	72.14	17.69	20.04
UFAPVC-ESBO-DBM5	134.81	160.34	60.86	68.28	17.51	22.06
UFAPVC-ESBO-DBM10	146.24	157.64	66.72	72.65	16.82	22.80
FFAPVC-ESBO-DBM1.5	145.19	203.78	48.49	21.64	21.70	19.96
FFAPVC-ESBO-DBM3	142.77	153.54	41.17	41.99	18.93	20.82
FFAPVC-ESBO-DBM5	145.67	114.22	46.99	42.45	19.96	21.53
FFAPVC-ESBO-DBM10	147.42	134.94	46.10	47.75	16.85	20.27

Table 6 Thermal data of PVC/ESBO/Ca/Zn stearates/DBM in the absence and presence of fly ash from TG and DTG analysis

Compositions	UFAPVC-ESBO20	FFAPVC-ESBO20-FA20	UFAPVC-ESBO20-DBM5	FFAPVC-ESBO20-FA20-DBM5
Weight loss (%)[a]	55.012	50.718	53.04	53.344
T_{max} (°C)[a]	304.79	319.85	317.63	287.24
$Ti - Tf$ (°C)[a]	266.9–355.4	265.02–356.1	262.62–354.71	259.56–346.48
Weight loss (%)[b]	14.09	16	14.82	13.46
T_{max} (°C)[b]	459.58	468.57	451.54	408.01
$Ti - Tf$ (°C)[b]	437.01–488.65	439.6–488.13	441.04–487.4	444.02–486.3
Residue at 800 (°C) (%)	5.42	22.87	5.96	24.65

[a]First step, [b]Second step
i initial; f final; T_{max} maximum weight loss temperature
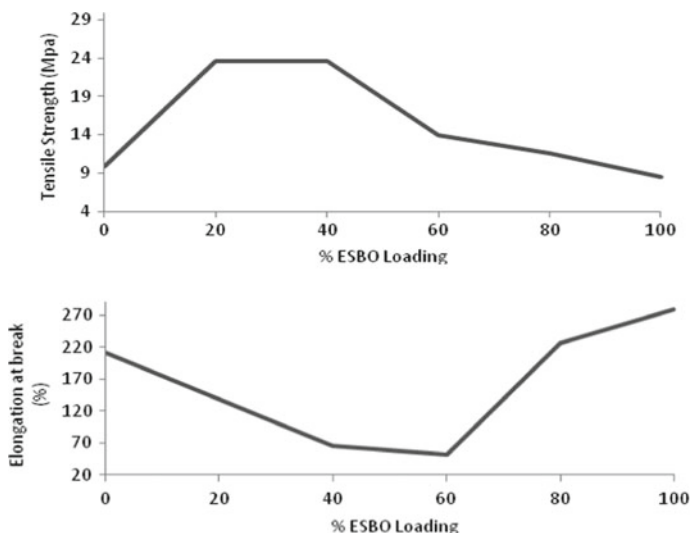
Fig. 5 Variation in tensile strength and percent elongation at break values of unfilled PVC/ESBO compositions
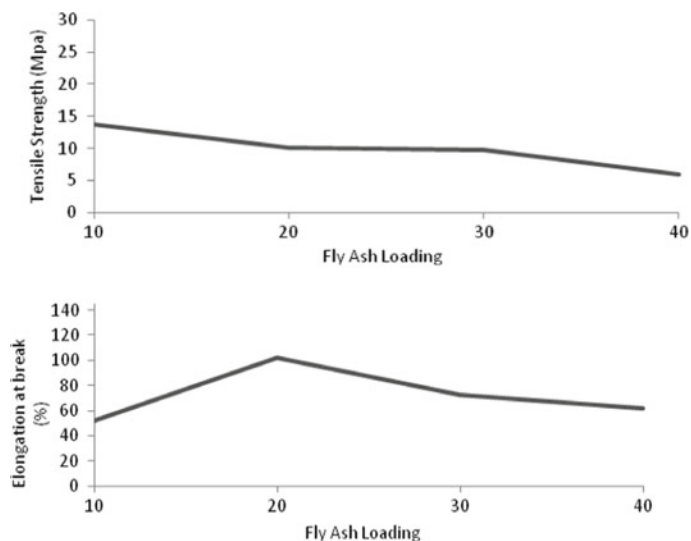
Fig. 6 Variation in tensile strength and percent elongation at break values of fly ash filled PVC/ESBO (20 phr) compositions

FTIR spectra of ESBO (20 phr) plasticized unfilled and fly ash (20 phr) filled PVC formulations after 100 h exposed to the accelerated QUV weathering condition in the presence of zinc and calcium stearates and in the presence of DBM (1.5–10 phr) are shown in Fig. 9a–b, respectively. From these spectra, it is observed that
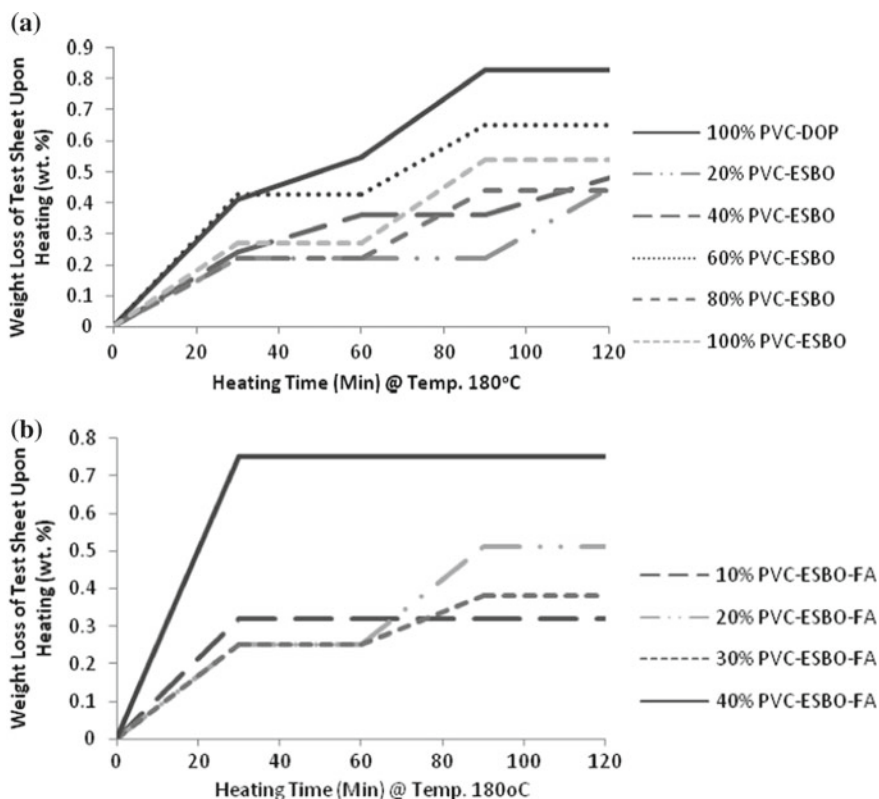
Fig. 7 a Evaporation of plasticizer of unfilled PVC/ESBO compositions. **b** Evaporation of plasticizer of fly ash filled PVC/ESBO compositions

the intensity at 633 cm^{-1} which is C–Cl band prominent in PVC does not decrease even after exposure to accelerated QUV weathering condition. Also, the peak at 1737 cm^{-1} corresponding to the photo-oxidation process (formation of carbonyl groups) does not increase much with the addition of DBM and fly ash which confirms their stabilization effect. The efficiency of ESBO is decided by the number of epoxy groups in the molecule, as the formation chlorohydrins due to the facile reaction of HCl with epoxy groups which results in the reduction of the autocatalytic effect of HCl.

4   Conclusions

This study showed that epoxidized soybean oil (ESBO) could be used as a primary plasticizer for PVC. They can be used to replace DOP up to 100%. Epoxidized

Fig. 8 TG and DTG curves for unfilled and fly ash (20 phr) filled stabilized PVC/ESBO (20 phr)/Ca/Zn stearates/with and without DBM (5 phr) compositions
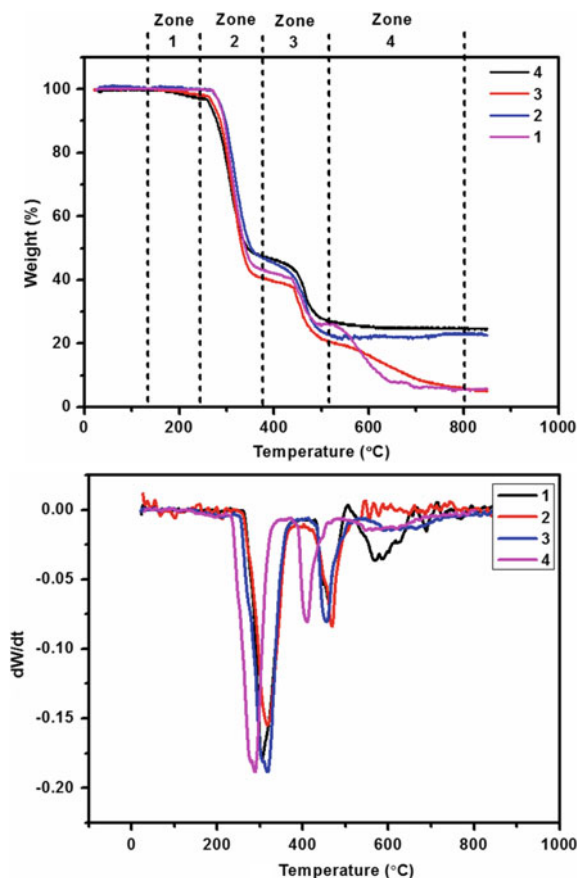
soybean oil indicated the excellent properties as a co-stabilizer for PVC when used in combination with the Ca/Zn stearates. The ternary system helped to improve plasticization effect and thermal stability of PVC compositions. Fly ash filled PVC system showed better thermal stabilization effect. Novel beta-diketones stabilizers along with fly ash filled PVC system showed better UV and thermal stabilization effect.
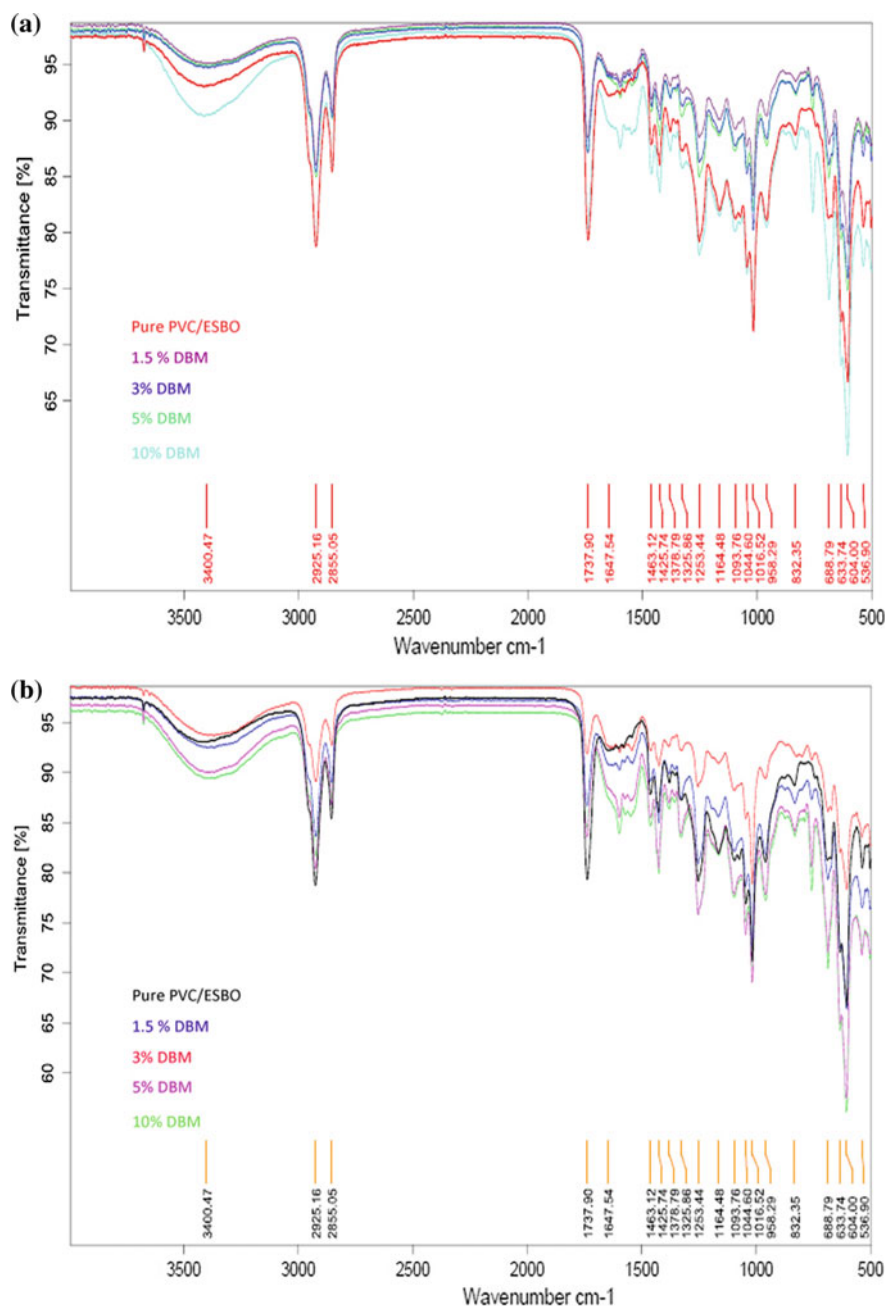
Fig. 9 a FTIR spectra of unfilled PVC/ESBO/Ca/Zn stearates/DBM (After 100 h accelerated QUV weathering condition). **b** FTIR spectra of fly ash filled PVC/ESBO/Ca/Zn stearates/DBM (After 100 h accelerated QUV weathering condition)

References

1. Brydson, J.A.: Plastics Materials, 7th edn. Butterworth-Heinemann, UK (1999)
2. Brebu, M., Vasile, C., RovanaAntonie, S., Chiriac, M., Precup, M., Yang, J., Roy, C.: Study of the natural ageing of PVC insulation for electrical cables. Polym. Degrad. Stab. **67**(2), 209–221 (2000)
3. Baltacioglu, H., Balkose, D.: Effect of zinc stearate and/or epoxidised soybean oil on gelation and thermal stability of PVC-DOP plastigels. J. Appl. Polym. Sci. **74**(10), 2488–2498 (1999)
4. Hollande, S., Laurent, J.: Study of discoloring change in PVC, plasticizer and plasticized PVC films. Polym. Degrad. Stab. **55**(2), 141–145 (1997)
5. Okieimen, F.E., Ebhoaye, J.E.: Thermal dehydrochlorination of PVC in the presence of rubber seed oil. Macromol. Mater. Eng. **206**(1), 11–20 (1993)
6. Martinez, J.G., Oliverio, S., Rodriguez, F., Sanchez, S.L., Ramirez, E.V., Allen, N.S.: Prediction of photoageing stability of plasticised PVC films containing UV-stabilisers. Polym. Degrad. Stab. **54**(1), 49–55 (1996)
7. Benaniba, M.T., Belhaneche-Bensemrab, N., Gelbard, G.: Stabilization of PVC by epoxidized sunflower oil in the presence of zinc and calcium stearates. Polym. Degrad. Stab. **82**(2), 245–249 (2003)
8. Turoti, M., Olayemi, J.Y., Adeniyi, J.B., Peters, O.: The photooxidative degradation of poly-(vinyl chloride)-2. The stabilising action of dibutyltin maleate and trisnitro (1,3-dihydroxyl-2-hydroxylmethyl-2-nitropropane) on PVC from ultraviolet light radiation. Polym. Degrad. Stab. **61**(2), 297–302 (1998)
9. Fang, L., Song, Y., Zhu, X., Zheng, Q.: Influence of lanthanum stearate as a co-stabilizer on stabilization efficiency of calcium/zinc stabilizers to polyvinyl chloride. Polym. Degrad. Stab. **94**(5), 845–850 (2009)
10. Howell, B.A., Besto, S.R., Meltzer, J.A., Smith, P.B., Debney, M.F.: Thermal degradation of epoxidized soybean oil in the presence of chlorine-containing polymers. Thermochimica Acta **166**(15), 207–218 (1990)

Multifunctional Compatibilizer for Polypropylene Blends with PMMA and EVA

A. M. Khare and **S. Radhakrishnan**

Abstract Recycling of plastics is very much hindered due to the process of segregation and sorting of individual polymer and also lack of compatibility between the different polymers. There is no single compatibilizer which can be effective for different pairs of polymer. If one could develop a multifunctional compatibilizer (MFC) that can be effective for a various range of polymers, the mixed plastics waste can be processed as such with minimal sorting/segregation. There are a number of reports on compatibilizer for specific pairs of polymer blends but there are practically no reports on single compatibilizer which works for different pairs of polymers. In the present studies, we have investigated the possibility of introducing different functional groups on a single polymer chain by chemical grafting. This multifunctional polymer has been used as compatibilizer for polypropylene blend with polymethyl methacrylate (PMMA) and ethylene vinyl acetate (EVA).

Keywords Polypropylene (PP) · Polymethyl methacrylate (PMMA)
Ethylene vinyl acetate (EVA) · Multifunctional compatibilizer (MFC)

1 Introduction

Plastic waste in the environment has been growing and posing challenges to product manufacturers as well as users. Polyolefin-based materials make up a great percentage of our daily single-life cycle plastic products [1]. Highest amount of plastic is consumed in its packaging application. Plastic-based packaging sector in India consumes about 35% of total plastic manufactured [2]. A number of studies have been undertaken within the last 15 years on various options for the treatment of post-consumer plastic waste, including techniques such as mechanical recycling,

A. M. Khare (✉) · S. Radhakrishnan
Maharashtra Institute of Technology, S124 Paud Road, Kothrud, Pune 411038, India
e-mail: anagha.khare@mitpune.edu.in

S. Radhakrishnan
e-mail: radhakrishnan.s@mitpune.edu.in

feedstock recycling, incineration with energy recovery, and landfilling [3]. Plastic waste consists of a variety of polymers like PET, LDPE, PVC, HDPE, PP, PS, PA, etc. To manage this waste, there are two options: either dispose in an environment which is not a good choice since degradation is a major problem or reusing and recycling which is a better option. In order to recycle properly, one needs the segregation of individual polymer from the mixed waste. To avoid segregation, blending is possible, provided right compatibilizer is used. Generally, compatibilizer is added to two polymer systems to modify the interfacial properties, e.g., PP-g-MA on Nylon-6. In this case, we will use multifunctional compatibilizer system for the mixture of plastic waste. Compatibility of blends may be improved by adding a third compatibilizing component or by adding suitable functionalized polymers capable of enhanced specific interactions and chemical reactions in reactive systems. This is important because compatibilization through a third component, acting as a bridge between the two incompatible phases, becomes necessary to stabilize the blend and to improve its mechanical performance [4]. There is an intense commercial interest in multiphase polymer blends or alloys because of the potential opportunities for combining the attractive features of several materials into one, or to improve decent characteristics of a particular material including recycled plastics. However, most blends are immiscible and have poor physical properties compared to their components. This problem is rooted in the lack of favorable interaction between blend phases. This leads to a large interfacial tension between the components in the blend melt which makes it difficult to deform the dispersed phase of a blend during mixing and to resist phase coalescence during subsequent processing. It also leads to poor interfacial adhesion in the solid state which frequently causes premature mechanical failure, depending on the nature of the applied stress and the failure mechanism [5, 6].

Recycling of plastics is very much hindered due to the process of segregation and sorting of individual polymer and also lack of compatibility between the different polymers. There is no single compatibilizer which can be effective for different pairs of polymer. If one could develop a multifunctional compatibilizer (MFC) that can be effective for a various range of polymers, the mixed plastics waste can be processed as such with minimal sorting/segregation. There are a number of reports on compatibilizer for specific pairs of polymer blends but there are practically no reports on single compatibilizer which works for different pairs of polymers. In the present study, we have investigated the possibility of introducing different functional groups on a single polymer chain by chemical grafting. This multifunctional polymer has been used as compatibilizer for polypropylene blend with polymethyl methacrylate (PMMA) and ethylene vinyl acetate (EVA).

2   Experimental

2.1   Synthesis of Multifunctional Compatibilizer (MFC)

Introducing malic anhydride (MA) and vinyl acetate (VA) are different functional groups on LLDPE polymer chain by chemical grafting to give multifunctional compatibilizer (MFC). In a reaction vessel, linear low-density polyethylene (LLDPE) samples were dissolved in xylene at 130 °C and then reacted with varying percentages (0, 0.5, 1, 1.5, and 2) of MA in the presence of dicumyl peroxide (0.2%). Melt flow index (MFI) was measured for the MA-grafted LLDPE so as to optimize the concentration at which the MFI decreases to original value. LLDPE grafted with 2% MA was used for further synthesis of MFC. In order to introduce another functional group, viz., VA, the MA-grafted LLDPE was further reacted by the addition of more amount of DCP (0.2%) + vinyl acetate monomer (2 and 3% of the LLDPE) as indicated in Scheme 1. The reaction was carried out at 130 °C for 4 h. The product was precipitated washed and dried. FTIR was run to check the grafting of both functional groups on LLDPE. MFC with MA + VA was used for further blending.

2.2   Blending of PP-PMMA and PP-EVA with MFC

The blending is carried out of PP-PMMA and also PP-EVA in solvent xylene using different percentages of MFC. PP and PMMA were dissolved in xylene at 130 °C in different proportions, to which was added MFC in different amounts ranging from 0, 5, 10, 15, and 20%. Similarly, PP and EVA were dissolved in xylene at 130 °C in different proportions, to which was added MFC in different amounts ranging from 0, 5, 10, 15, and 20%. The grafting reaction was confirmed by MFI as well as FTIR spectra. The peaks at 1418, 1303, and 1202 cm^{-1} and splitting of the –CH$_2$ peaks (Fig. 1) indicate grafting of MA and VA.

2.3   Determination of Cloud Point

The cloud point temperature is the temperature at which precipitation in the form of colloid from the solution starts. At this temperature, the solution becomes turbid/cloudy due to the formation of polymer-rich emulsion droplets. Cloud point (CP) is dependent on polymer concentration. The cloud point temperature indicates the extent of solubility and mixing property of polymer blends. Most of the polymer blends which form homogeneous and optically clear solution at elevated temperatures tend to separate and give a phase-separated system as the temperature drops down. CP is associated with lower critical solution temperature (LCST). CP indi-

Fig. 1 FTIR scan of PP-PMMA-BLEND+MFC

cates the soluble fraction of PP in the blend with PMMA and indicates the extent of compatibility due to the MFC.

In order to test the efficiency of the compatibilizer, polypropylene (PP) and PMMA were dissolved in xylene at 130 °C in different proportions (90/10 and 80/20) to which was added MFC in different amounts ranging from 0, 5, 10, 15, and 20%. In each case, the solution was slowly cooled and the cloud point (CP) was noted, i.e., temperature at which the blend is seen to precipitate in the form colloid or cloudiness appears in the solution. Cloud point indicates the soluble fraction of PP in blend with PMMA at room temperature and indicates compatibility due to the compatibilizer.

2.4 Optical Microscopy to Study the Effect of Compatibilizer (MFC)

Sample of each composition (with varying percentage of MFC) in very small quantity was taken on a glass slide. The glass slide was kept on hot plate. As temperature rises, the material on slide start to fuse and melts, and at this point the coverslip was placed over material on glass slide. Gently, the coverslip was pressed so as to distribute the melt uniformly and get a transparent and thin film layer. Later, the glass slide is allowed to cool. Then, cooled glass slides were marked with sample composition and observed under optical microscope with magnification of 400X. Phase structure and morphology detected by optical camera were displayed on computer screen.

2.5 Melt Flow Index of the Blend Composition of PP-PMMA with Varying Percentage of MFC

Melt flow indexer was used to find MFI at 190 °C using 5 kg load for the following compositions. For each composition, the percentage of MFC was varied from 0 to 20% to see the effect of MFC.

Composition I—PP-PMMA(80:20)+MFC
Composition II—PP-PMMA(90:10)+MFC
Composition III—PP-EVA(90:10)+MFC
Composition IV—PP-EVA(90:10)+MA

2.6 DSC to Study Effect of MFC on Crystallinity

DSC plots for system (PP+PMMA+MFC) with varying percentages of MFC were obtained using HITACHI DSC 7020. Heating cycle was from room temperature to 250 °C with nitrogen atmosphere.

3 Results and Discussion

After synthesis of multifunctional compatibilizer (MFC), FTIR was used to check the grafting of both functional groups on LLDPE. FTIR results of MFC showed (Figs. 1 and 2) the grafting done of MA and VA on LLDPE and also FTIR showed compatibility of MFC with the blends as there was shift of the individual major peaks seen in the IR of blends as shown in the following (Table 1).

Cloud point is dependent on polymer concentration. The cloud point temperature indicates the extent of solubility and mixing property of polymer blends. Most of the polymer blends which form homogeneous and optically clear solution at elevated temperatures tend to separate and give a phase-separated system as the temperature drops down. The compatibilizer increases the miscibility of the blends and lowers the cloud point.

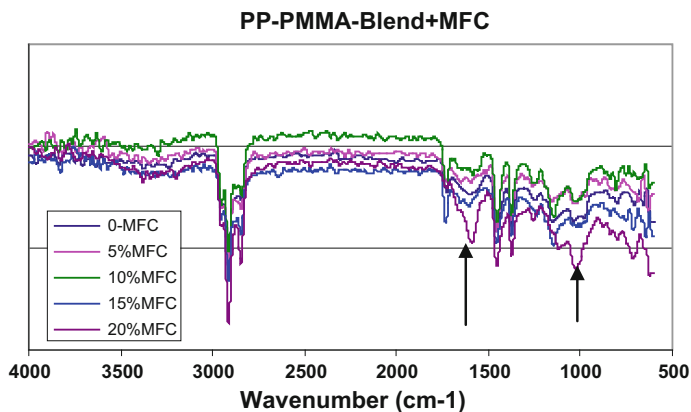The cloud point indicates the soluble fraction of PP in the blend with PMMA and indicates the extent of compatibility due to the MFC. The compatibilizer increases the miscibility of the blends and lowers the cloud point. Each blend solution having different % of MFC was slowly cooled, and the cloud point (CP) was noted, i.e., temperature was recorded at which the blend is seen to precipitate in the form of colloid or cloudiness as shown in Fig. 3. The compatibilizer increases the miscibility of the blends and lowers the cloud point as shown in Fig. 4.

Carl Zeiss microscopy having magnification range from 10X to 1000X was used to study the phase structure and morphology of the blends with the addition of MFC.
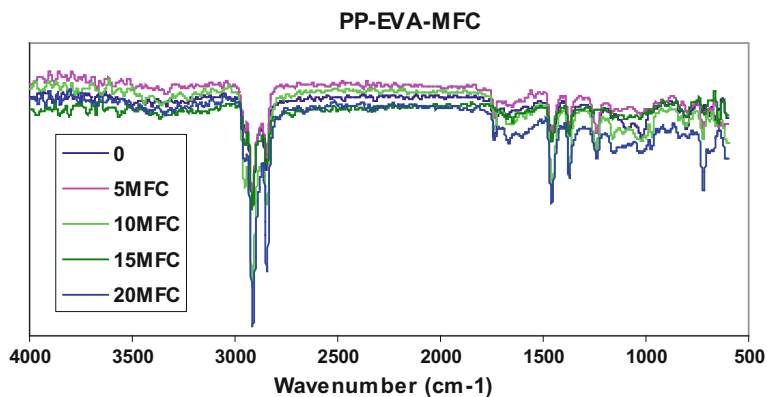
Fig. 2 FTIR scan of PP-EVA-BLEND+MFC

Table 1 Major peaks seen in the FTIR spectra of Blends + MFC

Blend PMMA	PP	VA	MA	PMMA	EVA	BLENDEVA
2936	2926	2920		2958	2922	2932
2912	2912				2852	2914
2843	2834	2850				
1725		1737	1782	1732	1739	1735
1650				1641		1650
1580						1579
1450	1440	1468	1458	1444	1465	1456
1368	1361	1371		1388	1371	1371
1245		1241	1227	1244	1242	1233
1138	1161	1181		1192		1136
1092	1099		1068	1062		1102
1012	995	1020			1020	1073
966	976		922	987		994
	837		899	843		966
801	806					786
786		720	756	754	720	718
701		610				614

Bold units indicate major changes noted in the spectra

The domain size is seen to reduce with increase in MFC giving better compatibility. Domains of dispersed phase which is PMMA are shown as black spots in the microscopic images, while crystalline PP forms matrix phase. It is seen that as concentration of compatibilizer increases, the domain size of PMMA as dispersed phase decreases as shown in Fig. 5.

Fig. 3 Cloud point showing the effect of compatibilizer

Fig. 4 Cloud point showing drop in cloud point due to increase in the miscibility of the blends
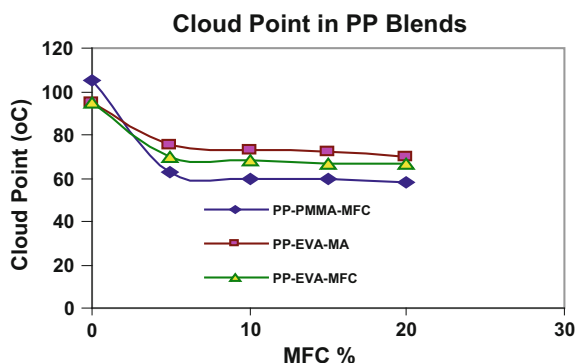
Table 2 MFI values in gms/10 min

S. No.	% MFC	MFI (gms/10 min)
1	0	3.02
2	5	4.35
3	10	3.28
4	15	4.36
5	20	4.85

Melt flow indexer was used to find MFI at 190 °C using 5 kg load for the blend composition with varying percentages of MFC. It was observed in each composition that MFI value increases (i.e., viscosity decreases) with increase in MFC percentage. Domain size decreases with increase in MFC leading to better melt flow and rise in MFI values as shown in Table 2.

DSC results for PP-PMMA with varying percentages of MFC showed a large dcrease in the intensity of melting peak of PP at 162 °C as shown in Fig. 6 indicating that the crystallinity is lowered by the addition of compatibilizer. There is distinct melting of the LLDPE component of MFC at 122 °C which increases with the increase of MFC as shown in Table 3. There is a large decrease in the intensity of melting peak of PP at 162 °C indicating that the crystallinity is lowered by the addition of
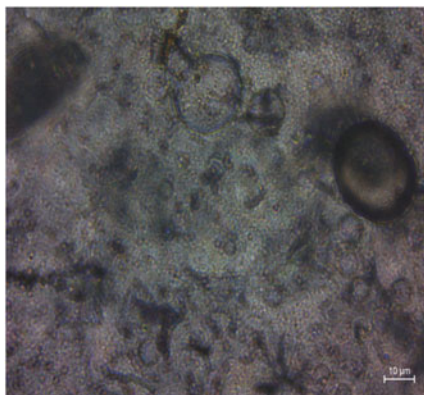
Image for PP + PMMA + 0%MFC
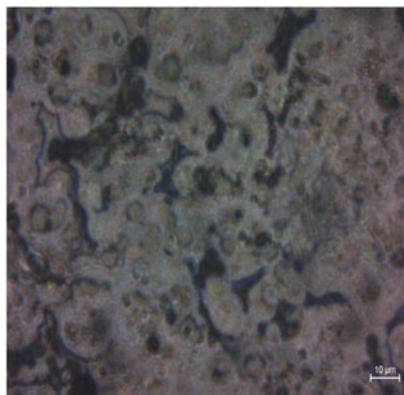
Image for PP + PMMA + 5%MFC
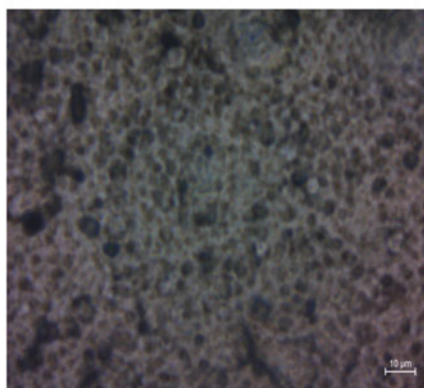
Image for PP + PMMA + 15% MFC
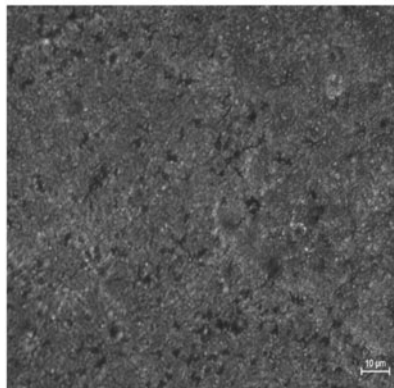
Image for PP + PMMA + 20% MFC

Fig. 5 Optical microscopy images with 400X

Table 3 Heat capacity values for different %MFC

S. No.	MFC %	122 °C Peak ΔH J/g	162 °C Peak ΔH J/g
1.	0	0	15.2
2.	5	0.78	14.3
3	10	3.03	12.4
4	15	2.28	11.8
5	20	4.04	7.77

compatibilizer. There is distinct melting of the LLDPE component of MFC at 122 °C which increases with the increase of MFC.
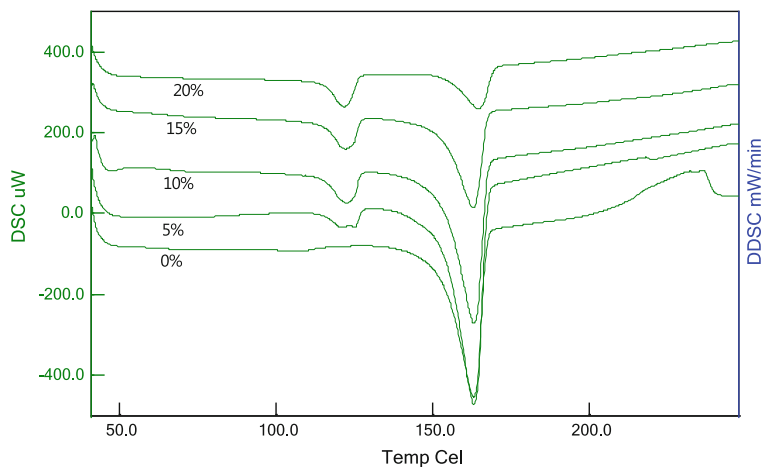
Fig. 6 DSC plot for PP-PMMA with varying percentages of MFC

4 Conclusions

We all are aware of the problems caused to environment due to plastic wastage for which recycling is the process used. Lot of efforts are required in the segregation of plastic during recycling. Multifunctional compatibilizer obtained can thus be used to compound many materials together. The functional groups on the MFC can be used to compound a variety of polymers like nylons, PET, PMMA, PVC, PP, LDPE, EVA, etc., which are generally the major part of the plastic disposed on routine basis. The added advantage offered besides cost saving by avoiding segregation is that the compounded material obtained shall have a combination of properties giving options to be used for various applications.

A. M. Khare and S. Radhakrishnan
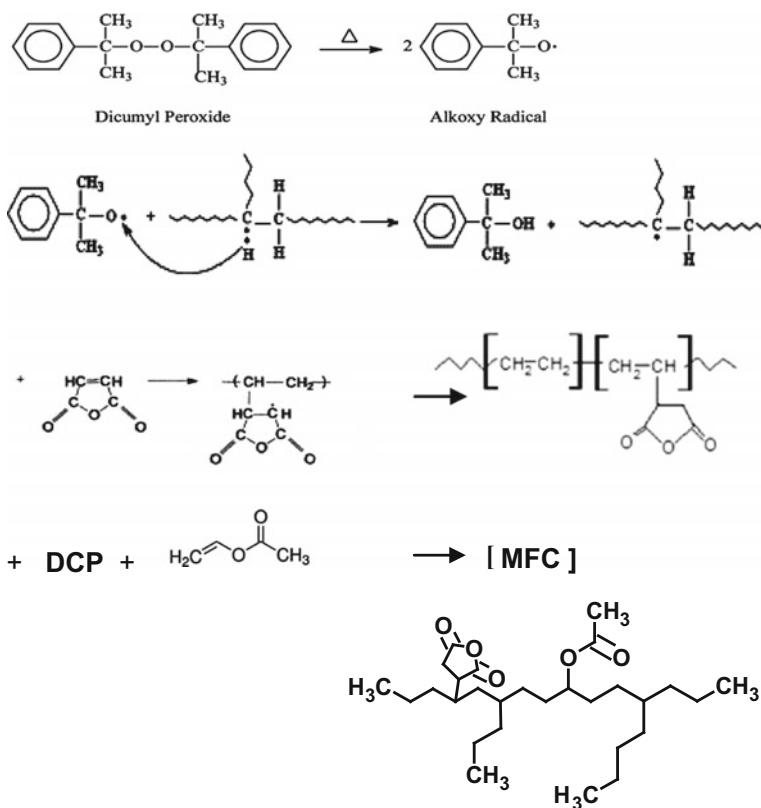
Scheme 1 .

References

1. Al-Salem, S.M., Lettieri, P., Baeyens, J.: Recycling and recovery routes of plastic solid waste (PSW): a review. Waste Manage. **29**, 2625–2643 (2009)
2. British Plastic Federation-Plastic industry in India, A BPF overview (2011)
3. Lazarevic, D., Emmanuelle, A., Bucklet, N., Nils, Brandt: Resources conservation and recycling. Plastic waste management in the context of a European recycling society: comparing results and uncertainties in a life cycle perspective **55**(2), 246–259 (2010)
4. Utracki, L.A.: Commercial Polymer Blends. Chapman & Hall, London (1998)
5. Folkes, M.J.: Polymer Blends and Alloys. Blackie, London (1993)
6. Paul, D.R., Barlow, J.W., Keskkula, H.: Encyclopedia Polymer Science and Engineering, 2nd edn, vol. 12, p. 399 (1988)

Development of Hybrid Composites and Joining Technology for Lightweight Structures

S. Deepak, K. P. Bhuvana, R. Joseph Bensingh, K. Prakalathan and S. K. Nayak

Abstract Advanced engineered composites are being increasingly in demand to increase the strength-to-weight ratio for structural performance in automobile and aerospace components for reducing fuel consumption and gas emission. Hybrid composites/laminates using lightweight metal and plastics are one of the emerging trends to create such structures. The number of methods for controlling the joints of metal and plastic interface in laminate structure has been opened for research. The present study endeavors toward the effect of surface modification of the metal skin on the adhesion strength between metal skin and polymer composite core. A laminate structure with aluminum skin and epoxy-expanded polystyrene (EPS) composite was developed. The surface modification on the surface of aluminum sheet was done using sand and glass bead blasting at various pressures (3, 4, 5, 6, and 7 bar). The effect of blasting pressure and blasting medium on the adhesion strength of the laminate structure was studied. The adhesion strength between the laminate structures was observed to be improved at the optimal blasting pressure of 5 bar blasted using SS sand.

Keywords Hybrid composite laminate · Surface roughness · Adhesion strength

1 Introduction

The hybrid lightweight material developed in the composition with capabilities of withstanding the mechanical stresses and deformation as well as plastic metal bonding with damage tolerance of sandblasted materials in various pressures and its surface roughnesses have been the interest of research for several decades. Hybrid structures are the need for today's lightweight developments in aerospace, auto-

S. Deepak (✉) · K. Prakalathan
Central Institute of Plastics Engineering & Technology, Chennai, Tamil Nadu, India
e-mail: naamphd@gmail.com

K. P. Bhuvana · R. J. Bensingh · S. K. Nayak
Advanced Research School for Technology and Product Simulation, Chennai, Tamil Nadu, India

motive, civil, and marine structural applications. Honeycomb-like sandwich architectures have been widely observed in natural materials, such as turtle shell [1] or beetle forewings [2], which comprise several layers including two exterior face sheets and inner cores. These nature-inherent materials are found to be effective to enhance the energy absorption capability and have gained growing popularity in high-performance applications for crashworthiness [3]. Researchers have developed lightweight hybrid composite structures with cellular expendable foams sandwiched between blasted metal face to experience better strength and impact energy absorption [4–10]. Aluminum is an attractive material due to its some excellent properties and potential applications of aluminum sheet resists corrosion from water, but can be attacked by acids and alkalis. In order to achieve the proper surface finish, the surfaces need to clean properly with strong oxidizing agents, and hence deterioration of properties can be prevented [11–16]. Aluminum sheet can be high blast pressure; it gives low surface roughness value due to molecular collision of blasting material and is used, as a low-pressure blast gives best result to protect metal skin damage. The optimized pressure is 5 bar for glass and SS sand material. In this case, an abrasive low molecular collision of suitable blast material in aluminum layer prevents surface damage of metal skin. Because of some of these excellent properties, aluminum sheet is used as skin for the developed sandwich structure.

Adhesive joining helps us to joint two dissimilar materials which are commonly used in aviation, automotives, and building industries. Adhesive joining involves bonding of two surfaces using a suitable binder, called adhesives [10]. The mixture of Bisphenol-A epoxy resin and aliphatic polyamine hardener gives low viscosity, hence nano form aerosil powder was added to improve the viscosity and used as matrix material for the sandwich structure. This matrix material will create bonding between the expanded polystyrene and the skin. Generally, polystyrene foam (Expanded polystyrene) is used in a wide variety of application. Thermoplastic polystyrene resin was soften using steam and expands up to 40 times of its actual volume through natural gas assistance. EPS of densities ranges from 8 to 48 kg/m^3 that are manufactured depending upon the desired physical/mechanical characteristics. Expanded polystyrene (EPS) is the most common and low-cost polymer used in commercial practice [17]. Harris and Fay et al. [18] have reported that the composite structure with thinner layer of adhesive exhibits better fatigue resistance at the joining [19]. In this paper, the bonding strength changes in pressure difference, surface roughness affects molecular collision, and surface damage occurs in blast process in two cases, with glass powder blast and stainless steel sandblast in the sandwich structure at room temperature with uniform compression in compression molding machine.

2 Experimental

2.1 Materials

The laminate was developed using aluminum (Al 1100) sheet of 0.3 mm thick as skin. Expanded polystyrene (EPS) procured from Supreme Petrochem Ltd., India reinforced with epoxy was used as a core. The sandwich layer was developed by mixing 10–12 g of hardener, aliphatic polyamine (Aradur HY 951) to bisphenol—A epoxy resin (Araldite LY556). 2.5% of aerosil powder was added in order to control the thixotropic characteristics of the epoxy resin and to obtain the homogeneous mixture of EPS and epoxy.

2.2 Methods

The bottom surface (in contact with the epoxy/EPS composite) was blasted using sand and glass beads at various pressures (3, 4, 5, 6, and 7 bar) in order to modify the surface. Colorless transparent glass beads of approximately 150-micron size are used to create abrasive blast along the surface. The surface roughness of aluminum surface was measured using Surface and Form measurement equipment (Make: Taylor Hobson, Model: Talysurf PGI Optics). The morphology of the blasted surface was obtained using vision measurement system (Make: OPUS, Model: 3020T) having the maximum lens magnification of 4.5× and the surface roughness was measured by surface and form measurement profilometer (Make: Taylor Hobson, Model: Talysurf PGI Optics) having resolution of 0.8 nm. The laminate structure was developed by sandwiching the epoxy/EPS composite between the aluminum sheets. The following flowchart depicts the sequence of process (Fig. 1).

The laminate structure was subjected to adhesion strength using universal testing machine (Instron 3382). The nature of failure was studied using scanning electron microscopy (SEM).

3 Results and Discussion

3.1 Optimization of Blast Pressure

The blasted surface was subjected to surface roughness measurement and vision measurement analysis in order to study the effect of blasting on the surface roughness and surface morphology. During blasting, due to the molecular collisions, the surface was subjected to abrasiveness and creates roughness. However, the blasting pressure plays a vital role to create the desired roughness. Figure 2 depicts the variation in
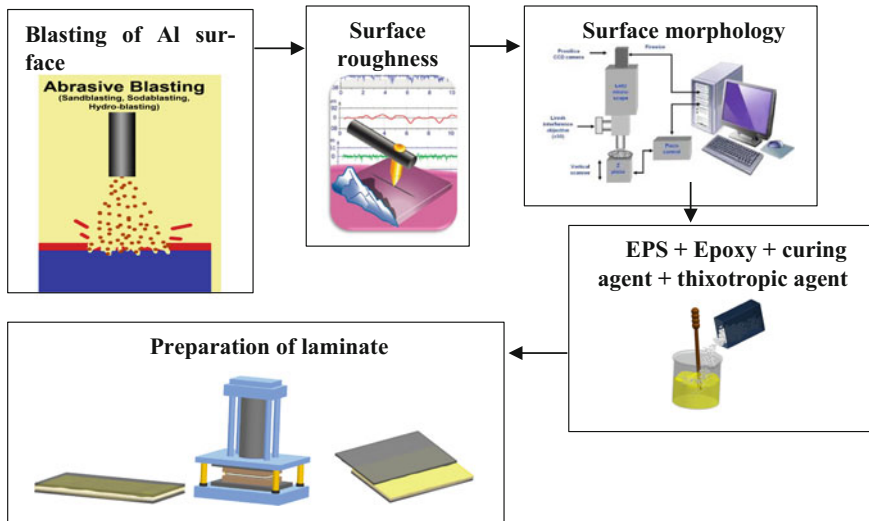
Fig. 1 Flowchart of sequence of process for preparation of composite laminate

Fig. 2 Surface roughness for different blasting pressures
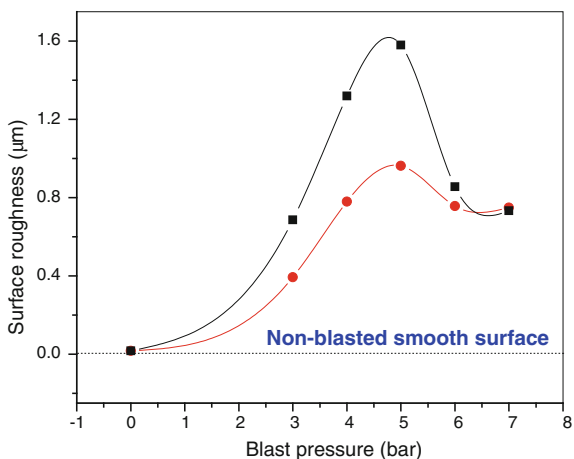
surface roughness for various blasting pressures. It is evident from the figure that the average surface roughness (R_a) increases with the increase of blast pressure. The surface roughness was observed to be increased up to 5 bar of blasting pressure while using both glass and SS sand, and further increase of pressure shows the decrease in surface roughness.

Figure 3 shows the 3D image of the surface roughened using glass and SS sand. From the image, it is evident that the surface blasted using SS sand creates higher roughness than the glass bead. This might be due to the higher hardness of the SS sand which creates more abrasion on the surface.

Glass bead blasted	SS sand blasted
Blasted @ 3 bar pressure	Blasted @ 3 bar pressure
R_a = 0.3935 µm	R_a = 0.6865 µm
Blasted @ 4 bar pressure	Blasted @ 4 bar pressure
R_a = 0.7794 µm	R_a = 1.3191 µm
Blasted @ 5 bar pressure	Blasted @ 5 bar pressure
R_a = 0.9627 µm	R_a = 1.5795 µm
Blasted @ 6 bar pressure	Blasted @ 6 bar pressure
R_a = 0.7569 µm	R_a = 0.8560 µm
Blasted @ 7 bar pressure	Blasted @ 7 bar pressure
R_a = 0.7486 µm	R_a = 0.7330 µm

Fig. 3 3D image depicting the surface roughness of the blasted Al sheet

The surface morphology of the blasted surface was also studied using 2D vision measurement. Figure 4 depicts the morphology of the blasted surface. From the image, it is clearly evident that the surface roughness up to 5 bar is found to be increasing with damaging the surface. However, the blast pressure above 5 bar creates the void and damages the surface of the aluminum sheet. Hence, 5 bar is the optimal blast pressure to create the maximum surface roughness without damaging the surface. Also, the surface occurs the damage failure at pressures higher than 5 bar.

3.2 Adhesion Strength

The test specimen of length 200 mm and width 25 mm was prepared to perform the adhesion strength test using universal testing machine. Adhesion between the aluminum and core was tested under 180° peel off tensile mode at the crosshead speed of 10 mm/min. The non-blasted surface does not adhere to the core surface. It was readily peeled out from the core without any adhesion. The removed skin surface was observed to be smooth, and no adherence failure was observed from the non-blasted surface. Figure 5 shows the adhesion strength as a function of blasting pressure. The test witnesses that the adhesion strength is found to be increased as the blast pressure increases up to 5 bar, and further increase of pressure reduces the adhesion strength. This is due to the damage failure on the aluminum surface during blasting at higher pressure.

3.3 Scanning Electron Microscopy

The delaminated surface during adhesion test was subjected to SEM analysis in order to study the nature of failure. Figure 6 shows the magnified SEM image of the delaminated surface of aluminum plate from the laminate structure. Figure 6a shows the SEM image of non-blasted laminate, which shows there is no adherence of core (Epoxy/EPS) on the surface of aluminum. Figure 6b shows the delaminated surface from the blasted aluminum skin at 5 bar pressure using SS sand. The image shows that the adherence failure was occurred at the interface due to the strong adhesion between the skin and epoxy/EPS composite.

4 Conclusions

A hybrid composite laminate was developed using aluminum skin and epoxy/EPS core. The surface of aluminum skin was modified through sandblasting in order to increase the adhesion strength between skin and core. The surface was modified through blasting at different pressures (3, 4, 5, 6, and 7 bar) using glass beads and
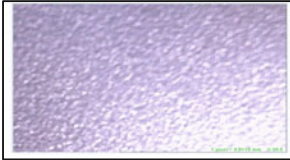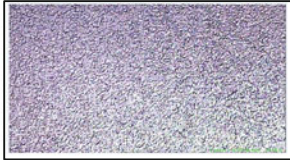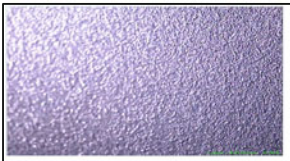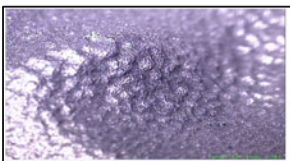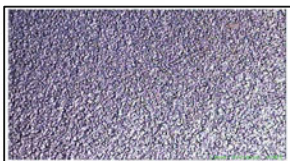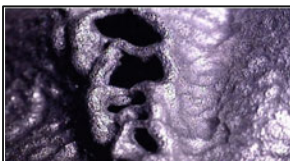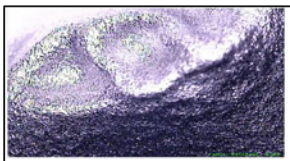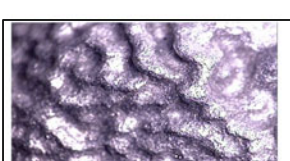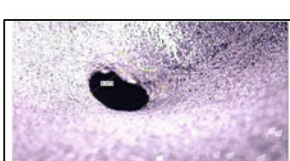
Glass bead blasted	**SS sand blasted**
Blasted @ 3 bar pressure	Blasted @ 3 bar pressure
Blasted @ 4 bar pressure	Blasted @ 4 bar pressure
Blasted @ 5 bar pressure	Blasted @ 5 bar pressure
Blasted @ 6 bar pressure	Blasted @ 6 bar pressure
Blasted @ 7 bar pressure	Blasted @ 7 bar pressure

Fig. 4 Surface morphology of the blasted surface

SS sand. The non-blasted surface does not adhere to the composite core; however, the adhesion strength between core and skin was gradually increased in the blasted surface as a function of blasting pressure. The optimal blastic pressure of 5 bar using
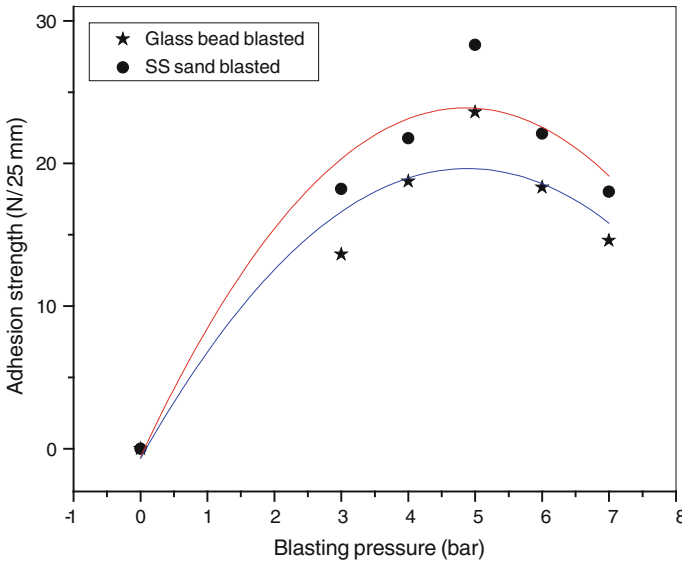
Fig. 5 Adhesion strength of the laminate as a function of blasting pressure
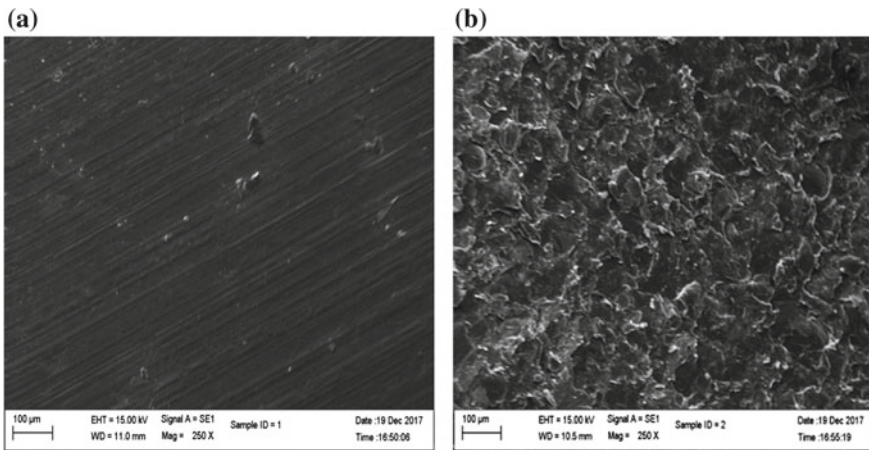
Fig. 6 SEM image of delaminated skin surface during adhesion test **a** non-blasted surface **b** blasted surface at 5 bar pressure using SS sand

SS sand possess better adhesion strength than glass beads, and this might be due to the higher hardness of the SS sand than glass bead. The higher blasting pressure causes the damage failure on the surface. SEM image also evidences that the surface modified using optimal blastic pressure exhibits the adhesion failure along the skin surface during delamination.

References

1. Rhee, H., Horstemeyer, M.F., Hwang, Y., Lim, H., Kadiri, H.E., Trim, W.: A study on the structure and mechanical behavior of the Terrapene carolina carapace: a pathway to design bio-inspired synthetic composites. Mater. Sci. Eng. C **29**(8):2333e9 (2009)
2. Chen, J., Gu, C., Guo, S., Wan, C., Wang, X.: Integrated honeycomb technology motivated by the structure of beetle forewings. Mater. Sci. Eng. C **32**(7), 1813e7 (2012)
3. Hou, S., Shu, C., Zhao, S., Liu, T., Han, X., Li, Q.: Experimental and numerical studies on multi-layered corrugated sandwich panels under crushing loading. Compos. Struct. **126**, 371e85 (2015)
4. Gibson, L.J., Ashby, M.F.: Cellular solids: structure and properties (2nd ed.). Cambridge University Press, Cambridge (1999)
5. Lu, G., Yu, T.Y.: Energy absorption of structures and materials. Wood head Publishing Ltd, Cambridge (2003)
6. Banhart, J.: Manufacture, characterisation and application of cellular metals and metal foams. Prog. Mater Sci. **46**(6), 559–632 (2001)
7. Wadley, H.N.G.: Multifunctional periodic cellular metals. Philos. Trans. R Soc. A Math. Phys. Eng. Sci. **1838**(364), 31–68 (2006)
8. Karlsson, K.F., Tomas, Å.B.: Manufacturing and applications of structural sandwich components. Compos. Pt. A-Appl Sci. Manuf. **28**(2), 97–111 (1997)
9. Zhu, F., Lu, G.: A review of blast and impact of metallic and sandwich structures. Load Struct 2007, EJSE Special Issue, pp. 92–101 (2007)
10. Yuen, S.C., Nurick, G.N., Theobald, M.D., Langdon, G.S.: Sandwich panels subjected to blast loading. In: Shukla, A., Ravichandran, G., Rajapakse, Y.D.S. (eds.) Dynamic failure of materials and structures, pp. 297–325. Springer, US (2010)
11. Saleema, N., et al.: A simple surface treatment and characterization of AA 6061 aluminum alloy surface for adhesive bonding applications. Appl. Surf. Sci. **261**, 742–748 (2012)
12. Kim, M.C., Yang, S.H., Boo, J.H., Han, J.G.: Surface treatment of metals using an atmospheric pressure plasma jet and their surface characteristics. Surf. Coat. Technol. **174–175**, 839–844 (2003)
13. Piva, E., Azevedo, E.C., Ogliari, A.O., Pilownic, K.J., Pinto, M.B., Camacho, G.B., et al.: Evaluation of experimental phosphate and sulfur-based primer bonding to metal casting alloys. Int. J. Adhes. **58**, 59–62 (2015)
14. Pantoja, M., Abenojar, J., Martínez, M.A., Velasco, F.: Silane pretreatment of electrogalvanized steels: effect on adhesive properties. Int. J. Adhes. **65**, 54–62 (2016)
15. Ho, B.J., Tsoi, J.K.-H, Liu, D., Lung, C.Y.-K, Wong, H.-M, Matinlinna, J.P.: Effects of sandblasting distance and angles on resin cement bonding to zirconia and titanium. Int. J. Adhes. **62**, 25–31 (2015)
16. Bang, C.S., Kim, J.G., Lee, D.G.: Performance improvement by glass fiber of adhesively bonded metal joints at the cryogenic temperature. Compos. Struct. **96**, 321–331 (2013)
17. Khodai, M., Parvin, M.: Pressure measurement and some observation in lost foam casting. J. Mat. Pro. Tec. **206**, 1–6 (2008)
18. Harris, J., Fay, P.: Fatigue life evaluation of structural adhesives for automotive applications. Int J Adhes. **12**(1), 9–18 (1992)
19. Grant, L., Adams, R., da Silva, L.F.: Effect of the temperature on the strength of adhesively bonded single lap and T joints for the automotive industry. Int J Adhes. **29**(5), 535–542 (2009)

Starch–Chitosan Blend Cross-Linked with Calcium Chloride

Jaya Maitra and Neena Singh

Abstract   In this research, different compositions of starch and chitosan blends are prepared by cross-linking with calcium chloride. Starch and chitosan ratios are fixed, i.e., 10:10 mL and the calcium chloride concentration varies between 0.8 and 2.4 mL (0.8, 1.2, 1.6, 2.0, and 2.4 mL). Totally five samples are prepared. Prepared blends were characterized by FTIR, SEM, and TGA Swelling behavior of the prepared blends is observed. The results showed that at 2.0 mL concentration of calcium chloride, the blend showed the highest swelling behavior. Antibacterial property of the same bend having 2.0 mL concentration of calcium chloride was studied against *Escherichia coli*.

Keywords   Blend · Chitosan · Cross-linking · Calcium chloride

1   Introduction

Chitosan and starch both are biodegradable, nontoxic, hydrophilic and biocompatible polymer [1]. Chitosan is a natural polysaccharide formed during the deacetylation of chitin in alkaline condition. It has antimicrobial property and excellent film-forming ability, which makes it suitable for obtaining antimicrobial films [2]. It has wide application in pharmaceutical, medical, and cosmetic industries due to its positive electrical charge which allows it to combine with negative electrical charge of skin and hair [3]. It is used in shampoos, hair gels, tooth paste, mouth wash, and skin care products [4]. Because of its biological properties, biodegradability, bioactivity, and biocompatibility, it has attracted much attention in the field of biomaterials, food coating, and packaging industry [5, 6]. The drawback associated with chitosan hydogels is relatively low mechanical strength due to its hydrophilic nature and greater solubility in acidic medium.

J. Maitra (✉) · N. Singh
Department of Applied Chemistry, School of Vocational Studies
and Applied Sciences, Gautam Buddha University, Greater Noida, India
e-mail: jaya@gbu.com

The other natural polymer is starch which is most abundant, cheap, biodegradable, and renewable, i.e., it can be regenerated from carbon dioxide and water by photosynthesis in plants [7–9]. It is a semi-crystalline polymer, composed of two repeating units of 1, 4-α-D-glucopyranosyl: amylose and amylopectin. Starch has different proportions of amylose and amylopectin ranging from about 10–20% amylase and 80–90% amylopectin [10]. It is hydrophilic in nature. The drawback associated with articles prepared from starch and water is their brittleness and sensitivity to atmospheric moisture [11].

Complimentary nature of chitosan and starch has attracted considerable attention in the areas such as biotechnology, biomedicine, food ingredients, and cosmetics [12, 13]. Hydrogels of chitosan and starch are widely used for various purposes such as drug delivery and tissue engineering systems [14].

2 Experimental Setup: Preparation of Starch–Chitosan Blends/Films

2.1 Polymers and Reagents

Chitosan from HiMedia, Acetic acid glacial, free aldehyde.A.R. from HiMedia, Calcium chloride from HiMedia, Starch, from Titan Biotech Ltd.

2.2 Preparation of Chitosan–Starch and Calcium Chloride Solutions

Stock of 1% (v/v) acetic acid aqueous solution was prepared by dissolving 1 mL acetic acid in 99 mL distill water. Chitosan solution (2% w/v) was prepared by dissolving 2 gm of chitosan in 100 mL of 1% acetic acid aqueous solution with the help of magnetic stirrer. 2% (w/v) starch solution was also prepared by dissolving 2 g of starch in 1% acetic acid aqueous solution. Solvent for the chitosan and starch was the same. Calcium chloride 2% (w/v) aqueous solution was prepared by dissolving the 2 mL calcium chloride in 100 mL distill water.

2.3 Preparation of Chitosan–Starch Films Cross-Linked with Calcium Chloride

Five different samples of starch and chitosan are prepared. All the samples contains fixed ratios of starch and chitosan, i.e., 10 mL each and change the volume calcium chloride, i.e., 0.8, 1.2, 1.6, 2.0, and 2.4 mL. Different ratios of calcium chloride are

added dropwise into starch and chitosan (10:10 mL) blend with continuous stirring at 600 rpm. After that, the blends are poured in the Petri plates and set aside at room temperature for drying. After drying, thin films are placed in hot air oven at 25–30 °C for 15 min and then placed at room temperature. Resulting dried films are stored in plastic poly bags.

3   Characterization

The surface morphology of the prepared film is observed by exploring the microstructures through the Scanning Electron Microscopy (SEM). Prepared films are also characterized by Fourier-Transform Infrared Spectroscopy (FTIR) and Thermogravimetric analysis (TGA).

3.1   Fourier-Transform Infrared (FTIR) Studies

FT-IR analyses of starch–chitosan-blended films cross-linked with $CaCl_2$ is measured in the wave number range 500–4000 cm^{-1} (Tables 1, 2, and 3).

FTIR spectrum of pure chitosan Fig. 1 (A1) shows a broad band in vibration spectrum due to stretching vibrations of OH groups in the range from 3744 to 3000 cm^{-1} [ν_{OH}], which are overlapped to the stretching vibration of N–H (3500–3000 cm^{-1}); and C–H bond in –CH_2 ($\nu_1 = 2920$ cm^{-1}) and –CH_3 ($\nu_2 = 2875$ cm^{-1}) groups,

Table 1 FTIR peaks positions for starch

S. No.	Peak (cm^{-1})	Functional group
1	3000–3600	– OH Str.
2	2800–3000	– CH_2 deformation
3	1642	Presence of water in the amorphous region of structure
4	1415	CH_2 bending and COO-Str
5	1344	C–OH bending and CH_2 twisting
6	1242	CH_2OH (side chain) related mode
7	1163	C–O and C–C str.
8	1094	C–OH bending
9	1067	C–H bending
10	930	α 1–4 glycosidic linkage
11	764	C–C str.
12	537	Skeletal mode of pyranose ring

Table 2 FTIR peaks positions for chitosan

S. No.	Peak (cm^{-1})	Functional group
1	3007–3744	– OH/NH vibrations
3	2880	– C–H stretching (reduced)
4	2356	Symmetric and asymmetric C–H vibrations
5	1650	1650–1660 cm^{-1} amide I/–NH$_3$+str
6	1560	N–H bending peak
7	1458	– H$_2$C–N– str. (amide group)
8	1260	C–N vibration
9	1154	C–O stretching bend
10	1097	C–O–C stretching/water molecule present in chitosan
11	1028	C–O–C stretching

Table 3 FTIR peaks positions for chitosan

S. No.	Peak (cm^{-1})	Functional group
1	2800	– C–H stretching symmetric and asymmetric
2	1759	– C=O interaction with Ca^{++}
3	1650–1660	Amide I Stretch in (CONH$_2$)
4	1458	– CONH str.
5	1260	C–N vibration
6	1154	C–O bend

respectively. A broad absorption in the range of 1654–1260 cm^{-1} [$\nu_{C=O}$] is due to the vibrations of carbonyl bonds of the amide group CONHR (secondary amide, $\nu_1 = 1645$ cm^{-1}) and vibrations of protonated amine group (δ_{NH_3}, $\nu_2 = 1574$ cm^{-1}). The presence of CH$_2$ can be also confirmed from the presence of bending vibrations of methylene and methyl groups were also visible at $\nu = 1375$ cm^{-1} and $\nu = 1426$ cm^{-1}, respectively. Absorption in the range from 1154 to 1000 cm^{-1} has been attributed to the vibrations of CO group. The band located near $\nu = 1154$ cm^{-1} is related to asymmetric vibrations of CO in the oxygen bridge resulting from deacetylation of chitosan. The bands near 1080–1025 cm^{-1} are attributed to ν_{CO} of the ring C–OH, C–O–C and CH$_2$OH. The small peak at ~890 cm^{-1} corresponds to wagging of the saccharide structure of chitosan.

Figure 1(A2) shows the FTIR spectra of starch. O–H stretching mode of starch was between 3000 and 3600 cm in the spectrum. The C–H stretching modes were observed in the 2800–3000 cm^{-1} region. Bands at 2922 and 2856 cm^{-1} depict the CH$_2$ deformation band of methylene hydrogen atom. On the other hand, a band at 1415 cm^{-1} is assigned to CH$_2$ bending or C–O–O stretching band of starch subunit.
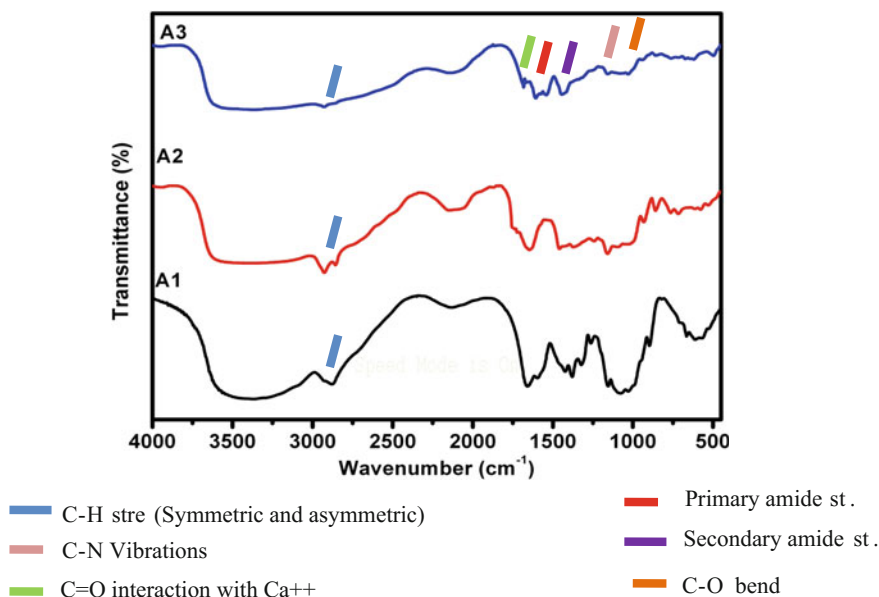
Fig. 1 FTIR of soluble chitosan (**A1**), starch (**A2**), and blend (**A3**)

Similarly, bands at 1259 and 1095 cm^{-1} can be assigned to CH$_2$OH (side chain) related and C–O–H bending mode, respectively. The band at 1743 cm^{-1} in the spectrum of starch was assigned to stretching vibrations of carbonyl groups ($\nu_{C=O}$). The appearance of band at 1643 cm^{-1} shows characteristic IR band of tightly bound H$_2$O molecules to the starch chain. The vibrations originating from the C–O–C of R-1,4 glycosidic linkages could be observed as a strong Raman band in the vicinity of 920–960 cm^{-1}. The major bands at 647 cm^{-1} and minor bands between 560 and 400 cm^{-1} can be attributed to the skeletal modes of the pyranose ring.

Figure 1(A3) shows the FTIR spectra of starch–chitosan blend cross-linked with calcium chloride. The peak at 2800 cm^{-1} for C–H stretching symmetric and asymmetric. The weak peak at about 1790 cm^{-1} is due to the C=O bonding of Ca^{++}. Peaks around 1650–1660 cm^{-1} show the C–N stretch of amide I. Peaks around 1458 cm^{-1} show the stretch of amide II. Peaks around 1238 cm^{-1} show the C–N vibrations. Peaks around 1157 cm^{-1} show the C–O bending. The peaks from 600 to 1400 cm^{-1} can be attributed to the C–O, C–C, and C–N bonding of chitosan and Ca^{++}.

4   Scanning Electron Microscopy

The scanning electron microscopy (SEM) of the prepared film from the blending of starch and chitosan and cross-linked with CaCl$_2$ have been analyzed by Carl Zeiss EVO-50.

Surface morphology of the films is characterized by SEM at the magnification of 10 μm. Figure 2 shows the SEM microstructures of starch film (A) and starch and chitosan blend cross-linked with calcium chloride (B). The surface of starch film is rough and contains non-dissolved lumps on the surface. Microstructure observations demonstrated that inclusion of chitosan concentration with the starch (for a blend) leads to the formation of fine surface. The surfaces of chitosan and starch blended film is homogenous and nonporous, it demonstrates the uniform distribution of chitosan and starch molecules all over the films, which predict the hydrogen bonds/ionic bonds between the functional groups of the chitosan and starch, i.e., –OH and –NH$_2$ groups in chitosan and –OH groups in starch (Fig. 2). The morphology of the starch–chitosan-blended film cross-linked with CaCl$_2$ demonstrated that addition of chitosan to the starch and cross-linking with CaCl$_2$ improved the surface morphology of the film and lessening the non-dissolved lumps on the surface of the film, which predict the interaction between chitosan, starch, and calcium chloride.

5   Thermogravimetric Analysis (TGA)

TGA thermograms of starch–chitosan blend cross-linked with calcium chloride (in the temperature range 0–500 °C under nitrogen) are shown in Fig. 3.

5.1   TGA of Pure Chitosan

Thermal details (TGA) of 75% deacetylated chitosan are shown in Table 4 and Fig. 3. Figure 3 shows that 10% decomposition of pure chitosan takes place at 130 °C while 20, 30, 40, 50, and 60% decomposition of chitosan takes place at 235, 275, 287, 320, and 415 °C, respectively.

Figure 3 also shows the two consecutive weight loss steps in the pure chitosan. The first weight loss was 12% in the range of 75–130 °C temperature, which was accountable for the loss of moisture content and demonstrated the hygroscopic nature of the chitosan. The second weight loss from 20 to 50% in the range of 235–320 °C, which was due to breakage of ether linkage in the chitosan backbone. The weight loss of 66% in the range of 415–500 °C predicts the thermal decomposition of glucosamone units.
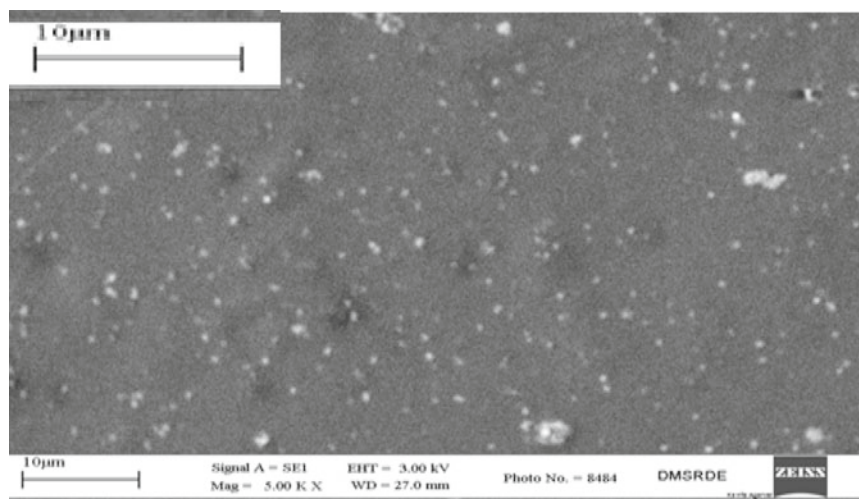
A=Starch film

B=Starch-Chitosan blend with CaCl₂

Fig. 2 Microstructures of starch (**a**) and blend with calcium chloride (**b**)

5.2 TGA of Pure Starch

Thermal details (TGA) of pure starch is given in Table 5 and Fig. 3. Figure 3 shows that 10% decomposition of pure starch takes place at 163 °C while 20, 30, 40, 50,
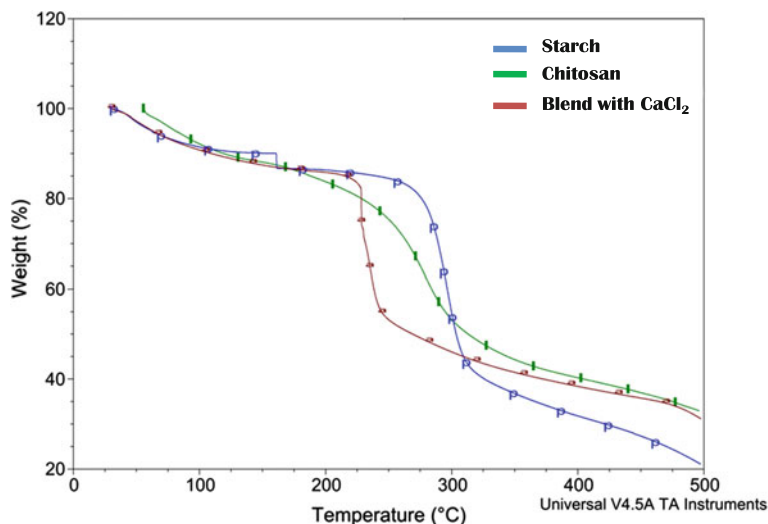
Fig. 3 TGA thermogram of pure chitosan

Table 4 TGA of pure chitosan

Percentage decomposition (%)	Decomposition temperature (°C)
10	130
20	235
30	275
40	287
50	320
60	415
66	500

60, and 70% decomposition of starch takes place at 285, 299, 302, 310, 330, and 415 °C respectively.

Figure 3 shows the three consecutive weight loss steps in the pure starch. The first weight loss was at 163 °C. Almost 10% weight loss at temperature 163 °C is accountable for the loss of moisture content and demonstrated the hygroscopic nature of starch. The second steep weight loss from 20 to 40% in the range of 285–302 °C is due to the dehydration of the saccharide rings and depolymerization. Degradation between the range of 310–330 °C is attributed to the degradation of starch components, i.e., amylase and amylopectin. Amylose degrades first because of its straight chain structure. A thermal reaction of condensation between hydroxyl groups and dehydration of neighboring hydroxyl group in the glucose ring (causing ring scission) starts at 300 °C. In the third stage, the weight loss was started at the temperature 415 °C onwards, and until the temperature 500 °C the weight loss was

Table 5 TGA of pure starch

Percentage decomposition (%)	Decomposition temperature (°C)
10	163
20	285
30	299
40	302
50	310
60	330
70	415
79	500

Table 6 TGA of chitosan–starch blend cross-linked with CaCl$_2$

Percentage decomposition (%)	Decomposition temperature (°C)
10	110
20	231
30	232
40	237
50	270
60	377
70	498

79% which predicts the thermal decomposition thermal decomposition of glucose residues.

5.3 TGA of Starch–Chitosan Blend Cross-Linked with CaCl$_2$

Thermal details (TGA) of chitosan–starch blend crosslinked with CaCl$_2$ are shown in Table 6. Figure 3 shows the 10% decomposition of chitosan–starch blend cross-linked with CaCl$_2$ takes place at 110 °C while 20, 30, 40, 50, 60, and 70 decomposition of starch takes place at 231, 232, 237, 270, 377, and 498 °C, respectively

Figure 3 shows the two consecutive weight loss steps in the chitosan–starch blend cross-linked with CaCl$_2$. The first weight loss was 10–16% at 30–225 °C temperature, which was accountable for the loss of moisture content and demonstrated the hygroscopic nature of the blend. Suddenly, a steep loss of 54.5 wt% in the range of 231–272 °C temperature was observed which was due to cleavage of the ionic linkage. The second weight loss was at 400 °C and the total weight loss until this temperature is 62%, which predicts the thermal decomposition of glucosamine residues. At the temperature 500 °C, the total weight loss was 68%.

Table 7 Rate of thermal decomposition (%) of chitosan, starch, and blend with calcium chloride

Temperature (°C)	Chitosan % weight loss	Starch % weight loss	Blend % weight loss
100	7	8	8
200	18	12	14
300	45	34	54
400	58	68	62
500	66	79	68

Table 7 and Fig. 3 represent the TGA thermogram details of pure chitosan, pure starch, and starch–chitosan (10:10) blend cross-linked with $CaCl_2$. Figure 3 shows the chitosan decomposes the least at 100 °C, i.e., 7% while blend and starch decompose 8% of their weight while at 500 °C chitosan decomposes 66% and blend decomposes 68% of its weight which shows that the blend is quite stable with respect to its parent material chitosan and starch.

6   Swelling Property

The % swelling ratios of the films are measured. The known weight, i.e., W_d of each film are immersed into the distill water at room temperature one hours. After one hour, films are removed from the distill water and are weighed, i.e., W_s. The % swelling ratio of the films are calculated by using equation,

$$E = \left[(W_s - W_d) / W_d\right] \times 100$$

where

E percent swelling ratio;
W_d weight of film in dry state;
W_s weight of film in swollen state.

The swelling behavior of starch and chitosan-blended films as shown in Fig. 4 increases as the calcium chloride ratio increase up to 2 mL of 2% $CaCl_2$ solution is added into starch–chitosan blend and it gives the highest swelling behavior at 2 mL concentration of calcium chloride as shown in Table 8 and Fig. 4. After that, suddenly the films containing 2.4 mL solution of calcium chloride shows decline in the swelling behavior.

Fig. 4 Swelling behavior of starch–chitosan films (cross-linked with calcium chloride)
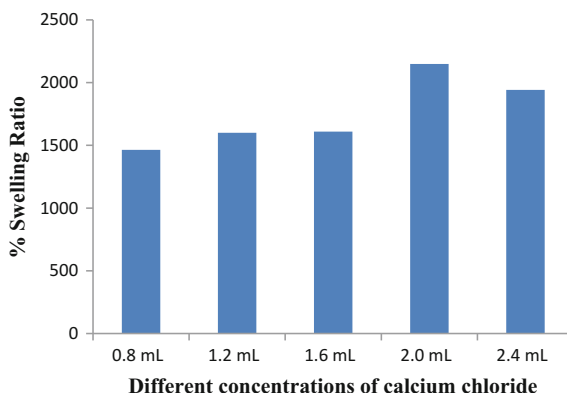
Table 8 % swelling ratio of starch–chitosan-blended films cross-linked with calcium chloride

St: Chi + CaCl$_2$ (mL)	Dry Wt. (g)	Wet Wt. (g)	Wet–Dry Wt. (g)	% swelling $E = \left[(W_s - W_d)/W_d\right] \times 100$
10:10 + 0.	0.072	1.126	1.054	1463.88
10:10 + 1.2	0.034	0.578	0.544	1600.00
10:10 + 1.6	0.064	1.094	1.030	1609.375
10:10 + 2.0	0.061	1.372	1.311	2149.18
10:10 + 2.4	0.024	0.490	0.466	1941.66

7 Antibacterial Assay

Disc diffusion method is used to check the antibacterial property of the blend. LB agar Petri plates are prepared by dissolving the 2.5 g of LB and 2 g of agar in 100 mL distill water. After autoclaving at 120 °C, 25 mL of solution was poured in one Petri plate in slight warm condition. Over night grown culture of *Escherichia coli* is diluted to 10^{-4} dilution and 20 µL of the diluted culture is spread on the Petri plate of size 90 × 15 mm. 6 mm sized discs are placed in the petriplate. 15 µL of the starch–chitosan cross-linked with CaCl$_2$ blend (2 mL of 2% CaCl$_2$ is applied on 6 mm size disc A. Petri plates are placed in incubator at 37 °C and zone of inhibitions are observed after 24 h.

7.1 Antibacterial Activity of Polymeric Blend

The ionic cross-linking of starch–chitosan-blend with cross-linker 2 mL of 2% CaCl$_2$ shows zone of inhibition of 6.4 mm in diameter, supporting the antibacterial activity of the blend against *E. coli* (Figs. 5 and 6).

Fig. 5 LB Agar plate of *E. coli*
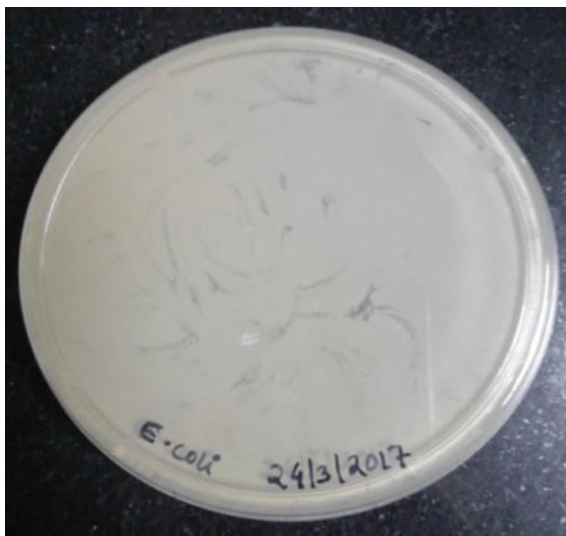
Fig. 6 Antibacterial activity of blend against *E. coli*

8 Conclusion

Present research is based on the development of starch and chitosan-based biodegradable films for the biomedical, pharmaceutical, and packaging purposes. The blend of starch and chitosan is cross-linked with calcium chloride is prepared. Prepared blend is characterized by Fourier-Transform Infrared (FTIR), Scanning Electron Microscopy (SEM), and Thermogravimetry Analysis (TGA). The results of FTIR studies demonstrated the peak at 1790 cm^{-1}, which shows the C=O bonding with Ca^{++} and the reduced peak intensity of the blend between the range 600 and

$1400 \mathrm{~cm}^{-1}$ which further confirms the interaction of Ca^{++} with C–O, C–C, and C–N of chitosan.

SEM microstructures studies of the blend demonstrating the smooth surface with reduced non-dissolved granules of the starch at the surface of the pure starch film further confirms the interaction between starch, chitosan, and $CaCl_2$. Thermogravimetry Analysis (TGA) explains the degradation of blend at the higher temperature, which again supports the blending of the constituents and supports that the blend is thermally stable.

Swelling behavior observation of the blend concludes the chitosan–starch blend cross-linked with $CaCl_2$ shows the highest swelling behavior at 10:10:2 mL concentration of starch, chitosan, and $CaCl_2$. The antibacterial evaluation of the blends also shows that the blend having 10:10:2 mL concentration is effective against *E. coli*.

References

1. Çetinus, S.A., Sahin, E., Saraydin, D.: Preparation of Cu(II) adsorbed chitosan beads for catalase immobilization. Food Chem. **114**, 962–969 (2009)
2. Dutta, P.K., Tripathi, S., Mehrotra, G.K., Dutta, J.: Perspectives for chitosan based antimicrobial films in food applications. Food Chem. **114**(4), 1173–1182 (2009)
3. Chenite, A., Buschmann, M.D., Wang, D., Chaput, C., Kandani, N.: Rheological characterization of thermogelling chitosan/glycerol-phosphate solutions. Carbohyd. Polym. **46**, 39–47 (2001)
4. Kordestani S.S., Bahrami, S.B.: Chitin polymer for medical applications. In: Proc. of the Int. Sem. On Polym. Sci. & Technology, ISPST-97, Iran Polymer Institute, Vol II, pp. 742–747 (1997)
5. Xu, J., McCarthy, S.P., Gross, R.A.: Chitosan film acetylation and effects on biodegradability. Macromolecules **29**, 3436–3440 (1996)
6. Niamsa, N., Baimark, Y.: Preparation and characterization of highly flexible chitosan films for use as food packaging. Am. J. Food Technol. **4**, 162–169 (2009)
7. Teramoto, N., Motoyama, T., Yosomiya, R., Shibata, M.: Synthesis, thermal properties, and biodegradability of propyl-etherified starch. Eur. Polym. J. **39**, 255–261 (2003)
8. Zhang, J.-F., Sun, X.Z.: Mechanical properties of PLA/starch composites compatibilized by maleic anhydride. Biomacromol **5**, 1446–1451 (2004)
9. Araújo, M.A., Cunha, A., Mota, M.: Enzymatic degradation of starch-based thermoplastic compounds used in protheses: identification of the degradation products in solution. Biomaterials **25**, 2687–2693 (2004)
10. Ramesh, M., Mitchell, J.R., Harding, S.E.: Amylose content of rice starch. Starch **51**, 311–313 (1999)
11. Jie, R., Hongye, F., Tianbin, R., Weizhong, Y.: Preparation, characterization and properties of binary and ternary blends with thermoplastic starch, poly(lactic acid) and poly(butylene adipate-*co*terephthalate). Carbohydr. Polym. **77**, 576–582 (2009)
12. Singla, A.K., Chawla, M.: Chitosan: Some pharmaceutical and biological aspects – an update. J. Pharm. Pharmacol. **53**, 1047–1067 (2001)
13. Kumari, K., Rani, U.: Controlled release of metformin hydrochloride through crosslinked blends of chitosan-starch. Pelagia Res. Libr. Adv. Appl. Sci. Res. **2**(2), 48–54 (2011)
14. Giri, T.K., Thakur, A., Alexander, A., Ajazuddin, Badwaik, H., Tripathi, D.K.: Modified chitosan hydrogels as drug delivery and tissue engineering systems: present status and applications. Acta Pharmaceutica Sinica B **2**(5), 439–449 (2012)

Titania–Gelatin-Based Nanohybrids: A Versatile Material for Removal of Organic Dyes (Congo Red, Malachite Green, Crystal Violet and Methylene Blue) from Aqueous Solution

Samjeet Singh Thakur and Ghanshyam S. Chauhan

Abstract Removal of organic and synthetic dyes from water bodies is an environmental concern of highest priority as these are stable to biodegradation. A new mesoporous nanohybrid material was synthesized from titania and gelatin backbone in the presence of tetraethoxysilane and sodium dodecyl sulphate via sol–gel technique. These hybrid materials are better adsorbents for eliminating organic dyes such as congo red (CR), malachite green (MG), crystal violet (CV), methylene blue (MB) from their aqueous solutions. High surface area of inorganic material (titania) and the high density of ammonium groups, and carboxylate groups of the bio-polymeric backbone (gelatin) can serve as a selective adsorbent for the exclusion of anionic acid dye (CR) as well as cationic basic dyes (MG, CV, MB). All the four dyes have followed Langmuir isotherm for adsorption. The rate determining studies have followed pseudo-second-order kinetics for all dyes. Experimental studies and their results hold good and are in agreement with kinetic and isotherm modelling. Hybrid materials made are further used for the photocatalytic degradation of dyes by direct exposure to the sunlight to five repeated cycles. The biocompatible and biodegradable nature of the gelatin–titania-based nanohybrid material has a prospective for the various applications in the different fields like water treatment, pH-responsive drug delivery and controlled release, since it has elevated adsorption capacity (>70 mg/g), high pH sensitivity, easy renewal, and good reusability. Hence, an adsorbent that can remove dyes by adsorption and at the same time has the photocatalytic ability is being described in this work.

S. S. Thakur (✉)
Department of Chemistry, RGM Govt. College JoginderNagar,
Mandi 175015, India
e-mail: samjeet23chem@gmail.com

G. S. Chauhan
Department of Chemistry, Himachal Pradesh University,
Shimla 171005, India
e-mail: ghanshyam_in2000@yahoo.com

Graphical Abstract

Silica Network from TEOS

Gelatin

Colloidal Titania

Silica based TiO$_2$-Gelatin
Hybrid Material (**H$_{11}$**)

Water+CR   Water+MB   Water+MG   Water+CV

H$_{11}$ **H$_{11}$**   **H$_{11}$**   **H$_{11}$**

Sunlight   Sunlight   Sunlight   Sunlight
hv   *hv*   *hv*   *hv*
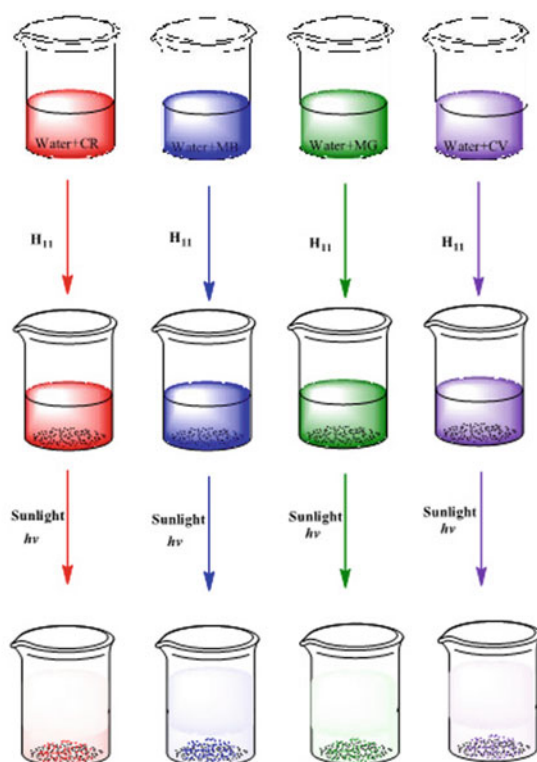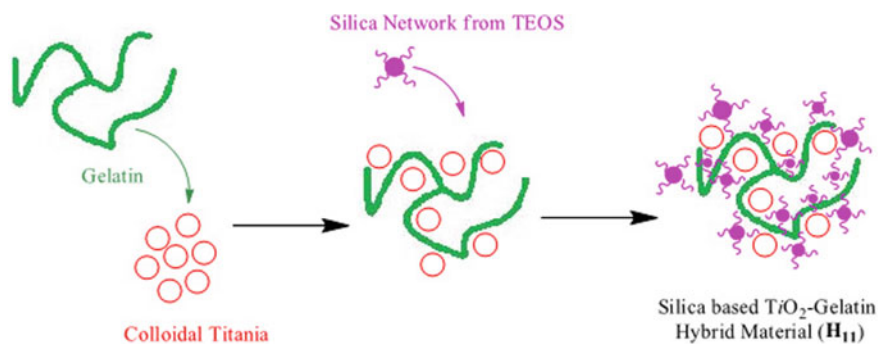
1 Introduction

Dyes are pollutants of most serious nature [1, 2]. They are discharged untreated in water bodies from the textile, paper and pulp mills, electroplating units and tanneries [3]. Mostly, dyes are toxic, carcinogenic, skin irritants and allergy-causing [4]. The treatment methods for dye removal have restrictions due to high operational cost and low efficiency [5]. Numerous conventional methods are reported elsewhere such as ion-exchange, oxidation, membrane-filtration or flocculation–precipitation for dyes elimination [6–12]. However, the efficiency of conventional wastewater management methods for various dyes is very low; organic and synthetic dyes are stable to chemical and biological treatment methods [13, 14]. Adsorption is an effective as well as an inexpensive method for the removal of coloured dyes from the wastewater [15–20]. A range of adsorbents were reported for the elimination of different dyes present in water include activated charcoal [21–29], bio-waste [30–37], clays [38–40], carbon nanotubes [41], silica–titania network [42], and hybrid polymer–silica networks [43–45]. The later are efficient adsorbents for various dyes.

Inview of above discussion, we are reporting a gelatin, silica and TiO_2-based new nanohybrid material with an objective to combine the elements of large dye adsorption capacity of gelatin and inherent photocatalytic degradation capability of TiO_2 in the nanohybrid material to have adsorption efficiency. Titania, photo-catalytically degrades dyes from their aqueous solution [42, 46–48]. Gelatin is a useful biopolymer that has many active functional groups available on its surface and it is effective in the removal of ionic species from their solutions [49–51]. The existence of two components along with silica results in the construction of a low-cost adsorbent which is an efficient one. Biopolymer-based new adsorbents are also reported in previous manuscripts for the elimination of different metal ions from their solution [51–55]. The four model dyes: congo red (CR), malachite green (MG), crystal violet (CV) and methylene blue (MB) were considered to examine the adsorption studies using the titania–gelatin-based nanohybrid material. It is also the first report regarding the investigation of nanohybrid material for the exclusion of these CR, CV, MG and MB organic dyes using such type of adsorbent material [56, 57]. The molecular formula and chemical structures of the model organic dyes are shown in Scheme 1. Different models were investigated and comparative studies were made for different kinetic and isotherm models. An attempt was also made to observe the photodegradation of these dyes in sunlight. To the best knowledge of the authors, there are very few reports available in the literature, where such an adsorbent have been used for the removal of cationic dyes (MB, CV, and MG) and anionic dye (CR) from aqueous solution.
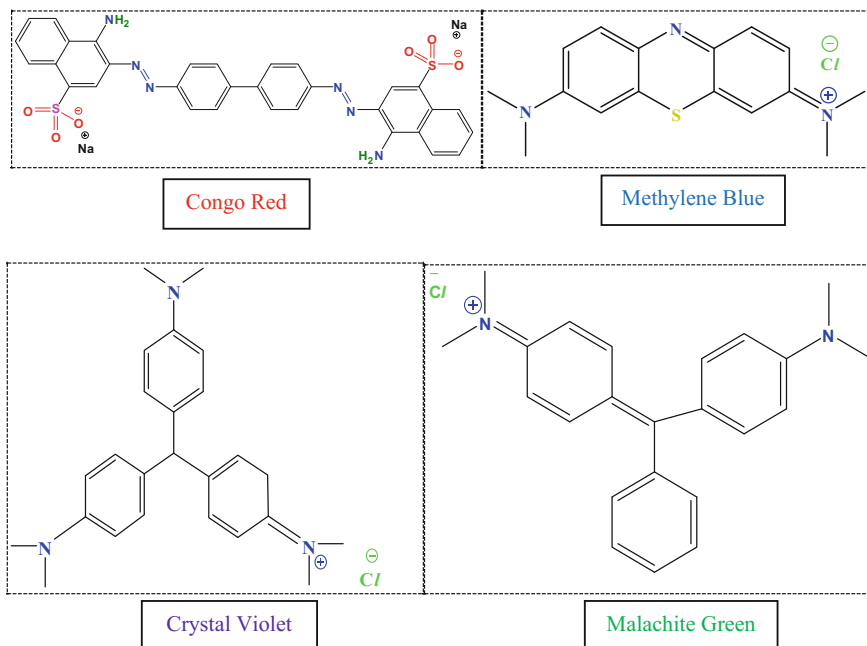
Scheme 1 Structure of model organic dyes

2 Experimental

2.1 Materials

Gelatin (Glaxo India Ltd., India), tetraethyl orthosilicate (TEOS, Sigma-Aldrich, Germany), 99.5% titania (Himedia Labs Pvt. Ltd., India), sodium dodecyl sulphate (SDS) suprapure, *n*-Hexane, NaOH, disodium phosphate (Na_2HPO_4), dihydrated monosodium phosphate ($NaH_2PO_4 \cdot 2H_2O$) (SD Fine Chem. Ltd., India), HCl (RANKEM, Faridabad, India), Congo red (CR), methylene Blue (MB), malachite green (MG), crystal violet (CV), (Merck, Schuchardt, Germany) were used as received and all were of analytical grade.

2.2 Synthesis and Characterization of Gelatin–Titania-Based Hybrid Material

A sol and gel method was used to synthesize titania–gelatin-based hybrid materials via a two-stage process by amending a previously reported protocol [51, 58]. Herein, gelatin–titania-based mesoporous bio-hybrid nanomaterial was prepared with the

emulsion method in two stages where the composition of gelatin and TiO_2 is 1:1 (weight ratio) 2.5 g each. 10 g solution of TEOS (by weight) and 20 mL of *n*-hexane were mixed in a flask followed by 0.1 mL of HCl (5% by weight) and then the whole content was stirred for 30 min. Oil in water (o/w) emulsion was formed by mixing 140 mL *n*-hexane, 50 mL doubly deionized water, 5% HCl (by wt.), and 150 mg of sodium dodecyl sulphate. It followed the addition of 2.5 g each of gelatin and TiO_2 to the emulsion and the whole contents were stirred for about half an hour before mixing with TEOS solution. The mixture was kept uninterrupted for 120 h at 37 °C. The nanoparticles get precipitated from the solution and these were successively washed with acetone, methyl alcohol and finally with water. As-prepared sample, H_1 was calcined at 550 °C to obtain calcined material, H_{11}.

2.3 Characterization of Titania and Gelatin-Based Hybrid Material

Various characterization techniques and methods were used for structural, chemical and mechanical studies of the as-synthesized and calcined material. Elemental analysis, FTIR spectroscopy, XRD analysis, SEM-EDS, TEM and BET analysis was also done. Elemental analysis was recorded using Elemental Analyzer vario EL CHNS. FTIR spectra were taken in transmittance mode using KBr pellets by Nicolete 5700. Bruker D8 ADVANCE Diffractometer (Cu–$K\alpha$ radiation with $\lambda = 1.54$ Å, 40 kV, 30 Am) was used for XRD patterns. The range of diffraction angle (2θ) was studied from 5° to 70°. SEM-EDS method was used to study the surface morphology of material, where SEM was recorded with Leica Cambridge Stereoscan 440 SEM model and EDS were recorded on SEM QUANTA 250 D9393, which provides the % weight of elements (C, N, O and Si) from the EDAX data. Transmission electron microscopy (TEM) images were taken using Philips CM 200 (and it was operated with a Cu electron source (maximum accelerating voltage 200 kV, resolution: 2.4 Å, magnification range 5–300X). SMART SORB 92/93 was used as BET surface area analyzer for pore size and surface area of materials. The hybrid material was degassed at 100 °C just before the measurements. Eutech 20 (pH metre) was used to determine the pH of the solution.

2.4 Parameters Optimization of Adsorption Experiments

Only H_{11} was used for adsorption studies. Stock solutions (10, 20, 30, 40 and 50 ppm) were prepared in distilled water. The standard curves were obtained at respective wavelengths, already by using UV-Visible spectrophotometer (Photolab 6600) for the known concentrations (1–50 ppm). Batch experiments for dye solutions with the 50 mL@150 rpm were carried out. Effects and variation of different physicochemical

adsorption parameters were optimized. It includes the optimization study of time variation from 30 to 840 min, temperature variation from 20 to 45 °C, pH change from 2.0 to 9.2 and initial dyes solution concentration from 10 to 80 ppm using 50 mL (stock solution) of dyes per 100 mg of the adsorbent material. The strength of the unadsorbed dyes solution was determined at 481 nm for CR, 595 nm for MG, 598 nm for CV, and 628 nm for MB by using UV-Visible spectrophotometer. The adsorption isotherm studies were plotted between the equilibrium adsorption capacity (q_e) and the equilibrium concentration of the leftover dyes in the solution (C_e). Therefore, q_e was calculated by the formula as given below in the Eq. (1):

$$q_e = \frac{C_o - C_e}{W} \times V \tag{1}$$

where q_e is expressed in mg g^{-1}, the initial (C_o) and equilibrium (C_e) are dye concentrations expressed in parts per million (ppm), V is volume taken in litres (L) and W is the amount of H$_1$ or H$_{11}$ in g. The percentage uptake (P$_u$) was calculated from Eq. (2) as given below:

$$P_u = \frac{C_o - C_e}{C_o} \times 100 \tag{2}$$

For kinetic studies 0.1 g of H$_1$ or H$_{11}$ and 50 mL of 20 ppm dye solution were taken, which was followed by the agitation for definite time periods ranging from 30, 60, 120, 240, 360 up to 840 min. Maximum adsorption capacity (MAC) of these materials was also evaluated at the optimum physicochemical parameters by using the same materials repeatedly for multiple cycles.

2.5 Reusability Studies

Reusability studies of the hybrid materials were carried out for five repeated adsorption and desorption cycles consecutively using 50 ppm dye solution per 0.1 g of H$_1$ and H$_{11}$ at 7.0 pH, for 360 min at 35 °C with agitation speed@150 rpm. The materials (H$_1$ and H$_{11}$) adsorbed with dyes were detached from the solution by filtration process and then it was mixed to the stripping solution of N/10 sodium hydroxide (NaOH) 20 mL followed by constant stirring@150 rpm for half an hour at 35 °C and the final dye concentration was measured. The hybrid material was washed with the distilled or deionized water after each cycle, and used in the successive cycle.

2.6 Kinetic Modelling

Evaluation of mechanism and kinetics of the adsorption process was performed by using four different kinetic models. The linear form of pseudo-first-order equation was used [59] in which slope and intercept provide the value of k_1 and q_e when $\log(q_e - q_t)$ was plotted against t:

$$\log(q_e - q_t) = \log(q_e) - \frac{k_1}{2.303} \cdot t \tag{3}$$

The linear form of the pseudo-second-order equation was used, wherein the plot of t/q_t against t provides values of k_2 and q_e from slope and intercept, respectively [60].

$$\frac{t}{q_t} = \frac{1}{k_2 q_e^2} + \frac{1}{q_e} \cdot t \tag{4}$$

Value of β was found from the slope of the linear form of the Elovich equation in [61] and α from the intercept when q_t was plotted against $\ln(t)$ as follows:

$$q_t = \frac{1}{\beta} \ln(\alpha\beta) + \frac{1}{\beta} \ln(t) \tag{5}$$

Weber–Morris Model [62] explains the intraparticle diffusion process and herein the diffusion constants "a" and k_{id} values were obtained from the slope and intercept when $\log q_t$ was plotted against $\log t$ and represented by the Eq. (6):

$$\log q_t = \log k_{id} + a \, \log(t) \tag{6}$$

2.7 Adsorption Isotherm Modelling

Three isotherm models, specifically Langmuir, Freundlich, and Redlich—Peterson were tested for q values as dye concentration function. According to Langmuir adsorption isotherm, all the adsorption sites have a uniform affinity for an adsorbate, meaning thereby that the adsorbent has homogeneous surface [63]. Its linear form, Eq. (7), yields K_L and q_m from slope and intercept of a plot of $1/q_e$ against $1/C_e$ as represented:

$$\frac{1}{q_e} = \frac{1}{K_L q_m} \cdot \frac{1}{C_e} + \frac{1}{q_m} \tag{7}$$

Heterogeneous or multilayer adsorption phenomenon is proved by Freundlich isotherm [64]. From its linear form plot of $\ln q_e$ versus $\ln C_e$ constants, n and K_F were obtained from the slope and intercept.

$$\ln q_e = \ln K_F + \frac{1}{n} \cdot \ln C_e \tag{8}$$

The linear dependence on ion concentration as illustrated by the nonlinear form of the equation presented as

$$q_e = \frac{AC_e}{1 + BC_e^g} \tag{9}$$

where its linear form obtained is as given below:

$$\ln\left(A\frac{C_e}{q_e} - 1\right) = g \ln C_e + \ln B. \tag{10}$$

Equation (10) provides isotherm constants, A, B and g. Adsorption follows the Langmuir and the Freundlich isotherm when the values of g is 0 or 1, respectively, and g ($0 \leq g \leq 1$) characterizes three parameter isotherm known as Redlich–Peterson adsorption isotherm [65, 66]. Correlation coefficient, R^2 was determined using a method where a series of values for A in the linear regression of ln (C_e) on ln $[A(C_e/q_e) - 1]$ were also determined and the best value of A was selected and which further helps to yields the most 'optimized' R^2 value.

2.8 Thermodynamic Studies

The spontaneous or non-spontaneous adsorption processes are always concluded from the Gibbs free energy change ($-\Delta G°$) [67]. Equilibrium constant, K_c, was determined from the formula given below:

$$K_c = \frac{C_e}{C_o} \tag{11}$$

where C_e and C_o are the dye solutions defined earlier and $\Delta G°$, $\Delta H°$ and $\Delta S°$ are related to the K_c as

$$\Delta G° = -RT \ln K_c \tag{12}$$

where $\Delta G°$ is the standard free energy change (joules/mol), R universal gas constant (8.314 J/mol K), and T is the temperature in kelvin.

$$\ln K_c = -\frac{\Delta H°}{RT} + \frac{\Delta S°}{R} \tag{13}$$

Slope and intercept obtained from the plot of ln K_c against $1/T$, give values of $\Delta H°$ and $\Delta S°$.

Table 1 Elemental analysis

S. No.	Hybrid materials (sample codes)	Weight (mg)	C/N ratio	CHNS analysis			
				Carbon %	Nitrogen %	Hydrogen %	Sulphur %
1	H_1	5.1370	0.496	1.747	3.525	1.794	0.000
2	H_{11}	4.9630	0.046	0.159	3.493	1.404	0.000

3 Results and Discussion

Blending of gelatin and TiO_2 via two-stage sol-gel method, wherein TEOS was a crosslinking agent, leads to a new hybrid material (H_1). A new functional hybrid material (H_{11}) was generated upon calcination of as-synthesized hybrid material (H_1) at 550 °C. Calcination process has liberated the moisture and also removed the unbounded material and therefore, further improved the surface properties of H_1 and H_{11}. The hybrids were characterized using various techniques for the verification of the material. It was then applied as an adsorbent for the uptake of CR, MG, CV and MB dyes [68].

3.1 Characterization Studies

Elemental analysis (CHNS) was recorded and it confirms the hybrid synthesis with gelatin as one of the components (Table 1). Presence of around 3.5% N in both the samples again provides evidence that gelatin is present on both the samples. Thermal degradation studies reveal that the synthesized hybrids are more stable than gelatin (Table 2). The hybrid series resulted in 24.3 and 24.2% weight loss for H_1 and H_{11}, in which more than 15% loss is in the second stage up to 400 °C (Fig. 1). It is the only free gelatin component or the non-bonded material which is primarily lost from the hybrids below 500 °C. The as-synthesized material lost more weight than the corresponding calcined material between 100 and 500 °C, which may have impurities present in addition to gelatin. These interpretations are important to synthesize modified hybrid materials with well-controlled composition and the property profile. These degradation stages indicate that the structure of gelatin changed after synthesis.

FTIR spectrum reveals that pure gelatin absorbs at 3600, 2925, 1740 and 1103 cm^{-1} due to N–H, C–H, C $=$ O and C–O–C stretching mode, respectively [49]. Gelatin spectrum also has two bands at 1684 cm^{-1} for C $=$ O stretching of secondary amide, and 1555 cm^{-1} for –NH bending. The FTIR spectra of the gelatin–titania hybrid (H_1 and H_{11}) have broadband around 3450 cm^{-1} that corresponds to –NH$_2$

Table 2 TGA analysis of hybrid materials at three different stages

TGA (% loss)						
S. No.	Hybrid material		100 °C	400 °C	>700 °C	Total loss
1. 2.	Modified Gelatin–Ti-tania hybrid	H_1	4.7	14.4	5.2	24.3
		H_{11}	6.5	10.2	7.5	24.2
3.	Gelatin		9.49	64.28	13.96	87.73

(2°) stretching (Fig. 2). The peaks between 1300 cm^{-1} and 1050 cm^{-1} are mostly of C–O stretching, whereas two amide bands present in gelatin are reduced to only one peak at 1640 cm^{-1} (C=O stretching of secondary amide and NH bending). Peaks are present below 800 cm^{-1} due to out of plane –NH deformation at about 780 cm^{-1}, and Si–O stretching is at 700–400 cm^{-1}. One additional absorption band at 1097 cm^{-1} is due to Si–O–Ti, and those below 500 cm^{-1} are assigned to Ti–O–Ti [69]. Thus, the modification of gelatin and formation of the network or hybrid materials comes from the presence of additional absorption peaks of functional groups of gelatin and two inorganic components introduced in the network formed. Furthermore, network formation is supported by the shift in the position and intensities of peaks on backbones in different networks. FTIR spectra of the dye-loaded gelatin–titania-based hybrid materials (Fig. 3). Therefore shift in the bands and presence of additional peaks, especially one broad and less intense near 1630 cm^{-1} due to aromatic rings of dye and a sharp band near 1095 cm^{-1} provides evidence of dye adsorption.

XRD analysis provides information on the structural morphology of these materials. When the diffraction patterns are plotted between intensities of the diffracted X-rays against angle (2θ), FWHM can be calculated therefrom. XRD spectra of gelatin–titania hybrid materials (Fig. 4). Both H_1 and H_{11} have crystalline nature with sharp and high intensity (1609 and 2645) peaks at 2θ 25.34 and 25.37, respectively. Both the materials show exactly the same XRD pattern, however, the latter is more crystalline with the intense peaks due to the intense alignment of the gelatin chains. The crystallite size was calculated using the Scherer formula $D_p = \frac{0.94}{\beta_{1/2} \cos\theta} \lambda$, comes out to be 0.339 nm less than a nanometer (<1 nm) with lattice strain 0.4920 for both H_1 and H_{11}.

Samples were analysed for elemental composition using SEM–EDX studies and their % composition by weight and % atoms were found (Table 3). SEM images of H_{11} after of dye adsorption are presented in Fig. 5. A close observation from the SEM image makes quite evident that the adsorbent exterior is fairly rough whereas adsorption of different dyes leads to smoothness on the surface of particles due to the filling of available spaces of the material by the dye molecules.

This also provides physical evidence of the adsorption process. Transmission electron microscopy (TEM) images of hybrid particles reveal that the size of these
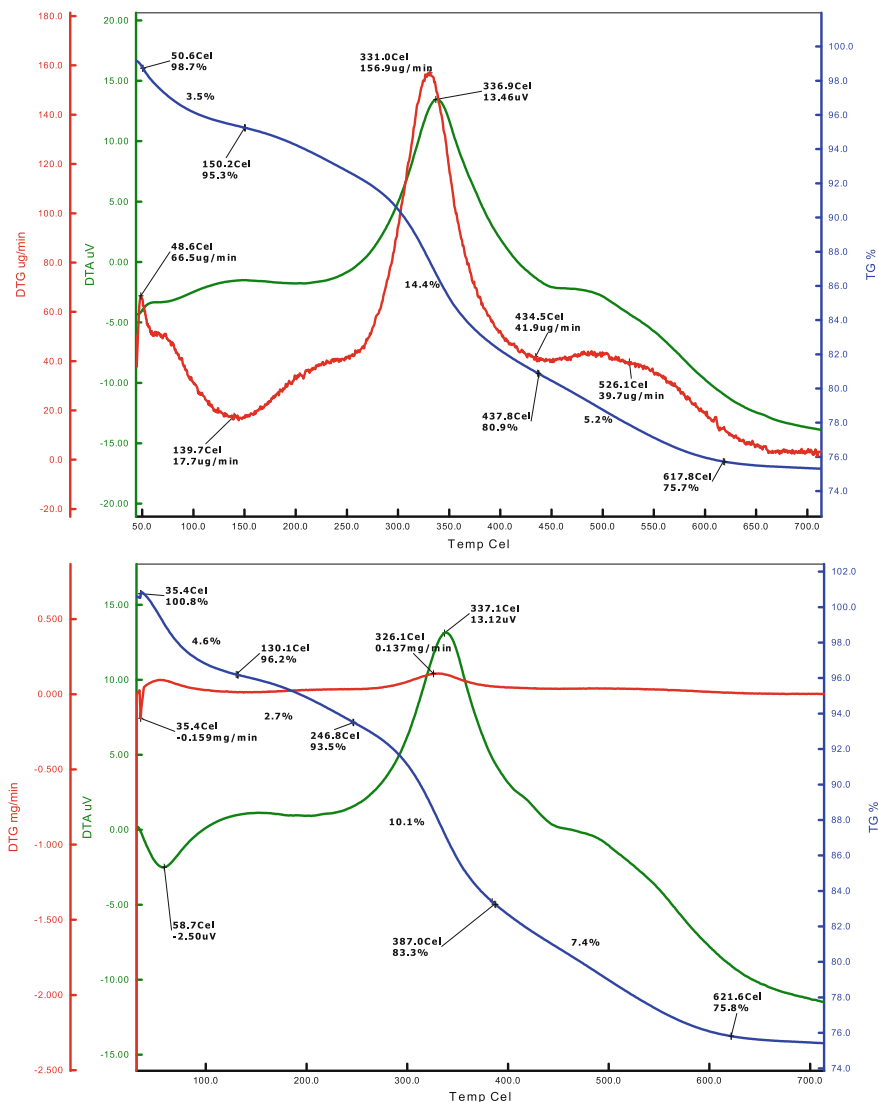
Fig. 1 TGA of Hybrid Material (H_1 and H_{11})

materials is in 50–100 nm range (Fig. 6). TEM images reveal that particles are well dispersed and have uniform shape and size.

BET surface area analysis was carried out by N_2 physico-sorption at a liq. N_2 temperature (Table 4). Pore size was calculated from equation $D = \frac{6 \times 10^3}{SA \times Density}$ nm. The calcination process affected the properties of as-synthesized materials with a positive effect on the surface properties. It decreased pore size whereas increased
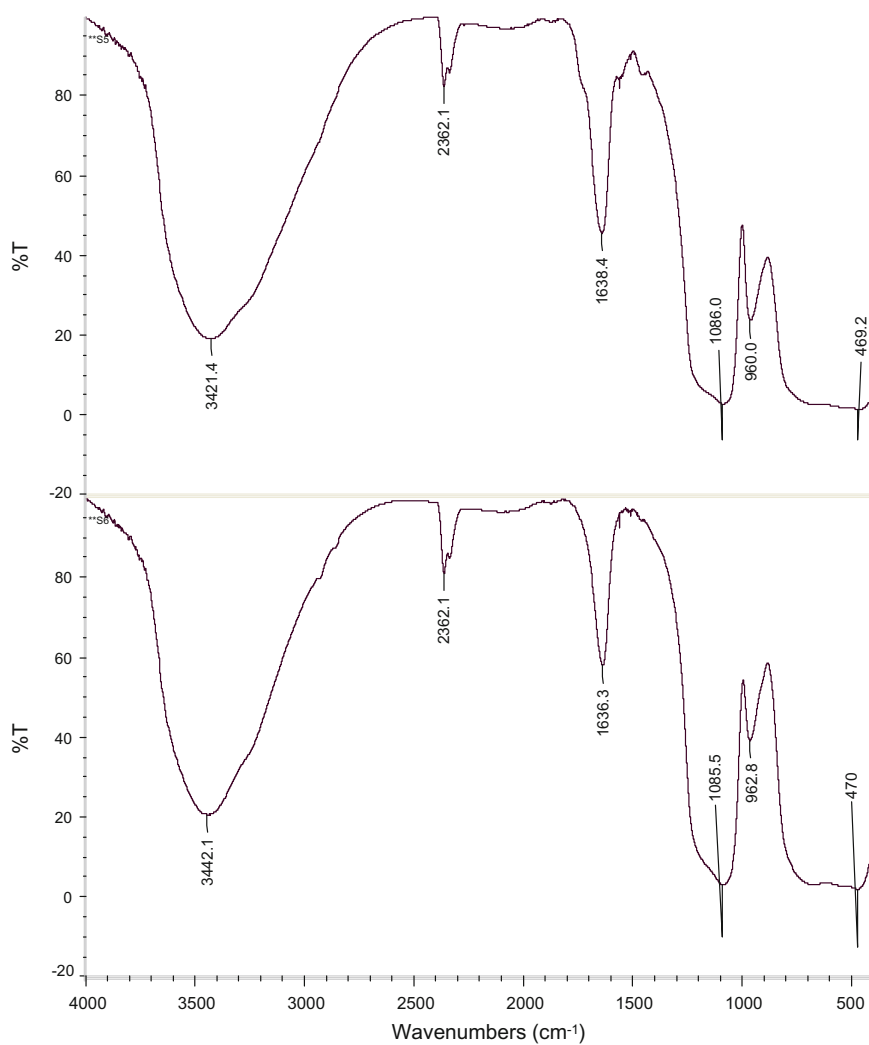
Fig. 2 FTIR spectrum of gelatin-hybrid nanohybrids and its methylene blue-loaded counterpart

the surface area of H_{11}. Hence, the calcined hybrid material (H_{11}) was chosen as an adsorbent for dyes removal studies.
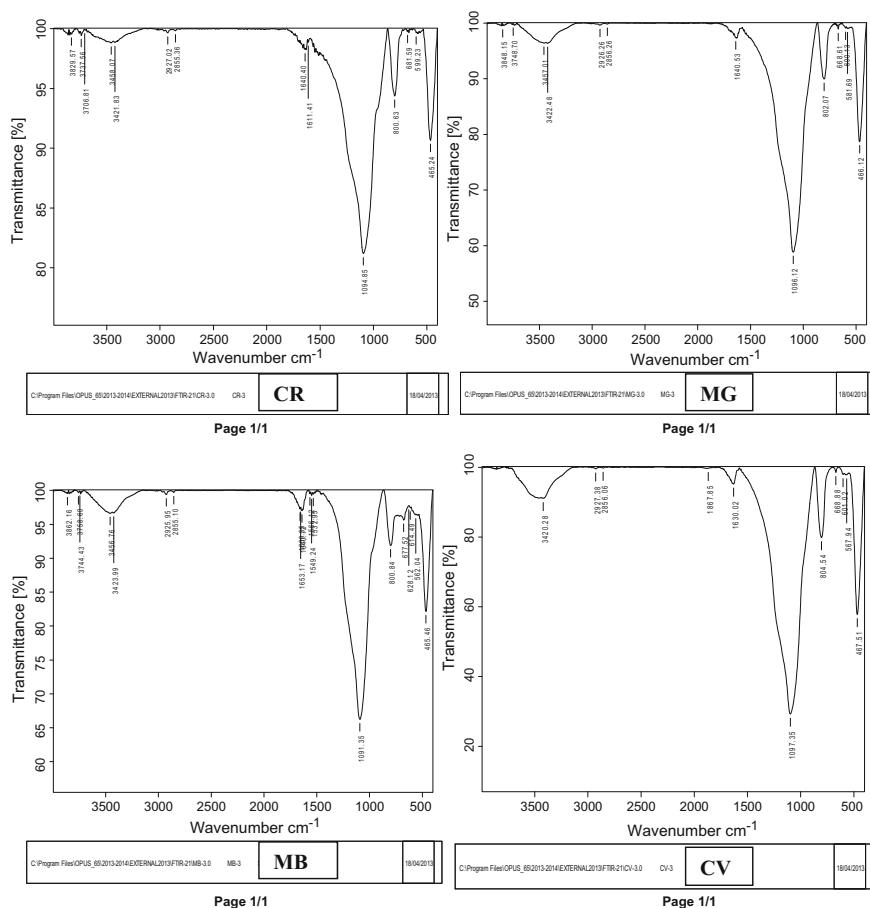
Fig. 3 FTIR of loaded dyes on hybrid material (H_{11})

3.2 Effect of Different Physico-Chemical Parameters on Dye Adsorption

Equilibrium was reached at 360 min for 20 ppm of dye at 35 °C with @150 rpm and initial pH 7.0 (Fig. 7a). The maximum uptake under the operating conditions of 20 ppm, pH 7.0, and 360 min. and change of temperature (25–45 °C) was observed at 35 °C for CR and CV, but for 30 and 25 °C for CV and MB. q_e rises linearly from 3.78 to 8.62 for CR up to 30 °C; 2.21–8.26 for MG up to 35 °C; 3.02–8.48 for CV at 35 °C, and 5.34–8.31 mg g^{-1} for MB at 25 °C (Fig. 7b). Effect of pH variation (2.0–9.2) on dye adsorption is presented as Fig. 7c. At acidic pH (2.0), dye uptake was low, but it shows a gradual rise with an increase in the initial pH of the dye
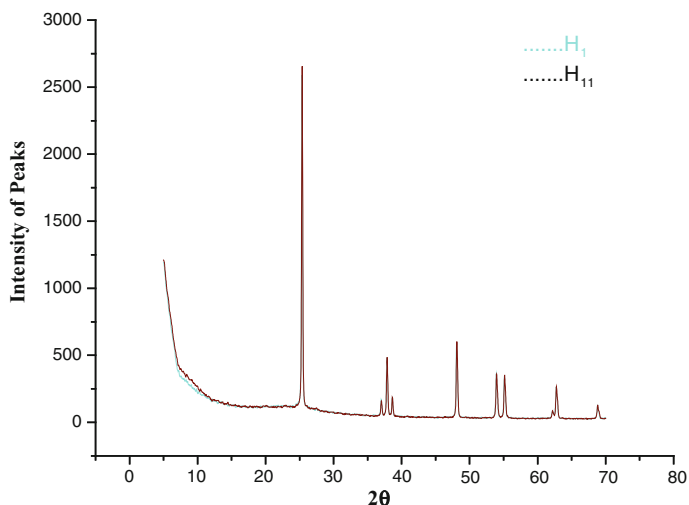
Fig. 4 XRD patterns of H_1 and H_{11} nanohybrids particles

Table 3 EDS compositional analysis for hybrid material (H_1 and H_{11})

Hybrid material	EI	AN	Series	unn. C [wt%]	nor. C [wt%]	Atom. C [wt%]	Error [wt%]
H_a	O	8	K–series	47.03	47.71	69.16	50.7
	Ti	22	K–series	36.38	36.14	17.51	1.1
	Si	14	K–series	16.25	16.14	13.33	0.7
	Total			100.66	100.00	100.00	
H_c	O	8	K–series	50.44	50.69	71.04	43.5
	Ti	22	K–series	31.41	31.56	14.78	0.9
	Si	14	K–series	17.66	17.75	14.17	0.8
	Total			99.51	100.00	100.00	

Table 4 Surface area and pore size comparison

Hybrid material	Density (g cm^{-3})	Surface area (m^{2}g^{-1})	Pore size (nm)
Silica	2.65	458	4.943
Titania	4.23	45	31.520
Gelatin–Titania hybrid	H_1 H_{11}	303.08 327.18	4.680 4.335

solution. For CR, the q values increased with pH from 2.0 to 7.0. At neutral pH, CR showed high adsorption.

The capacity of 8.60 mg g^{-1} for the hybrid material, while for MG, CV and MB it rises by changing pH from 2.0 to 9.2. But, CR has shown a decrease in adsorption when the pH of the solution is further increased beyond neutral pH. The amino
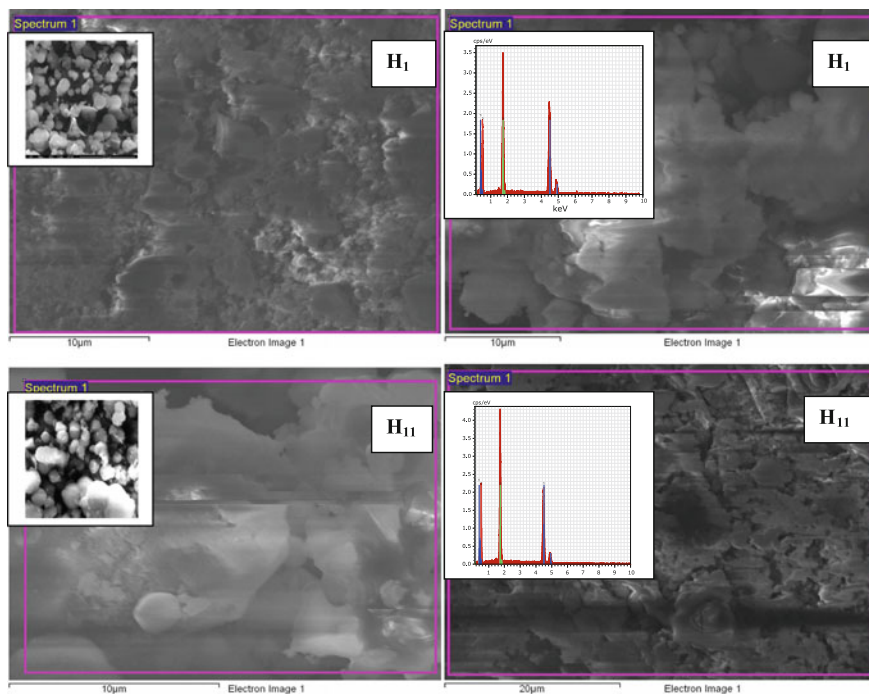
Fig. 5 SEM-EDX before and after dye adsorption
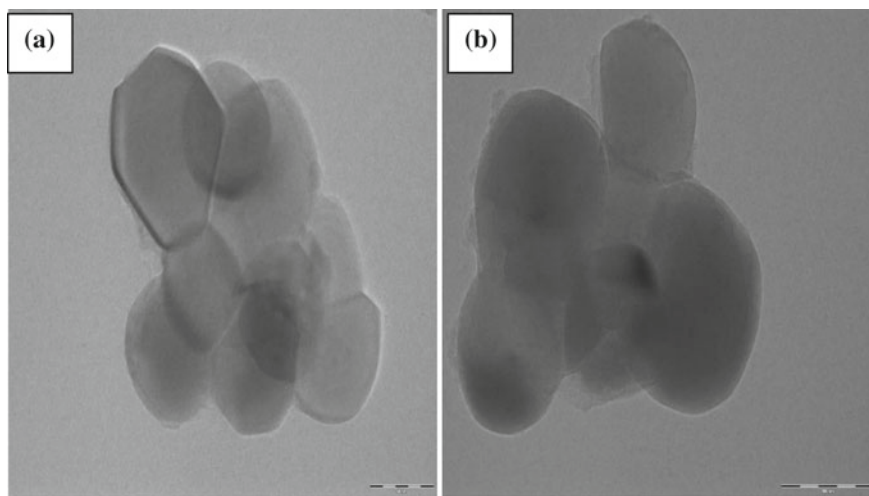
Fig. 6 TEM images of H_1 and H_{11}

groups on dyes get protonated at low pH, and do not get attached to the adsorbent

(20 mg/L; @150 rpm, pH 7.0, 360 minutes)   **(20 mg/L; 360 min; @ 150 rpm, 35 °C)**

(20 mg/L; @150 rpm, pH 7.0, 35 °C, 840 minutes)   **(360 minutes, s@150 rpm, pH 7.0, 35 °C)**
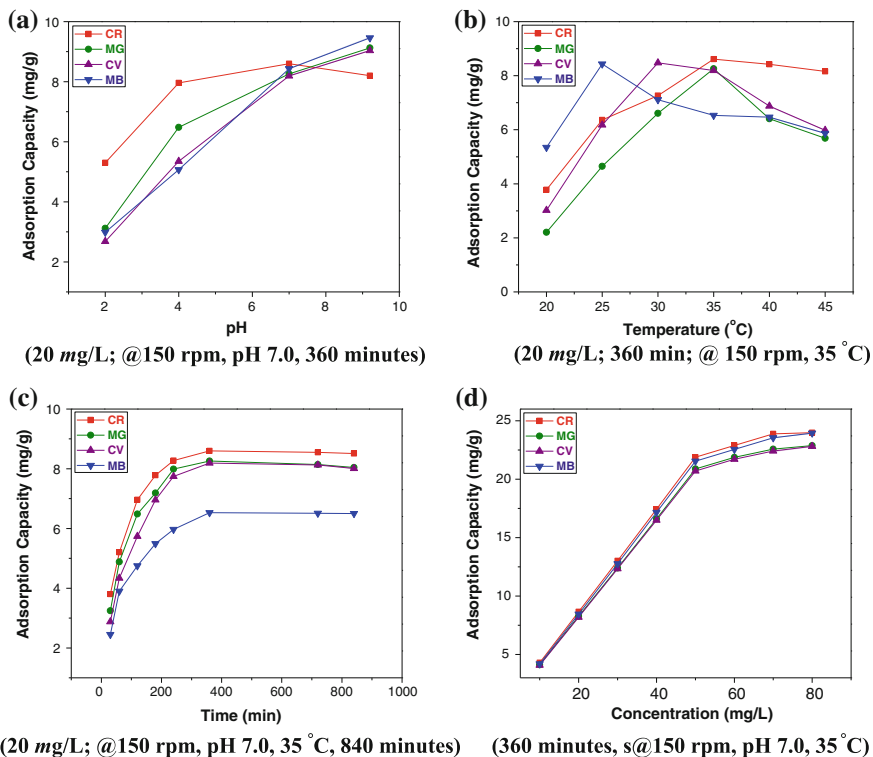
Fig. 7 **a** Effect of pH, **b** effect of temperature, **c** effect of time, **d** Effect of dye concentration on adsorption

surface. At pH 9.2, q values for MG, CV and MB were 9.13, 9.04 and 9.46 mg g^{-1}, respectively. Adsorption of cationic dyes (MG, CV and MB) is influenced by the surface charge and the latter is influenced by the solution pH. As a consequence, it showed that availability of the anionic groups on the hybrid material is essential for the basic dyes adsorption, whereas under acidic pH there is a net positive charge on the adsorbent. Thus, with the pH, more anionic surface charge results in more dye adsorption. The dye adsorption dependence upon pH variation was confirmed from the conductivity measurements as after each adsorption step the conductivity was found to be the minimum meaning thereby maximum adsorption (Table 5). A similar trend in the pH-dependency at pH 7.0 for the CR adsorption is reported [26], and at pH higher than neutral pH for MG, CV and MB [34, 35, 70].

Table 5 Conductivity measurements

Conductivity and λ_{max} comparison of the dye solutions in case of H_{11} as pH function				
pH	2.0	4.0	7.0	9.2
Congo red dye				
λ_{max} (nm)	200	237	481	504
Conductance (mS)	81.82	2.16	0.36	0.38
P_u (%)	53.03	79.62	86.02	82.02
Malachite green dye				
λ_{max} (nm)	618	613	595	624
Conductance (mS)	84	1.53	1.02	0.91
P_u (%)	31.19	64.83	82.60	91.25
Crystal violet dye				
λ_{max} (nm)	285	602	598	574
Conductance (mS)	90	2.18	1.06	1.00
P_u (%)	26.81	53.51	81.93	90.37
Methylene blue dye				
λ_{max} (nm)	602	603	628	313
Conductance (mS)	89	2.41	1.94	1.18
P_u (%)	29.86	50.70	84.31	94.60
Distilled water	373 µS			

3.3 Evaluation of Thermodynamic Parameters

The results from the thermodynamic plots between ln (K_c) versus $1/T$ are presented in Fig. 8. The calculation of standard $\Delta G°$, $\Delta H°$ and $\Delta S°$ for four dyes confirmed that q values augmented with temperature due to higher dye ions mobility. As the temperature rises, a greater number of molecules acquires energy to experience an interaction with the active sites on the adsorbent surface.

Moreover, with temperature, the interiors of the hybrid material may open up and results in more dye penetration. The +ve $\Delta H°$ confirms that dye adsorption was of endothermic nature. The possibility of diffusion of dyes into the interior of the particles is very much there due to the porous nature of this material. It results in higher adsorption due to the larger number of adsorption sites generated when some bonds are broken near the active sites of the hybrid material. The negative values of free energy ($-\Delta G°$) and standard entropy ($-\Delta S°$) during adsorption indicate spontaneity and favours adsorption process. The thermodynamic parameters were calculated (Table 6).
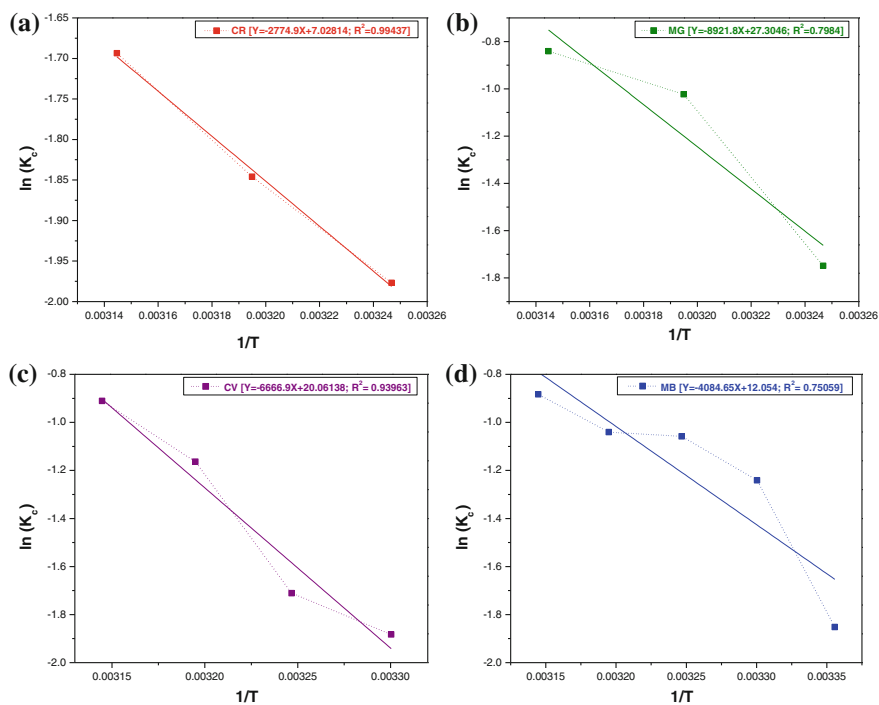
Fig. 8 Thermodynamic Plot of ln (K_c) versus (1/T) of **a** CR, **b** CV, **c** MG, **d** MB

Table 6 Thermodynamic parameter measurement studies

Sample (H₁)	Temperature (K)	$-\Delta G°$ (KJ/mol)	$\Delta H°$ (KJ/mol)	$-\Delta S°$ (J/mol/K)
CR	308	5.062	23.07	58.43
	313	4.804		
	318	4.477		
MG	308	4. 477	74.18	227.01
	313	2.663		
	318	2.223		
CV	303	4.743	55.43	166.79
	308	4.381		
	313	3.020		
	318	2.408		
MB	298	4.588	33.96	100.22
	303	3.126		
	308	2.710		
	313	2.708		
	318	2.335		

3.4 Comparison of Kinetic Studies

Adsorption kinetics were studied by using four kinetic models, pseudo-first order, pseudo-second order, Elovich equation and intraparticle diffusion model were used. The q_e and rate constants k were calculated and results (Table 7). Out of these four models, pseudo-second-order model best fits the experimental data, because its correlation values (R^2) are almost unity. Theoretical values calculated are in close agreement with the experimental values (q_t) (Fig. 9). Thus, the pseudo-second-order model best describes the adsorption kinetics [37]. The diffusion process results in the transportation of dye molecules and it involves peripheral mass transfer resistance, bulk diffusion and intraparticle diffusion through the adsorbent pores. The intraparticle diffusion rate constants (k_{id}) were calculated (Table 7) and its correlation value also favours the intraparticle diffusion process which is the rate-limiting step. Elevated values of k_{id} demonstrate an enhanced bonding between dye molecules and the hybrid material. Due to the different extent of adsorption at the initial and final stage of the process, the result is nearly a linear curve due to the intraparticle diffusion. However, it is clear from Fig. 9 that apart from the intraparticle diffusion the other factor which controls reaction rate as the plot did not intersect the origin and its deviation from the origin signifies peripheral resistance effect. Dye adsorption has a propensity to follow by two different phases, wherein the smooth curve is followed by a linear portion. There are two phases in the plot in which the adsorption process is the sum of intraparticle diffusion and surface sorption. The first non-linear portion of the plot is mainly due to the boundary-layer outcome, whereas the linear portion is because of intraparticle diffusion. Such behaviour was expected as the silica-network and gelatin are two distinct entities. This is further supported from the intraparticle diffusion coefficient (δ), using relation $\delta = 0.03 r^2/t_{1/2}$ [71]. Where r (cm) represents the average radius of the adsorbent particle and $t_{1/2}$ is the half lifetime (in minutes) for adsorption process; the value of $\delta \approx 10^{-11}$ cm^2 s^{-1} points that intraparticle diffusion is the rate determining step. Herein, δ obtained for the four dyes are found to be $(4.153 \times 10^{-17}, 3.531 \times 10^{-17}, 3.667 \times 10^{-17}, 3.327 \times 10^{-17}$ cm^2 s^{-1} respectively, at 35 °C) which are almost 10^{-17} cm^2 s^{-1} or six order less by magnitude. Thus, it is obvious that intraparticle diffusion contributes both to the rate controlling step and boundary-layer mechanism.

Furthermore, results obtained from the kinetic models were compared with the experimental values, where q_t was plotted versus t (Figs. 10). The nonlinear equations of the kinetic models were used for calculating q_t using the slope and intercept values from their corresponding linear fits used. For all the four dyes, pseudo-second-order kinetic model best fits with the experimental data (Fig. 10). It can also be confirmed from their linear fit plots that R^2 value of pseudo-second-order kinetic model are closest to unity in comparison to other models. Thus, adsorption of all four dyes follows pseudo-second-order kinetic model.

Table 7 Comparison of correlation coefficients and rate constants for different kinetic models applied

Kinetic model applied	Kinetic parameters	H_{11}			
		CR	MG	CV	MB
Pseudo-first-order	q_e	15.57022	16.08264	16.72748	17.06876
	k_1	10.36×10^{-4}	10.36×10^{-4}	11.28×10^{-4}	7.37×10^{-4}
	R^2	0.79239	0.80882	0.870251	0.85774
Pseudo-second-order	q_e	9.8039	9.7087	10.00	7.6336
	k_2	2.06×10^{-3}	1.74×10^{-3}	1.27×10^{-3}	2.01×10^{-3}
	R^2	**0.99925**	**0.99853**	**0.99658**	**0.99719**
Elovich equation	α	0.667	0.354	0.265	0.266
	β	0.420	0.478	0.448	0.619
	R^2	0.98046	0.98457	0.99047	0.99247
Intraparticle diffusion model	a	0.3399	0.3802	0.4304	0.3814
	k_{id}	0.956	1.005	1.066	1.059
	R^2	0.9524	0.94602	0.97196	0.94423
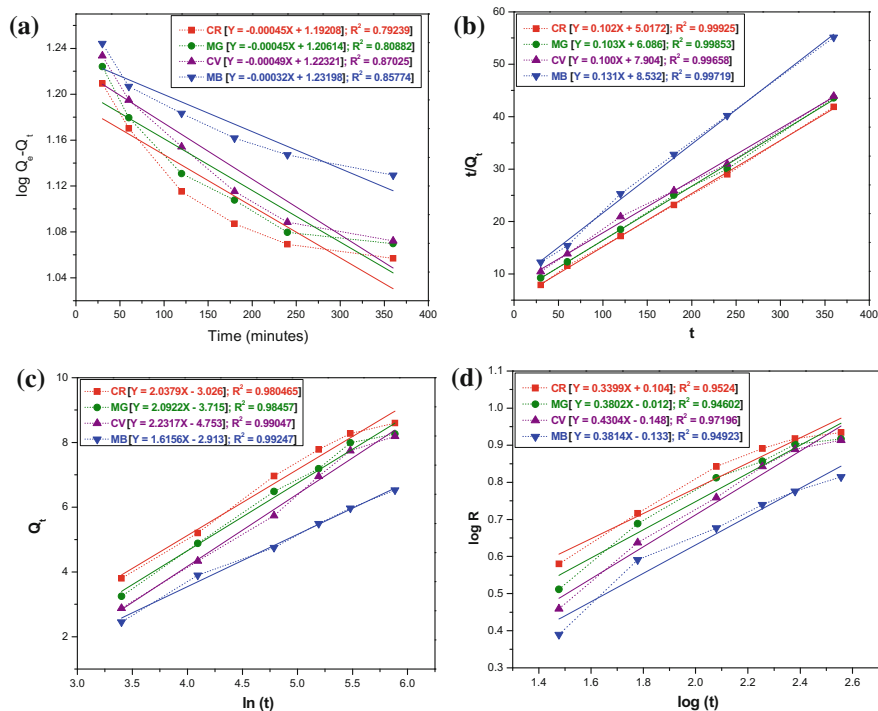
Fig. 9 **a** Pseudo-first-order kinetic model, **b** pseudo–second-order kinetic model, **c** Elovich equation model, **d** Intraparticle diffusion model, **e** plot of separation factor (R_L) against initial dye conc. (C_o)
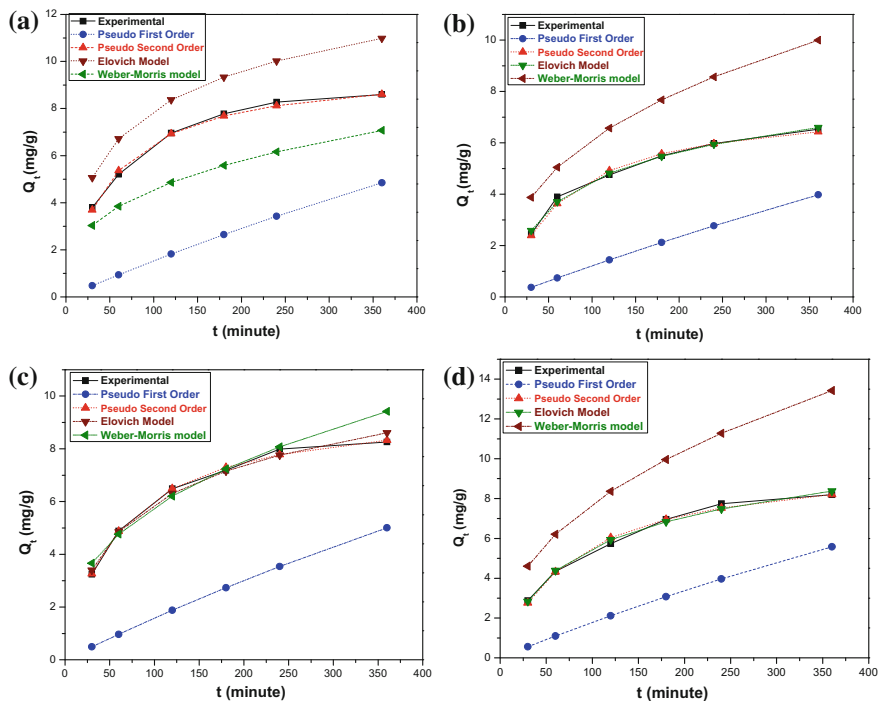
Fig. 10 Comparison of adsorption kinetic models with experimental data for **a** CR, **b** MB, **c** MG and **d** CV on H_{11}

3.5 Comparison of Isotherm Studies

Three adsorption isotherms: Langmuir, Freundlich and Redlich–Peterson isotherms were studied and their results were discussed and compared. The isotherm constants and maximum adsorption capacities (q_{max}) were calculated (Table 8). Plots of Langmuir isotherm, Freundlich isotherm, and Redlich–Peterson isotherms are all shown in Fig. 11. Though the Langmuir and Freundlich isotherms models have a higher value of R^2, yet the Langmuir isotherm model is the better fit with homogeneous adsorption process. Also, the hybrid material surface is crystalline in nature as confirmed by its XRD pattern. Furthermore, it is seen that the theoretical value of q_e determined from the Langmuir isotherm is very close to the experimental values. Adsorption process takes place not only on the interior of the hybrid material but also on its exterior. As a consequence, the adsorptions of dyes are uniform and homogeneous on this hybrid material. It accounts for the same type of binding sites and their interactions, surface uniformity and the power of the hybrid material surface [19].

Thus, Langmuir isotherm provides a more logical picture of adsorption on the gelatin–titania-based hybrid material. Furthermore, to compare different isotherms with the experimental data, q_e and C_e were plotted against each other (Fig. 11).

Table 8 Comparison of isotherm constants and correlation coefficients for different adsorption isotherm models applied

| Adsorption isotherms	Isotherm constants	Calcined hybrid material H_c			
		CR	MG	CV	MB
Langmuir	q_m	1.21×10^2	2.0×10^2	2.004×10^2	8.20×10^3
	K_L	2.44×10^{-2}	1.14×10^{-2}	1.09×10^{-2}	3.02×10^{-2}
	R^2	0.99996	0.99999	1.00000	0.99997
Freundlich	n	0.92	0.95	0.95	0.89
	K_F	2.96	2.25	2.14	2.41
	R^2	0.99943	0.99978	0.99979	0.99896
Redlich–Peterson	A	200	200	200	200
	B	66.62	87.79	92.39	81.86
	g	0.086	0.052	0.050	0.125
	R^2	0.91282	0.91312	0.91107	0.91861
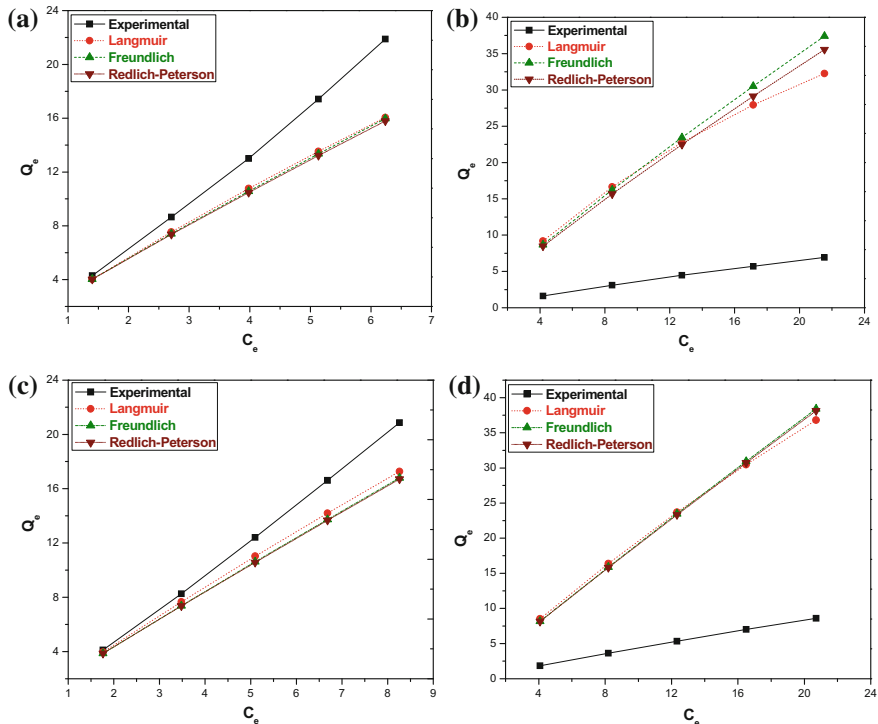
Fig. 11 Comparison of isotherm models with experimental data for **a** CR, **b** MB, **c** MG and **d** CV on H_{11}

The nonlinear equations of the isotherms are used for calculating q_e values and all the three isotherms have the same pattern and follow each other. Out of these three
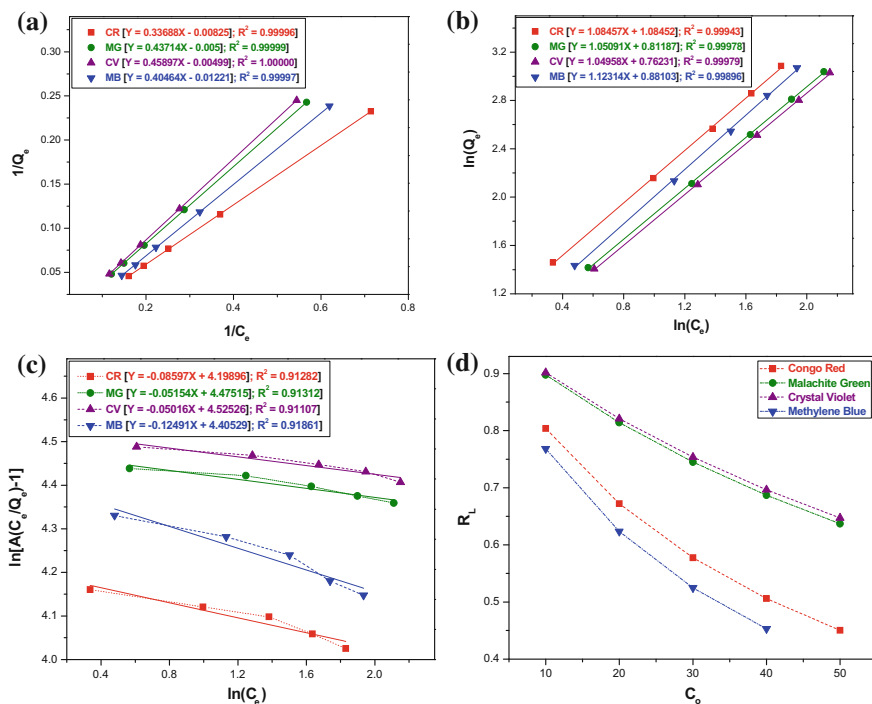
Fig. 12 **a** Langmuir isotherm, **b** Freundlich isotherm, **c** Redlich–Peterson isotherm

isotherms, Langmuir isotherms approach the experimental data for all four dyes (Figs. 11). From their linear fits also the R^2 value of Langmuir is the closest to unity as compared to other isotherms. Thus, all the four dyes follow Langmuir isotherms by physical adsorption method.

A dimensionless constant, separation factor (R_L) is one of the most important characteristics of the Langmuir isotherm and spot out adsorption process feasibility. Separation factor R_L was calculated from Eq. (14) and results are tabulated from Fig. 12.

$$R_L = \frac{1}{1 + K_L C_o} \tag{14}$$

where the symbol C_o represents initial concentration ($mg\,L^{-1}$ or ppm) of dye. R_L lies between zero to one for the favourable adsorption, while adsorption is non-favourable when $R_L > 1$ represents. $R_L = 1$ represents linear adsorption whereas it is irreversible if $R_L = 0$ [72]. Herein, the values of R_L were found to be less than unity meaning thereby the process is highly encouraging for all the four dyes. The plot of R_L versus C_o shows the essentials of the Langmuir isotherm [73]. Figure 12d shows R_L values

of four dyes at 35 °C. R_L values signify that adsorption is more complimentary for the higher initial dye concentration than the smaller initial dye concentrations.

3.6   Reusability, Maximum Adsorption Capacity (MAC) and Photocatalytic Degradation of the Loaded Dyes

Assessment of MAC of the nanohybrid material was studied by subjecting to five feeds of repeated dye uptake in a 50 ppm solution, at 35 °C temperature pH 7.0 and stirring @150 rpm for 360 min in each feed experiment (Table 9). A percentage uptake (P_u) of 79.23% (19.80 mg g^{-1}) for CR, 71.84% (17.96 mg g^{-1}) for MG, 70.09% (17.52 mg g^{-1}) for CV and 75.93% (18.98 mg g^{-1}) for MB was experimentally determined. After the five cumulative feeds, the MAC was 71.17, 67.41, 74.82 and 76.56 mg g^{-1} for CR, MG, CV and MB on hybrid materials (H_{11}), respectively (Fig. 13a). For reusability measurements and studies, desorption of dyes was carried out with 0.1N NaOH and the regenerated material was reused repeatedly for six adsorption–desorption cycles (Fig. 13b).

Preliminary experiments to demonstrate that the loaded dyes are easily photodegraded was conducted as the dyes loaded onto hybrid material were exposed directly to sunlight and observed for seven days. Photocatalytic degradation was examined by evaluating the absorbance using UV-Visible spectrophotometer at pH 7.0 (Fig. 13c). Dyes were decolorized or degraded photocatalytically into smaller molecules [72–75]. The fluorescence spectrum of CR difference time for the photodegradation is presented in Fig. 13d. It shows that photodecolorization is directly dependent on the direct exposure to the sunlight.

4   Conclusions

New eco-friendly gelatin–titania-based nanohybrid material was synthesized and its properties were improvised by calcination at 550 °C. The nanohybrid material is an efficient adsorbent for acidic dye (congo red) and basic dyes (crystal violet, malachite green and methylene blue). Adsorption process followed Langmuir adsorption isotherm and pseudo-second-order kinetic model for all four dyes. Experimental data are in good agreement with pseudo-second-order kinetic model and Langmuir adsorption isotherm. The MAC of the dyes (CR, MB, MG and CV) was 71.17, 76.56, 67.41 and 74.82 mg/g, respectively. Complete exclusion of the dyes can be realized using the optimized conditions worked out in the present study. The results are practical and valuable for the design of treatment plants for adsorption and degradation of dyes present in wastewater as the materials are cost-effective and efficient candidates for water purification technologies.

Table 9 Reusability and MAC of the dye solution in hybrid material (H_{11})

Conductivity and percentage uptake (P_u) of the dye solutions as a function of repeated use

Cycle	I	II	III	IV	V
Congo red dye ($\lambda_{max} = 598$)					
Conductance (μS)	1043	894	1338	1407	1569
P_u (%)	75.927	79.228	74.205	68.612	70.341
Malachite green dye ($\lambda_{max} = 595$)					
Conductance (mS)	4.36	15.27	16.31	16.12	16.89
P_u (%)	71.839	69.994	65.584	68.168	43.759
Crystal violet dye ($\lambda_{max} = 598$)					
Conductance (μS)	780	773	1245	1180	1070
P_u (%)	70.092	69.417	70.017	51.769	53.941
Methylene blue dye ($\lambda_{max} = 628$)					
Conductance (mS)	4.0	4.9	13.9	13.4	16.52
P_u (%)	75.930	74.934	75.367	72.904	45.501
Pure water	373 μS				
MAC					

Dye	λ_{max}	Total cycles	Adsorption capacity (mg/g)
Congo red	481 nm	5	71.17
Malachite green	595 nm	5	67.41
Crystal violet	598 nm	5	74.82
Methylene blue	628 nm	5	76.56

(a)

(50 *m*g/L; @150 rpm, pH 7.0, 35 °C, 360 minutes)

(b)

(50 *m*g/L; @150 rpm, pH 7.0, 35 °C, 360 minutes)
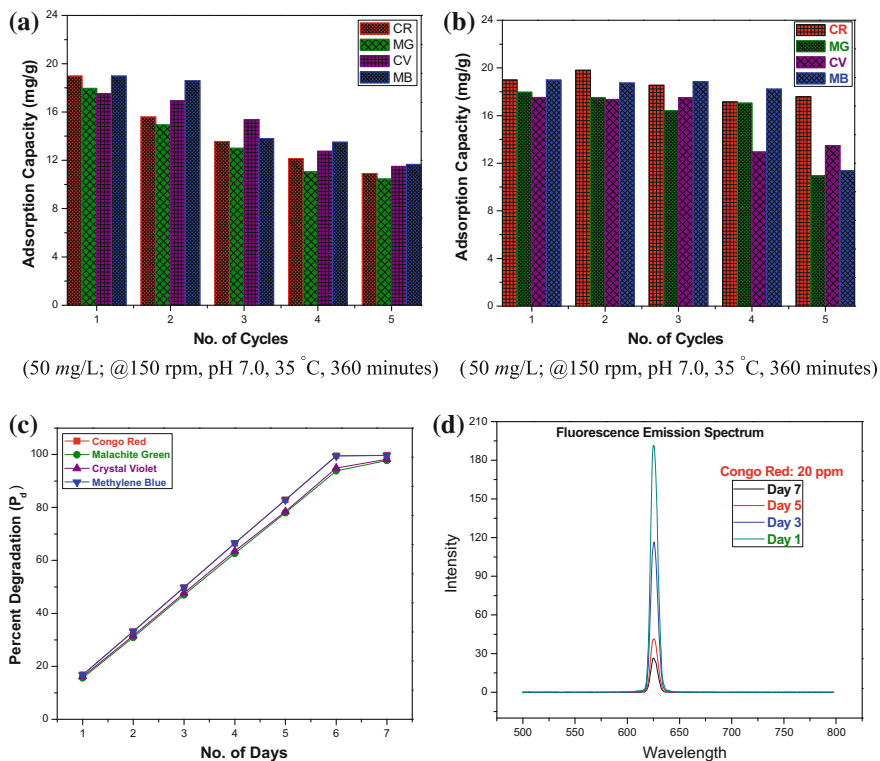
(c)

(d)

Fig. 13 **a** Reusability, **b** maximum adsorption capacity, **c** photocatalytic degradation, **d** fluorescence spectra of CR

References

1. Tollefson, J., Gilbert, N.: Earth summit: rio report card. Nature **486**, 20–23 (2012). https://doi.org/10.1038/486020a
2. Sullivan, R.K., Erickson, M., Oyanedel-Craver, V.A.: Understanding the microbiological, organic and inorganic contaminant removal capacity of ceramic water filters doped with different silver nanoparticles. Environ. Sci. Nano. **4**, 2348–2355 (2017). https://doi.org/10.1039/c7en00443e
3. Clive, T.: Persistent organic pollutants: are we close to a solution? Can. Arct. Resour. Committee **26**(1), Fall/Winter (2000)
4. Tsuboy, M.S., Angeli, J.P.F., Mantovani, M.S., Knasmuller, S., Umbuzeiro, G.A., Ribeiro, L.R.: Genotoxic, mutagenic and cytotoxic effects of the commercial dye CI disperse blue 291 in the human hepatic cell line HepG2. Toxicol. In Vitro **21**, 1650–1655 (2007). https://doi.org/10.1016/j.tiv.2007.06.020
5. Banat, I.M., Nigam, P., Singh, D., Marchant, R.: Microbial decolorization of textile dye containing effluents. Bioresour. Technol. **58**, 217–227 (1996). https://doi.org/10.1016/S0960-8524(96)00113-7
6. Singh, K., Arora, S.: Removal of synthetic textile dyes from wastewater: a critical review on present treatment technologies. Crit. Rev. Environ. Sci. Technol. **41**, 807–878 (2011). https://doi.org/10.1080/10643380903218376
7. Alinsafi, A., Khemis, M., Pons, M.N., Leclerc, J.P., Yaacoubi, A., Benhammou, A., Nejmeddine, A.: Electro-coagulation of reactive textile dyes and textile wastewater. Chem. Eng. Process. **44**, 461–470 (2004). https://doi.org/10.1016/j.cep.2004.06.010
8. Chakraborty, S., Purkait, M.K., Gupta, S.D., De, S., Basu, J.K.: Nanofiltration of textile plant effluent for color removal and reduction in COD. Sep. Purif. Technol. **3**, 141–151 (2003). https://doi.org/10.1016/S1383-5866(02)00177-6
9. Davila-Jimenez, M.M., Elizalde-Gonzalez, M.P., Gutierrez-Gonzalez, A., Pelaez-Cid, A.A.: Electrochemical treatment of textile dyes and their analysis by high-performance liquid chromatography with diode array detection. J. Chromatogr. A **889**, 253–259 (2000). https://doi.org/10.1016/S0021-9673(00)00603-8
10. Pandit, P., Basu, S.: Removal of ionic dyes from water by solvent extraction using reverse micelles. Environ. Sci. Technol. **38**, 2435–2442 (2004). https://doi.org/10.1021/es030573m
11. Hsu, Y.-C., Chen, J.-T., Yang, H.-C., Chen, J.-H.: Decolorization of dyes using ozone in gas-induced a reactor. AIChE J. **47**, 169–176 (2001). https://doi.org/10.1002/aic.690470116
12. Tan, B.H., Teng, T.T., Omar, A.K.M.: Removal of dyes and industrial dye wastes by magnesium chloride. Water Res. **34**, 597–601 (2000). https://doi.org/10.1016/S0043-1354(99)00151-7
13. Mondal, S.: Methods of dye removal from dye house effluent an overview. Environ. Eng. Sci. **25**, 383–396 (2008). https://doi.org/10.1089/ees.2007.0049
14. Ting, H., Chi, H.-Y., Lam, C.H., Chan, K.-Y., Kang, D.-Y.: High-permeance metal–organic framework-based membrane adsorber for the removal of dye molecules in aqueous phase. Environ. Sci. Nano **4**, 2205–2214 (2017). https://doi.org/10.1039/c7en00639j
15. Ramakrishna, K.R., Viraraghavan, T.: Dye removal using low cost adsorbents. Water Sci. Technol. **36**, 189–196 (1997). https://doi.org/10.1016/S0273-1223(97)00387-9
16. Tunay, O., Kabadasli, I., Eremektar, G., Orhan, D.: Color removal from textile wastewater. Water Sci. Technol. **34**, 9–16 (1996). https://doi.org/10.1080/09593332808618824
17. Wang, L., Zhang, J., Wang, A.: Removal of methylene blue from aqueous solution using Chitosan-G poly(acrylic acid)/montmorillonite super-adsorbent nanocomposite. Colloids Surf. A **322**, 47–53 (2008). https://doi.org/10.1016/j.colsurfa.2008.02.019
18. Sankar, M., Sekaran, G., Sadulla, S., Ramasami, T.: Removal of diazo and triphenylmethane dyes from aqueous solutions through an adsorption process. J. Chem. Technol. Biotechnol. **74**, 337–344 (1999). https://doi.org/10.1002/(SICI)1097.4660(199904)74:4%3c337:AID-JCTB39%3e3.0.CO;2-U

19. Chatterjee, S., Kumar, A., Basu, S., Dutta, S.: Application of response surface methodology for methylene blue dye removal from aqueous solution using low cost adsorbent. Chem. Eng. J. **181–182**, 289–299 (2012). https://doi.org/10.1016/j.cej.2011.11.081
20. Cai, Z., Dwivedi, A.D., Lee, W.-N., Zhao, X., Liu, W., Sillanpaa, M., Zhao, D., Huang, C.-H., Fu, J.: Application of nanotechnologies for removing pharmaceutically active compounds from water: development and future trends. Environ. Sci. Nano (2018). https://doi.org/10.1039/c7en00644f
21. Khodaie, M., Ghasemi, N., Moradi, B., Rahimi, M.: Removal of methylene blue from wastewater by adsorption onto $ZnCl_2$ activated corn husk carbon equilibrium studies. J. Chem. **213**, 1–6 (2013). https://doi.org/10.1155/2013/383985
22. Senthilkumaar, S., Varadarajan, P.R., Porkodi, K., Subbhuraam, C.V.: Adsorption of methylene blue onto jute fiber carbon: kinetics and equilibrium studies. J. Colloid Interface Sci. **284**, 78–82 (2005). https://doi.org/10.1016/j.jcis.2004.09.027
23. Malik, P.K.: Used activated carbons prepared from sawdust and rice-husk for adsorption of acid dyes: a case study of acid yellow 36. Dyes Pigm. **56**, 237–249 (2003). https://doi.org/10.1016/S0143-7208(02)00159-6
24. Kannan, N., Sundaram, M.M.: Kinetics and mechanisms of removal of methylene blue by adsorption on various carbons—a comparative study. Dyes Pigm. **51**, 25–40 (2001). https://doi.org/10.1016/s0143-7208(01)00056-0
25. Emad, N., Stephen, J., Gavin, M.: Adsorption of methylene blue onto activated carbon produced from steam activated bituminous coal: a study of equilibrium adsorption isotherm. Chem. Eng. J. **124**, 103–110 (2006). https://doi.org/10.1016/j.cej.2006.08.015
26. Okeola, O.F., Odebunmi, E.O., Bakare, O.F.: Equilibrium and kinetics studies of adsorption of congo red by activated carbon. Middle-East J. Sci. Res. **19**, 1425–1431 (2014). https://doi.org/10.1016/j.arabjc.2014.01.020
27. Namasivayam, C., Kavitha, D.: Removal of congo red from water by adsorption onto activated carbon prepared from coir pith, an agricultural solid waste. Dyes Pigm. **54**, 47–58 (2002). https://doi.org/10.1016/S0143-7208(02)00025-6
28. Pereira, M.F.R., Soares, S.F., Orfao, J.J.M., Figueiredo, J.L.: Adsorption of dyes on activated carbons: influence of surface chemical groups. Carbon **41**, 811–821 (2003). https://doi.org/10.1016/S0008-6223(02)00406-2
29. Purkait, M.K., Maiti, A., Gupta, S.D., Deb, S.: Removal of congo red using activated carbon and its regeneration. J. Hazard. Mater. **145**, 287–295 (2007). https://doi.org/10.1016/j.jhazmat.2006.11.021
30. Bulut, Y., Audin, H.: A kinetics and thermodynamics study of methylene blue adsorption on wheat shells. Desalination **194**, 259–267 (2006). https://doi.org/10.1016/j.desal.2005.10.032
31. Ho, Y.S., Chiu, W.T., Wang, C.C.: Regression analysis for the sorption isotherms of basic dyes on sugarcane dust. Bioresour. Technol. **96**, 1285–1291 (2005). https://doi.org/10.1016/j.biortech.2004.10.021
32. Deniz, F., Karaman, S.: Removal of basic red 46 dye from aqueous solution by pine tree leaves. Chem. Eng. J. **170**, 67–74 (2011). https://doi.org/10.1016/j.cej.2011.03.029
33. Mahmoodi, N.M., Hayati, B., Arami, M., Lan, C.: Adsorption of textile dyes on pine cone from colored wastewater: kinetic, equilibrium and thermodynamics studies. Desalination **268**, 117–125 (2011). https://doi.org/10.1016/j.desal.2010.10.007
34. Baek, M.H., Ijagbemi, C.O., Jin, O.S., Kim, D.S.: Removal of malachite green from aqueous solution using degreased coffee bean. J. Hazard. Mater. **176**, 820–828 (2010). https://doi.org/10.1016/j.jhazmat.2009.11.110
35. Courtie, M., Mawere, Epias: Kinetic modeling of methylene blue and crystal violet dyes adsorption on alginate-fixed water hyacinth in single and binary systems. Am. J. Anal. Chem. **4**, 17–24 (2013). https://doi.org/10.4236/ajac.2013.410A3003
36. Sharma, U.Y.C.: Removal of malachite green from aqueous solutions by adsorption on to timber waste. Int. J. Environ. Eng. Manage. **4**, 631–638 (2013)
37. Sivaraj, R., Namasivayam, C., Kadirvelu, K.: Orange peel as an adsorbent in the removal of acid violet 17 (acid dye) from aqueous solutions. Waste Manage. **21**, 105–110 (2001). https://doi.org/10.1016/S0956-053X(00)00076-3

38. Gill, A., Assis, F.C.C., Albeniz, S., Korili, S.A.: Removal of dyes from wastewater by adsorption on pillared clays. Chem. Eng. J. **168**, 1032–1040 (2011). https://doi.org/10.1016/j.cej.2011.01.078

39. Wang, S.B., Zhu, Z.H.: Characterization of environmental application of an Australian natural zeolite for basic dye removal from aqueous solution. J. Hazard. Mater. **136**, 946–952 (2006). https://doi.org/10.1016/j.jhazmat.2006.01.038

40. Roulia, M., Vassiliadis, A.A.: Sorption characterization of a cationic dye retained by clays and perlite. Micropor. Mesopor. Mater. **116**, 732–740 (2008). https://doi.org/10.1016/j.micromeso.2008.03.017

41. Ma, J., Yu, F., Zhou, L., Jin, L., Yang, M., Luan, J., Tang, Y., Fan, H., Yuan, Z., Chen, J.: Enhanced adsorptive removal of methyl orange and methylene blue from aqueous solution by alkali activated multi-walled carbon nanotubes. ACS Appl. Mater. Interfaces. **4**, 5749–5760 (2012). https://doi.org/10.1021/am301053m

42. Mahmoodi, N.M., Najafi, F.: Synthesis, amine functionalization and dye removal ability of titania/silica nano-hybrid. Micropor. Mesopor. Mater. **156**, 153–160 (2012). https://doi.org/10.1016/j.micromeso.2012.02.026

43. Sanchez, C., Julia´n, B., Belleville, P., Popall, M.: Applications of hybrid organic–inorganic nanocomposites. J. Mater. Chem. B **15**, 3559–3592 (2005). https://doi.org/10.1039/b509097k

44. Hu, Q., Li, J., Qiao, S., Hao, Z., Tian, H., Ma, C., He, C.: Synthesis and hydrophobic adsorption properties of microporous/mesoporous hybrid materials. J. Hazard. Mater. **164**, 1205–1212 (2009). https://doi.org/10.1016/j.jhazmat.2008.09.023

45. Jin, X., Li, Y., Yu, C., Ma, Y., Yang, L., Hu, H.: Synthesis of novel inorganic–organic hybrid materials for simultaneous adsorption of metal ions and organic molecules in aqueous solution. J. Hazard. Mater. **198**, 247–256 (2011). https://doi.org/10.1016/j.jhazmat.2011.10.040

46. Lachheb, H., Puzenat, E., Houas, A., Ksibi, M., Elaloui, E., Guillard, C., Herrmann, J.M.: Photocatalytic degradation of various types of dyes (Alizarin S, Crocein Orange G, Methyl Red, Congo Red, Methylene Blue) in water by UV-irradiated titania. Appl. Catal. B: Environ. **39**, 75–90 (2002). https://doi.org/10.1016/S0926-3373(02)00078-4

47. Senthilkumaar, S., Porkodi, K.: Heterogeneous photocatalytic decomposition of crystal violet in UV-illuminated sol-gel derived nanocrystalline TiO_2 suspensions. J. Colloid Interface Sci. **288**, 184–189 (2005). https://doi.org/10.1016/j.jcis.2005.02.066

48. Houas, A., Lachheb, H., Ksibi, M., Elaloui, E., Guillard, C., Herrmann, J.M.: Photocatalytic degradation pathway of methylene blue in water. App. Catal. B: Environ. **31**, 145–157 (2011). https://doi.org/10.1016/S0926-3373(00)00276-9

49. Chauhan, G.S., Kumar, S., Kumari, A., Sharma, R.: Study on the synthesis, characterization, and sorption of some metal ions on gelatin and acrylamide-based hydrogels. J. App. Polym. Sc. **90**(14), 3856–3871 (2003). https://doi.org/10.1002/app.13086

50. Kumari, M., Chauhan, G.S.: Adsorption capacity, kinetics, and mechanism of copper (II) uptake on gelatin-based hydrogels. J. App. Polym. Sc. **119**(1), 363–370 (2011). https://doi.org/10.1002/app.32632

51. Thakur, S.S., Chauhan, G.S.: Gelatin–silica-based hybrid materials as efficient candidates for removal of chromium (VI) from aqueous solutions. IECR **53**(12), 4838–4849 (2014). https://doi.org/10.1021/ie401997g

52. Chauhan, G.S., Singh, B., Chauhan, S., Verma, M., Mahajan, S.: Sorption of some metal ions on cellulosic-based hydrogels. Desalination **181**(1), 217–224 (2005). https://doi.org/10.1016/j.desal.2005.03.002

53. Chauhan, G.S., Chauhan, S., Kumar, S., Kumari, A.: A study in the adsorption of Fe^{2+} and on pine needles based hydrogels. Biores. Technol. **99**(14), 6464–6470 (2008). https://doi.org/10.1016/j.biortech.2007.11.044

54. Thakur, S., Kumari, S., Dogra, P., Chauhan, G.S.: A new guar gum-based adsorbent for the removal of Hg (II) from its aqueous solutions. Carbo. Polym. **106**, 276–282 (2014). https://doi.org/10.1016/j.carbpol.2014.02.041

55. Kumari, S., Chauhan, G.S.: New cellulose-lysine schiff-base-based sensor-adsorbent for mercury ions. ACS Appl. Mater. Interfaces. **6**(8), 5908–5917 (2014). https://doi.org/10.1021/am500820n

56. Croissant, J.G., Cattoën, X., Durand, J.-O., Manc, M.W.C., Khashab, N.M.: Organosilica hybrid nanomaterials with a high organic content: syntheses and applications of silsesquioxanes. Nanoscale **8**, 19945–19972 (2016). https://doi.org/10.1039/c6nr06862f
57. Qin, Y., Wang, L., Zhao, C., Chen, D., Ma, Y., Yang, W.: Ammonium-functionalized hollow polymer particles as a pH-responsive adsorbent for selective removal of acid dye. ACS Appl. Mater. Interfaces. **8**(26), 16690–16698 (2016)
58. Guo, W., Luo, G.S., Wang, Y.J.: A new emulsion method to synthesize well-defined mesoporous particles. J. Colloid Interface Sci. **271**, 400–406 (2004). https://doi.org/10.1016/j.jcis.2003.08.056
59. Singh, K.K., Rastogi, R., Hasan, S.H.: Removal of Cr(VI) from wastewater using rice bran. J. Colloid Interface Sci. **290**, 61–68 (2005). https://doi.org/10.1016/j.jcis.2005.04.011
60. Ho, Y.S., McKay, G.: Pseudo-second order model for sorption processes. Process Biochem. **34**, 451–465 (1999). https://doi.org/10.1016/S0032-9592(98)00112-5
61. Weber, W.J., Morris, J.C.: Kinetics of adsorption on carbon from solution. J. Sanit. Eng. Div. Am. Soc. Civ. Eng. **89**, 31–60 (1963)
62. Chien, S.H., Clayton, W.R.: Application of Elovich equation to the kinetics of phosphate release and sorption on soils. Soil Sci. Soc. Am. J. **44**, 265–268 (1980). https://doi.org/10.2136/sssaj1980.03615995004400020013x
63. Langmuir, I.: The constitution and fundamental properties of solids and liquids. J. Am. Chem. Soc. **38**, 2221–2295 (1916). https://doi.org/10.1021/ja02268a002
64. Freundlich, H.M.F.: Over the adsorption in solution. J. Phys. Chem. **57**, 385–470 (1906)
65. Allen, S.J., McKay, G., Porter, J.F.: Adsorption isotherm models for basic dye adsorption by peat in single and binary component systems. J. Colloid Interface Sci. **280**, 322–333 (2004). https://doi.org/10.1016/j.jcis.2004.08.078
66. Wua, F.-C., Liub, B.-L., Wuc, K.-T., Tseng, R.-L.: A new linear form analysis of Redlich-Peterson isotherm equation for the adsorptions of dyes. Chem. Eng. J. **162**, 21–27 (2006). https://doi.org/10.1016/j.cej.2010.03.006
67. Wang, S., Boyjoo, Y., Choueib, A., Zhu, Z.H.: Removal of dyes from aqueous solution using fly ash and red mud. Water Res. **39**, 129–138 (2005)
68. Feinle, A., Elsaesser, M.S., Husing, N.: Sol-gel synthesis of monolithic materials with hierarchical porosity. Chem. Soc. Rev. **45**, 3377–3399 (2016). https://doi.org/10.1039/c5cs00710k
69. Sabataityte, J., Oja, I., Lenzman, F., Volobujeva, O., Krunks, A.: Characterization of nanoporous TiO_2 films prepared by sol-gel method. C. R. Chim. **9**, 708–712 (2006). https://doi.org/10.1016/j.crci.2005.05.019
70. Saltabas, O., Teker, M., Konuk, Z.: Biosorption of cationic dyes from aqueous solution by water hyacinth roots. Global Nest J. **14**, 24–31 (2012)
71. Michelson, L.D., Gideon, P.G., Pace, E.G., Kutal, L.H.: Removal of soluble mercury from wastewater by complexing technique. US Department of Industry Office of the Water Research and Technology (1975). http://hdl.handle.net/10919/25731
72. Crini, G.: Kinetic and equilibrium studies on the removal of cationic dyes from aqueous solution by adsorption onto a cyclodextrin polymer. Dyes Pigm. **77**, 415–426 (2008). https://doi.org/10.1016/j.dyepig.2007.07.001
73. He, J., Hong, S., Zhang, L., Gan, F., Ho, Y.-S.: Equilibrium and thermodynamic parameters of adsorption of methylene blue onto rectorite. Fresenius Environ. Bull. **19**, 2651–2656 (2010)
74. Xu, P., Shen, X.., Luo, L., Shi, Z., Liu, Z., Chen, Z., Zhu, M., Zhang, L.: Preparation of TiO_2/Bi_2WO_6 nanostructured heterojunctions on carbon fibers as a weaveable visible-light photocatalyst/photoelectrode. Environ. Sci.: Nano (2018). https://doi.org/10.1039/c7en00822h
75. Mahmoodi, N.M., Arami, M., Limaee, N.Y., Tabrizi, N.S.: Kinetics of heterogeneous photocatalytic degradation of reactive dyes in an immobilized TiO_2 photocatalytic reactor. J. Colloid Interface Sci. **295**, 159–164 (2006). https://doi.org/10.1016/j.jcis.2005.08.007

Development of CNT–Polymer Film-Based Electrode for the Detection of Glucose

Neha Gopal, Prashant Shukla and Rachana Sahney

Abstract Carbon nanotubes (CNTs) have gained considerable attention due to their exceptional properties including high surface area, excellent electrical, mechanical, and thermal properties. Since outer walls of CNTs are chemically inert and hydrophobic in nature, it is of primary importance to make them compatible for their use. Among various methods, oxidation of CNTs surfaces by simple acids provides a mean to immobilize biomolecules and new surfaces. Protein–CNT conjugates are being developed for a wide range of biomedical devices and therapies including drug delivery, cancer therapy, and biosensing applications. The ability of CNTs to promote electron transfer in various redox reactions suggests great promise for oxidases-based amperometric biosensor and this has led to the development of electrode modified with CNTs in the application of electrocatalytic oxidation of glucose, uric acid, cytochromec, nitric oxide, 4-aminophenol etc. Here our study presents the application of functionalized CNT for electro-conductive filmmaking using simple fabrication method. The fabricated CNT film has been used to study the immobilization of enzyme and its application as glucose biosensor. We have studied the surface morphology of CNT film by transmission electron microscopy (TEM) and Fourier-transform infrared (FTIR) spectrometer while the biosensor/ bioelectronic properties of the CNT film-based electrode was studied by bio-electrochemical techniques like cyclic voltammetry. The results suggest that CNT–polymer-based film can uniformly disperse the functionalized CNTs by molding methods which were found to be suitable for preparing transducers and it can be used for the measurement of glucose in an aqueous system.

Keywords Electrode · Amperomtric biosensor · Bio-electrochemical techniques

N. Gopal · R. Sahney (✉)
Amity Institute of Biotechnology, Amity University Uttar Pradesh, Noida 201313, Uttar Pradesh, India
e-mail: rachanasahney@gmail.com

P. Shukla
Amity Institute for Advanced Research and Studies (Materials & Devices), Amity University Uttar Pradesh, Noida 201313, Uttar Pradesh, India

1 Introduction

Diabetes mellitus is the leading cause of deaths worldwide [1], due to which precise glucose determination is of great importance in diabetic patients for their diagnosis, treatment, and survival [2, 3]. Since older conventional methods of glucose determination like spectrophotometric and chromatographic approaches suffer from drawbacks such as lack of sensitivity, reproducibility, shelf life, and long analysis time [4–6], therefore, there has been an increased need of compact, portable devices which can be repeatedly used by a person [7]. For the detection of glucose, development of enzyme-based biosensor exclusively uses glucose oxidase enzyme (GOx) which is a homodimer, redox enzyme having two molecules of co-factor flavin adenine dinucleotide (FAD), tightly bound inside deep pocket of GOx. The deep-seated redox center present in the enzyme molecule hampers fast electron transfer between electrode and redox center—flavin adenine dinucleotide (FAD) [8–10]. Therefore, the non-physiological electron acceptor is used for shuttling electron in the modern day's biosensors available in the market. Biosensors based on nanomaterials like nanoparticles [11–13], graphene [14], graphite [15, 16], carbon nanotubes (CNTs) [17–19], and their composites are also reported, as they can act as an electrical connector between the electrode and the GOX redox center—FAD [8, 20, 21]. Recently, a novel study by Gokoglan et al. [22] has reported the fabrication of a glucose biosensor by the combination of vertically aligned CNTs and a conjugated polymer. Another study conducted by Baghayeri [23] has developed an amperometric glucose biosensor by immobilizing GOx on glassy carbon electrode modified with a nanocomposite. However, these are complicated and expensive methods for biosensor fabrication. For the past two decades, attempts have been made to fabricate CNTs-based films for their applications in the field of biosensing [24–32]. CNT–polymer composites are proving better performer in glucose detection [33–38].

In the present work, we have reported the application of functionalized MWCNTs for thick filmmaking using simple fabrication method. These MWCNT films have been further used to study the immobilization of enzyme and its application as glucose biosensor (Fig. 1). Dispersion morphology and successful
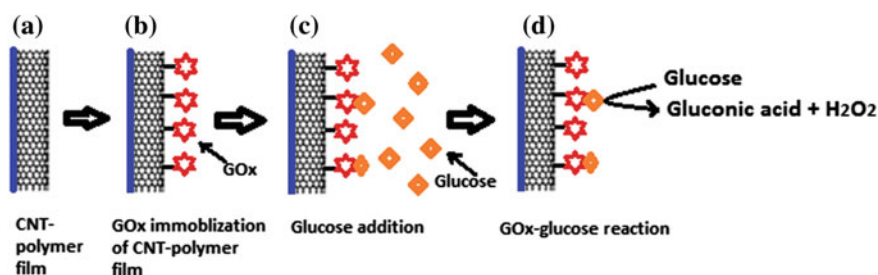

Fig. 1 shows **a** CNT–polymer-based film electrode. **b** Attachment of GOx on electrode. **c–d** Addition of glucose on CNT–polymer film-based electrode

functionalization by transmission electron microscopy and functional group determination by Fourier-transform infrared spectroscopy was performed. Bio-electronic properties of MWCNTs—polymer-based electrode were studied by bioelectrochemical techniques.

2 Materials and Methods

2.1 Reagents and Solutions

Non-functionalized MWCNTs were purchased from Chengdu Organic Chemistry Co. Ltd. Glucose oxidase (GOx) from *Aspergillus niger*, N-hydroxysuccinimide (NHS) and 1-(3 dimethylaminopropyl)-3-ethyl carbodiimide hydrochloride (EDC) was supplied from Sisco Research Laboratory Pvt. Ltd. For the preparation of buffer and electrolyte, sodium dihydrogen phosphate dehydrate ($NaH_2PO_4 \cdot 2H_2O$), sodium hydrogen orthophosphate anhydrous (Na_2HPO_4), potassium chloride, potassium ferricyanide, sulfuric acid, nitric acid, and ethanol were obtained from Fisher Scientific, India and Merck, India. Double distilled water was used throughout the experiments.

2.2 Development of Different Functional Groups on MWCNTs and Electrode Preparation

Oxidation of MWCNTs was done by stirring 100 mg of MWCNTs in 100 ml of sulfuric acid/nitric acid 3:1 (v/v) solution at 60 °C for 9–10 h. The solution was then washed with distilled water until pH 7.0 was maintained and dried in an oven for 24 h. CNTs were sonicated with ethanol for 8–10 hours. These were transferred to a glass plate (diameter 2.5 in., 1 mm thickness) with the help of micropipette. After leaving it overnight at room temperature for proper drying of ethanol, MWCNTs are heated with a polymer film (parafilm) in Muffle furnace at 80 °C after. After cooling up to room temperature, MWCNTs get transferred to parafilm surface forming a MWCNT–parafilm composite.

2.3 GOx Immobilization on CNT–Polymer-Based Film Electrode and Characterization

After pretreating with 0.1 M NaOH for 90 s, MWCNT–parafilm-based electrode was stirred in 400 mM (EDC) and NHS solution at pH 7.0 for 2 h at room temperature. After washing the MWCNT–parafilm-based film with cold water, it was further treated with GOx in 0.1 M sodium phosphate buffer at pH 7.4 with continuous stirring

for additional 2 h at room temperature. Washing is done with 0.1 M phosphate buffer containing 0.5% BSA and store at 4 °C till use. Dispersion and functionalization of MWCNTs were confirmed by TEM from Gatan and Quorum Technologies. Functionalization of MWCNTs and different bonds formation was confirmed by FTIR spectrometer from Perkin Elmer model—Spectrum RX1-mid IR.

2.4   Electrochemical Measurement

All electrochemical studies were performed in 50 mM potassium ferricyanide and 1 M potassium chloride solutions prepared in double distilled water. Electrochemical measurements were done by Gamry Interface 1000 model no. ESA 410, USA. Experiments were performed in a three-electrode setup consisting of a working electrode (MWCNT–parafilm-based electrode), Ag/AgCl reference electrode, and a platinum wire as a counter electrode. Potassium chloride–potassium ferricyanide solution was used as an electrolyte during experiments.

3   Results and Discussion

3.1   Morphological Study of Functionalized MWCNT and Fabricated MWCNT Electrodes

Oxidation of multi-walled CNT (MWCNT) using acid generates carboxylic, alcoholic, ether, or ketone groups on their surfaces, which further support immobilization of biomolecules on the CNT surfaces. Presence of various functional group appeared by the oxidation process was confirmed by taking FTIR spectra as shown in Fig. 2. There are three particularly relevant spectral bands present in the FTIR spectra of functionalized MWCNT (Fig. 2b), which are absent in non-functionalized MWCNT (Fig. 2a). The broadband at about 3420 (Fig. 2b) confirms the presence of O–H bond. Band at 1670 $\bar{\upsilon}$ and 1090 $\bar{\upsilon}$ corresponds to the C=O stretching vibrations and C–O–C stretching frequency, respectively.

Figure 3a shows the TEM image of aggregated MWCNTs showing tube structure. A striking difference could be discerned from the microstructure of MWCNTs shown in Fig. 3a and functionalized MWCNT (f-MWCNT) (Fig. 3b). The oxidized MWCNTs are dispersed with multiple darker notches at the surfaces representing points of functionalization as shown by arrows. Similar TEM images are also shown by other groups [39], which confirms the presence of functional moieties on f-MWCNT surfaces.

These functionalized CNTs are further used for the preparation of the electrode as mentioned above.
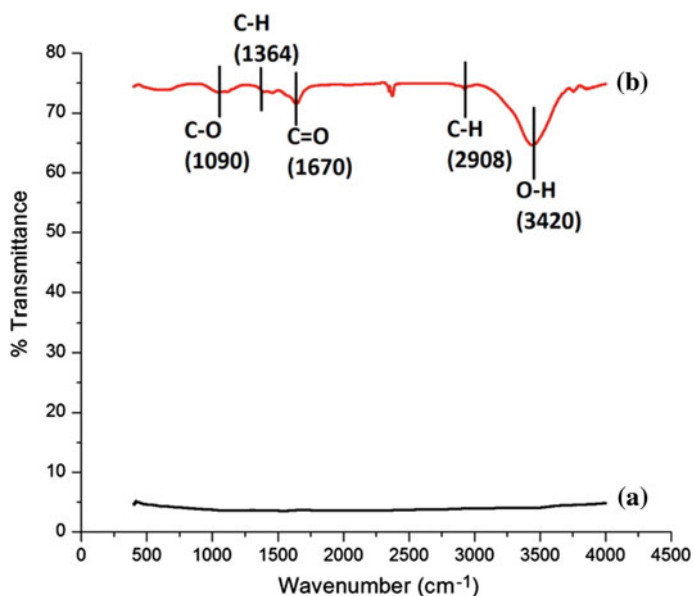
Fig. 2 FTIR spectra of **a** non-functionalized MWCNTs and **b** acid-functionalized MWCNTs
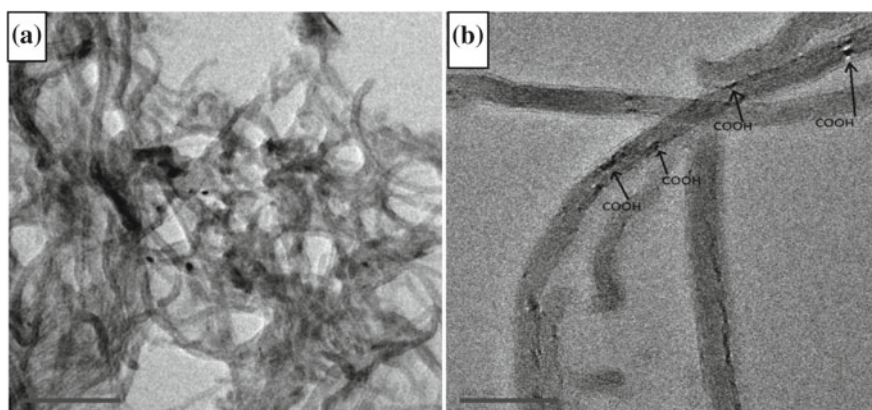

Fig. 3 TEM images: **a** non-functionalized MWCNTs showing individual fiber disaggregation, **b** functionalized MWCNTs after acid treatment showing points of functionalization by arrows

Figure 4 represents the fabrication of CNT–polymer-based film electrode by drop casting method, where CNT–ethanol suspension is drop-casted onto a clean glass plate (Fig. 4a) and subsequently, the functionalized MWCNT (f-MWCNT) film is transferred onto polymer parafilm by heat treatment in a muffle furnace (Fig. 4b). f-MWCNT embedded onto polymer surface is then further processed for the
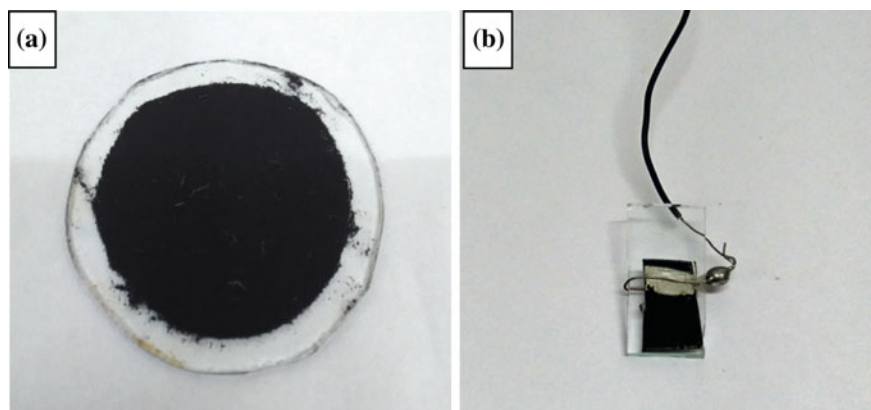
Fig. 4 Preparation of MWCNT—parafilm-based film electrode: **a** MWCNT film on glass plate by drop casting method, **b** MWCNT–parafilm-based electrode with electrical contacts

preparation of electrode by using poly circuit board as a surface and electrical contacts were made for conductivity measurements.

The immobilization of GOx on f-MWCNT–parafilm composite film is achieved by using EDC-NHS chemistry, which generates amide-linkage between f-MWCNT–parafilm composite film and GOx molecule. The f-MWCNT–parafilm composite film can be differentiated from other films, i.e., non-functionalized MWC-NT–parafilm composite film by comparing their electrochemical properties.

3.2 Cyclic Voltammetric (CV) Analysis

The step-wise assembly of GOx enzyme electrode is characterized by CV using 50 mM $[Fe(CN)_6]^{3-/4-}$ with 0.1 M KCl as the redox probe, and the results are presented in Fig. 5 shows cyclic voltammogram of non-functionalized MWC-NT–parafilm based electrode (--), f-MWCNT–parafilm-based electrode (--) and GOx immobilized-f-MWCNT–parafilm-based electrode (--) in potassium ferri-cyanide–potassium chloride system [40]. The considerable differences in peak heights (amperometric current) and peak shifts are observed with cathodic currents 87.92, 206.9 and 229.1 µA and anodic currents −157.9, −354.0 and −335.2 µA for non-functionalized MWCNT–parafilm-based electrode, f-MWCNT–parafilm-based electrode and GOx immobilized f-MWCNT–parafilm-based electrode respectively. The variation of peak current and shifts has also been studied by changing scan rate, i.e., 50, 100, 150, 200, 300, 400, and 500 mV/s. Figure 5b represents cyclic voltammogram of f-MWCNTparafilm-based electrode showing an increase in peak heights with an increase in scan rate, which is a characteristic feature for the redox process of potassium ferrocyanide at the surface of the f-MWCNT film. The results
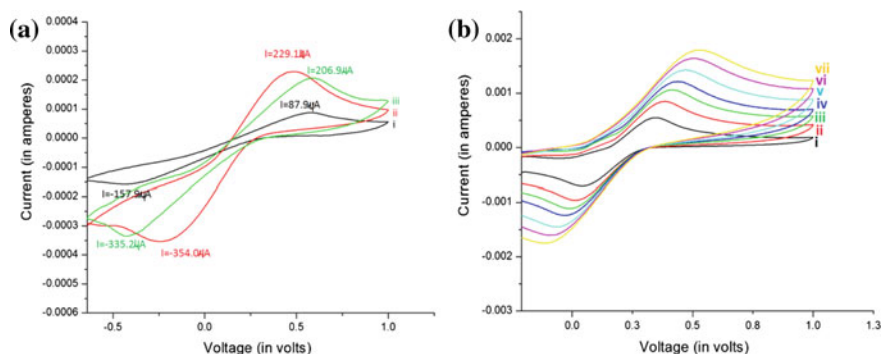
Fig. 5 Cyclic voltammetry of **a** non-functionalized MWCNT–parafilm-based electrode (i) (--), functionalized MWCNT–parafilm-based electrode (ii) (--) and GOx immobilized-functionalized MWCNT–parafilm-based electrode (iii) (--) **b** effect of increasing scan rate (i) 50 mV/s (ii) 100 mV/s (iii) 150 mV/s (iv) 200 mV/s (v) 300 mV/s (vi) 400 mV/s (vii) 500 mV/s
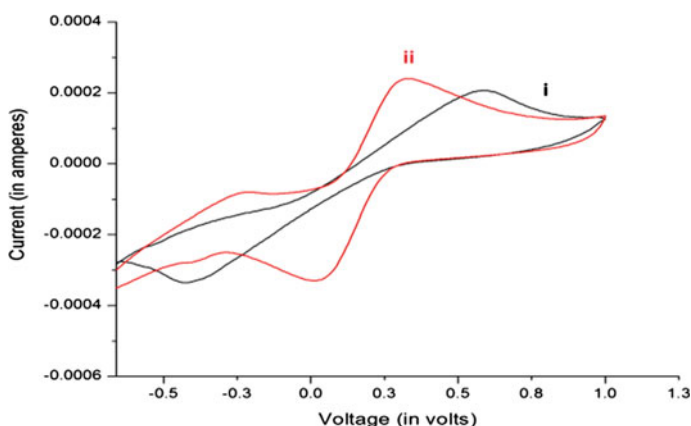
Fig. 6 shows cyclic voltammogram of MWCNT–parafilm-based film electrode response in the absence (--) (i) and presence (--) (ii) of glucose

suggest that the fabricated f-MWCNT–parafilm-based electrodes are efficient enough to measure the redox changes between ±1.0 V, which include the redox potential of redox process occurring in the active site of GOx enzyme, i.e., FAD $\rightleftharpoons$ FADH$_2$.

The biosensing capability of GOx-immobilized f-MWCNT–parafilm-based electrode was also checked by performing cyclic voltammetry in presence of glucose as shown in Fig. 6.

The cyclic voltammogram step I represents the redox process of potassium ferrocyanide at the GOx immobilized f-MWCNT–parafilm-based electrode only. Addition of glucose in the electrochemical setup leads to the following biochemical process:

$$\text{Glucose} + [\text{GOx}]_{ox} \rightarrow \text{Gluconic acid} + [\text{GOx}]_{red} \text{ (step 1)}$$

$$[\text{GOx}]_{red} + \text{Fe}^{3+} \rightarrow [\text{GOx}]_{ox} + \text{Fe}^{2+} \qquad \text{(step 2)}$$
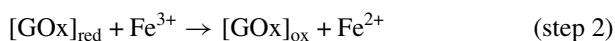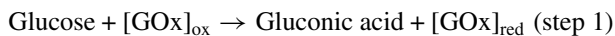
Here, potassium ferricyanide is acting as an electron mediator for conversion of Fe(III) into Fe(II) in step 2. Consequently, the oxidation and reduction peaks shift from 590.4 to 330.4 and -424.8 to -10.26 mV, respectively, in cyclic voltammogram of GOx-immobilized f-MWCNT–parafilm-based electrode as shown in Fig. 6. Current the profile also shows variation, i.e., cathodic current increases from 229.1 to 239.8 µA and anodic current increases from -335.2 to -330.0 µA after the addition of glucose solution at the electrode surface.

4 Conclusion

In summary, we have developed a simple strategy to fabricate a glucose biosensor based on f-MWCNT–parafilm-based electrode system. The structural features and electrochemical studies suggest that it can be used efficiently for the measurement of glucose in the aqueous medium. Other biosensor properties are under study to establish the GOx-immobilized f-MWCNT–parafilm-based electrode as advanced glucose biosensor.

References

1. Zimmet, P., Alerti, K.G., Magliano, D.J., Bennett, P.H.: Diabetes mellitus statistics on prevalence and mortality: facts and fallacies. Nat. Rev. Endocrinol. **12**, 616–622 (2016)
2. Saydah, S., Imperatore, G., Cheng, Y., Geiss, L.S., Albright, A.: Disparities in diabetes deaths among children and adolescents-United States, 2000–2014. Morb. Mortal. Wkly Rep. **66**(19), 502–505 (2017)
3. Li, J., Zhang, D., Li, Y., Wu, J., Zhang, B.: Joint similar and specific learning for diabetes mellitus and impaired glucose regulation detection. Inf. Sci. **384**, 191–204 (2017)
4. Galant, A.L., Kaufman, R.C., Wilson, J.D.: Glucose: detection and analysis. Food Chem. **188**, 149–160 (2015)
5. Daines, T.L., Morse, K.W.: A spectrophotometric method for determination of glucose in blood serum. Logan **53**, 126–127 (1976)
6. Dohnal, L., Kalousova, M., Zima, T.: Comparison of three methods for determination of glucose. Prague. Med. Rep. **111**, 42–54 (2010)
7. Lin, T., Gal, A., Mayzel, Y., Horman, K., Bahartan, K.: Non-invasive glucose monitoring: a review of challenges and recent advances. Curr. Trends. Biomed. Eng. Biosci. **6**(5), 001–008 (2017)

8. Goran, J.M., Mantilla, S.M., Stevenson, K.J.: Influence of surface adsorption on the interfacial electron transfer of flavin adenine dinucleotide and glucose oxidase at carbon nanotube and nitrogen-doped carbon nanotube electrodes. Anal. Chem. **85**, 1571–1581 (2012)

9. Deng, C., Chen, J., Nie, Z., Si, S.: A sensitive and stable biosensor based on the direct electrochemistry of glucose oxidase assembled layer-by-layer at the multiwall carbon nanotube-modified electrode. Biosens. Bioelectron. **26**, 213–219 (2010)

10. Tsai, T.W., Heckert, G., Neves, L.F., Tan, Y., Kao, D.Y., Harrison, R.G., Resasco, D.E., Schmidtke, D.W.: Adsorption of glucose oxidase onto single-walled carbon nanotubes and its application in layer-by-layer biosensors. Anal. Chem. **81**, 7917–7925 (2009)

11. Xian, Y., Hu, Y., Liu, F., Xian, Y., Wang, H., Jin, L.: Glucose biosensor based on Au nanoparticles-conductive polyaniline nanocomposite. Biosens. Bioelectron. **21**, 1996–2000 (2006)

12. Han, X., Zhu, Y., Yang, X., Li, C.: Amperometric glucose biosensor based on platinum nanoparticle encapsulated with a clay. Microchim. Acta **171**, 233–239 (2010)

13. German, N., Ramanavicius, A., Ramanaviciene, A.: Amperometric glucose biosensor based on electrochemically deposited gold nanoparticles covered by polypyrrole. Electroanalysis **29**, 1267–1277 (2017)

14. Guo, S., Dong, S.: Graphene nanosheet: synthesis, molecular engineering, thin film, hybrids, ad energy and analytical applications. Chem. Soc. Rev. **40**, 2644–2672 (2011)

15. Gallay, P., Tosi, E., Madrid, R., Tirado, M., Comedi, D.: Gluocse biosensor based on functionalized ZnO nanowire/graphite films dispersed on a Pt electrode. Nanotechnology **27**, 425501–425508 (2016)

16. Hui, Z.H., Hong, C., Hua, C.J., Fei, K.Y.: Polyaniline-graphite composite film glucose oxidase electrode. J. Cent. South Univ. Technol. **13**, 653–657 (2006)

17. Zhang, H., Meng, Z., Wang, Q., Zheng, J.: A novel glucose biosensor based on direct electrochemistry of glucose oxidase incorporated in biomediated gold nanoparticles-carbon nanotubes composite film. Sens. Actuators. **158**, 23–27 (2011)

18. Mani, V., Devadas, B., Chen, S.: Direct electrochemistry of glucose oxidase at electrochemically reduced grapheme oxide-multiwalled carbon nanotubes hybrid material modified electrode for glucose biosensor. Biosens. Bioelectron. **41**, 309–315 (2013)

19. Gao, W., Tjiu, W.W., Wei, J., Liu, T.: Highly sensitive non enzymatic glucose and H_2O_2 sensor based on $Ni(OH)_2$/electroreduced graphene oxide-Multiwalled carbon nanotube film modified glass carbon electrode. Talanta **120**, 484–490 (2014)

20. Liu, J., Sun, S., Shang, H., Lai, J., Zhang, L.: Electrochemical biosensor based on bioenzyme and carbon nanotubes incorporated into an Os-complex thin film for continuous glucose detection in human saliva. Electroanalysis **28**, 1–7 (2016)

21. Wu, Y., Hu, S.: Biosensors based on direct electron transfer in redox proteins. Microchim. Acta **159**, 1–17 (2007)

22. Gokoglan, T.C., Soylemez, S., Kesik, M., Dogru, I.B., Turel, O., Yuksel, R., Unalan, H.E.: Toppare, L: a novel approach for the fabrication of a flexible glucose biosensor: The combination of vertically aligned CNTs and a conjugated polymer. Food Chem. **220**, 299–305 (2017)

23. Baghayeri, M., Veisi, H., Ghanei-Motlagh, M.: Amperometric glucose biosensor based on immobilization of glucose oxidase on a magnetic glassy carbon electrode modified with a novel magnetic nanocomposite. Sens. Actuators B, **249**, 321–330 (2017)

24. Jacobs, C.B., Peairs, M.J., Venton, B.J.: Review: carbon nanotube based electrochemical sensors for biomolecules. Anal. Chim. Acta **662**, 105–127 (2010)

25. Shan, C., Yang, H., Han, D., Zhang, Q., Ivaska, A., Niu, L.: Graphene/AuNPs/chitosan nanocomposites film for glucose biosensing. Biosens. Bioelectron. **25**, 1070–1074 (2010)

26. Saglam, O., Dilgin, Y.: Fabrication of photoelectrochemical glucose biosensor in flow injection analysis system using ZnS/CdS-Carbon nanotube nanocomposite electrode. Electroanalysis **29**, 1–10 (2017)

27. Shrestha, B.K., Ahmad, R., Mousa, H.M., Kim, I., Kim, J., Neupane, M.P., Park, C.H., Kim, C.S.: High-performance glucose biosensosr based on chitosan-glucose oxidase immobilized ploypyrrole/Nafion/functionalized multi-walled carbon nanotubes bio-nanohybrid film. J. Colloid Interface Sci. **482**, 39–47 (2016)

28. Saei, A.A., Najafi-Marandi, P., Abhari, A., Guardia, M., Dolatabadi, J.E.N.: Electrochemical biosensors for glucose based on metal nanoparticles. Trends. Anal. Chem. **00**, 1–12 (2012). https://doi.org/10.1016/j.trac.2012.09.011

29. Gao, G., Luo, J., Ge, Z., Chen, S., Chen, S., Yang, H.: Self-assembling of electrochemical glucose biosensor with bacteriostatic materials via layer-by-layer method. J. Electrochem. Soc. **164**, 189–192 (2017)

30. Wooten, M., Karra, S., Zhang, M., Gorski, W.: On the direct electron transfer, sensing and enzyme activity in the glucose oxidase/carbon nanotubes system. Anal. Chem. **86**(1), 752–757 (2014). https://doi.org/10.1021/ac403250w

31. Turkmen, E., Bas, S.Z., Gulce, H., Yildiz, S.: Glucose biosensor based on immobilization of glucose oxidase in electropolymerized poly(o-phenylenediamine) film on platinum nanoparticles-polyvinylferrocenium modified electrode. Electrochimica Acta. **123**, 93–102 (2014). https://doi.org/10.1016/j.electacta.2013.12.189

32. Prasad, R., Bhat, B.R.: Multi-wall carbon nanotube-NiO nanoparticle composite as enzyme-free electrochemical glucose sensor. Sens. Actuators B Chem. **220**, 81–90 (2015). https://doi.org/10.1016/j.snb.2015.05.065

33. Liu, Y., Wang, M., Zhao, F., Xu, Z., Dong, S.: The direct electron transfer of glucose oxidase and glucose biosensor based on carbon nanotubes/chitosan matrix. Biosens. Bioelectron. **21**, 984–988 (2005)

34. Luo, X., Xu, J., Wang, J., Chen, H.: Electrochemically deposited nanocomposite of chitosan and carbon nanotubes for biosensor application. Chem. Commun. **16**, 2169–2171 (2005)

35. Vashist, S.K., Zheng, D., Al-Rubeaan, K., Luong, J.H.T., Sheu, F.: Advances in carbon nanotube based electrochemical sensors for bioanalytical applications. Biotechnol. Adv. **29**, 169–188 (2011)

36. Wang, Y., Liu, L., Li, M., Xu, S., Gao, F.: Multifunctional carbon nanotubes for direct electrochemistry of glucose oxidase bioassay. Biosens. Bioelectron. **30**, 107–111 (2011)

37. Lin, Y., Lu, F., Tu, Y., Ren, Z.: Glucose biosensors based on carbon nanotubes nanoelectrodes ensembles. Nano Lett. **4**(2), 191–195 (2004)

38. Pan, D., Chen, J., Yao, S., Tao, W., Nie, N.: An amperometric glucose biosensor based on glucose oxidase immobilized in electropolymerized poly(o-aminophenol) and carbon nanotubes composite film on a gold electrode. Anal. Sci. **21**, 367–371 (2005)

39. Saifuddin, N., Raziah, A.Z., Junizah, A.R.: Carbon nanotubes: a review on structure and their interaction with proteins. J. Chem. **013**, 1–18 (2013)

40. Mobbott, G.A.: An introduction of cyclic voltammetry. J. Chem. Educ. **60**, 697–702 (1983)

Formulation and Characterization of Poly (D, L-Lactide-Co-glycolide) Nanoparticles Loaded with *Achyranthes aspera* for Increasing Bioavailability

Aditi Sangal and Sunita Rattan

Abstract The use of traditional medicines has increased tremendously to improve health conditions as they symbolize safety in contrast to synthetic medicines, which tend to produce undesirable side effects The components of medicinal plants have shown promising potential to prevent and treat a wide range of chronic diseases but a scientific approach is needed to increase the bioavailability of components and their delivery in a sustained manner to avoid repeated administration. The low bioavailability may be attributed to low aqueous solubility, degradation in the gastrointestinal tract, increased metabolism, or more systemic elimination. However, nanotechnology-based new processes are being explored worldwide to enhance their bioavailability, improve cellular uptake, increased dissolution rates, good blood stability, and controlled release. Hence, the integration of these nanocarriers with the traditional medicine system is very essential. *Achyranthes aspera* grows throughout the world and belongs to the family Amaranthaceae. It is a small, much branched, and perennial herb of about 1–2 m in height. It has been a well-known plant drug in different systems of medicine and various home remedies and is traditionally valued as an effective medicinal agent having antibacterial, anti-inflammatory, anticoagulant, antitumor, antiarthritic, antidepressant, antinociceptive, antihepatocarcinogenic activity, hypoglycaemic, and various other important medicinal properties. To overcome the bioavailability limitations and prolong the efficacy of its components, the overall aim of the present study was to synthesize poly (D, L-lactide-co-glycolide) (PLGA) nanoparticles loaded with *A. aspera* by solvent evaporation method using Pluronic F-68 as a surfactant. The nanoparticles exhibited a smooth and spherical shape with an average size between 150 and 180 nm. Characterization of PLGA nanoparticles loaded with *A. aspera* showed the successful encapsulation of the drug. The entrapment efficiency and percentage yield was nearly 60.0 and 58.0%, respectively. X-ray diffraction (XRD) analysis demonstrated that *A. aspera*-loaded nanoparticles are amorphous in nature. No apparent shifts were observed in the IR bands indicating the absence of direct molecular interactions between the polymer

A. Sangal (✉) · S. Rattan
Department of Chemistry, Amity Institute of Applied Sciences, Amity University,
Sector 125, Noida 201303, Uttar Pradesh, India
e-mail: asangal@amity.edu

and drug. The in vitro release pattern from PLGA nanoparticles loaded with *A. aspera* at pH 7.2 was characterized by an initial burst and then a sustained release. The study demonstrates the successful encapsulation of *A. aspera* in PLGA for the first time for enhancing bioavailability and also to sustain its release. This nanoparticulate drug delivery system has a great potential for future clinical application.

Keywords *Achyranthes aspera* · Nanoparticles · Bioavailability

1 Introduction

Plants have been used as medicine to maintain human health from ages [1]. Indian Materia Medica has about 2000 drugs of natural origin, which are derived from different traditional systems. However, there are a number of plants, which have not been mentioned in these reports, in spite of their usage in the traditional and folk medicinal systems. These unexplored sources have the potential for development of new therapy which might help in overcoming the problem of resistance and toxicity of currently available medicines. These traditional medicines are relatively safer and cheaper as compared to modern synthetic medicines. *Achyranthes aspera* is a plant distributed throughout the world and belongs to Amaranthaceae family [2]. It is an important medicinal herb, which plays an important role in various systems of medicine in India. Different parts of the plant have various active ingredients used for different health remedies. It is traditionally used in the treatment of inflammation, diabetes, wounds, hypertension, pneumonia, diarrhea, dysentery, asthma, cough, dropsy, pain, rheumatism, and other diseases [3–5].

Conventional drug delivery involves periodic dosing of a drug, which results in drug-level oscillations around a desired steady-state level. Nowadays, PLGA-based nanotechnology [6] is used in many medical applications, such as drug delivery, sustained release of drug, and treatment due to its properties such as biocompatibility, bioavailability, changing degradation kinetics, high drug loading capability, stability, and increased drug release over other carriers. They also help in protecting sensitive ingredients from the unwanted reaction that may cause different structural changes [7]. Thus, the controlled drug delivery strategies involving polymeric nanoparticles are expected to change the landscape of pharmaceutical industries in the future. The present work provides a simple and effective nanoformulation loaded with *A. aspera* for prolonging the efficacy and sustained release of drug in patients suffering from different ailments.

2 Materials and Methods

The polymer poly (D,L-lactide-co-glycolide) (PLGA), having a copolymer ratio of DL-lactide to glycolide of 50:50 ($M_w = 24{,}000$ to 38,000) was obtained from

Sigma-Aldrich. The surfactant Pluronic F-68 was procured from Sigma-Aldrich. The organic solvents used methanol, dichloromethane, ethyl acetate, and acetone were of analytical grade. Sodium dihydrogen phosphate, disodium hydrogen phosphate and trisodium phosphate used are of analytical grade. Dialysis bag was used for in vitro release studies.

2.1 Preparation of Achyranthes aspera Extract

A. aspera plant was obtained from the region of Himachal Pradesh. The different parts of the plant were separated, impurities were removed, shade dried, and the leaves were powdered in a mixer. The powder was then sieved to get a uniform size range. This sieved powder was stored in airtight bottles. Methanol was used for further extraction. 10 g of the powder was soaked in 100 ml methanol for 24 h. This preparation was further filtered through a Whatman No. 1 filter paper and the solvent was allowed to evaporate from the filtered extract at room temperature. The dried extract so obtained was stored in bottles for further use.

2.2 Preparation of Achyranthes aspera-Loaded PLGA Nanoparticles

Solvent evaporation method was used to prepare PLGA nanoparticles with or without methanolic extract of A. aspera. First, the organic phase was prepared on dissolving 50 mg of PLGA in 10 ml of acetone, dichloromethane and ethyl acetate with or without 10 mg of the methanolic extract of A. aspera. The organic phase was then added to 25 ml of the aqueous solution containing 0.1% Pluronic F-68, under stirring at room temperature. This resulting solution was then sonicated for 3 min with the help of microtip probe sonicator set at 55 W of energy output (Misonix Sonicator®). From the resulting dispersion of nanoparticles, the highly volatile organic solvent was evaporated at room temperature by constant stirring at 300 rpm with a magnetic stirrer. The nanoparticles were recovered by centrifugation (REMI, India) for 15 min at 15,000 rpm, washed with double distilled water. The purified nanoparticles were freeze-dried. An attempt was also made to optimize the nanoparticles formulation by using different solvents.

2.3   Evaluation of Morphology of Nanoparticles by Scanning Electron Microscopy (SEM)

The shape and surface morphology of *A. aspera*-loaded PLGA nanoparticles was examined using a Zeiss EVOMA10 scanning electron microscope. An appropriate sample of nanoparticles was dispersed on the metal stubs which were coated with double-sided adhesive tape. The samples were dried under vacuum and then coated with a gold layer using an ion sputter. Observations were carried out at an accelerating voltage of 20 kV and 10 Pa after 30 nm coating.

2.4   X-Ray Diffractometry (XRD)

The XRD patterns of *A. aspera*, PLGA, and *A. aspera*-loaded PLGA nanoparticles were determined using PANalytical X-ray diffractometer. The measurements were taken at an accelerating voltage of 45 kV and an anodic current of 40 mA. XRD patterns were obtained at diffraction angles (2θ) ranging from 5 to 90° at a scanning speed of 2° per minute.

2.5   Fourier Transform Infrared (FTIR) Spectroscopy

To confirm the compatibility between *A. aspera*, PLGA, and *A. aspera*-loaded PLGA nanoparticles, the samples were analyzed with FTIR spectroscopy. The spectra were recorded in the range 400–4000 cm^{-1}. The powdered samples were compressed into pellets after dispersing in KBr.

2.6   Determination of Achyranthus aspera Entrapment

Briefly, 1 ml methanol was added to 10 mg of *A. aspera*-loaded PLGA nanoparticles sample and vortexed for 20 min at room temperature. This suspension was centrifuged for 30 min at 12,000 rpm on room temperature. The concentration of *A. aspera* in the supernatant was measured. All analyses were done three times and an average of them are reported.

2.7 *In Vitro Drug Release Studies*

The in vitro drug release studies from *A. aspera*-loaded PLGA nanoparticles were performed, using phosphate-buffered saline (PBS) solution at pH 7.2 and a study was carried out under physiological conditions up to 6 h. About 10 mg each of *A. aspera* and *A. aspera*-loaded PLGA nanoparticles were placed in a dialysis bag. The dialysis bag was immersed in a beaker containing 20 ml of PBS at pH 7.2. The entire system was kept at room temperature with magnetic stirring at 100 rpm. At certain intervals of time (30 min, 1, 2, 4, 8, 24 h) 3 ml of the solution was withdrawn. The withdrawn samples were assayed for the drug release by recording absorbance at a wavelength of 671 nm, using Shimadzu UV–Vis spectrophotometer. The cumulative release of the drugs was plotted as a function of time.

3 Results and Discussion

3.1 *Evaluation of Morphology and Determination of Nanoparticles Size*

The *A. aspera*-loaded PLGA nanoparticles exhibited a smooth and spherical shape as shown in Fig. 1. SEM images showed the formation of distinct nanoparticles in the range of 150–180 nm with dichloromethane as the solvent. Moreover, it was observed that there is a substantial change in the size of the nanoparticles ranging from 200 to 350 nm in *A. aspera*-loaded PLGA nanoparticles during the use of acetone and ethylacetate in different formulations F2 and F3 respectively as shown in Table 1. The smaller size of *A. aspera*-loaded PLGA nanoparticles of formulation F1 was considered for further studies, which are assumed to be a contributory factor for the slow drug release. The encapsulation efficiency was comparable in the different formulations.

Table 1 Characteristics of *A. aspera*-loaded PLGA nanoparticles

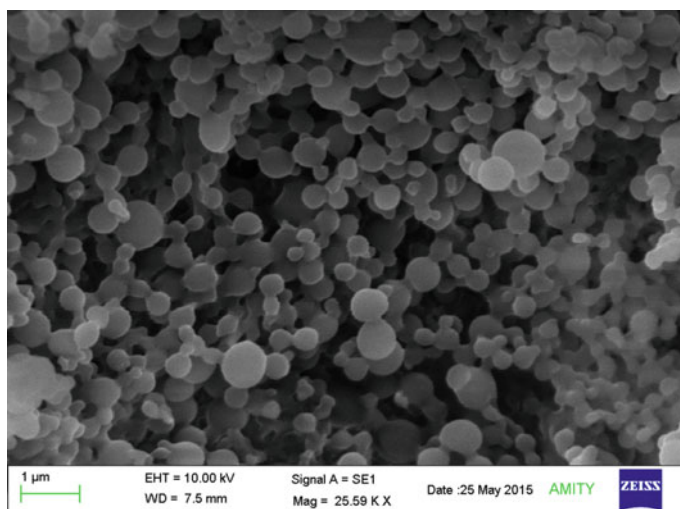| Formulation	Stabilizer	Solvent	Drug–polymer ratio	Encapsulation efficiency (%)	Mean particle size (nm)
F1	Pluronic F-68	Dichloromethane	1:5	63	150
F2	Pluronic F-68	Acetone	1:5	70	308
F3	Pluronic F-68	Ethylacetate	1:5	59	243

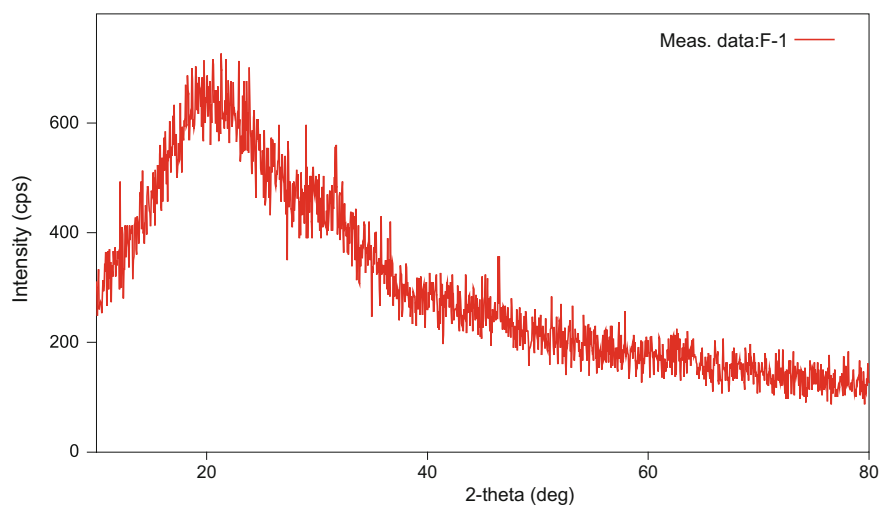**Fig. 1** SEM images of polymeric nanoparticles loaded with *A. aspera*

Fig. 2 XRD diffractogram of *A. aspera*-loaded PLGA nanoparticles

3.2 XRD Studies

The X-ray diffraction patterns for *A. aspera*-loaded PLGA nanoparticles of formulation F1 (Fig. 2) was obtained. No characteristic peak was observed for the drug and also for the drug, which is entrapped into nanoparticles due to the amorphous nature of the drug.
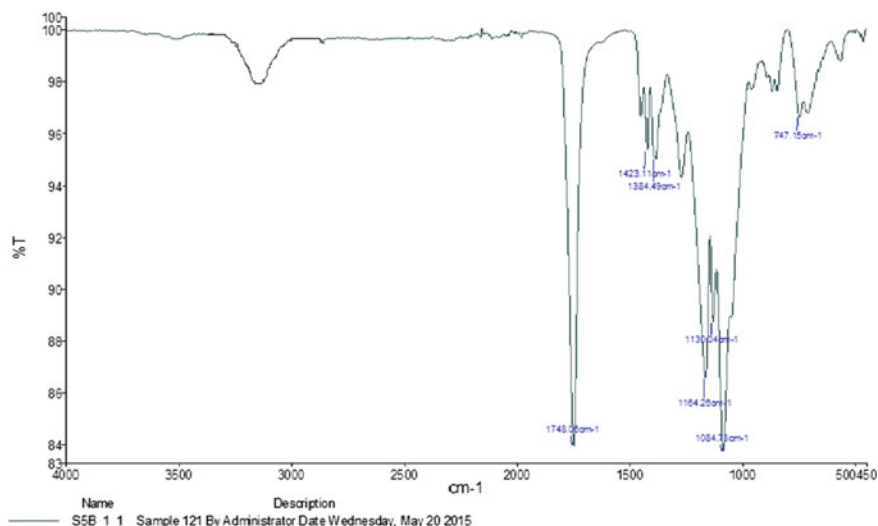
Fig. 3 FTIR spectra of *A. aspera*-loaded PLGA nanoparticles

3.3 FTIR of **Achyranthes aspera**-*Loaded PLGA Nanoparticles*

Fourier transform infrared (FTIR) spectroscopic studies were carried out to study the drug–polymer interactions. To confirm the compatibility between PLGA and *A. aspera*-loaded PLGA nanoparticles, the FTIR spectra were recorded in the range 400–4000 cm^{-1}. The powdered samples were dispersed in KBr and compressed into pellets. The structural characteristics of the pure drug, PLGA and *A. aspera*-loaded PLGA nanoparticles, studied by FTIR spectroscopy were comparable and intact as shown in Fig. 3. The characteristic peaks of PLGA were observed at 3394, 2942, 1708, 1442, 1344, 1346, 1149, 1051, 730, 548 cm^{-1}. Besides the characteristic groups for the copolymer PLGA, the *A. aspera*-loaded PLGA nanoparticles spectra showed all the characteristic groups of *A. aspera* with no major shifting as well as loss of functional peaks, which indicates that no chemical interactions occur between *A. aspera* and the polymer.

3.4 In Vitro Release of Drug from **Achyranthes aspera**-*Loaded PLGA Nanoparticles*

The release study of a drug from *A. aspera*-loaded PLGA nanoparticles in vitro was examined by UV spectroscopy as shown in Fig. 4. The drug-loaded PLGA nanoparticulate formulations prepared showed biphasic release profile. That is a
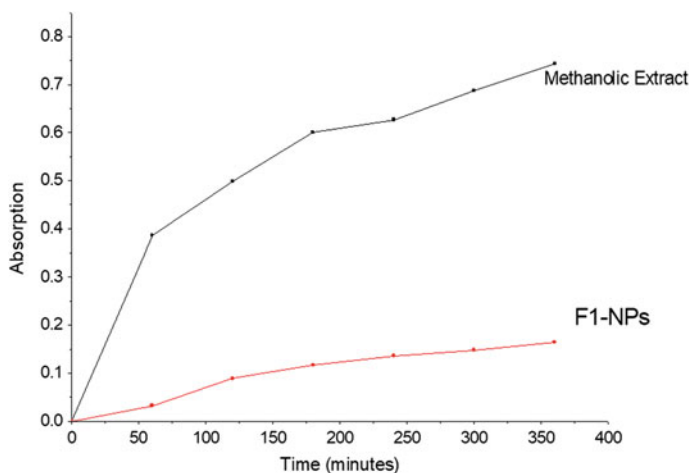
Fig. 4 Comparative sustained release of *A. aspera* from PLGA nanoparticles

rapid release followed by a slower release. It was found that the nanoparticulate formulation has a slow release of the drug. It is clear from Fig. 4 that the time taken by *A. aspera*-loaded PLGA nanoparticles is less as compared to *A. aspera*.

4   Conclusion

In this work, for the first time, *A. aspera*-loaded PLGA nanoparticles have been prepared successfully for increasing the bioavailability of the active components in the leaves which possess slow and sustained release to be used against the treatment of various ailments. Due to the hydrophobicity of the components, its application is limited. Here *A. aspera*-loaded PLGA nanoparticles are produced by solvent evaporation method. The *A. aspera*-loaded PLGA nanoparticles have 63% encapsulation efficiency. The release property of *A. aspera* from the nanoparticles is slow and sustained leading us to the conclusion that *A. aspera*-loaded PLGA nanoparticles have strong potential for ailments.

References

1. Kingston, D.G.I.: Modern natural products drug discovery and its relevance to biodiversity conservation (review). J. Nat. Prod. **74**(3), 496–511 (2011)
2. Srivastav, S., Singh, P., Mishra, G., Jha, K., Khosa, R.: *Achyranthes aspera*-an important medicinal plant: a review. J. Nat. Prod. Plant Resour. **1**(1), 1–4 (2011)

3. Rafiqkhan, M., Saranya, : Pharmacognostic profile and phytochemical investigation on the leaves of *Achyranthes aspera*. Int. J. Pharm. Pharm. Sci. **5**(3), 368–370 (2013)
4. Dwivedi, S., Dubey, R., Mehta, K.: *Achyranthes aspera* Linn. (Chirchira): a magic herb in folk medicine. Ethnobotanical leaflets **12**, 670–676 (2008)
5. Chakraborty, A., Branter, A., Mukainaka, T., Nobukuni, Y., Kuchide, M., Konoshima, T., Tokuda, H., Nishino, H.: Cancer chemopreventive activity of *Achyranthes aspera* leaves on on Epstein-Barr virus activation and two-stage mouse skin carcinogenesis. Cancer Lett. **177**(1), 1–5 (2002)
6. Dinarvand, R., Sepehri, N., Manoochehri, S., Rouhani, H., Atyabi, F.: Polylactide-co-glycolide nanoparticles for controlled delivery of anticancer agents. Int. J. Nanomed. **6**, 877–895 (2011)
7. Zohri, M., Shafiee, A.M., Haririan, I., Shafiee, A.M., Sadat, E.S.E., Tarighati, S.H., Sadjadi, S.K.: A comparative study between the antibacterial effect of nisin and nisin-loaded chitosan/alginate nanoparticles on the growth of staphylococcus aureus in raw and pasteurized milk samples. Probiotics Antimicrob. Prot. **2**, 258–266 (2010)

Anticancer Drug-Loaded Folate-Conjugated Multiwalled Carbon Nanotubes

Bharti Mangla, Kuldeep Singh Patel, Pankaj Kumar and Kanchan Kohli

Abstract The proposed study was to assess the in vitro development of folate-conjugated anthracycline antibiotic-loaded multiwalled nanotubes. These prepared systems have the advantage of direct penetration to the cancer cells and have a targeting ability. Doxorubicin was selected as a drug due to its high loading capacity in nanotubes and a BCS class III drug. Nanotubes were purified and functionalized with folic acid using *N*-Hydroxysuccinimide and 1-ethyl-3-(-3-dimethylaminopropyl) carbodiimide hydrochloride chemistry. After purification and functionalization, various evaluation parameters were performed like zeta potential, dispersion characteristics, Fourier-transform infrared spectroscopy, X-ray diffraction, elemental analysis, and transmission electron microscope analysis. The drug was loaded after folic acid conjugation, and then characterized with parameters like drug loading efficiency and in vitro drug release. As the degree of functionalization increases like first was purified multiwalled carbon nanotubes, then carboxylated and then folate-conjugated carbon nanotubes, entrapment also increases however due to its high dispersity with high steric hindrance and sustained release. Prepared folate-conjugated multiwalled nanotubes have great potential as a novel drug delivery system and tremendous beneficial properties. This anticancer targeted on the body which reduces the side effects and enhancing the therapeutic efficacy.

Keywords Multiwalled carbon nanotubes · Functionalization · Anticancer drugs Folic acid · Purified nanotubes etc.

B. Mangla (✉) · K. Kohli
Department of Pharmaceutics, Jamia Hamdard, New Delhi 110062, India
e-mail: bharti.mangla91@gmail.com

K. S. Patel
Amity Institute of Pharmacy, Amity University, Noida 201303,
Uttar Pradesh, India

P. Kumar
Department of Pharmaceutics, Advanced Institute of Pharmacy, Palwal 121102,
Haryana, India

1   Introduction

Cancer, main cause of death, and thus, great efforts have been done to improve the outcome of cancer therapy [1]. Current conventional treatments for cancers include surgery, radiation therapy, hormone therapy, and chemotherapy [2]. These conventional therapies frequently lack accurate tools for detection of early-stage tumors and anticancer agents distributing nonspecifically in the whole body, hence, associated serious side effects of anticancer agents [3]. So, urgent treatment is needed.

Nanoscience provides an alternative approach to overcome the limitation of conventional anticancer therapy [4]. Nanoscience, the compact science constitutes a system in nano range which provides us a better, efficient, developed and rapidly expanding form of science. The last few years constitutes the era of nanoscience that involves the discovery, development, and production of novel materials of the nanometric size range. These are either organic or inorganic matter and in most cases, are untouched by pharmaceutical sciences.

The majority of nanoparticles are used for diagnosis and cancer therapy i.e. liposomes, polymers, nanolipid carrier system, SMEDDS, SNEDDS, micelles, proteins, antibodies, gold nanoparticles, silver nanoparticles, multiwalled and single-walled carbon nanotubes [5]. Out of these nanoparticles, multiwalled nanotubes have shown great potential for cancer as targeted anticancer drug delivery [6, 7]. These novel nanomaterials, nanoparticles, nanocomposites constitute a growing field known as nanomedicine.

CNTs, cylindrical graphite structure which exhibits massive physical properties as determined by their graphite structure. Due to their chemical functionalization strategies, carbon nanotubes are used in a wide variety of application ranging from electronics, mechanical and structural composite to medicine [8]. Nanotubes also be used in the active targeting. Inactive targeting, a nanoparticle (CNTs) is combined with some specific targeting moieties [9] like folic acid, polyunsaturated fatty acids, hyaluronic acid, peptides [10], and thereby permitting accumulation of the drug within selected cancer tissues, cells, or intracellular organelles that are associated with particular molecules in cancer cells [11].

Folate targeting has some additional advantages [12] like folic acid is inexpensive, nonimmunogenic, small in size, low weight and could be easily coupled with a variety of therapeutic drugs and radio imaging agents as it is found to be stable against organic solvents [13], acids and bases [14]. Cancer cells, unlike normal human cells, overexpress folate receptors which have a high affinity for folic acid [13]. These receptors can be used for the uptake of folic acid in the cell and allow it to cross the membrane through receptor-mediated endocytosis [15].

The proposed work envisages the development and characterization of folic acid conjugated doxorubicin-loaded multiwalled nanotubes. The advantage of this system is to direct penetration of drug to the cells and conjugation with folic acid, and have targeting ability. Doxorubicin was selected as a drug in this study due to its high loading of nanotubes.

2 Materials

Multiwalled nanotubes (MWCNTs) generated by chemical vapor deposition; (carbon content >98.9%) having dimensions of 110–170 nm × 5–9 μm, was obtained from Sigma-Aldrich, USA. PTFE filters with size 0.22 μ (Axiva Sichem, New Delhi), Folic acid (Himedia, India), and Dialysis bag (Himedia, India). 1-ethyl-3-(-3-dimethylaminopropyl) carbodiimide hydrochloride (EDC) and *N*-Hydroxysuccinimide (Himedia, Mumbai). All other chemicals and reagents were of AR grade with greater than 90% purity. Deionized water has been used.

2.1 Purification

(a) *Acid Treatment*

MWCNTs (10 mg) was taken and transferred to a glass beaker containing hydrochloric acid (concentrated) and agitated on the stirrer at for 7 h. The resulting mixture then filtered through 0.22 μ poly tetra fluoro ethylene (PTFE) filter to remove catalytic impurities.

(b) *Oven Heating*

The acid-purified multiwalled CNTs placed into a hot air oven (250 °C) for 1 h to remove the amorphous carbon and metallic impurities.

2.2 Cutting and Oxidation

Purified raw MWCNTs were reacted with the acid mixture of sulphuric acid and nitric acid (3:1, v/v) and two variables, time and temperature have been evaluated to optimize the size and extent of oxidation to achieve carboxylated nanotubes. In the first case, treatment time was kept constant (6 h) and the temperature was varied between 25 and 100 °C. In the second case, the temperature was kept constant (70 °C) while treatment time was varied between 4 and 16 h. The various treated multiwalled CNTs were collected, washed, and filtered until pH becomes neutral. Finally, the black solid was dried at room temperature overnight, under vacuum. Carboxylated solid MWCNTs were sonicated for 20 min.

2.3 Synthesis of Folate-Conjugated MWCNTs

Synthesis of folate-conjugated multiwalled carbon nanotubes was the same as performed by **Mangla B**, Patel KS, Joshi SK, Kulkarni G.: Ligand Mediated CNTs

Based Delivery of an Anticancer Agent. **Lat Am J Pharm** 36, 1 (2017). Then, the prepared folate-conjugated carboxylated multiwalled carbon nanotube was confirmed by various characterization parameters [16].

(a) **Activation of Carboxylated multiwalled nanotube (MWCNT-COOH)**

The prepared carboxylated-multiwalled nanotube was activated by adding 1-ethyl-3-(-3-dimethylaminopropyl) carbodiimide hydrochloride (EDC) and *N*-Hydroxysuccinimide (NHS) in dimethyl sulfoxide for 5 h at room temperature [17].

(b) **Activation of Folic acid**

From the above reaction, folic acid (250 mg) and 0.5 mL of triethylamine were taken in the presence of NHS and EDC in solvent methanol. After 3–4 h, ethylenediamine was added and then kept at room temperature (48 h) for folate–NH_2 reaction [18].

(c) **Conjugation of Folate–NH_2 with carboxylated multiwalled carbon nanotube**

The prepared folate–NH_2 mixture was added to the activated acid multiwalled carbon nanotubes in solvent DMSO and continued for 72 h. The mixture was then dialyzed to remove unreacted folate–NH_2 [19].

2.4 Drug Loading

Uniformly dispersed purified raw and various functionalized MWCNTs (10 mg) were accurately weighed and incubated with a methanolic solution of the drug at various intervals between 2 and 24 h at room temperature on the shaker incubator and allowed to stand for 1 day to achieve the equilibrium. For the determination of entrapped and un-entrapped drug, dialysis bags were used. The resulting mixture obtained after loading was dialyzed against 25 ml double deionized water for 20 min to remove un-entrapped doxorubicin [20]. Figure 1 describes a flowchart of doxorubicin-loaded folate-conjugated MWCNTs

2.5 Evaluation Parameters of Raw and Various Functionalized MWCNTs [16, 20, 21]

Raw and various prepared functionalized MWCNTs were characterized via following methods [16].

(a) **Elemental Analysis**

Elemental analysis of raw and various functionalized CNTs was performed using an elemental analyzer (Flash EA112, CE Instrument, Italy).
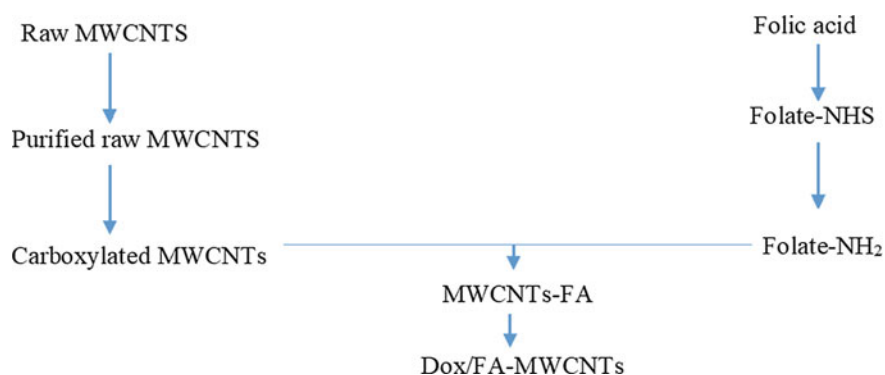
Fig. 1 Flowchart of doxorubicin-loaded folate-conjugated MWCNTs

(b) **Dispersion characteristics of functionalized MWCNTs**

Dispersion characteristics of the purified and functionalized MWCNTs were determined qualitatively in deionized water. The acidic media was maintained by 0.1 N HCL, whereas basic media by 0.1 N NaOH. After sonication (for 10 min) of various prepared MWCNTs, visualization was carried.

(c) **FTIR Spectroscopy**

The investigation of the functional group present on the surface of various functionalized MWCNTs was performed using FTIR spectroscopy (Perkin Elmer, USA).

(d) **Determination of Particle Size and Zeta Potential**

The *Zeta Potential* and particle size were measured by Zetasizer (Malvern Instrument, UK).

(e) **Transmission Electron Microscopy (TEM)**

Length and conjugation of the various functional groups of the treated MWCNTs were determined by the transmission electron microscope (Morgagni 268D, Holland) with an accelerating voltage of 100 kV.

(f) **X-Ray Diffraction (XRD) Studies**

XRD spectra of the raw and various functionalized MWCNTs were recorded at X-ray diffractometer (X'pert pro, PANalytical, Netherlands).

(g) **In Vitro Drug Release**

The in vitro doxorubicin release was measured in PBS (pH 7.4) at room temperature as dialysis media by using a dialysis bag diffusion technique. The drug-loaded, purified raw, and functionalized MWCNTs were placed in the dialysis sac, tied and immediately suspended in methanolic receptor medium, with stirring on a magnetic stirrer at 100 rpm. The drug release was determined by withdrawn of the sample at a specific time interval and replaced with an equal amount of fresh methanolic medium. Then the sample was diluted properly with methanol and analyzed.
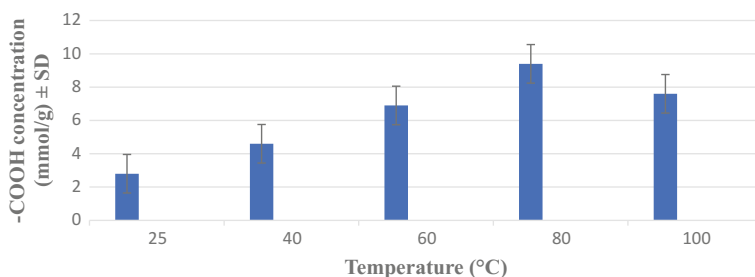
Fig. 2 Effect of temperature on cutting and oxidation of MWCNTs

(h) **Stability Studies**

Drug-loaded, purified MWCNTs, carboxylated multiwalled carbon nanotube and folate-conjugated MWCNTs dispersion was kept in a tightly closed screw-capped glass vial. The samples were kept in dark (in amber-colored tubes) at 4 ± 1 °C, in room temperature (25 ± 2 °C), and elevated temperature (35 ± 1 °C, in hot air oven) for a period of 7 weeks. The same procedure was repeated with the colorless vial in order to observe the effect of light if any. The samples were analyzed periodically every week up to 7 weeks for any consistency, precipitation, turbidity, color change [22].

3   Results and Discussion

Raw multiwalled nanotubes were purified in two ways; first by heating in an oven to remove amorphous carbon and metallic impurities, second by treatment with the acid mixture to remove catalytic impurities. Also, acid treatment was done in two ways by changing temperature at constant time and by changing time at constant temperature. It was seen from an experiment that by increasing temperature and time, the length of MWCNTs decreases. The effect of variables has been shown in Figs. 2 and 3. The time and temperature at which the optimum length obtained were 12 h and 80 °C. An optimum number of acidic groups also produced at this optimized condition.

Elemental analysis of raw MWCNTs was done to determine the purity. The carbon content was found to be greater than 90% which clearly indicates that no other element was present in carbon nanotubes that would affect the integrity and properties of MWCNTs. Purified raw MWCNT showed the increased percentage of atomic hydrogen which clearly indicated that some oxygenated groups have been generated during purification. The results in Table 1 suggest that increased % of atomic hydrogen in carboxylated MWCNTs is because of –COOH groups and increased oxygen. Folate-conjugated MWCNTs depicts increased % of nitrogen. X-ray diffraction of various MWCNTs showed that there is no change in the structural integrity of MWC-
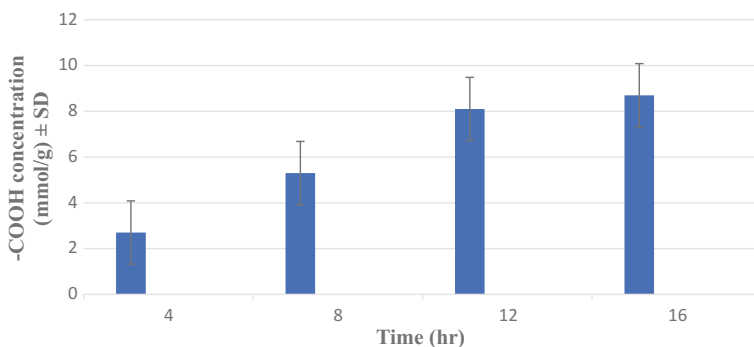
Fig. 3 Effect of time on cutting and oxidation of MWCNTs

Table 1 Elemental analysis of different functionalized MWCNTs

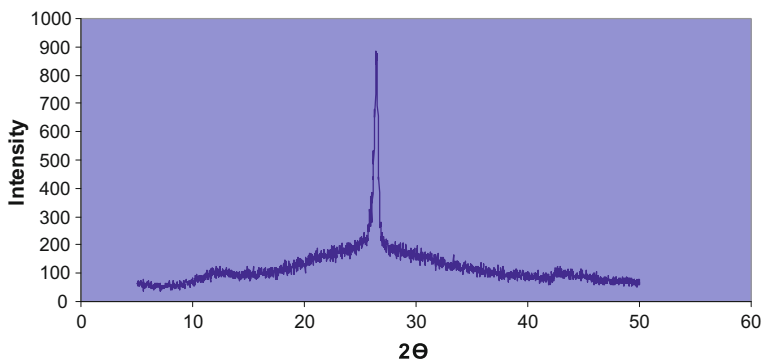| Sample	Atomic percentage ± SD (%)			
	Carbon	Hydrogen	Oxygen	Nitrogen
Raw MWCNTs	+	−	−	−
Purified raw MWCNTs	+	+	−	−
Carboxylated MWCNTs	+	+	+	−
Folate-conjugated MWCNTs	+	+	+	+

Present (+), Absent (−)

Fig. 4 X-ray diffraction of raw MWCNTs

NTs after functionalization. The XRD of various MWCNTs such as raw, purified raw, carboxylated, and folate conjugated were shown in Figs. 4, 5, 6 and 7.

FTIR spectral study was performed on various functionalized MWCNTs to assess the functional groups on the surface of multiwalled nanotubes. The purified raw
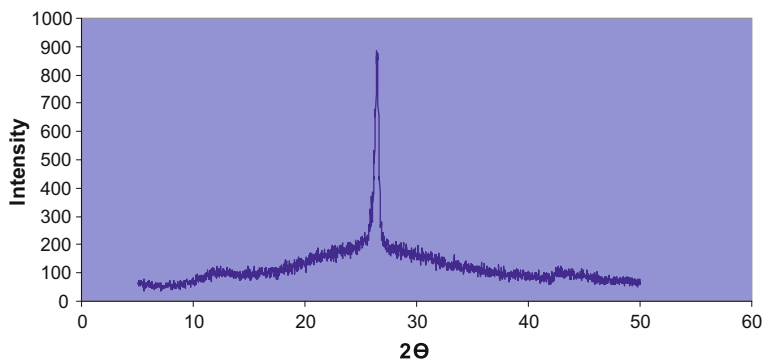
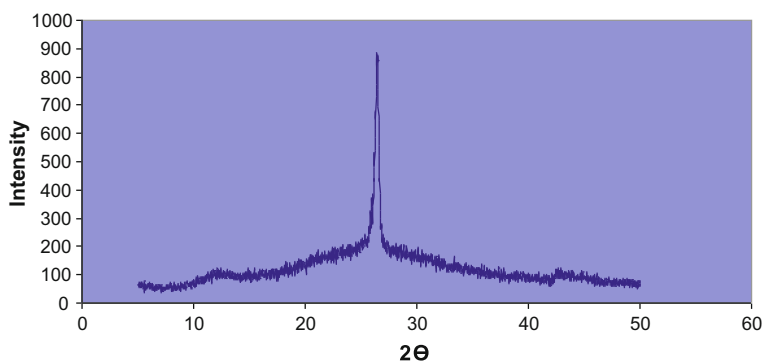**Fig. 5** X-ray diffraction of purified MWCNTs

Fig. 6 X-ray diffraction of carboxylated MWCNTs
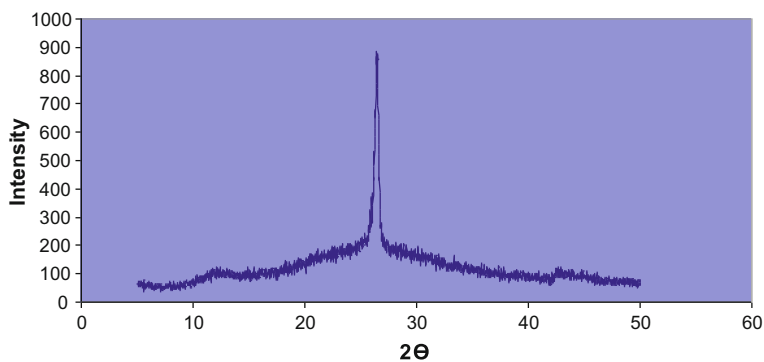

Fig. 7 X-ray diffraction of folate-conjugated MWCNTs

MWCNTs showed less dense peaks at 3478, 2753, and 1054 cm^{-1} which could be ascribed to the C–H stretching, O–H stretching, and O–H in-plane bending (Fig. 8).
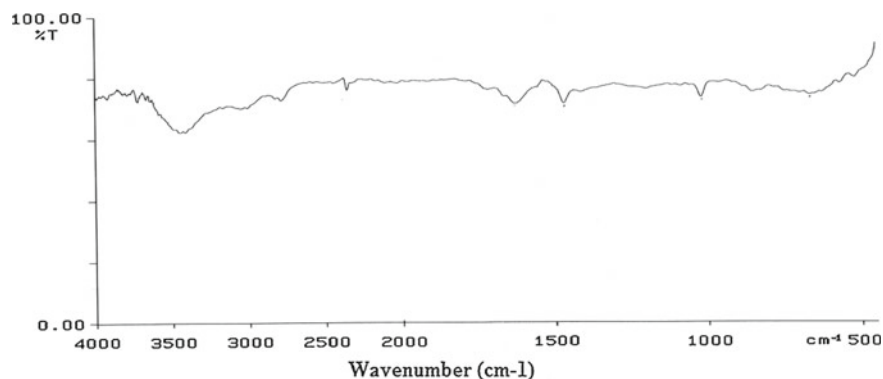
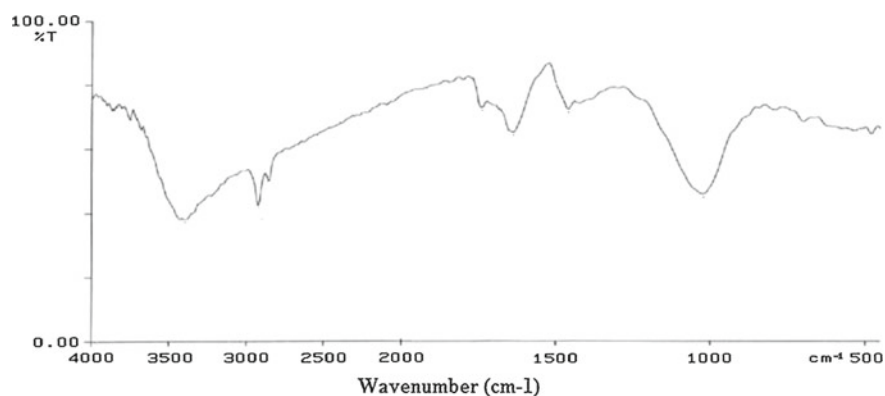**Fig. 8** FTIR spectrum of purified raw MWCNTs

Fig. 9 FTIR spectrum of carboxylated MWCNTs

This data confirms the presence of some oxygenated groups generated after the purification process.

Carboxylated MWCNTs showed the broad strong peaks at 3397.0, 2923.5, 1799.6, 1627.6, 1471.1, and 1034.1 cm^{-1}, which could be ascribed to stretching of O–H, C–H, C=O, C=C, C–O, and bending of O–H (Fig. 9). The data confirms the presence of carboxylic (–COOH) groups present on the surface of MWCNTs. As the functionalization proceeds, the numbers of peaks were increased due to the further attachment of various functional groups.

Folate-conjugated MWCNTs showed the peaks at 3420.4, 2924.3, 2356.6, 1781.3, 1596.9, 1445.1, and 1054.5 cm^{-1} (Fig. 10). The peaks at 3426.5 and 2344.9 cm^{-1} ascribed to symmetrical N–H stretching. The peaks at 2924.3 and 1781.3 cm^{-1} suggests C–H stretching and C=O stretching respectively and confirms the free –COOH groups at the surface remained after folic acid attachment.

The purified CNTs show positive zeta potential in the wide range of pH, whereas purified raw MWCNTs shows the slightly negative value at pH 9.0. Due to the
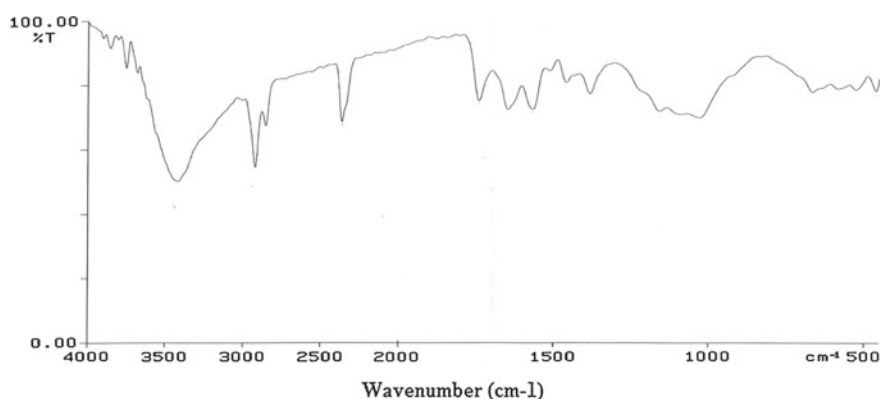
Fig. 10 FTIR spectrum of folate-conjugated MWCNTs

Table 2 Zeta potential of various MWCNTs

Samples	Zeta potential (mV)		
	Acidic pH	Neutral pH	Alkaline pH
Raw MWCNTs	Positive	Positive	Negative
Purified raw MWCNTs	Negative	Negative	Negative
Carboxylated MWCNTs	Positive	Negative	Negative
Folate-conjugated MWCNTs	Positive	Positive	Positive

generation of the acid group during the purification steps, which is usually ionized in the basic pH, thus causing the negative zeta potential. As the carboxylation of the purified MWCNTs was performed at different conditions (like temperature and time), there was no change in zeta potential. Though this change in zeta potential depends on the pH of the medium. The acid-treated MWCNTs showed high negative zeta potential at each pH, which proved that carboxylic groups were generated in the large concentration. Zeta potential value decreases by increasing the solution pH. On the other side, zeta potential value changes into the positive when MWCNTs functionalized with folic acid or folate conjugation. Folic acid functionalized shows the positive value in the acidic medium, due to the protonation of the amino group. It also showed positive zeta potential in the basic medium, but lesser than in acidic medium due to an amino group in the non-protonated state (Table 2).

The electron microscopic analysis of MWCNTs displayed nanometer size range, as well as multiwalled nature of carbon nanotubes. The TEM images also suggest a reduction in the size of nanotubes and also explain the Y shape of MWCNTs; the outgrowth or branching of carbon nanotubes occurs at the time of their synthesis (Figs. 11, 12 and 13).
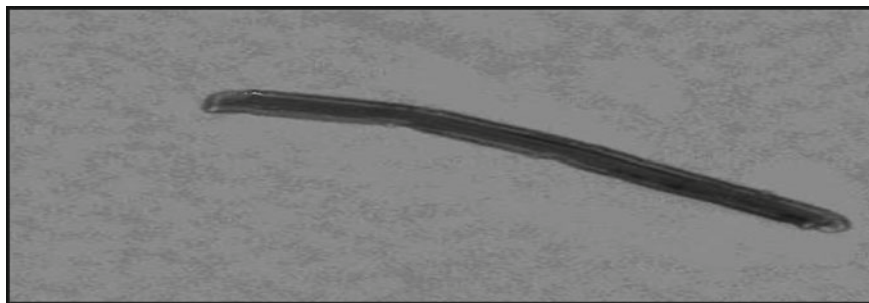
Fig. 11 TEM photomicrographs of purified raw MWCNTs
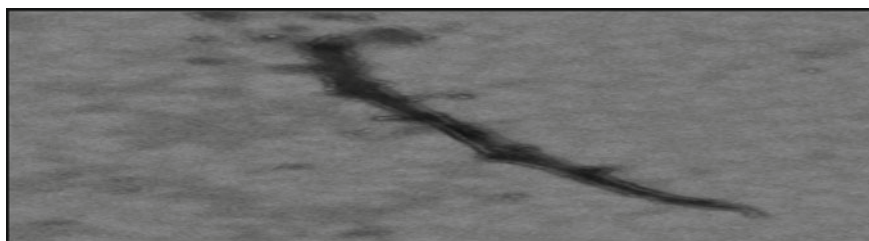
Fig. 12 TEM photomicrographs of carboxylated MWCNTs

Fig. 13 TEM photomicrographs of folate MWCNTs
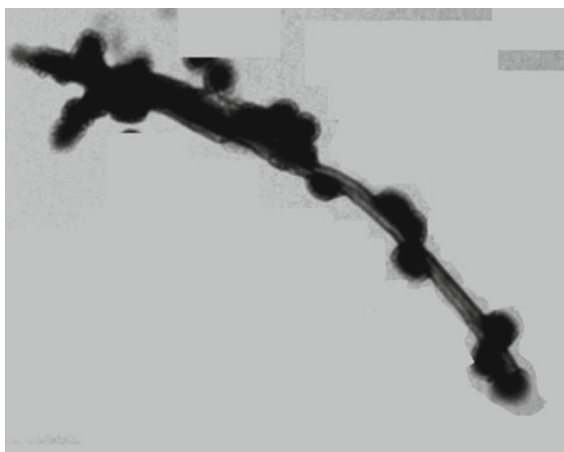
The prepared drug-loaded multiwalled carbon nanotubes were characterized by entrapment efficiency and the results are shown in Fig. 14. The drug was entrapped in raw MWCNTs and various functionalized MWCNTs. The entrapment efficiency was measured at various intervals; which increased with the time and after a particular time the entrapment was constant; suggests saturation and trafficking of drug solution. Raw MWCNTs showed high drug loading because of the possible interaction
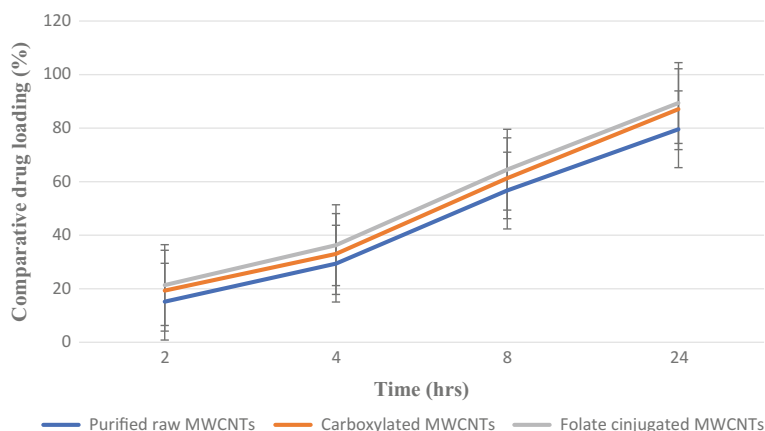
Fig. 14 Comparative drug loading in various MWCNTs

between drug and graphene ring of MWCNTs (π–π interaction). But the limiting entrapment concentration for purified raw MWCNTs was due to the little possibility of entrapment of doxorubicin to the inner cavity of purified raw MWCNTs. This could be attributed to the fact that purified raw MWCNTs were present in the bundle state and very little surface area was available for the entrapment of drug in bundled MWCNTs. Drug loading in carboxylated MWCNTs showed a larger amount of entrapped drug due to unbundling of purified raw MWCNTs and various pores generated by acid treatment. This provides more surface area and easy penetration into the inner cavity of carboxylated MWCNTs. MWCNTs containing folic acid showed comparatively less entrapment of drug that could be due to trafficking of groups around functionalized MWCNTs.

The free doxorubicin was almost completely released in 2 h in PBS (pH 7.4). Like entrapment, in vitro release could be due to the hydrophobic π–π interactions of the graphene MWCNTs and drug molecule. These hydrophobic interactions could be responsible for the sustained release of doxorubicin from raw MWCNTs as well as purified raw MWCNTs. Carboxylated MWCNTs showed release for a longer duration, i.e., approximately 67% in 48 h; due to the generation of carboxylate ion at pH 7.4 on carboxylated MWCNTs. Since the folic-acid-conjugated MWCNTs could create the hindrance for the loading of the drug likewise it would create the hindrance for the release of the drug (Fig. 15).

The stability data of the dispersed formulations, i.e., drug-loaded purified multiwalled carbon nanotubes, multiwalled carbon nanotube-containing the carboxylic group, and folate-conjugated MWCNTs were evaluated at various temperatures. The prepared formulation was most stable in dark at a temperature of 4 ± 1 °C. The probable reason could be the intactness of *Vanderwall* bonds and π–π interactions between encapsulated drug and MWCNTs in the dark which get cleaved in light due to higher reaction kinetics and may result in leakage of the drug. Among all formulations, the
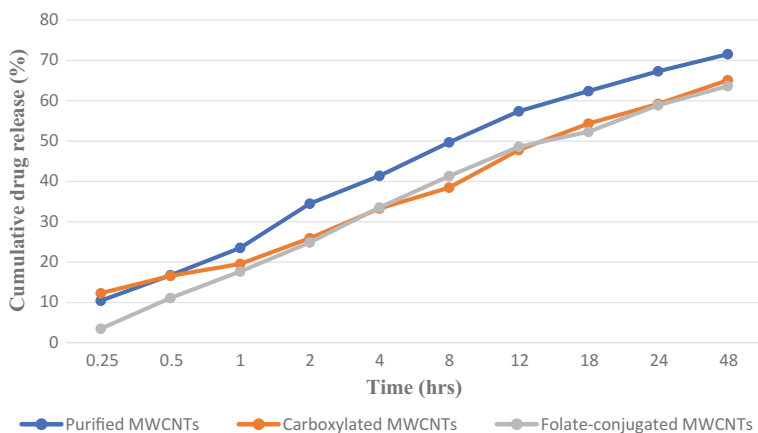
Fig. 15 Percent cumulative drug release of various MWCNTs (raw and functionalized)

Folate-conjugated formulation was more stable at 4 ± 1 °C in dark due to its thermolabile nature. Hence, the formulation always is stored in amber-colored vials in a cool place.

4 Conclusion

The work summarizes sequential functionalization of multiwalled carbon nanotubes via purification, carboxylation, and folate conjugation. Various evaluation parameter data confirms the successful functionalization had been carried out. Prepared folate-conjugated MWCNTs shows great potential in the advanced delivery system. Some properties that make them a suitable carrier are high drug loading, sustained release, excellent biocompatibility, large inner volume, distinct surfaces (inner and outer), ability to enter the cell by spontaneous mechanism without endo-lysosomal uptake. Also, functionalized multiwalled carbon nanotubes may open novel platform in the medical or biomedical application for the complete cure of various cancer in coming years.

References

1. Greish, K.: Enhanced permeability and retention of macromolecular drugs in solid tumors: a royal gate for targeted anticancer nanomedicines. J. Drug Target. **15**, 457–464 (2007)
2. Nguyen, K.T.: Targeted nanoparticles for cancer therapy: promises and challenges. J. Nanomedic. Nanotechnol. **2**, 103e (2011)
3. Bazak, R., Houri, M., Achy, S., Kamel, S., Refaat, T.: Cancer active targeting by nanoparticles: a comprehensive review of literature. J. Cancer Res. Clinoncol. **141**, 769–784 (2015)

4. Piktel, E., Niemirowicz, K., Wątek, M., Wollny, T., Deptuła, P., Bucki, R.: Recent insights in nanotechnology-based drugs and formulations designed for effective anti-cancer therapy. J. Nanobiotech. **14**, 39 (2016)
5. Baetke, S.C., Lammers, T., Kiessling, F.: Applications of nanoparticles for diagnosis and therapy of cancer. B J. Radiol. **88**, 20150207 (2015)
6. Madani, S.Y., Naderi, N., Dissanayake, O., Tan, A., Seifalian, A.M.: A new era of cancer treatment: carbon nanotubes as drug delivery tools. Int. J. Nanomed. **6**, 2963–2979 (2011)
7. Lacerda, L., Bianaco, A., Kostarelos, K.: Carbon nanotubes as nanomedicines: from toxicology to pharmacology. Adv. Drug Deliv. Rev. **58**, 1460–1470 (2006)
8. Rey, D.A., Batt, C.A., Miller, J.C.: Carbon nanotubes in biomedical applications. Nanotech. Law Bus. **3**, 263–292 (2006)
9. Zhao, X., Li, H., Lee, R.J.: Targeted drug delivery via folate receptors. Expert Opin. Drug Deliv. **5**, 309–319 (2008)
10. Jaracz, S., Chen, J., Kuznetsova, L.V., Ojima, I.: Recent advances in tumor-targeting anticancer drug conjugates. Bioorg. Med. Chem. **13**, 5043–5054 (2005)
11. Sinha, R., Kim, G.J., Nie, S., Shin, D.M.: Nanotechnology in cancer therapeutics: bioconjugated nanoparticles for drug delivery. Mol. Cancer Ther. **5**, 1909–1917 (2006)
12. Yan, C., Chen, C., Hou, L., Zhang, H., Che, Y., Qi, Y., Zhang, X., Cheng, J., Zhang, Z.: Single-walled carbon nanotube-loaded doxorubicin and Gd-DTPA for targeted drug delivery and magnetic resonance imaging. J. Drug Target. **25**, 163–171 (2017)
13. Tyagi, S., Rawat, S., Saxena, S.: Folate conjugates: a boon in the anti-cancer therapeutics. Int. J. Pharm. Sci. Res. **7**, 4278–4303 (2016)
14. Panczyk, T., Wolski, P., Lajtar, L.: Coadsorption of doxorubicin and selected dyes on carbon nanotubes. theoretical investigation of potential application as a pH-controlled drug delivery system. Langmuir **32**, 4719–4728 (2016)
15. Spreadbury, J.: Folic acid and its receptors. Graduate Literary Review Project, [Online] Governors State University, University Park, I (2013)
16. Mangla, B., Patel, K.S., Joshi, S.K., Kulkarni, G.: Ligand mediated carbon nanotubes based delivery of an anticancer agent. Lat. Am. J. Pharm. **36**, 1 (2017)
17. Hami, Z., Amini, M., Ghazi-Khansari, M., Rezayat, S.M., Gilani, K.: Doxorubicin-conjugated PLA-PEG-folate based polymeric micelle for tumor-targeted delivery: synthesis and in vitro synthesis. DARU J. Pharm. Sci. **30**, 1–7 (2014)
18. Lee, R.J., Low, P.S.: Delivery of liposomes into cultured KB cells via folate receptor-mediated endocytosis. J. Biol. Chem. **269**, 3198–3204 (1994)
19. Dai, L., Cao, X., Liu, K.F., Li, C.X., Zhang, G.F., Deng, L.H., Si, C.L., He, J., Lei, J.D.: Self-assembled targeted folate-conjugated eight-arm-polyethylene glycol–betulinic acid nanoparticles for co-delivery of anticancer drugs. J. Mater. Chem. B **3**, 3754–3766 (2015)
20. Singh, R., Mehra, N.K., Jain, V., Jain, N.K.: Gemcitabine-loaded smart carbon nanotubes for effective targeting to cancer cells. J. Drug Target. **21**, 581–592 (2013)
21. Zmudka, C.: Evaluation and in vitro studies of folate PEG biotin and other PEG agents. Capstone Projects [Online], Governors State University, University Park, IL (2011)
22. Lodhi, N., Mehra, N.K., Jain, N.K.: Development and characterization of dexamethasone mesylate anchored on multi walled carbon nanotubes. J. Drug Target. **21**, 67–76 (2013)

Efficient Extraction of Antioxidants and Lubricants from Commercial Polypropylene Pellets and Their Quantification Using HPLC

Pramod K. Hegde and M. G. Manjunatha

Abstract Additive analysis in commercially available plastic materials is a somewhat challenging task owing to the complex nature of the polymer matrix. This is due to the presence of the complex nature of the constituents present in the total matrix. Various types of stabilizing additives are added to the polymer at the production stage for the stabilization of the crude plastic resins especially polyolefins like polypropylene. A number stabilizing additives, viz, branched phenolic antioxidants that scavenge acidic radicals and organo-phosphites that decompose peroxides, and amide lubricant additives like oleamide and erucamide gives slippery nature to the plastic films. Due to the complex nature and response of these additives, different methods are employed to their quantification such as FTIR, GC, LCMS, etc. In this article, a method for effective extraction and subsequent quantification of both primary and secondary antioxidants (antioxidant and phosphite) and lubricants (oleamide and erucamide) using HPLC Agilent C18 column in a single run with a reverse-phase octadecylsilane (ODS) column with less than. Detections of the analytes were carried out using the VVD detector at 202 nm with an analysis time of less than 25 min.

Keywords Polypropylene · Antioxidants · Lubricants · C18 · HPLC

1 Introduction

The additive analysis in commercially available plastic materials is a somewhat challenging task owing to the complex nature of the polymer matrix. This is due to the presence of the complex nature of the constituents present in the total matrix. Various types of stabilizing additives are added to the polymer at the production stage for the stabilization of the crude plastic resins especially polyolefins like polypropylene

P. K. Hegde (✉) · M. G. Manjunatha
Research and Development (R&D) Division, Mangalore Refinery and Petrochemicals Ltd (MRPL), Mangalore 575030, India
e-mail: pramodhegde@mrpl.co.in

211

[1–4]. Stabilizing additives shield the material from degradation of the polymer from thermal, mechanical and impact failures. Generally, light stabilizers (antioxidants) and other additives are incorporated based on specific applications [2]. Even, the ubiquitous polypropylene is said to have eluded practical application in the absence of a light stabilizer [2]. The control of a material's COF is achieved using slip agents, such as silicone or fatty acid amides. Slip agents modify the surface properties of the material to which they are added. Stearamide, oleamide, and erucamide are common slip agents used to reduce friction effects in PE or PP film processing. A knowledge of the concentrations in the product is accordingly vital for quality control and materials design [5].

The technique HPLC with reverse-phase method by employing the modified silica-based column as a stationary phase is an attractive method for the separation of the stabilizers and the lubricants [6–13]. Application of this method is also suggested in standard methods like ASTM D6042 [14]. Usually, acetonitrile (ACN) and water gradients are used in almost all standard methods. As per the literature compared to acetonitrile/water and methanol/water gradients [14], the later method will end up with poor separations and the first is the better separation method. Here, in acetonitrile/water the challenge is the development of the exact concentration of the mobile phase and their optimization of the gradient method. Also, there are problems in separating various classes of additives simultaneously by a single HPLC method.

In this communication, we report the effective extraction and subsequent quantification of both primary and secondary antioxidants (antioxidant and phosphite) and lubricants (oleamide and erucamide) using HPLC Agilent C18 column in a single run. In this newly developed HPLC technique, a reverse-phase ODS column with ACN/H_2O mobile phases was employed for separation. Detections were carried out by a VVD detector with a selected wavelength of 202 nm. The required analysis time is about 25 min and more importantly well separation of all the four additives in a single run. The results were compared with the standard and in-house prepared real samples were cross-checked and the comparisons are in excellent agreement.

2 Experimental Setup

2.1 Materials

Commercial-grade Polypropylene (PP) pallets have been obtained from Mangalore Refinery and Petrochemicals Ltd. (MRPL, India, PP Plant Technology Licenser: Novolen Germany) polypropylene plant. The known concentrations of the additives were added to the crude polypropylene resin from the same polypropylene plant and it was extruded in Dr. Collins (Germany) make palletizing instrument at MRPLs polymer testing division. Commercially available primary, secondary antioxidants (AO-1010 and Phosphite 168) and slip agents oleamide and erucamide were used for the experiments. Solvents, viz., acetonitrile, methanol, water, and acetone (all HPLC

grade) were purchased from commercially available source. Filter papers used in our experiments were No. 42 from Whatman Company.

2.2 Equipment

The HPLC used in the present study was Agilent 1260 Infinity Quartenary LC system with a quaternary pump (G1311C, DEAB818526), automated liquid sampler (G1329B DEAAC36410), oven (G1316A, DEACN39301) and a VVD detector (G1314F, DEABB15129), operated at 200–800 nm. Column: Eclipse plus C18, Length: 4.6 * 100 mm, Particle size: 3.5 μm, PN: 959961-902, SN: USUXR23748, LN: B15078 from Agilent-USA. Mobile phase—acetonitrile:water (60:40) mixture at 0.5 mL/minute flow rate. Sample injection volume: 10 μL. Separations were carried out at 60 °C column oven temperature.

Microwave extraction system (Anton Paar, microwave reaction system SOLV, Multiwave PRO, Germany) and cryomill (Spex-6870 freezer mill) were used for the sample preparation for HPLC. Shimadzu UV–Vis spectrophotometer (UV model 2600, Japan) is used for determining the optimal absorption wavelengths of the analytes of interest.

2.3 Extraction

The standard solutions required for the method standardization were prepared directly by dissolving the commercially available additives from the market. Analyte solutions were prepared by dissolving 4 g (divided into 2 g and taken in separate vessels) of powdered polymer sample and about 30 mL of extraction mixture (2:7:1 mixture of methylene dichloride, acetonitrile, and methanol, respectively) were taken in a PTFE vessel and the mixture is placed in the extraction system. The mixture was then kept for extraction at a programmed rate of 10 min dynamic rate and 40 min static conditions. The extraction conditions were temperature: 80 °C microwave power: 800 W and pressure: 60 bar. With this condition, the effective extraction of the additives will be achieved.

2.4 HPLC Experiments

Gradient elution method was applied for the separation of four additives. Acetonitrile and water from 0 to 2 min: 40/60; from 2 to 17 min: 5/95, from 17 to 17.1: 5/95, from 17.1 to 30: 0/100, and finally 40/60 gradient program was created and all the quantifications were determined using this program.

3   Results and Discussions

In this report, HPLC methods were proposed for the analysis of lubricants such as AO-1010, Phosphite-168, oleamide and erucamide. Commercial-grade PP homopolymers were used as real samples and additive contents were evaluated in a shorter analysis time instead of using multiple techniques. Analytes separation was carried out at around 30 min runtime.

3.1   Chemical Structures of Additives/Analytes

The chemical structures of different analytes taken in our report are given in Fig. 1

3.2   UV–Vis Absorption of Analytes

Lubricants, viz, oleamide and erucamide that were analyzed in this report are transparent in spectral wavelengths of UV–visible region 200 nm. Lubricants are transparent due to the absence of a proper chromophoric moiety in their structural arrange-
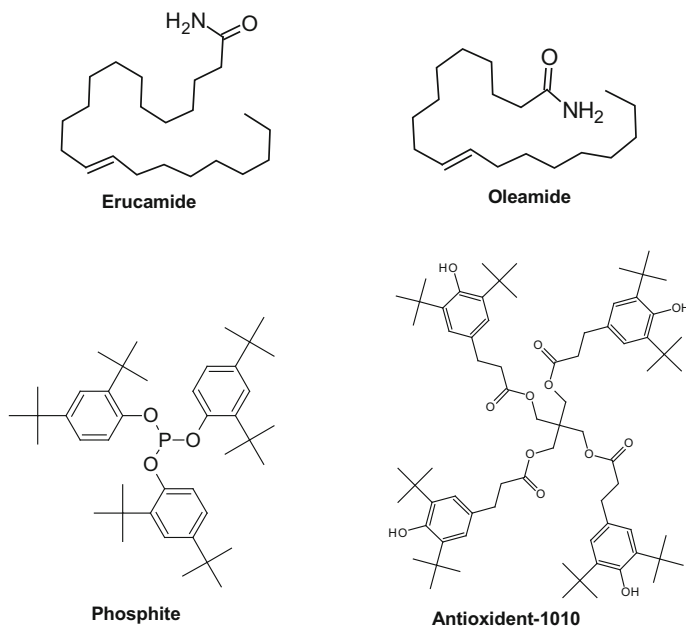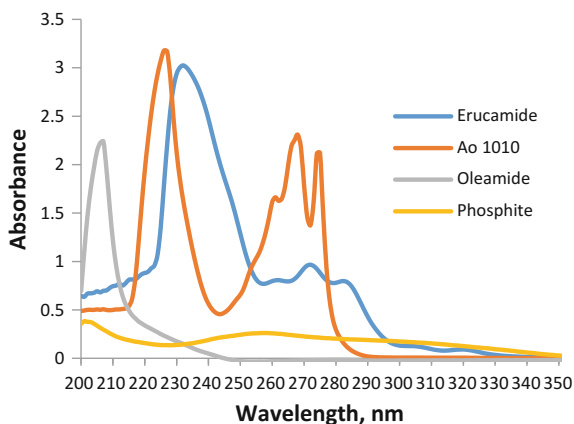

Fig. 1 Chemical structures of different additives

**Fig. 2** UV absorption spectra of different additives

ment. But both the antioxidants exhibit strong absorption at around 202 nm. Absorption spectra of the analytes were recorded and are given in Fig. 2. From this figure, it is concluded that the wavelength about 200–202 nm is appropriate for detection of all the four analytes since they are active in this wavelength.

3.3 Extraction of the Analytes

The commercial polypropylene pellets ready to dispatch to the market were crushed to a powder using cryomill and the powdered samples were used for our analysis. The effective migration of antioxidants and lubricants from polypropylene formulations was determined by two microwave extraction procedures with static and dynamic steps. All analytical conditions affecting the extraction were studied and optimized using Antioxidant 1010 as standard. As pressure and microwave flux increased, the efficiency of the extraction also increased and was more efficient as temperature increased and it was effective at the pressure of 60 bar and microwave energy of 80 W. During the static step in which the samples were exposed to the fluid without flux. The introduction of acetonitrile and methanol as fluid modifiers significantly improved the extraction. The large molecular volume of these antioxidants and slip agents may be responsible for the considerable reduction of extraction efficiency. Particle size and shape of crushed polymer pellets were also important. Greater the surface-to-volume ratio, greater is the extraction efficiency.

Table 1 Concentration versus peak area of five different additive standards

Standard 1				Standard 2			
Retention time	Area of peak	Concentration (ppm)	Additive	Retention time	Area of peak	Concentration (ppm)	Additive
4.281	87.996	14.00	Oleamide	4.281	179.06	28.00	Oleamide
5.927	47.481	7.00	Erucamide	5.928	94.209	14.00	Erucamide
13.082	283.365	3.53	AO-1010	13.105	586.825	7.05	AO-1010
24.162	557.854	7.50	Phosphite-168	24.173	1238.595	15.00	Phosphite-168
Standard 3				Standard 4			
Retention time	Area of peak	Concentration (ppm)	Additive	Retention time	Area of peak	Concentration (ppm)	Additive
4.282	350.214	56.00	Oleamide	4.282	869.177	140.00	Oleamide
5.93	186.118	28.00	Erucamide	5.931	461.837	70.00	Erucamide
13.118	1194.856	14.10	AO-1010	13.112	3046.416	35.20	AO-1010
24.177	2623.163	30.00	Phosphite-168	24.161	6928.356	75.00	Phosphite-168

Standard 5			
Retention time	Area of peak	Concentration (ppm)	Additive
4.28	1674.323	280.00	Oleamide
5.929	907.531	140.00	Erucamide
13.102	6098.913	70.40	AO-1010
24.128	14302.2	150.00	Phosphite-168
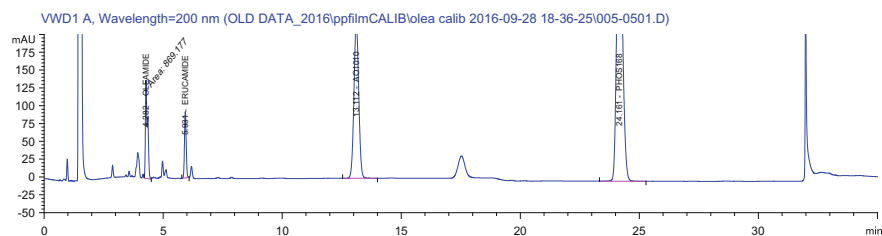
Fig. 3 HPLC chromatogram of standard 1

3.4 HPLC Separations

The chromatograms obtained for all the four components are depicted in Figs. 3 and 4 for the concentration given in the standard concentration 1 and 2 in Table 1. These chromatograms (Figs. 1 and 2) clearly indicate that the developed HPLC method is a highly efficient technique for separation of these type of additives based on their polarity. Chromatograms of the analytes show that the signals of lubricants (oleamide and erucamide) are separated with reasonably good resolution and antioxidants with excellent resolution. Calibration curves for the four additives are given in Fig. 5a–d and they show excellent linearity.

Recovery/validation tests were performed by adding the known quantity of all the four additives into the polymer matrix. The samples were subjected to extraction and
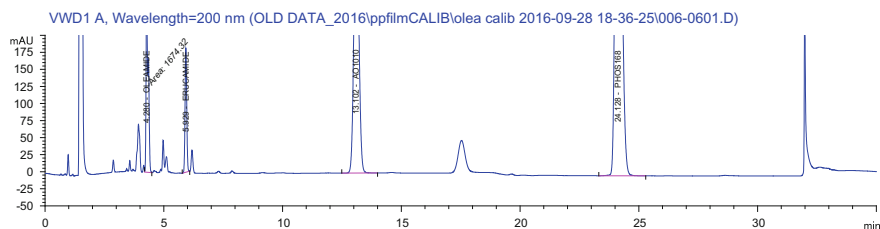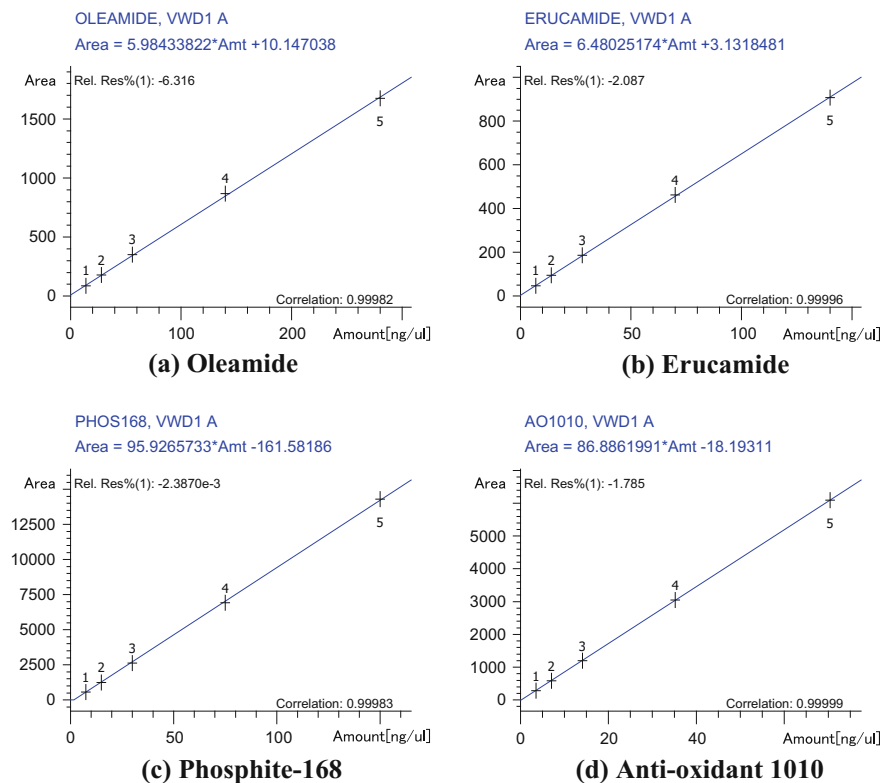
Fig. 4 HPLC chromatogram of standard 2

Fig. 5 Calibration curves of four different additives (**a–d**)

the dosed additives are quantified again. The results are in good agreement with the expected values and are tabulated in Table 2.

Table 2 Concentration and recovery of five different additive standards prepared and analyzed as per the developed method

Additive	Prepared concentration (ppm)	Obtained concentration in HPLC (ppm)	Percentage recovery (%)
Antioxidant 1010	380	1. 363 2. 365 3. 358 4. 368	95.66
Phosphite-168	750	1. 710 2. 715 3. 718 4. 725	95.60
Oleamide	700	1. 768 2. 775 3. 678 4. 681	96.5
Erucamide	1400	1. 1430 2. 1338 3. 1376 4. 1358	98.2

4 Conclusions

In this report, RP-HPLC technique is illustrated for the quantification of antioxidants and lubricant class of additives. Antioxidant, Phosphite-168, oleamide and erucamide were quantified by HPLC-VVD technique. For the extraction of these additives from the polymer matrix, the appropriate microwave digestion procedure has been described. The obtained values from the method employed on the sample and the standards were in excellent conformity with the expected results. Consequently, Versatile HPLC columns with different particle and pore sizes make this technique for such a complex separations. These columns have increased the very good peak capacity and their importance will continue to be an attractive technique for such separations. Hence, a bunch of additives can be extracted into appropriate solvent media and can be quantified using HPLC in a single run. This helps in reducing the analysis time and the avoiding the use of a variety of instruments for polymer additive quantifications.

References

1. Lutz, J.T.: Thermoplastic Polymer Additives. Marcel Dekker, New York (1989)
2. Mir Ali, F., Mortaza, E., Ali, R., Elham, F., Vali, B., Amir, A.M.: Microchim. Acta **153**, 73–78 (2006)
3. Stepek, J., Daoust, H.: Additives for Plastics. Springer, Berlin, Heidelberg, New York, Tokyo (1983)
4. Murphy, J.: The Additives for Plastics Handbook. Elsevier, Oxford (1996)
5. Takatori, E., Kagawa, N.: Nippon Gomu Kyokaishi (J. Soc. Rubber Ind. Jpn.) **79**, 359–366 (2006)
6. Riedel, T.: In: Gachter, R., Muller, H. (eds.) Plastics Aadditives, 4th edn. Hanser and Gardner, Cincinnati, OH (1993)
7. Forrest, M.F.: Analysis of plastics. Rapra Review Report No. 149. Rapra Technology Ltd, Shawbury (2002)
8. Crompton, T.R.: Manual of Plastics Analysis. Plenum Press, New York (1998)
9. Crompton, T.R.: Practical Polymer Analysis. Plenum Press, New York (1993)
10. Crompton, T.R.: Analysis of Polymers. An Introduction. Pergamon Press, Oxford (1989)
11. Mitchell, J.: Applied Polymer Analysis and Characterization: Recent Developments In Techniques, Instrumentation, Problem Solving. Hanser Publishers, Munich (1987)
12. Krause, A., Lange, A., Ezrin, M.: Plastics Analysis Guide—Chemical and Instrumental Methods. Hanser Verlag, Munich (1983)
13. Johnson, W., Keck-Antoine, K., Lee, R.E., Callierotti, C.: Plast. Addit. Compd. **3**, 14 (2001)
14. ASTM D-6042 Standard test method

Polymer Nanocomposites: Modification Through Swift Heavy Ions

Payal Mazumdar, Prachi Singhal and Sunita Rattan

Abstract Ion implantation through swift heavy ion irradiation is a processing technique in which sample is bombarded with a beam of energetic heavy ions to create buried layers of ions in a material. The modification in the irradiated material is attributed to electronic energy deposition at low fluence of 10^{11}–10^{12} ions/cm^2. In the present work, Polymethacrylate (PMMA) nanographite nanocomposites have been synthesized through a one-pot in-situ polymerization method. The as-prepared nanocomposites are subjected to Ni ion implantation through SHI irradiation (Ni ion beam, 80 meV) at a fluence of 1×10^{10} to 1×10^{12} ions/cm^2. The nanocomposite films were characterized before and after Ni ion irradiation through SEM and XRD and were evaluated for their electrical and electrochemical properties.

Keywords Polymethacrylate · Nanographite platelets · Nanocomposites
Swift Heavy Ion (SHI)

1 Introduction

Polymer nanocomposites with the incorporation of metal nanoparticles show great potential for organic electronic device applications due to their attractive features such as mechanical flexibility, low-temperature processing, low cost, etc. Ion implantation through ion beam irradiation has been proven to be a versatile tool for dopant incorporation and modification of polymers as penetration of energetic ions changes polymer structure and its properties considerably. Different studies show that the energetic ion bombardment modifies the transport properties of the polymer nanocomposites by the deposition of energy rather than depositing as a dopant [1]. Many studies regarding the modification of properties of polymers based on ion implantation have been reported [2, 3].

P. Mazumdar · P. Singhal · S. Rattan (✉)
Amity Institute of Applied Sciences, Amity University, Noida 201303, Uttar Pradesh, India
e-mail: srattam@amityu.edu

Ion implantation through the beam of ions at energy in the range of few KeV provides the irradiated material with a thin surface layer with modified properties as low-energy ions do not penetrate deeply. This technique turned out to be a versatile tool for fabrication of sophisticated microelectronic devices. But such low-energy ion implantation is not able to exhaust all potential abilities possible in ion beam irradiated materials.

However, irradiation with Swift Heavy Ion (SHI) beams with energy in the range of few MeV can create buried layers in an irradiated material with modified electrical, optical, thermal, and chemical properties rather than only modified surface of the material. This happens because SHIs have sufficiently large projectile ranges in solids [4].

The change in material properties on ion irradiation is due to a large amount of energy deposition by ion beams, which may lead to material modification at the electronic level [5]. Energetic ions when passing through any material loses its energy in two ways, i.e., one electronic energy loss due to inelastic collisions with electrons (Se, Electronic Stopping) dominating at higher energies of few tens of MeV and higher and the other nuclear energy loss due to elastic collisions with the atoms of the solids (Sn, Nuclear Stopping) dominating at low energies of few tens of KeV to MeV. During SHI irradiation, the relatively large value of Se enables the reduction of ion fluence from 1011 to 1013 cm^{-2}. Low fluence reduces the processing time and thus preserving the original properties of target materials [6, 7].

Two phenomenological methods, i.e., thermal spike model and Coloumb explosion model explain the transfer of electronic energy to the material generated due to ion–matrix interaction. According to the thermal spike model, excited electrons rapidly transfer energy to phonons, very large energy deposition leads to localized melting and rapid cooling. However, in Coulomb explosion model electronic excitation causes ionization around its path, followed by strong atomic repulsion and explosion among these charges leading to a cylindrical shock wave. In case of polymer nanocomposite materials, it is expected that neutralization of charges occurs much before the Coloumb explosion due to conduction of electrons, thus ion irradiation and energy deposition can be explained based on thermal spike model [8]. Thus, the deposited energy by SHI is transmitted to the atomic lattice by electron–phonon coupling inducing a localized heating along the ion track on nanometric dimension resulting in transient thermal spike lasting for few picoseconds. This leads to modification at the electronic level which may be attributed to factors such as cross-linking, creation of defects, molecular rearrangements, etc.

Poly methylmethacrylate (PMMA) nanographite nanocomposites attracted a great deal of attraction for organic electronic device applications such as energy conversion, energy storage, etc., due to its easy processability, easy moldability, low cost, good physical and mechanical properties, etc [9–11]. The combination of PMMA with nanographitic platelets was reported for use as electrode material in various applications but an agglomeration of nanographitic platelets limit its application. Swift heavy ion irradiation of PMMA/nanographite nanocomposites results in incorporation of metal ions into the matrix and brings about uniform distribution of nanographitic layers within the matrix. It modifies the electrical properties of polymer membranes and thus improves their energy storage applications.

In the present work, PMMA/nanographite nanocomposites were subjected to SHI irradiation using Ni ions (80 meV) to modify the electrical properties of the nanocomposites. The irradiated nanocomposites were characterized for structural and morphological properties and evaluated for electrochemical applications. This study was found to be an efficient way to improve the performance of the hybrid nanocomposites for energy storage application.

2 Experimental

2.1 Materials

The graphite flakes were purchased by Asbury Carbons to synthesize nanographite platelets. The methylmethacrylate monomer was purchased by Sigma Aldrich. All reagents, initiators, and solvents were of analytical grade. The characteristic parameters of ion implantation are the energy and ion dose of the particular ion used. Because of the sensitivity of PMMA material, the energy could not be too high and the dose was selected experimentally. The energy used for irradiation was determined by utilizing Stopping and Range of Ions in Matter (SRIM) software [12]. The energy chosen was such that the projected range of the irradiation beam was less than the thickness of the film so that the ions were incorporated in the nanocomposite matrix (Table 1).

2.2 Synthesis of Nanographite

The nanographite platelets were synthesized by modified Hummers method as reported earlier by our group [13, 14]. The graphite flakes were obtained by exfoliation followed by intercalation of graphite flakes.

2.3 Synthesis of PMMA/NGP Films

The polymer nanocomposites were synthesized by in situ polymerization of MMA with nanographite platelets in one pot. In a typical experiment, nanographite flakes

Table 1 Energy and fluence for Ni ion used for irradiation

Ion	Energy (MeV)	Projected range (μm)	Fluence (ions/cm^2)
Nickel	80	26	1×10^{10} to 3×10^{12}

are dispersed in 10 ml methyl methacrylate solution at a ratio of 3:1. The as-prepared mixture of PMMA nanocomposite was dissolved in chloroform solvent to fabricate durable and robust composite films.

2.4 Fabrication of Polymer Nanocomposite Supercapacitors

To determine the electrochemical properties of PMMA/NGP films before and after irradiation, a two-electrode setup was fabricated. The device was fabricated by What-man sandwiched between identically sized films. The electrochemical study was performed using 1 M NaOH solution as an electrolyte.

3 Results and Discussion

The Swift heavy ion irradiation of PMMA/NGP nanocomposite films results in the incorporation of Ni metal ions into the composite films and brings about homoge-neous distribution and strong interaction between the polymer and nanographitic layers. Moreover, the implantation of Ni metal ion at high fluencies leads to the for-mation of high-performance PMMA/NGP films as depicted in Fig. 1. High energy deposition due to ion irradiation leads to main chain scission and cross-linking result-ing from electronic excitation, nuclear collision, and carbonization of the irradiated material which modifies the material at the electronic level. As a consequence, the irradiated nanocomposite film imparts high electrical conductivity and improved electrochemical capacitance.

The SEM images of NGP and composite prepared by in situ polymerization are depicted in Fig. 2. The graphite layers are uniformly coated with PMMA polymer. The interconnected structure of PMMA/NGP consists of nanosheets of range 40–80 nm and length up to 2 μm. Figure 2b depicts a strong interconnected network between the polymer matrix and filler after irradiation [15].

Figure 3 shows a characteristic diffraction peak of NGP at 24.6°, which is slightly lower than that of pristine graphite (JCPDS No. 75–1621). After the synthesis of the polymer nanocomposites, the PMMA/NGP before Ni irradiation shows a slight diminish in the peak which is due to the intercalation of NGP platelets. Moreover, after irradiation of Ni at high meV, the peak shows a significant decrease along with the broadening of the peak. The diminishing of the peak is due to the exfoliation of nanographite platelets in PMMA matrix, which tends to expand the intermolecular chain spacing and reduces the intramolecular distances between the rigid polymer chains. Moreover, the broad diffraction peak around $2\theta = 17°$ arises due to the presence of amorphous PMMA chains [16–18].
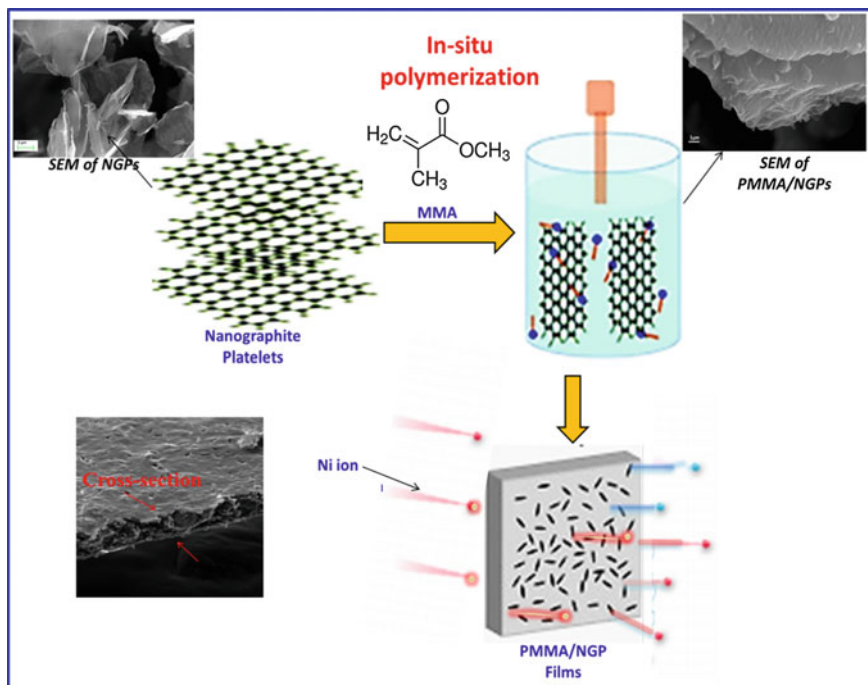
Fig. 1 Schematic depicting the fabrication of PMMA/NGP films after Ni irradiation
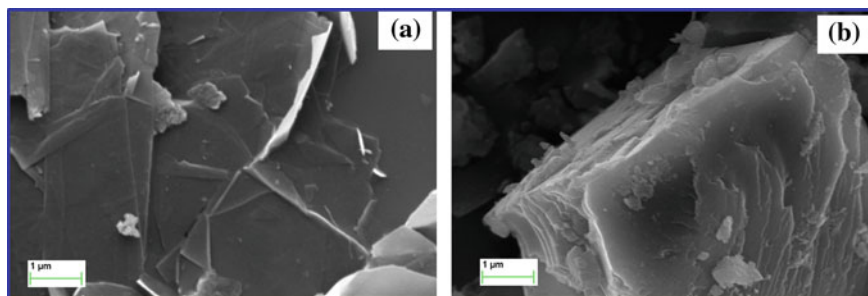

Fig. 2 SEM image of **a** NGP and **b** PMMA/NGP composite after irradiation

4 Electrical Measurements

The resistance of PMMA nanographite nanocomposites before and after Ni ion irradiation is compared in Table 2. It is clearly evident from the results that the electrical properties of the naocomposite films are greatly enhanced after Ni ion irradiation.

Fig. 3 XRD diffraction
pattern of **a** NGP, **b**
PMMA/NGP before
irradiation, **c** PMMA/NGP
after irradiation
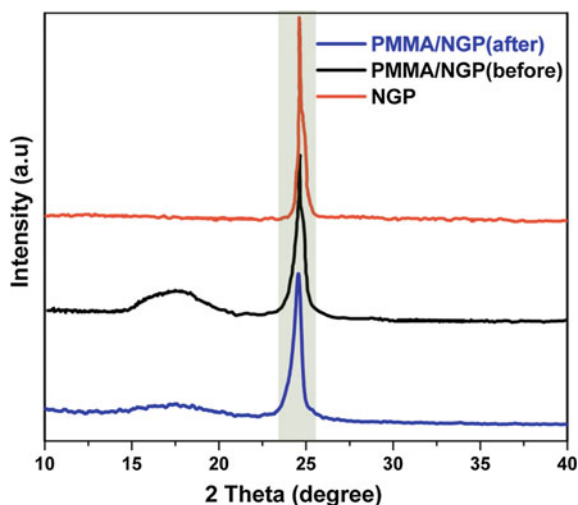
5 Electrochemical Study

Electrochemical studies [19] have been performed by using robust PMMA/NGP polymer nanocomposite films by taking 1 M NaOH electrolyte. Here, we study the detailed electrochemical performance of polymer nanocomposite before and after high beam ion implantation. Both cyclic voltammetry (CV) and charge–discharge experiments of the composite have been studied in a potential range of 0–0.6 V.

In Fig. 4a, PMMA/NGP composite after ion irradiation shows a significant rise in the area of the CV curve in comparison with composite before irradiation. Moreover, the rectangular-like shape reveals the ideal capacitive behavior of the material. Figure 4b shows galvanostatic charge–discharge curve behavior of composites before and after irradiation of metal ion at in the meV range. The discharge curve of PMMA/NGP after irradiation is relatively symmetrical with its charge counterparts indicating good charge–discharge behavior. Moreover larger time is taken for the potential discharge of the material is indicative of its higher specific capacitance [20, 21].

The specific capacitance for the electrodes are acquired from charge–discharge performance of the material and it can be calculated by using Eq. (1)

Table 2 Table depicting electrical properties of PMMA/NGP after Ni irradiation

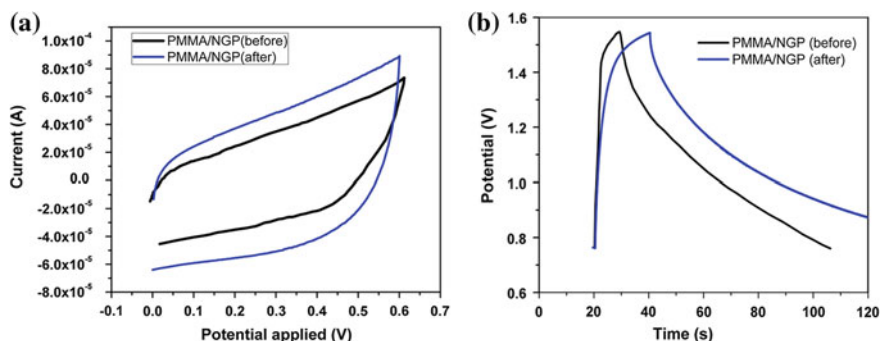| Composition of films	Resistance before implantation (kΩ)	Resistance after implantation (kΩ)	Percentage decrease in resistance after implantation
1%	~5.7	~0.8	85.9%

Fig. 4 a CV and **b** charge–discharge curve of PMMA/NGP composite after Ni implantation

$$C = \frac{I \times \Delta t}{m \times \Delta V}.$$ (1)

where $C(\mathrm{Fg}^{-1})$ is the specific capacitance, $I(\mathrm{A})$ is the constant discharging current, $\Delta t(\mathrm{s})$ is discharging time ΔV is potential and $m(\mathrm{g})$ is active mass [8].

The Ni ion incorporated PMMA/NGP composite exhibits a large specific capacitance of 220 F/g, and characteristic EDLC behavior associated with carbon-based capacitor as a high-performance electrode material for electrochemical supercapacitor. This rise in capacitance is due to the Ni ion incorporation into the polymer matrix which improves the polarizability of the polymer, in turn, assisting in larger charge storage. In contrast, the films without ion irradiation result in agglomeration of graphite nanoplatelets leading to poor interlayer interaction which hinders the overall electrochemical performance significantly.

6 Conclusion

A novel method is used to fabricate a Ni-incorporated PMMA/nanographite nanocomposites through SHI irradiation. PMMA/nanographite nanocomposites were prepared through in situ polymerization and subjected to SHI irradiation using Ni (80 meV) ion beam at fluence between 10^{11} and 10^{12} cm^{-2}. Synthesized nanocomposites were morphologically characterized by SEM and XRD. Electrochemical properties of the synthesized PMMA/NGP nanocomposites before and after irradiation were investigated using two-electrode electrochemical cell and NaOH electrolyte.

PMMA/nanographite nanocomposite after Ni irradiation shows a significant increase in electrochemical capacitance compared to the nanocomposite before irradiation. The higher value of electrochemical capacitance is evidenced by the large area of the CV curve. During a charge–discharge process, the charging curve of PMMA/NGPs is almost symmetric to its corresponding discharge counterpart with a

slight curvature, suggesting high reversibility of the materials. The high electrochemical capacitance of Ni irradiated PMMA/NGP nanocomposites may be attributed to improved dispersion of nanographite platelets in the nanocomposite, increased polarizability due to Ni incorporation and modification in the structure of the polymer due to high energy deposition at the interface. Irradiated nanocomposites with significant high electrochemical capacitance are suitable for energy storage applications as potential capacitor materials.

References

1. Bridwell, L.B.: Ion implantation of polymers for electrical conductivity enhancement. Solid State Phenom. **27**, 163 (1992)
2. Srivastava, A.K., Virk, H.S.: 50 MeV lithium ion beam irradiation effects in poly vinylidene fluoride (PVDF) polymer. Bull. Mater. Sci. **23**, 533 (2000)
3. Pignataro, B., Fragalà, M.E., Puglisi, O.: AFM and XPS study of ion bombarded poly(methyl methacrylate). Nucl. Instr. Methods **131**, 141–148 (1998)
4. Biswas, A., Gupta, R., Kumar, N.: Recrystallization in polyvinylidene fluoride upon low fluence swift heavy ion impact. Appl. Phys. Lett. **78**, 4136 (2001)
5. Sarmah, S., Kumar, A.: Irradiation induced crossover from 1D to 3D transport behaviors of PEDOT-titanium dioxide hybrid nanocomposites. Phys. Status Solid. **209**, 2546–2551 (2012)
6. Yao, X., Wu, H., Wang, J., Qu, S., Chen, G.: Carbon nanotube/poly(methyl methacylate)(CNT/PMMA) composite electrode fabricated by in situ polymerization for microchip capillary electrophoresis. Chem. Eur. J. **13**, 846–853 (2007)
7. Bang, Y.H., Choo, D.C., Kim, T.W.: High-transparency and low-resistivity poly (methylmethacrylate) films containing silver nanowires and graphene-oxide nanoplatelets. Appl. Surf. Sci. **376**, 69–73 (2016)
8. Sahoo, G., Sarkar, N., Sahu, D., Swain, S.K.: Nano gold decorated reduced graphene oxide wrapped polymethylmethacrylate for supercapacitor applications. RSC Adv. **7**, 2137 (2017)
9. Slowinski, B.: New possibilities of swift heavy ion implantation in material science and technology. Acta Physica Polonica A **96** (1999)
10. Chen, F.: Photonic guiding structures in lithium niobate crystals produced by energetic ion beams. J. Appl. Phys. **106**, 081101 (2009)
11. Chen, C.: Second harmonic generation of diamond-blade diced KTiOPO$_4$ ridge waveguides. Opt. Express **24**, 16434–16439 (2016)
12. Ziegler, J.F., Ziegler, M.D., Biersack, J.P.: SRIM—The stopping and range of ions in matter. Nucl. Instrum. Methods Phys. Res. B **268**, 1818–1823 (2010)
13. Mazumdar, P., Rattan, S., Mukherjee, M.: Polymer nanocomposites using click chemistry: novel materials for hydrogen peroxide vapor sensors. RSC Adv. **5**, 69573–69582 (2015)
14. Singhal, P., Rattan, S.: Swift heavy ion irradiation as a tool for homogeneous dispersion of nanographite platelets within the polymer matrices: toward tailoring the properties of PEDOT:PSS/Nanographite nanocomposites. J. Phys. Chem. B **120**, 3403–3413 (2016)
15. Lee, M., Lee, J., Park, S.Y., Min, B., Kim, B., In, I.: Production of graphene oxide from pitch-based carbon fiber. Sci. Rep. **5**, 11707 (2015)
16. Wang, J., Shi, Z., Ge, Yu., Wang, Y., Fan, J., Yin, J.: Functionalization of unzipped carbon nanotube via in situ polymerization for mechanical reinforcement of polymer. J. Mater. Chem. **22**, 17663–17670 (2012)
17. Ye, Y., Yen, Y., Cheng, C., Syu, Y., Huang, Y., Chang, F.: Polytriazole/clay nanocomposites synthesized using in situ polymerization and click chemistry. Polymer **51**, 430–436 (2010)
18. Potts, J.R., Lee, S.H., Alam, T.M., An, J., Stoller, M.D., Piner, R.D., Ruoff, R.S.: Thermomechanical properties of chemically modified graphene/poly(methyl methacrylate) composites made by in situ polymerization. Carbon **49**, 2615–2623 (2011)

19. Ambrosi, A., Chua, C.K., Mohamad Latiff, N., Loo, A.H., Wong, C., Sheng Eng, A., Bonanni, A., Pumera, M.: Graphene and its electrochemistry—an update. Chem. Soc. Rev. **45**, 2458–2493 (2016)
20. Chen, C., Pang, L., Lu, Q., Lei, W., Tan, Y., Wang, Z., Chen, F.: Refractive index engineering through swift heavy ion irradiation of LiNbO3 crystal towards improved light guidance. Sci. Rep. **7**, 10805 (2017). https://doi.org/10.1038/s41598-017-11358-y
21. Kuila, T., Mishra, A.K., Khanra, P., Kim, P.H., Hee Lee, J.: Recent advances in the efficient reduction of graphene oxide and its application as energy storage electrode materials. Nanoscale **5**, 52–71 (2013)

Homopolymer, Copolymers, and Terpolymer Synthesis Via Esterification-Cum-Addition of N-Substituted Phthalimide with Acrylates: Studies on Influences of Macromolecule Compositions on Thermal and Microbial Performances

Suman Jinger and Jyoti Chaudhary

Abstract Phthalimide, a single imide ring containing compound, and their polymers have many excellent properties such as transparency, hydrophobicity, high flexibility, chemical resistivity, high thermal stability, and biological activity. Acrylates show some specific properties; strong bond making capacity, moisture-resistivity, and good chemical binding properties and because of these properties, acrylate's played a significant role in framing of flexible high-performance polymers and the copolymerization between phthalimides and acrylates, products are demonstrated excellent properties such as to provide active drug binding site for biological system, used as optical brightening agent. In the present research article, the synthesis of homopolymer, copolymer, and terpolymer were synthesized by polymerization technique using N-substituted phthalimide and acrylate. The synthesis was focused to overcome the disadvantages of phthalimide and acrylate's individuals to form better addition-cum-esterification products with good implications. In this sequence, 4-(N-phthalimido) phenyl-2′-methylbutyacrylate (NPMBA) monomer was synthesized and characterized. The tailored new monomer has been polymerized to form homopolymer, copolymers, and terpolymer with different comonomer units in the presence of AIBN initiator and THF as solvent at 60–70 °C. The polymer's analytical characterization has been done to confirm structures and composition using FT-IR, ^{1}HNMR, and elemental analysis. The weight average molecular weight (Mw), number average molecular weight (Mn), and polydispersity (Mw/Mn ratio) of polymers were determined using Gel Permeation Chromatography (GPC) technique and ther-

S. Jinger (✉) · J. Chaudhary
Department of Polymer Science, Mohan Lal Sukhadia University,
Udaipur, Rajasthan, India
e-mail: sumanjinger@gmail.com

J. Chaudhary
e-mail: jyotichaudhary13@gmail.com

mal behavior was also studied by Thermo Gravimetric Analysis (TGA) and DSC techniques. All samples were screened out for biological activities against some bacterial and fungal colonies.

1 Introduction

Current trends toward the development and design of high-performance/high-thermal polymers for achieving high quality products. Polyimide families are known as high-performance polymers and the most popular family consisting of polyimide is considered to develop and design high-performance polymers [1, 2]. Polyimide class is widely used in manufacturing high temperature resistant plastics, adhesives working at high temperature, 2D optical materials, photoresistant materials, selective separation materials, film coating, and most importantly and significantly used in aerospace craft manufacturing, defense articles designing, optoelectronics, high-strength composites, electroluminescent devices, polymeric electro-cells, etc [3–5].

Several studies are dedicated to the synthesis of high-performance/thermal stable copolymers using N-substituted maleimides [6–9]. Homopolymerization and copolymerization with acrylics including N-phenyl maleimide monomer were showed a lot of utilized due to availabilities of a variety of prospects of style new materials with improved and desired qualities [10–17]. However, acrylics have poor heat resistance efficiency and low glass transition temperature (Tg) are consisting generally between 80 and 110 °C and not applicable directly in processing segments of industries. The copolymerization process for N-substituted maleimide and acrylates/vinyls has been used to improve the heat resistance capacity of acrylates/vinyls [18–21]. The presence of N-substituted maleimide structure in polymeric chain inevitably increases both the Tg and the decomposition temperature of polymers [22, 23]. In this sequence, the phthalimide structure is also targeted for the synthesis of high performing polymers. From the past investigations, phthalimide derivatives have been used in pharmaceuticals as DAN cleaving agent, anesthetics, tumericidals, optical brightener, fluoroprobes, and N-phthaloyl amino acid derivatives for peptide synthesis [24], etc. Further, phthalimide polymers have also been synthesized and used as thermal stable polymers [2, 25, 26]. Because of the great demand of high performance, thermally stable with other physically, chemically and biologically improved qualities, it is worthwhile to find out a simple, moderate, low cost, clean, effective, and convenient method. The present work represented the synthesis of copolymers and terpolymer of 4-(N-phthalimido) phenyl-2′-methylbutyacrylate (NPMBA) with acrylic acid and acrylonitrile using free radical polymerization method and compared results of products from its homopolymer properties and studied their thermal performances and antimicrobial properties.

2 Experimental

2.1 Materials

The details of used materials as suppliers, purity, CAS number, molecular weight, and density are listed in Table 1. All chemicals were used without any additional purifications.

2.2 Monomer Synthesis

Step 1:

4-(N-phthalimido) phenyl-2′-methylbutyacrylate (NPMBA) monomer was synthesized in two steps using 2-hydroxyethyl amine. In the first step, phthalic anhydride (0.01 mol) and ethyl amine (0.01 mol) were dissolved in DMF solvent (20 ml) separately, then the amine derivative solution charged in three-necked round bottom flask arranged with a dropping funnel, condenser for reflux and thermometer to measure temperature. Phthalic anhydride solution was added dropwise at room temperature then the solution mixture was refluxed for 3 h at 140 °C temperature. Cyclization reaction of phthaleamic acid was carried out at high temperature. Then, it was cooled and washed with cold water in twice and dried at 50 °C in vacuum oven for 8–10 h. The recrystallization was done by methanol-chloroform in 1:1 v/v ratio.

Step 2:

Table 1 Source, CAS No., molecular weight, purity, and density of utilized chemicals

Name	Source	CAS No.	Purity (%)	Mw (g/mol)	Density (g/cm^3)
Phthalic anhydride	Sigma	85-44-9	99	148.12	1.53
4-Hydroxy aniline	Sigma	123-30-8	98	109.128	1.13
Methyl butyacrylic acid	Sigma	80-59-1	99	100.12	0.969
DMF	Sigma	68-12-2	99	73.09	0.944
Methanol	Sigma	67-56-1	99.9	32.04	0.791
Chloroform	Sigma	67-66-3	99.5	119.38	1.492
p-toluene sulfonic acid	Sigma	19816-85-4	97	172.19	1.24
Hydroquinone	Sigma	123-31-9	99	110.11	1.3

1 mol of N-hydroxyethyl phthalimide was esterified with 1 mol of acrylic acid. The reaction ingredients were fed in 250 ml volumetric flask assembled with a dean-stark assembly and refluxed in toluene solvent with catalytic environment of p-toluene sulfonic acid and used hydroquinone as an inhibitor and the reaction mixture was stirred continuously for 4–5 h until the calculated amount of water was approximately obtained, distilled out by and solid product of 4-(N-phthalimido) phenyl-2′-methylbutyacrylate (NPMBA) monomers synthesized.
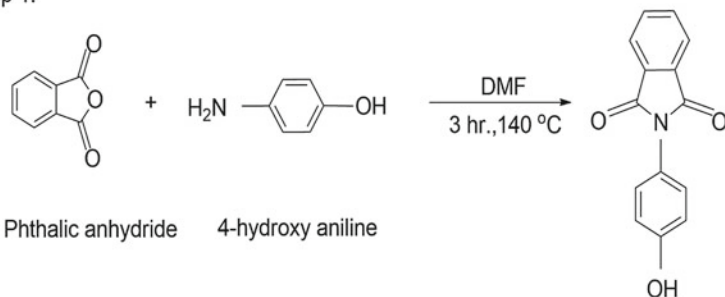
2.3   Polymer Synthesis

The equimolar amount of [NPEBA] monomer (0.01) (for homopolymer) and acrylate/vinyl comonomer (for copolymers and terpolymers) with 0.03 g (0.00019 mol) AIBN were added in THF solution into a 500 ml volumed two-necked R B flask attached with a reflux condenser. An oil bath was heated and held at a constant temperature of 70 °C then the reaction solution was allowed to reflux for 24 h. It seemed that after 2 h of refluxing a turbid—cloudy solution resulted and ejected the sample quantity amount of solution in intervals of 4-hour duration to get the status of yield % of product formations. At the completion of the reaction, the solution was held at room temperature to cool down then poured into mixture of methanol and distilled water (10% methanol–water solution) for precipitation. The product of copolymers and terpolymers were precipitated out from reaction medium and filtered using vaccum, washed with methyl alcohol and distilled water, dried at 40 °C for 8–10 h (Figs. 1 and 2).

2.4   Polymerization Yield

Percentage yield of synthesized products was variated by polymer synthesis processes and affected by chemical surrounding. Polymer feed components first examined with different solvent-initiator couple-system to score high polymer yield and according to the polymers production yield, It was observed that the production percentage yield in THF-AIBN system was obtained highest as compared to DMF, 1,4-Dioxane as solvents with BPO and AIBN initiators (Table 2).
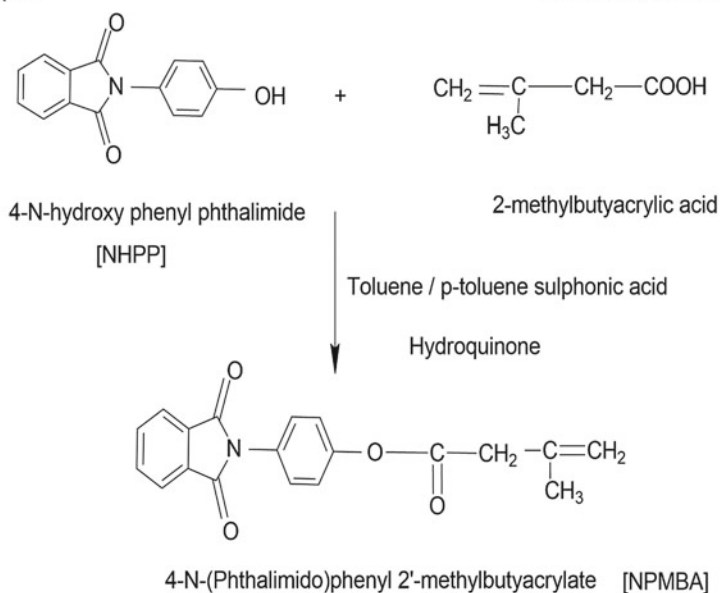
Step 1:

Phthalic anhydride   4-hydroxy aniline

DMF
3 hr.,140 °C

4-N-hydroxy phenyl phthalimide

Step 2:

4-N-hydroxy phenyl phthalimide
[NHPP]

2-methylbutyacrylic acid

Toluene / p-toluene sulphonic acid

Hydroquinone

4-N-(Phthalimido)phenyl 2'-methylbutyacrylate   [NPMBA]

Fig. 1 Reaction scheme of synthesis of NPMBA monomer

2.5 Instrumentation

The polymers were characterized by FT-IR, NMR. FT-IR spectra of the samples were recorded with Perkin-Elmer spectrometer mode RX-I FT-IR equipped with a high purity dried KBr pellets as beam splitter at room temperature. The ^{1}H-NMR spectra were recorded on Bruker Avance II 400 MHz NMR spectrophotometer using CDCl$_3$ as solvent and TMS as an internal reference. CHN microelement analysis was performed on Thermofinnigan Combustion Analyzer. Thermal properties were analyzed from TGA recorded on Perkin-Elmer-Purix-TGA Thermal Analyzer and
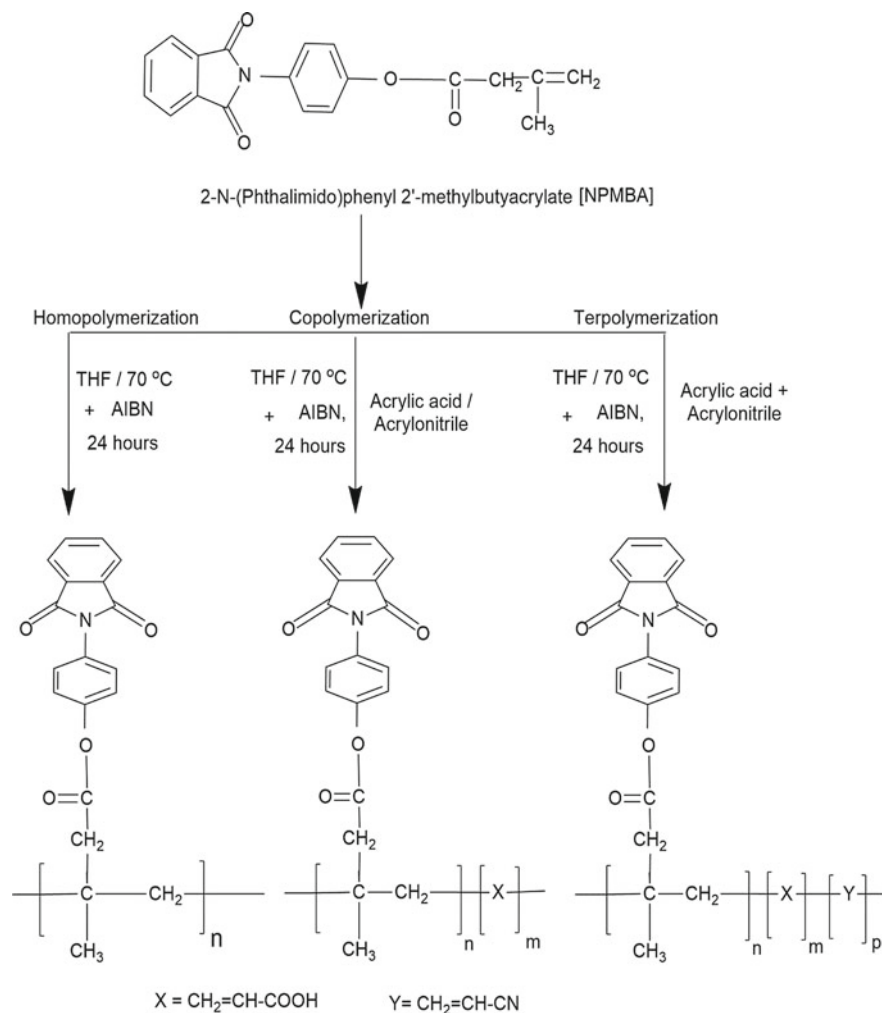
Fig. 2 Reaction scheme of homopolymerization, copolymerization, and terpolymerization of NPMBA

DSC recorded on NETZSCH DSC 204 Analyzer at a heating rate of 10 °C/min under oxygen atmosphere.

Table 2 Performance of initiator-solvent couples on product percentage yield of homopolymer [HNPMBA], copolymers [CNPMBA-AA], [CNPMBA-AN], and [TNPMBA-AA-AN]

Solvents	Solvent viscosity	Polymerization time duration (h)	% Yield of [HNPMBA]		% Yield of [CNPMBA-AA]		% Yield of [CNPMBA-AN]		% Yield of [TNPMBA-AA-AN]	
			AIBN	BPO	AIBN	BPO	AIBN	BPO	AIBN	BPO
DMF	1.299	18	63.34	55.23	69.15	62.31	68.27	42.55	72.12	48.17
Acetone	1.359	18	42.45	39.67	53.55	42.62	38.09	34.56	52.69	44.79
Dioxane	1.415	18	60.65	50.34	69.71	62.24	68.88	45.36	55.48	42.16
THF	1.496	18	89.23	43.54	90.14	67.21	87.54	62.33	78.12	62.27

Table 3 Physical properties of different polymers of NPMBA

Polymers	Color appearance	Phase	Yield (%)	Crystallization solvent
HNPMBA	Light brown	Solid	60.47	Acetone
CNPMBA-AA	Light brown	Solid	76.36	Ethyl acetate
CNPMBA-AN	Light brown	Solid	65.45	Ethyl acetate
TNPMBA-AA-AN	Brown	Solid	72.73	Ethyl acetate

3 Result and Discussion

3.1 Physical Properties

The study of various kinetic parameters of polymerization and their growth pattern of polymers show that the polymerization proceeds rapidly at first and then slows down. The decrease in the rate of polymerization is attributed to the low reactivity of phthalimide radicals to initiate the polymerization of phthalimide-acrylate double bond.

The color appearances, phase, and percentage yield with solvents used for crystallization are depicted in Table 3.

3.2 Solubility

The solubility was analyzed for all polymers and all polymers are soluble in polar solvents as N,N′-Dimethyl formamide (DMF), Tetra hydro furan (THF), Dimethyl sulphoxide (DMSO). The possible cause of solubility of polymers in polar organic solvent clearly indicates the polar nature of copolymers and terpolymers especially, which is probably due to the presence of nitrogen as a polar point.
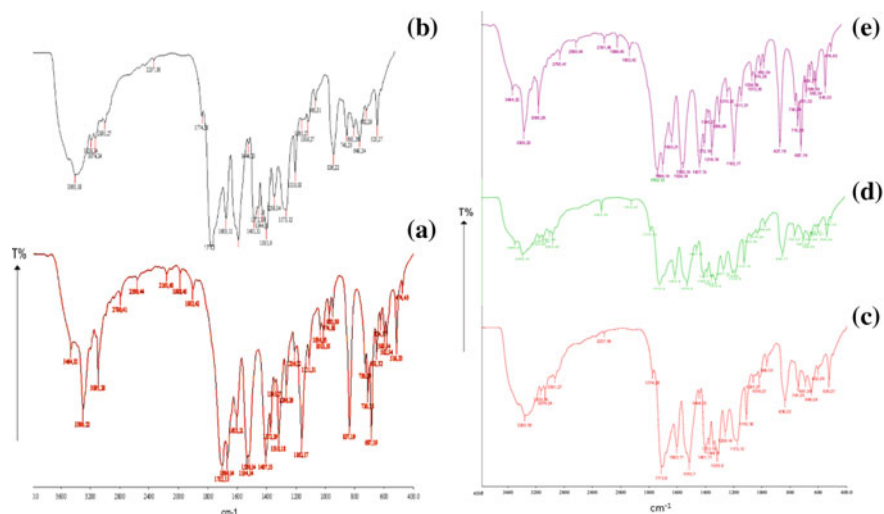
Fig. 3 FT-IR spectra of **a** NPMBA, **b** HNPMBA, **c** CNPMBA-AA, **d** CNPMBA-AN, **e** TNPMB-AA-AN

3.3 Spectral Analysis

The FT-IR spectra of the NPMBA based homopolymer, copolymers and terpolymer are shown in Fig. 3. From the studies of FT-IR spectra, they revealed that all four homo-, co- and terpolymers give rise to nearly similar spectral patterns and show the following characteristic absorption bands: 3300 cm^{-1} (amide (II) asymmetric stretching), 3095 cm^{-1} (C–H stretching in CH$_2$/Aromatic), 1702 cm^{-1} (–C=O stretching of phthalimide ring), 1666 cm^{-1}(–C=C stretching in –CH=CH in aliphatic), 1603 cm^{-1} (–C=O stretching of ester), 1266 cm^{-1} (–C–O–C bending in ester) Fig. 3a. 3363 cm^{-1} (amide (II) asymmetric stretching), 3074 cm^{-1} (C–H stretching in CH$_2$/Ar), 1774 cm^{-1} (–C=O stretching in ester), 1713 cm^{-1} (–C=O stretching of phthalimide ring), 1603 cm^{-1} (–C=O stretching in ester), 1259 cm^{-1} (–C–O–C bending in ester) Fig. 3b. 3466 and 3363 cm^{-1} (–OH asymmetric stretching broad band and amide (II) asymmetric stretching), 3074 cm^{-1} (C–H stretching in CH$_2$/Ar), 1774 cm^{-1} (–C=O stretching in ester), 1713 cm^{-1} (–C=O stretching of phthalimide ring), 1603 cm^{-1} (–C=O stretching in ester), 1259 cm^{-1} (–C–O–C bending in ester) Fig. 3c. 3466, 3359 cm^{-1} (–OH asymmetric stretching broad band and amide (II) asymmetric stretching), 3073 cm^{-1} (C–H stretching in CH$_2$/Ar.), 1774 cm^{-1} (–C=O stretching in ester), 1714 cm^{-1} (–C=O stretching of phthalimide ring), 1602 cm^{-1} (–C=O stretching in ester), 1257 cm^{-1} (–C–O–C bending in ester) Fig. 3d. 3460, 3360 cm^{-1} (–OH asymmetric stretching broad band and amide (II) asymmetric stretching), 3071 cm^{-1} (C–H stretching in CH$_2$/Ar.), 1774 cm^{-1} (–C=O stretching in ester), 1714 cm^{-1} (–C=O stretching of imide ring), 1602 cm^{-1} (–C=O stretching in ester), 1261 cm^{-1} (–C–O–C bending in ester) Fig. 3e.
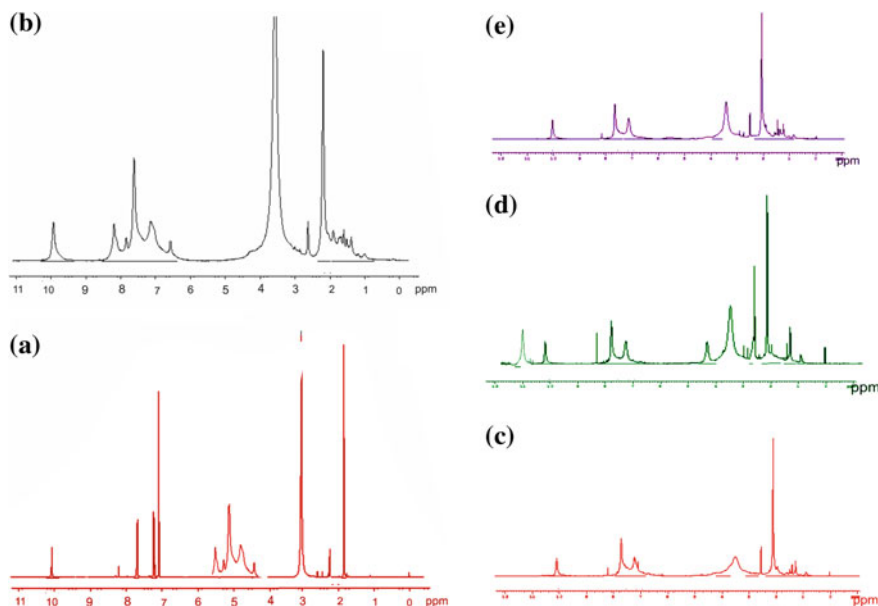
Fig. 4 ^{1}H-NMR spectra of **a** NPMBA, **b** HNPMBA, **c** CNPMBA-AA, **d** CNPMBA-AN, **e** TNPMB-AA-AN

The 1H-NMR spectra of all polymers are depicted in Fig. 4. The spectral data are given in Table 4. From the spectra, it is revealed that homopolymer, copolymers, and terpolymer have slightly different patterns of 1H-NMR spectra, since each polymer have a panel of protons showing slightly different proton generated electronic environment.

3.4 Molecular Weight

Molecular weight of homopolymer, copolymers, and terpolymer are determined from GPC and values are given in Table 5. The GPC data for the copolymers and terpolymer show that the small groups such as alkyl group in acrylates increases the molecular weights of polymers decreases, due to branching in comonomer units. Polydispersity index (PDI) value ranging from 1.18 to 1.34 clearly explain that the homopolymer, copolymers, and terpolymer were tailored through free radical polymerization process and the GPC-curve area distribution was narrow, i.e., indicated the molecular weight of polymers indicates relatively high molecular weight fraction so it is assumed as the polymers have high mechanical strength with good processing properties. The number average molecular weight (Mn), weight average molecular weight (Mw) and Polydisperity (Mw/Mn) are given in Table 5.

Table 4 ^{1}H-NMR spectral data monomer and polymers of NPMBA

Observed chemical shift (in ppm)					Nature of proton assigned
NPMBA	HNPMBA	CNPMBA-AA	CNPMBA-AN	TNPMBA-AA-AN	
7.07–7.69	6.59–7.91	6.61–7.90	6.59–7.92	6.58–7.93	Phenyl protons
4.43–5.67	1.24–1.77	1.37–1.78	1.24–1.92	1.20–1.98	(–CH=CH–)protons of acrylate moiety
3.43	3.50	3.49	3.52	3.37	methylene (–CH$_2$)protons
10.05	10.07	10.06	10.08	10.04	Protons of phthalimide
10.07	10.06	10.58	10.72	10.79	Proton of –OH of acrylic acid

Table 5 The weight average molecular weight (Mw), number average molecular weight (Mn) and polydisperity (Mw/Mn) of polymers of NPMBA

Polymer code	Weight average molecular weight (Mw) g/mol	Number average molecular weight (Mn) g/mol	Poly dispersity index (Mw/Mn)	Start molecular weight (start Mw)
HNPMBA	1104.88.8	928.9	1.1894	4085.4
CNPMBA-AA	1255.9	984.2	1.2760	7759.8
CNPMBA-AN	1213.1	962.8	1.2599	6132.0
TNPMBA-AA-AN	1313.7	977.7	1.3436	8261.7

3.5 Thermal Analysis

In Fig. 5, the TGA thermograms of homopolymer, copolymers, and terpolymer of NPMBA are displayed. The measurement of weight changes in form of decomposition was referred to as the function of time and temperature and analyzed the temperature stability/sustainability of polymers. The analysis was typically carried out in milligrams by sample size with oxy-decomposition environment and heating rate was framed at 10 °C/min. from 100–800 °C. The polymer thermograms of HNPMBA, CNPMBA-AA, CNPMBA-AN, and TNPMBA-AA-AN show the major weight loss beginning from 200 to 300 °C and ending at 600–700 °C in continuation format. Once the decomposition triggered out, it continues until the entire polymer is decomposed. In these thermograms, there were some small fluctuations detected with continuous degradations. The cause of continuous degradation is followed eliminations of attached pendant groups due to chain scission. The continuous
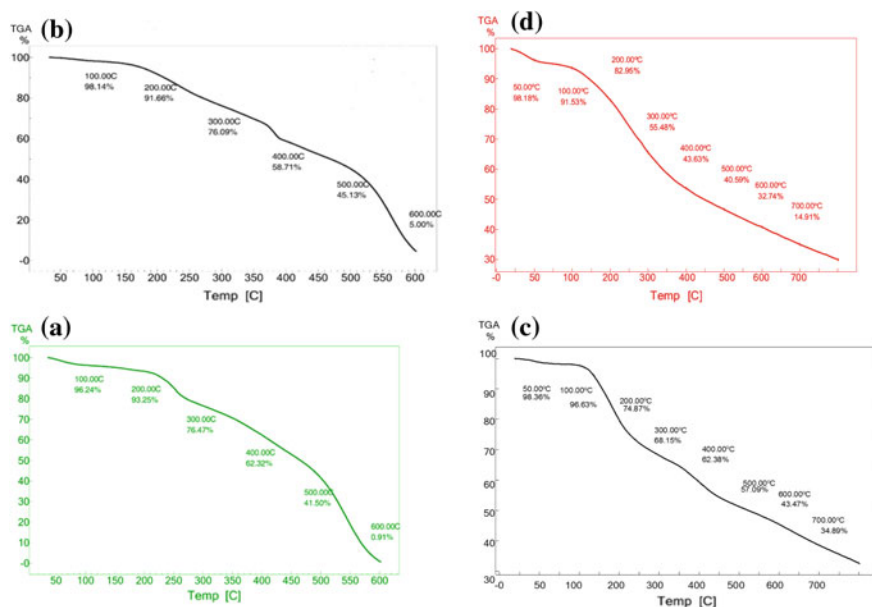
Fig. 5 TGA thermograms of **a** HNPMBA, **b** CNPMBA-AA, **c** CNPMBA-AN, **d** TNPMB-AA-AN

Table 6 Weight loss % of homopolymer, copolymers, and terpolymer at various temperature and Tg temperature

Polymer code	Weight loss (%)							Tg temperature in °C
	100 °C	200 °C	300 °C	400 °C	500 °C	600 °C	700 °C	
HNPMBA	1.86	8.34	23.91	41.29	54.87	95.00	–	183.8
CNPMBA-AA	8.47	17.05	44.52	56.37	59.41	67.26	85.09	135.8
CNPMBA-AN	3.76	6.75	23.53	37.68	58.50	99.09	–	123.2
TNPMBA-AA-AN	3.37	25.13	31.85	37.62	42.91	56.53	65.11	139.2

weight loss % curvature is explained in three segments. The first rapid stage (up to 200 °C) of decomposition may be due to losses of residue amount of moisture and polar solvents which was used in synthesis. The second stage (200–500 °C) may be due to bond breaking and releasing of attached pendant groups and the third stage (500–700 °C) high transition temperature may be located for the residue of char/carbon. The results in Table 6, indicated that the relative thermal stability were examined by the calculating % weight loss in polymers at high temperature.

The glass transition temperature (Tg) was evaluated from differential scattering colorimetric (DSC). The Tg value of homopolymer, copolymers, and terpolymer HNPMBA, CNPMBA-AA, CNPMBA-AN, and TNPMBA-AA-AN are, respec-
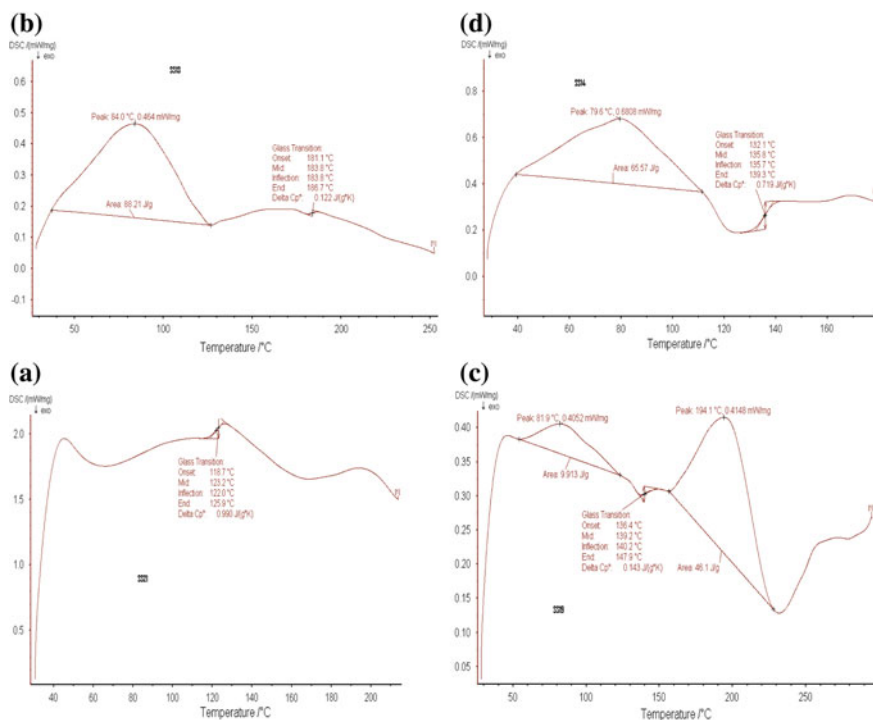
Fig. 6 DSC curves of **a** HNPMBA, **b** CNPMBA-AA, **c** CNPMBA-AN, **d** TNPMB-AA-A

tively, present in Table 6. From the analysis of Tg temperatures, it reflected that the presence of acrylic acid (AA) and acrylonitrile (AN) groups in copolymers and ter-polymer increases the Tg temperature than their homopolymer. The Tg temperature of copolymer and terpolymer TNPMBA-AA-AN are lower than their homopoly-mer, respectively, and the sequence seen as—TNPMBA-AA-AN > CNPMBA-AA > CNPMBA-AN. Due to the acidic functionality of acrylic acid in related copolymer and terpolymer shown exclusive Hydrogen-bond, that is the core rea-son to demonstrate low Tg temperature of TNPMBA-AA-AN terpolymer [139.2 °C] and copolymer CNPMBA-AA than their homopolymer [Fig. 6; Table 6] and appli-cable at low-temperature processing units (for low Tg polymers) in desired polymer industries and it may provide large opportunity for many applications in related sectors.

3.6 Antimicrobial Assessments

To examine the antimicrobial properties, the section of inhibition is the area on an agar dish where the growth of a control microorganism is blocked by an antimicro-
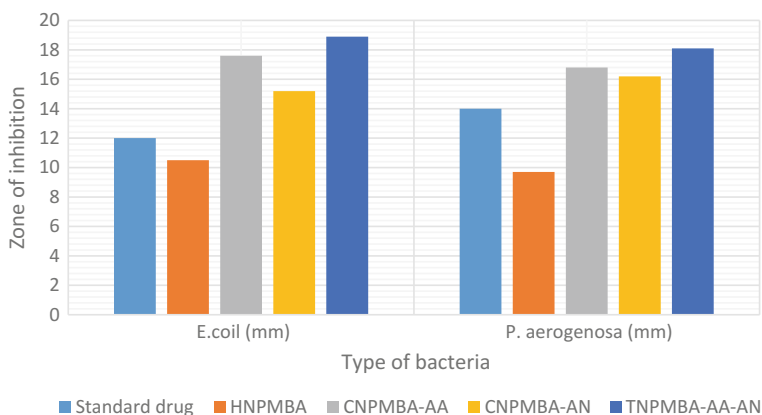
Fig. 7 Relative antibacterial activities of homopolymer, copolymers, and terpolymer of NPMBA as compared with standard drug

bial source normally put on the agar surface. If the assessment of microorganism is susceptible toward the antimicrobial sources, it will not grow where the source is present. The inhibition zone inversely deals with the minimum inhibitory concentration (MIC) so that lower concentration of antimicrobial source is consumed against the bigger zone of used control microorganism [25].

The sectors of inhibition created by microbes and the growth effects for homopolymer, copolymers, and terpolymer were measured using millimeter ruler at the completion of incubation period and evaluated with standard drug as a referral evaluator. The results are elucidated in Fig. 7 for antibacterial and Fig. 8 for antifungal activities. These results suggest that TNPEBA-AA-AN and CNPEBA-AA show highest antibacterial as well as antifungal activities against applied microbes as comparable with standard drugs such as Ciprofloxacin and Amphotericin-B. The experimental result show that the microbial activity changes with the launch of acrylates moieties and it has been suggested that the abundance of acrylate comonomers in copolymers and terpolymer with N and O donor system, may have restricted the enzyme and protein formation in microbes, because enzymes and protein are required free hydroxyl group for their growth activity and this is utilized in formation of H-bonds so that is the cause to responsible for deactivation of the polymers by the donor atoms [2]. The effectiveness feature of antimicrobial copolymers and terpolymer are related to their abilities to inhibit their growth. Antibacterial and antifungal properties can be granted to a coating and other relevant surficial applications, whenever it is pre-incorporated. Therefore, the microbiological activity of one's copolymers and terpolymer are increased including increases of acrylates (Tables 7 and 8).
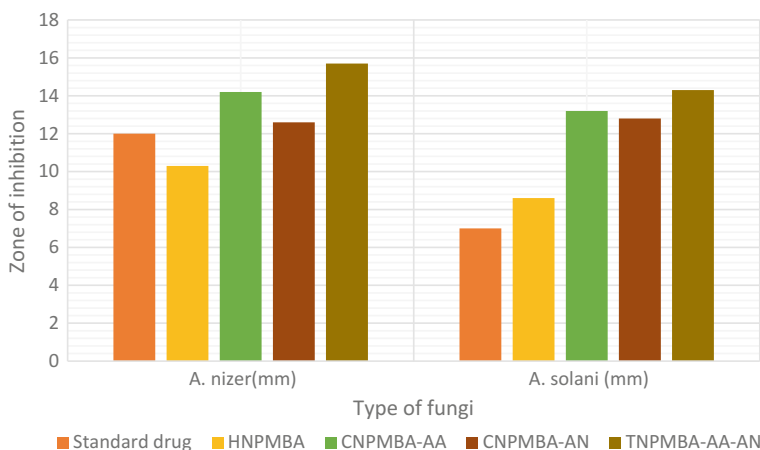
Fig. 8 Relative antifungal activities of homopolymer, copolymers, and terpolymer of NPMBA as compared with standard drug

Table 7 Relative antibacterial activity of polymers of NPMBA

Polymer code	500 (µg/ml) concentration of polymers taken	
	Zone of Inhibition for *E. coli* (mm)	Zone of inhibition for *P. aerogenosa* (mm)
Standard drug	12	14
HNPEBA	10.5	9.7
CNPEBA-AA	17.6	16.8
CNPEBA-AN	15.2	16.2
TNPEBA-AA-AN	18.9	18.1

Table 8 Relative antifungal activity of polymers of NPMBA

Polymer code	500 (µg/ml) concentration of compound taken	
	Zone of inhibition for A. nizer (mm)	Zone of inhibition for A. solani (mm)
Standard drug	12	7
HNPEBA	10.3	8.6
CNPEBA-AA	14.2	13.2
CNPEBA-AN	12.6	12.8
TNPEBA-AA-AN	15.7	14.3

4   Conclusions

Condensation-cum-addition typed free radical homopolymerization, copolymerization, and terpolymerization of NPMBA were executed in the medium of THF with the

incorporation of acrylic acid (AA), acrylonitrile (AN) as comonomer units. The maximum polymerization product yield percentage was achieved in AIBN-THF initiator-polar solvent system which was experimentally selected from various initiator-polar solvent systems. The characterization of polymers was carried out by elemental, FT-IR, and ^{1}H NMR spectral analysis. The synthesized polymers have shown good thermal stability, and thermal decomposition was followed in continuation pattern, which is probably due to the elimination of pendent groups and unzipping into macromeres. The thermal stabilities of polymers depends on the chemical compositions. Glass transition temperatures of polymers were investigated from DSC to finding thermal behavior in the form of flexibility with thermal stability and these properties achieved by mixing of acrylate moieties to reduce Tg temperature and phthalimides brittle property. The antimicrobial properties of the polymers were also investigated in this study. These copolymers and terpolymer may be auspicious materials for high thermal applications and antimicrobial coating applications.

References

1. Hergenrother, P.M.: The use, design, synthesis, and properties of high performance/high temperature polymers: an overview. High Perform. Polym. **15**, 3–45 (2003). https://doi.org/10.1177/095400830301500101
2. Liaw, D.J., Wang, K.L., Huang, Y.C., Lee, K.R., Lai, J.Y., Ha, C.S.: Advanced polyimide materials: syntheses, physical properties and applications. Prog. Polym. Sci. **37**, 907–974 (2012). https://doi.org/10.1016/j.progpolymsci.2012.02.005
3. Naito, K.: The effect of high-temperature vapor deposition polymerization of polyimide coating on tensile properties of polyacrylonitrile-and pitch-based carbon fibers. J. Mater. Sci. **48**, 6056–6064 (2013). https://doi.org/10.1007/s10853-013-7402-x
4. Yang, L., Sun, D.: Synthesis and characterization of terpolymer of N-cyclohexylmaleimide, methyl methacrylate and acrylonitrile. J. Appl. Polym. Sci. **104**, 792–796 (2006)
5. Yang, L., Zhang, L., Liu, G., Gao, J., Yang, S.Y., Jin, R.: Synthesis and thermoanalysis of emulsion terpolymers of N-phenylmaleimide, Styrene and Acrylonitrile. J. Appl. Polym. Sci. **79**, 1067–1073 (2001)
6. Li, Y., Xu, L., Yao, X., Luo, T., Liu, G.: Thermal degradation kinetics of poly {N-[(4-bromo-3,5-difluorine)-phenyl] maleimide-co-styrene} in nitrogen. Int. Symp. Funct. Mater. Conf. Ser. J. Phys. **339**, 2 (2012)
7. Lou, L., Tagaya, A., Ide, Y., Koike, Y., Okamoto, Y.: Copolymers of methyl methacrylate with N-trifluorophenyl Maleimides: high glass transition temperature and low birefringence polymers. J. Polym. Sci. Part A: Polym. Chem. **50**, 3530–3536 (2012)
8. Akihiro, T., Liping, L., Yoko, D.I., Yasuhiro, K., Yoshiyuki, O.: Improvement of the physical properties of poly(methyl methacrylate) by copolymerization with *N*-pentafluorophenyl maleimide; zero-orientational and photoelastic birefringence polymers with high glass transition temperatures. J. Sci. Chin. Chem. **55**, 850–853 (2012)

9. Chaudhary, J., Chauhan, N.P.S.: Synthesis, thermal and antimicrobial properties of copolymers derived from 2,4-dinitrophenylaminomaleimide and alkyl substituted acrylates. Malays. Polym. J. **8**, 18–25 (2013)

10. Hemalatha, P., Veeraiah, M.K., Prasannakumar, S., Anasuya, K.V.: Synthesis, characterization and antibacterial activity of copolymer (N-vinylpyrrolidone-maleic anhydride) with N-diethylethanolamine. Int. J. Res. Eng. Technol. **03**, 33–36 (2014)

11. Rzaev, Z.M.O., Medyakova, L.V., Akovali, G.: Complex-radical alternating terpolymerization of maleic anhydride, *trans*-stilbene and *N*-phenylmaleimide. Macromol. Chem. Phys. **196**, 1999–2009 (1995)

12. Menges, M., Schmidt-Naaka, G.: Effect of molecular structure and composition on rheological behaviour of (methyl methacrylate-Nphenyl maleimide) copolymers. Polymer **40**, 1271–1277 (1999)

13. Anand, V., Choudhary, V.: Studies on the copolymerization of *N*-arylmaleimides with alkyl(meth)acrylate. Macromol. Chem. Phys. **202**, 943–948 (2001)

14. Rzayev, Z.M.O.: Graft copolymers of maleic anhydride and its isostructural analogues: high performance engineering materials. Int. Rev. Chem. Eng. **3**, 153–215 (2011)

15. Teerenstra, M.N., Suwier, D.R., Van Mele, B., Teuwen, L., Maassen, M., Van Den Berg, H.J., Koning, C.E.: Flexibilized styrene- N-substituted maleimide copolymers. I. Multiblock copolymers prepared from styrene/ maleimide telechekics and polytetrahydrofuran. J. Polym. Sci. Part A: Polym. Chem. **38**, 3550–3557 (2000)

16. Woecht, I., Schmidt-Naaka, G.: Free radical copolymerization of methyl methacrylate and N phenylmaleimide in 1-butyl-3- methylimidazolium tetrafluoroborate. Macromol. Symp. **275**, 219–229 (2009)

17. Rzayev, Z.M.O., Turk, M., Uzgoren, A.: Bioengineering functional copolymers. XV. Synthesis and characterization of poly(Nisopropyl acrylamide-*co*-3,4-dihydro-2H-pyran-*alt*-maleic anhydride) s and their PEO branched derivatives. J. Polym. Sci. Part A: Polym. Chem. **48**, 4285–4295 (2010)

18. Ryttel, A.: Copolymerization of ethyl methacrylate with N-(3- or 4-halogenphenyl) maleimides: the monomer reactivity ratios. J. Appl. Polym. Sci. **74**, 2924–2930 (1999)

19. Rzaev, Z.M.O., Guner, A., Kibarer, G., Can, H.K., Asıcı, A.: Terpoly- merization of maleic anhydride, trans-stilbene and acrylic monomers. Eur. Polymer J. **38**, 1245–1254 (2002)

20. Kakimoto, M., Imai, Y.: Precursor method for polymeric LB films. Macromol. Symp. **98**, 1123–1128 (1995)

21. Yuruk, H., Rzaev, Z.M.O., Akovalı, G.: Complex-radical terpolymerization of allylglycidyl ether, maleic anhydride and methyl methacrylate. Design of self-crosslinking macromolecules. J. Polym. Sci. Part A: Polym. Chem. **33**, 1447–1454 (1995)

22. Sortino, S., Cechinel Filho, V., Corrêa, R., Zacchino, S.: N-Phenyl and N-phenylalkyl-maleimides acting against Candida spp.: time-to-kill, stability, interaction with maleamic acids. Bioorg. Med. Chem. **16**, 560–568 (2008)

23. Zhang, S., Li, Y., Yin, D., Wang, X., Zhao, X., Shao, Y., Yang, S.: Study on synthesis and characterization of novel polyimides derived from 2,6-bis (3-aminobenzoyl) pyridine. Eur. Polym. J. **41**, 1097–1107 (2005). https://doi.org/10.1016/j.eurpolymj.2004.11.014

24. Zhuo, L., Kou, K., Wang, Y., Pan, Y., Wu, G.: Synthesis of soluble and thermally stable polyimides with phthalimide as pendent group from pyridine-containing triamine. J. Mater. Sci. **49**, 5141 (2014). https://doi.org/10.1007/s10853-014-8222-3

25. Wang, J., Liu, C., Su, G., Jian, X.: Synthesis and characterization of organo-soluble polyimides containing phthalazinone and bicarbazole moieties in the main chain. High Perform. Polym. **24**, 356–365 (2012). https://doi.org/10.1177/0954008312437587

26. Kim, S.D., Kim, S.Y., Chung, I.S.: Soluble and transparent polyimides from unsymmetrical diamine containing two trifluoromethyl groups. J. Polym. Sci. Polym. Chem. **51**, 4413–4422 (2013). https://doi.org/10.1002/pola.26855